Molecular Dynamics Simulations of 2-(4-butyloxyphenyl)-5-octyloxypyrimidine and 5-(4-butyloxyphenyl)-2-octyloxypyrimidine Liquid Crystal Phases

by

Rodica Pecheanu

A thesis submitted to the Department of Chemistry

In conformity with the requirements for

the degree of Doctor of Philosophy

Queen's University

Kingston, Ontario, Canada

(October, 2009)

Abstract

Molecular dynamics simulations of the liquid crystal phases of 2-(4-butyloxyphenyl)-5-octyloxypyrimidine (2PhP) and 5-(4-butyloxyphenyl)-2-octyloxy-pyrimidine (5PhP) are the focus of this thesis. The 2PhP and 5PhP mesogens display different liquid crystalline phase sequences, despite having very similar molecular structures. Specifically, both mesogens consist of aromatic phenyl and pyrimidine cores in between two flexible alkoxy tails, but they differ in the preferred core conformation.

A multi-site coarse-grained model, in which the aromatic rings are represented by soft quadrupolar ellipsoids and the alkoxy chains are given a united atom representation, is proposed in this thesis. A parameterization route for the intra- and intermolecular potentials appropriate for liquid crystal simulations is developed. The *ab initio* based derivation of suitable molecular models for the two mesogens is discussed in detail, with particular emphasis on capturing proper phenyl-pyrimidine interactions which proved to be essential to correctly represent core-core interactions between neighboring molecules. A systematic determination of suitable Gay-Berne (GB) parameters has been adopted for the aromatic rings of 2PhP and 5PhP. To account for the π electron cloud below and above the ring plane, a quadrupole was added perpendicular to the ring. In the end, four parameterizations for aromatic rings have been selected for the simulations. Model characterization via pair interactions proved to be valuable in identifying and analyzing the short range structure in the phases.

Extensive molecular dynamics simulations of these fluids at various temperatures are performed. Intermolecular structure and order, in aromatic core and the flexible tail regions, are analyzed. Intermolecular structure is divided into contributions parallel and perpendicular to the layers, as indicated by a layer normal or by a director, to differentiate smectic A (SmA) from smectic C (SmC). The presence of a ring quadrupole in the molecular model is shown to be essential to the correct reproduction of the experimentally observed phases. Simulations correctly indicate phases in agreement with experiment: SmC and SmA phases for 2PhP, and only a SmA phase for 5PhP.

Acknowledgements

It is a great pleasure for me to acknowledge the many people who encouraged and helped me both personally and professionally throughout the years.

I would like to thank my supervisor Dr. Natalie M. Cann for her constructive criticism, and thoughtful suggestions during my study period at Queen's University. I learned a great deal about pursuing an idea, doing research, and communicating my results. I would also like to acknowledge the members of my Supervisory Committee, Dr. Robert Lemieux and Dr. Hugh Horton, who provided invaluable advice and encouragements during the meetings. Many thanks to the past and present members of Dr. Cann's research group: Irina Paci, Jenel Vătămanu, Sorin Niţă, Chunfeng Zhao, Shihao Wang, and Mohammad Ashtari, all of whom made my Queen's experience enjoyable.

I also hold deep gratitude for the long line of teachers who laid the foundation of this thesis: my chemistry teachers, Georgeta Podaru and the late Maria Verdeş, who sparkled my interest in chemistry, as well as Dr. Andrei F. Dăneţ from the Chemistry Department of Bucharest University, under whose guidance I worked toward my Master of Science degree. I am also indebted to Prof. Bill Newstead from the Chemistry Department of Queen's University, who helped me uncover my interest in teaching chemistry and improve my teaching skills.

I am deeply grateful to the Ban Righ Foundation for Continuing University Education at Queen's University, to all its staff members – Barbara Schlafer, Lisa Webb, Gamila Abdalla, and Karen Knight - for their friendship, help, advice, and encouragements.

One a more personal note, I would like to thank my husband, Cristi, who encouraged me in this endeavor and stood by me throughout this journey. I also thank my parents, Zinica and Visarion, for their love and support, and for teaching me the most important lesson of my life: to believe that I have the strength to realize my dreams. This thesis is dedicated to the loving memory of my grandmother, Saftica Ghinea.

Financial support from Queen's University and Ban Righ Foundation, and the use of computing resources on HPCVL, SHARCNET, and WESTGRID are also gratefully acknowledged.

Statement of Originality

I hereby certify that all of the work described within this thesis is the original work of the author. Any published (or unpublished) ideas and/or techniques from the work of others are fully acknowledged in accordance with the standard referencing practices.

Rodica Pecheanu

October, 2009

Table of Contents

Abstract ii

Acknowledgements iv

Statement of Originality vi

Table of Contents vii

List of Figures x

List of Tables xviii

List of Abbreviations xx

Chapter 1 Introduction to Liquid Crystals 1

1.1 History of Liquid Crystals 1

1.2 Types of Liquid Crystals 4

1.2.1 Nematic Phase 6

1.2.2 Smectic Phases 6

1.2.3 Chiral Phases 8

1.3 Molecular Structure 11

1.4 Chiral Induction in Liquid Crystal Phases 15

1.5 Computer Modelling of Liquid Crystals 20

1.5.1 Model Potentials for Liquid Crystal Phases 20

1.5.2 The Origin of the Tilt in the SmC Phase 29

1.6 Organization of the Thesis 32

Chapter 2 Computational Methods for Liquid Crystal Simulations 33

2.1 Quantum Mechanics Methods 35

2.1.1 *Ab initio* Method 36

2.1.2 Density Functional Theory Method 39

2.1.3 Basis Functions and Basis Sets 43
2.2 Molecular Dynamics 47
2.2.1 Periodic Boundary Conditions 50
2.2.2 Ewald Summation Technique 53
2.2.3 Velocity Verlet Algorithm for Integration of Equations of Motion 57
2.2.4 RATTLE Algorithm 59
2.2.5 Nosé-Hoover Thermostat 61
2.3 Hybrid Molecular Dynamics - Monte Carlo Method 65
2.4 Force Field 68
2.5 Analysis of Simulation Data 74
Chapter 3 Molecular Models 84
3.1 Intramolecular Potential 88
3.1.1 Host Models 90
3.1.2 Dopant Models 96
3.2 Aromatic Rings 105
3.2.1 Gay-Berne Models 108
3.2.2 Quadrupolar Contribution 112
3.2.3 *Ab initio* Fit 113
3.2.4 Fits to X-ray Data of Benzene 118
3.2.5 Potential Energy Curves of Benzene 126
3.2.6 A Test Case: Liquid Biphenyl 130
3.3 Conclusions 136
Chapter 4 Liquid Crystal Simulations 139
4.1 The Starting Configuration 143
4.2 Preliminary Simulations in the NVT Ensemble 147

4.3 Pair Energies 151
4.4 Simulations of Liquid Crystals in the NPT Ensemble 159
4.4.1 Simulations Details 159
4.4.2 Convergence Issues 162
4.4.3 The Impact of Ring Quadrupole 165
4.4.4 Structure and Order 168
4.4.5 Layering and Phase Behaviour 174
4.4.6 Dynamics 179
4.5 Conclusions 184
Chapter 5 Conclusions and Outlook 187
Bibliography 193
Appendix A Interaction Potentials for Liquid Crystal Molecules 201
Appendix B Interaction Potentials for Chiral Dopant Molecules 203
Appendix C NPT Ensemble Simulations Details 209

List of Figures

Figure 1.1 Schematic representation of the molecular order and arrangement in the nematic (a), smectic A (b), and smectic C (c) liquid crystal phases (reproduced from Ref.[15]).....7

Figure 1.2 Schematic diagram of the molecular order and arrangement in the cholesteric (N*) (a) and chiral SmC* (b) phases (reproduced from Ref.[15]).....9

Figure 1.3 The 4-pentyl-4'-cyanobiphenyl (5CB) (a), and 4-octyl-4'-cyanobiphenyl (8CB) (b) molecules. 12

Figure 1.4 The first three homologues of the phenyl alkyl-4-(4'-cyanobenzylidene)-amino-cinnamate series and the odd-even change of the shape of the fully extended conformation. 14

Figure 1.5 Structures of 2-(4-butyloxyphenyl)-5-octyloxypyrimidine (2PhP), and 5-(4-butyloxyphenyl)-2-octyloxypyrimidine (5PhP) liquid crystal molecules. 16

Figure 1.6 The phase sequences[25,26] for the 2PhP, and 5PhP molecules. Black vertical lines identify the temperatures (in Kelvin) under consideration in this thesis.....17

Figure 1.7 The relative orientation of two ellipsoidal particles defined by the vectors $\hat{u}_A$ and $\hat{u}_B$, describing the orientations of the two particles A and B, and the intermolecular vector $\vec{\mathbf{r}}_{AB}$ . ..22

Figure 1.8 The Gay-Berne potential for $k = 3$, $k' = 5$, $\nu = 2$, and $\mu = 1$ plotted in reduced units for four fixed relative orientations: side-to-side, cross, T-shape, and end-to-end.[42] The distance is plotted in terms of σ_0 whilst the potential is in terms of ε_0 24

Figure 2.1 A 2D periodic lattice built from square unit cells. The colored square illustrates the minimum image representation and the dashed circle shows a spherical cutoff. 51

Figure 2.2 The Ewald sum components of a one-dimensional point charge system.[128] 55

Figure 2.3 Schematic representation of the intramolecular equilibrium parameters r_{eq}, θ_0, and ϕ. 70

Figure 2.4 Schematic representation of an ABCD improper dihedral angle. 71

Figure 2.5 Representation of the Lennard-Jones potential as a function of interatomic separation. 73

Figure 2.6 Radial distribution function uses a spherical shell of thickness $d\mathbf{r}$ around the central particle. 78

Figure 2.7 Schematic representation of the $\vec{r}_{\parallel}^{\,L}$ and $\vec{r}_{\perp}^{\,L}$ vectors relative to layer normal $\vec{\mathrm{L}}$ in (a), and of the $\vec{r}_{\parallel}^{\,D}$ and $\vec{r}_{\perp}^{\,D}$ vectors relative to director $\vec{\mathrm{D}}$ in (b). The interparticle vector, $\vec{r}_{ij}$, is identified by a thick black arrow. 80

Figure 3.1 Single-site coarse-grained (a), multi-site coarse-grained (b), and full atomistic[50] (c) model representations of the 4'-n-pentyl-4-cyanobiphenyl (5CB) mesogen. 85

Figure 3.2 (a) A schematic multi-site coarse-grained representation of the 2PhP and 5PhP molecules. The aromatic units, oxygen atoms, methylene groups, and methyl groups are shown in yellow, red, grey, and blue, respectively. (b) Structure of the 2PhP molecule. (c) Structure of 5PhP molecule. The site numbering and the torsion indexing will be used throughout this thesis. 91

Figure 3.3 Comparison between the phenyl-pyrimidine angle torsional energies. *Ab initio* points are represented by filled squares for 2PhP molecule and open circles for 5PhP molecule, respectively. The solid lines show the torsional potentials obtained by fitting..... 92

Figure 3.4 Torsional barriers from B3LYP/6-311++G(d,p) *ab initio* calculations. The torsional potentials are given for the rotation about (a) GB(6)-O(5), and (b) O(8)-GB(7) bonds in the 2PhP molecule, corresponding to the ϕ_1 and ϕ_3 dihedral angles, respectively. *Ab initio* points are represented by filled squares and fitted potentials by solid lines. 94

Figure 3.5 Torsional barrier from B3LYP/6-311++G(d,p) *ab initio* calculations. The torsional potential are given for the rotation about (a) GB(6)-O(5), and (b) O(8)-GB(7) bonds in the 5PhP

molecule, corresponding to the ϕ_1 and ϕ_3 dihedral angles, respectively. *Ab initio* points are represented by filled circles and fitted potentials by solid lines. 95

Figure 3.6 (a) Schematic multi-site coarse-grained representation of Dop5a-NO_2 molecule. The ellipsoidal GB sites are colored yellow, the oxygen atoms and the methylene and methyl groups are represented by red and grey spherical LJ sites, respectively. (b) Structure of the Dop5a-NO_2 molecule. The site numbering and the torsion indexing will be used throughout this thesis..... 97

Figure 3.7 Torsional barrier from B3LYP/6-311++G(d,p) *ab initio* calculations for the rotation about the GB(7)-GB(6) bond corresponding to the ϕ_1 dihedral angle in the Dop5a-NO_2 molecule. *Ab initio* points are represented by filled diamonds and the fitted potential is given by a solid line. 99

Figure 3.8 Torsional barrier from B3LYP/6-311++G(d,p) *ab initio* calculations for the rotation about the GB(7)-O(8) bond corresponding to the ϕ_2 dihedral angle (a), and the O(8)-C(9) bond corresponding to the ϕ_3 dihedral angle (b), in the Dop5a-NO_2 molecule. *Ab initio* points are represented by filled diamonds and the fitted potentials are given by solid lines..... 100

Figure 3.9 Torsional barrier from B3LYP/6-311++G(d,p) *ab initio* calculations for the rotation about GB(10)-C(9) corresponding to the ϕ_4 dihedral angle, in (a), and the O(11)-GB(10) bond, corresponding to the ϕ_5 dihedral angle, in (b), in the Dop5a-NO_2 molecule. *Ab initio* points are represented by filled diamonds and the fitted potentials are given by solid lines..... 101

Figure 3.10 (a) A schematic multi-site coarse-grained representation of Spiro molecule. The ellipsoidal GB sites, replacing the spirobi[indene] cores, are colored blue, the oxygen atoms and the methylene and methyl groups are represented by red and grey spherical LJ sites, respectively. (b) Structure of the Spiro molecule. The site numbering and the torsion indexing will be used throughout this thesis. 103

Figure 3.11 Torsional barrier from B3LYP/6-311++G(d,p) *ab initio* calculations for the rotation about GB(9)-O(8) bond corresponding to the ϕ_1 dihedral angle in the Spiro dopant molecule. *Ab initio* points are represented by filled triangles and the fitted potential is given by a solid line. . 104

Figure 3.12 Schematic explanation of the parameterization procedure of the GB potential. 107

Figure 3.13 Sandwich (a), T-shaped (b), and parallel-displaced (c) configurations of the benzene dimer.[176] 113

Figure 3.14 The centre-centre radial distribution function, $g_{com\text{-}com}(r)$, evaluated from MD simulation of liquid benzene, using the GBQ1 set of parameters. 116

Figure 3.15 A snapshot obtained from the MD simulation of 500 liquid benzene molecules by employing the fitted GBQ1 set of parameters. The circles identify low density regions. 117

Figure 3.16 Comparison between the C-C radial distribution function of liquid benzene at 300K from X-ray data[155] and the ten selected GBQ2 sets of parameters. Results for ten GBQ2 ring models are shown: A1 (filled squares), A2 (filled diamonds), A3 (open triangle up), A4 (open triangle down), A5 (filled triangle up), A6 (filled triangle down), B1 (open squares), B2 (filled circles), B3 (open diamonds), and C1 (open circles). The *ab initio* data is shown by solid line. 123

Figure 3.17 Potential energy curves of benzene dimer computed using the GB ring models developed in this thesis and the *ab initio* data:[180] (a) face-to-face or sandwich configuration, (b) T-shaped configuration, and (c) slipped–parallel configuration. Results for six selected GBQ2 ring models are shown: A1 (filled squares), A2 (filled diamonds), B1 (open squares), B2 (filled circles), B3 (open diamonds), and C1 (open circles). The *ab initio* curves are shown by solid lines. 127

Figure 3.18 Snapshot of liquid biphenyl at 348 K and 0.9914 g/mL using GBQ2-A1 set of parameters. Each GB site of the biphenyl molecule is colored differently, to better show the random arrangement inside the liquid bulk structure. 132

Figure 3.19 The phenyl ring centre - phenyl ring centre radial distribution functions for liquid biphenyl at 348 K and 0.9914 g/mL, calculated using the six selected GBQ2 sets of parameters. Results for six GBQ2 ring models are shown: A1 (filled squares), A2 (filled diamonds), B1 (open squares), B2 (filled circles), B3 (open diamonds), and C1 (open circles). 133

Figure 3.20 The phenyl ring centre-phenyl ring centre radial distribution functions for liquid benzene and biphenyl, with two different choices of biphenyl ring-ring dihedral angle ($\phi = 30^\circ$ and 90°). The biphenyl MD simulations were carried out at 348 K and 0.9914 g/mL (reproduced from *Tao et al*.'s work[190]). 134

Figure 3.21 Comparison of the calculated and estimated self-diffusion coefficients of liquid biphenyl. Results for six GBQ2 ring models are shown: A1 (filled squares), A2 (filled diamonds), B1 (open squares), B2 (filled circles), B3 (open diamonds), and C1 (open circles). The experimental diffusion coefficients are shown in black line. 135

Figure 4.1 Initial nematic-like starting configuration of 256 2PhP molecules simulated in the NVT ensemble at 0.90 g/mL in a cubic simulation cell, using the A1 ring model. The alkyl chains are represented as grey spheres while the oxygen atoms are shown in red. The phenyl and pyrimidine rings are represented as bulky blue and orange spheres, respectively..... 145

Figure 4.2 Snapshots of 256 2PhP host molecules simulated in the NVT ensemble at 350K and 0.90 g/mL, using the A1 ring model, in simulation cells having different box length ratios. The alkyl chains are represented as grey lines, and oxygen atoms are shown in red. The phenyl and pyrimidine rings are represented as bulky blue and orange spheres, respectively..... 149

Figure 4.3 A schematic representation of a minimization procedure leading to the closest local minimum. 152

Figure 4.4 The pair energy plotted as a function of relative angle between two 2PhP molecules, by means of using the: (a) A1, (b) B1, (c) B2, and (d) C1 ring models, respectively. Each open

circle represents an energy minimization following a random initial structure of the dimer while every filled circle shows the lowest dimer energy obtained with a fixed core-core angle..... 153
Figure 4.5 The pair energy plotted as a function of relative angle between two 5PhP molecules, by means of using the: (a) A1, (b) B1, (c) B2, and (d) C1 ring models, respectively. Each open circle represents an energy minimization following a random initial structure of the dimer while every filled circle shows the lowest dimer energy obtained with a fixed core-core angle..... 154
Figure 4.6 Possible arrangements of 2PhP and 5PhP dimers. The alkyl chains and oxygen atoms are represented by grey and red spheres, respectively. The phenyl and pyrimidine rings are represented by bulky yellow and blue spheres, respectively. 155
Figure 4.7 The pair energy plotted as a function of relative angle between two 2PhP molecular cores in (a) and as a function of phenyl-phenyl ring separation in (b). Each dot in (a) represents an energy minimization following a random initial structure of the dimer. Results are presented for the A1 model. In (a), green, red, and blue circles identify configurations where the inter-phenyl distance is between 3.4-4.4 Å, 4.4-5.8 Å, and 5.8-7.3 Å, respectively. Only configurations with an energy less than -10 kJ/mol contribute in (b)..... 158
Figure 4.8 Convergence tests illustrated for 2PhP (B1 ring model) at 365K. (a) Phenyl-phenyl radial distributions are shown for five independent 2 ns simulations (open circles, filled circled, open diamonds, open squares, filled squares). Their average is shown with a thick solid line. (b) The distribution from a single 12 ns simulation (open triangle down) is compared with the average over five independent 2 ns simulations (thick solid line). (c) Aggregate distribution functions parallel (thick solid line) and anti-parallel (filled triangle up) starting configurations. 164
Figure 4.9 The impact of the ring quadrupole on the liquid crystal phase of 2PhP at 365K. Phenyl-phenyl distributions are compared for B1 model (open squares) and C1 model (open circles). Radial distributions, second order correlations, structure perpendicular to the director, and structure parallel to the director are compared in (a), (b), (c), and (d) respectively..... 166

Figure 4.10 A comparison between tail and core structures in the 5PhP liquid crystal phase at 370K, as predicted from the B1 model. In (a), (b), and (c), distributions between C(1)-C(1), phenyl-phenyl, pyrimidine-pyrimidine, and C(16)-C(16) are shown by solid circles, solid squares, open squares, and open circles, respectively. Panel (a) compares radial distribution functions while perpendicular and longitudinal distributions, relative to the director obtained from the phenyl-pyrimidine core axes, are shown in (b) and (c). Panel (d) shows intermolecular orientational distribution functions as determined from the phenyl-pyrimidine axis (solid circles), C(1)-C(2) axis (solid squares), and the C(15)-C(16) axis (solid diamonds). 170

Figure 4.11 The time evolution of order parameters for 5PhP, at 370K, as represented by the B1 model. Order relative to the "directors" defined from the phenyl-pyrimidine, C(1)-C(2), and C(15)-C(16) axes are represented by red, blue, and green, respectively. The P_2, P_3, and P_4 order parameters are shown in (a),(b), and (c), respectively. In (a), the P_2 order parameter describing the consistency between local (molecular) layers normal is shown in black. 173

Figure 4.12 Snapshots from the 256 molecule simulations using the B1 model. Snapshots from three independent simulations are shown for (a) 2PhP at 335 K, (b) 2PhP at 365K, and (c) 5PhP at 370K. The alkyl chains are represented as grey lines, and oxygen atoms are shown in red. The phenyl and pyrimidine rings are represented as bulky blue and orange spheres, respectively. ... 175

Figure 4.13 The distribution between phenyl rings in 2PhP (B1 ring model) analyzed according to contributions perpendicular and parallel to the director (filled squares) and the layer normal (open squares). Results are shown for 335K (a), 365K (b), 400K (c), and 450K (d). 177

Figure 4.14 The distribution between phenyl rings in 5PhP (B1 ring model) analyzed according to contributions perpendicular and parallel to the director (filled squares) and the layer normal (open squares). Results are shown for 370K (a), 400K (b), and 450K (c). 178

Figure 4.15 Instantaneous fluctuations for 2PhP at 365K (left) and 5PhP at 370K (right), as represented by the B1 model. Red, blue, and green pertain to the phenyl-pyrimidine, C(1)-C(2),

and C(15)-C(16) vectors in the molecule, respectively. In (a), the P_2 order parameter describing the consistency between local (molecular) layers normal is shown in black. Fluctuations in the order parameter associated with each of the vectors are shown in (a). The angles θ_1 and θ_2, evaluated from Equations (2.51) and (2.52), are given in (b) and (c). Fluctuations in the density are shown in (d). 180

List of Tables

Table 1.1 The phase sequence of the first four homologues of the phenyl alkyl-4-(4'-cyanobenzylidene)aminocinnamate series 13

Table 3.1 The GBQ1 set of parameters obtained by fitting to *ab initio* potential energy curves[180, 181] of benzene dimer. 115

Table 3.2 Parameters of the GB model potential. 119

Table 3.3 The six selected GBQ2-A n sets of parameters ($Q^* = -0.2486$ reduced units). 121

Table 3.4 The three selected GBQ2-B n sets of parameters ($Q^* = -0.1868$ reduced units). ... 121

Table 3.5 The selected GBQ2-C n set of parameters (no point quadrupole). 122

Table 3.6 Comparison of calculated and experimental self-diffusion coefficients of liquid benzene. 125

Table 4.1 Calculated average $\langle P_2 \rangle$ order parameters for systems of 256 2PhP host molecules simulated in the NVT ensemble using the A1 ring model, in parallelepipedic cells of different box length ratios..... 148

Table 4.2 Calculated average $\langle P_2 \rangle$ order parameters for systems of 256 5PhP host molecules simulated in the NVT ensemble using the A1 ring model, in parallelepipedic cells of 1:1:2 box length ratio. 148

Table 4.3 Average tilt angles, in degrees, P_2 order parameters for the director and the layer normal, and the average density, in g/mL. Results are reported for the averages over for 5PhP at 370K and 2PhP at 335K and 365K. The angles θ_1 and θ_2 are evaluated from Equations (2.51) and (2.52), respectively. The properties for 2PhP at 335K and 365K and 5PhP at 370K represent averages over five independent 2 ns simulations. Properties at 400K are obtained from averages

over three 2 ns simulations while 450K properties are obtained from averages over two 2 ns simulations. 183

List of Abbreviations

2D	2-Dimensional
2PhP	2-(4-butyloxyphenyl)-5-octyloxypyrimidine
5PhP	5-(4-butyloxyphenyl)-2-octyloxypyrimidine
5CB	4-pentyl-4'-cyanobiphenyl
8CB	4-octyl-4'-cyanobiphenyl
AO	Atomic Orbital
AMBER	Assisted Model Building with Energy Refinement
B3LYP	Becke three parameter exchange functional plus Lee-Yang-Par correlation functional
CG	Coarse-Grained
CGTO	Contracted Gaussian-Type Orbital
CHARMM	Chemistry at HARvard Molecular Modelling
CHELPG	CHarges from ELectronic Potentials using a Grid based method
D	Diffusion Coefficient
DFT	Density Functional Theory
Dop5X-NO_2	2,2',6,6'-tetramethyl-3,3'-dinitro-4,4'-bis[(4-alkyloxybenzoyl)-oxy]biphenyl, X indicates the length of the alkyl chain
GB	Gay-Berne

GBQ1	Gay-Berne model potential fitted to *ab initio* data
GBQ2	Gay-Berne model potential fitted to X-ray data
GTO	Gaussian-Type Orbital
HF	Hartree-Fock
LJ	Lennard-Jones
MC	Monte Carlo
MD	Molecular Dynamics
MM2,3,4	Molecular Mechanics Force Field - 2^{nd}, 3^{rd}, 4^{th} Edition
MP2	Möller-Plesset Perturbation Theory
MSD	Mean Square Displacement
OPLS	Optimized Potential for Liquid Simulations
PBC	Periodic Boundary Conditions
RDF	Radial Distribution Function
Spiro	5,5'-bis(heptyloxy)-2,2'-spirobi[indene]-1,1'(3*H*,3'*H*)-dione
STO	Slater-Type Orbital

Chapter 1

Introduction to Liquid Crystals

1.1 History of Liquid Crystals

It is a commonly held belief that the first material known to exhibit two distinct melting points (*i.e.* cholesteryl benzoate) was reported by the Austrian botanist Friedrich Reinitzer in 1888. He later turned for help to the German physicist Otto Lehmann, who realized that the cloudy liquid belongs to a league of its own and named the new state of matter "fliessende krystalle" to illustrate that it was something between a liquid and a solid.[1] In the beginning, all the liquid crystalline substances investigated were naturally occurring, but as early as 1890 the first synthetic liquid crystal, p-azoxyanisole, was prepared by Gatterman and Ritschke.[1]

Daniel Vorlänger, a German chemistry professor, is remembered as the "father of liquid crystal" technology because of his systematic synthetic work, done over a 30 year period, that shows the connection between the molecular structure of compounds and the occurrence of a liquid crystal phase, as well as of the discovery of polymorphism in 1906.[2]

In 1922, Friedel[3], a French crystallographer, suggested a classification scheme, which is still in use today, with different phases of liquid crystals called *nematics*,

smectics, and *cholesterics*. These mesomorphic ("meso" comes from the Greek word meaning "in between") forms of matter are distinct from the crystalline and liquid forms, and possess properties which cannot be found in either of the types of matter previously known. The most atypical feature is the combination of long range order (common to crystals) and mobility (as in liquids) which gives rise to materials having anisotropic physical properties (*i.e.* the properties of the materials differ depending on the direction in which they are measured) switchable under the influence of external stimuli.

Liquid crystalline materials remained a scientific curiosity for almost 80 years. In the early 1960s, only a few institutions and corporations were known to have been carrying out research in the field of liquid crystals.[4] Around that time, a French theoretical physicist, Pierre-Gilles de Gennes, turned his attention to liquid crystals and found captivating analogies between them and superconductors as well as magnetic materials. For his contribution to the modern development of liquid crystal science, de Gennes was awarded the Nobel Prize in Physics in 1991.[5]

Nowadays, liquid crystals are an important field of research for scientists from many different disciplines. For mathematicians, liquid crystals are a natural laboratory for broken symmetries and practical applications of pure mathematics (such as topology).[6] For the engineering community, cheap and compact liquid crystal display (LCD) technology provides the best replacement for the bulky cathode ray tube. LCD technology is now used in wrist-watches, telephones, computer monitors, and TV screens.[7] Chiral smectic materials are used for a wide range of electro-optical devices, including micro-colour filters, tunable colour filters, and spatial light modulators.[8] Liquid

crystalline materials are also used by biologists as building blocks for the much needed soft tissue out of which living cells and cell aggregates are made. The medical community is interested in liquid crystal research too. For example, liquid crystal temperature sensors are used in investigations of tumors and circulatory disorders.[9] Moreover, biosensors using liquid crystal technology are used for virus and bacterial detection.[9] Finally, for physicists and chemists, liquid crystals have been a source of considerable interest. More recent applications of liquid crystal technology involve polymer dispersed liquid crystals with wider viewing angle[10] or switchable windows[9] that can be changed from clear to opaque with a flip of a switch.

1.2 Types of Liquid Crystals

Liquid crystals are a different state of matter apart from the well-acknowledged *solid*, *liquid*, and *vapour* phases. A solid phase is characterized by its rigid arrangement of constituent molecules, which stay in a fixed position and orientation except for a small amount of variation. In the liquid phase, the molecules are free to move, having no fixed position and orientation, thus the phase is disordered although short range local structure exists. In the vapour phase, the motion of the molecules has increased to overcome intermolecular forces. As a consequence, the molecules spread out to fill any container that holds them.

Some substances exhibit intermediate states lacking some of the order found in solids, and still are more ordered than an isotropic liquid. These thermodynamically stable states, characterized by the simultaneous presence of both order and disorder, are either plastic crystals or liquid crystals. From the structural point of view, they are both formed by partial melting of solid crystals in which the plastic crystals retain translational order, whilst liquid crystals preserve orientational order. Plastic crystals exist over a narrow temperature range, sufficiently high to overcome any rotational energy barriers and sufficiently low to not disrupt the lattice structure. However, plastic crystals consist of highly symmetric molecules as opposed to liquid crystals, which are formed by elongated or disk shape molecules.

The liquid crystal (LC) phases are also called *mesophases* or *mesomorphic phases, s*ince these types of phases are observed on the temperature scale between the true crystalline and liquid phases. The particles forming liquid crystal phases are called *mesogenic*, thus the term *mesogen* refers to a molecule that forms a *mesophase.* Liquid crystal phases have some unique characteristics based on the fact that the constituent mesogens exhibit a strong *anisotropy* in their molecular shape: they tend to be either elongated or disk-like.

Liquid crystals can be divided into two main classes: *thermotropic* and *lyotropic*.[11] The liquid crystals Reinitzer discovered are called *thermotropic* liquid crystals. By raising the temperature, their state changed from crystal to liquid crystal at temperature T_1, and when increasing the temperature further the state changes again from liquid crystal to isotropic fluid at temperature T_2. In principle, the process is reversible by lowering the temperature, though there may be a small temperature hysteresis. Thus, the prefix *thermo* refers to phase transition generated by a change in temperature. By contrast, the *lyotropic* (*lyo* refers to concentration) liquid crystal phases form in solution and thus, the liquid crystallinity is controlled by both concentration and temperature. In addition, there are some compounds able to form thermotropic as well as lyotropic liquid crystals, and they are named *amphotropic*.[4]

Considering the shape of the constituent molecules, liquid crystals can be classified as: *calamitic* (occurring in rod-like or cigar-like molecules) - considered as classical liquid crystals, *discotic* (derived from disk-like molecules) - discovered by Chandrasekhar,[12] *banana-shaped* liquid crystals (bent-core molecules incorporating a

rather rigid bent aromatic core),[13] and *sanidic* (occurring in lath-like or board-like molecules) - first found in polymeric liquid crystals.[4, 14] The shape of the constituent molecules has a vital influence on the phase structure of the liquid crystals. Beside the fact that compounds with different shapes can form similar phases, the same compound may also exhibit several different phase structures. The liquid crystal phases can be divided into several types of sub-phases that differ in the degree of orientational ordering. Three important sub-phases, namely the nematic, smectic, and chiral phases, are discussed as follows.

1.2.1 Nematic Phase

In the nematic phase ("nematos" comes from the Greek word meaning "thread-like") there is no long range translational order, but the molecular axes tend to align more or less along a certain direction called the director, $\mathbf{D}$. This is a one-dimensional ordered phase and the simplest liquid crystalline phase, since the constituent molecules can translate freely and rotate around their long axes, resulting in a much lower viscosity than that for other liquid crystal phases. A schematic representation of a typical nematic phase is shown in Figure 1.1 (a).

1.2.2 Smectic Phases

In the smectic liquid crystal phases ("smectos" comes from the Greek word meaning "clay" or "grease"), the molecules are arranged in layers and show both orientational and translational order. For the latter, the order is short ranged within the layer but long ranged between layers. Thus, in the family of smectic phases, the long-range orientational

order is preserved and some degree of translational order is present in one dimension where the molecules are arranged on average in equidistant layers. The layers can slide relative to each other leading to high viscosity flow. The smectic phase is divided in several sub-phases with slightly different properties, and these are typically distinguished by a letter and denoted as smectic A, smectic B, etc. The most frequently observed phases, smectic A (SmA) and smectic C (SmC), are considered in this thesis and schematically presented in Figures 1.1 (b) and (c).

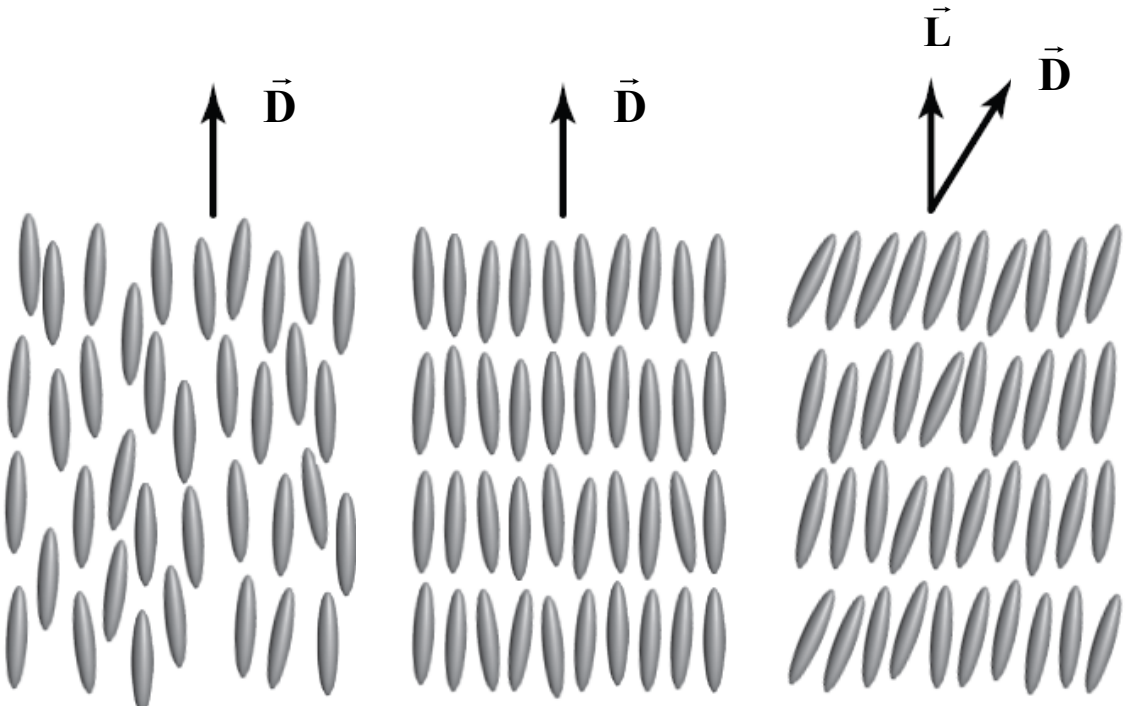

Figure 1.1 Schematic representation of the molecular order and arrangement in the nematic (a), smectic A (b), and smectic C (c) liquid crystal phases (reproduced from Ref.[15]).

In the SmA phase, the axes of orientational and positional order coincide, thus the director, $\mathbf{D}$, is parallel to the smectic layer normal, $\mathbf{L}$. Typically, the average distance between the layers (usually called "smectic layer spacing" or "layer thickness") is smaller than the molecular length in compounds having longer alkyl chains, and can exceed the length of the molecule in compounds having strongly polar groups (*i.e.* longitudinal cyano or nitro substituents).[4] Inside the layers, the molecules move like a liquid and there is little correlation among the molecules belonging to adjacent layers.

By contrast, in the SmC phase, orientational and positional orders are observed along different axes in space. In this case, the director is tilted compared to the layer normal and a twist occurs along the normal but not parallel to the layers. The molecules forming the SmC phase are tilted in a preferred direction inside the layers, and the tilt direction of the molecules in various layers is correlated. The director, $\mathbf{D}$, is tilted with respect to the layer normal, $\mathbf{L}$, by the tilt angle, θ.

1.2.3 Chiral Phases

A molecule which is not superimposable on its mirror image is known as a *chiral* molecule. In liquid crystalline phases, chirality gives rise to the formation of helical superstructures in nematic phases (so-called cholesteric phases, noted N*), and tilted SmC phases (noted SmC*), as seen in Figures 1.2 (a) and (b). Chirality can induce additional phases exhibiting complex structures which do not occur in non-chiral liquid crystals, *e.g.* blue phases, smectic blue phases, twist grain boundary phases and several other 3D-ordered mesophases.[13]

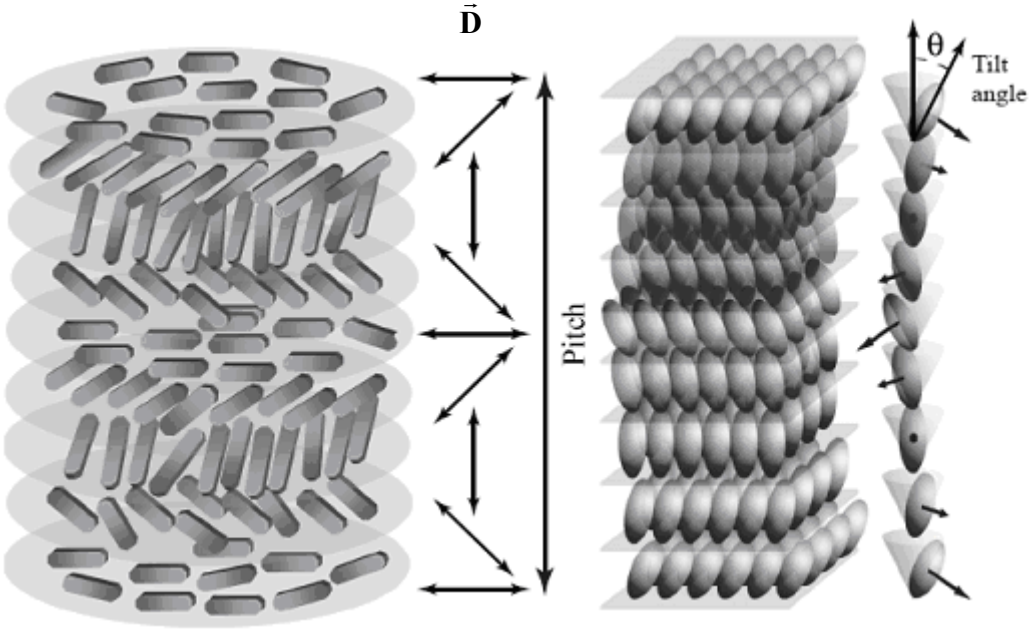

(a) (b)

Figure 1.2 Schematic diagram of the molecular order and arrangement in the cholesteric (N*) (a) and chiral SmC* (b) phases (reproduced from Ref.[15]).

The chiral nematic or cholesteric liquid crystal phase is actually a nematic phase with additional helical change in the orientation of the director. The chiral molecules arrange themselves in the direction normal to the director and they pack to form a helical macrostructure rotating the director in a direction perpendicular to the long axis of the molecules. Contrary to the nematic phase in which the director has a constant direction, in a cholesteric phase it changes direction throughout the fluid. The cholesteric helix axis, which is non-superimposable on its mirror image, gives rise to supermolecular chirality. Similar to the nematic phase, the molecules have no long range positional order, and no layering exists. The helical internal structure has a characteristic pitch along the helix in

which the director rotates a full 360 degrees. The fact that each chiral nematic liquid crystal reflects light, having a characteristic wavelength determined by its pitch and by the viewing angle, is the key to the operation of cholesteric liquid crystal displays.[7]

In *chiral smectic C* phases (SmC*), the director rotates from layer to layer around the cone generated by the tilt angle forming a helical structure. The helix can be suppressed by placing the liquid crystal between two glass plates.[7] When this occurs and the directors in each layer are forced to lie in the plane of the glass plate, the chiral nature of the molecules creates a spontaneous polarization within each layer. Ferro-electric (FE) and Antiferro-electric (AF) Liquid Crystal Displays operate by applying an electric field which couples with the spontaneous polarization and switches the director in the layers.[16] The apparition of spontaneous polarization gives rise to chiral smectic LC phases (*e.g.* SmC* and SmC_A* phases).[17]

It is important to point out that there are non-chiral liquid crystal molecules able to form chiral layers. Molecules with a bent core, also known as *banana-shaped molecules,*[13] show chiral layers in the liquid crystalline state. Here, the polar order in combination with the tilt of the molecules is responsible for the occurrence of chirality. In this configuration the layer normal, the tilt direction and the polar axis define a chiral system which is either right- or left-handed. Moreover, the polar packing of the banana-shaped molecules can induce FE or AF structures.[18]

To conclude, chirality plays a vital role for many liquid crystal applications, in particular for electro-optical diplays and thermochromic temperature displays.[13]

1.3 Molecular Structure

The type of LC phases that a mesomorphic material can form depends fundamentally on the molecular properties of the substance. One of the important factors in the formation of liquid crystal phases is an overall strong anisotropy of the molecular shape of the mesomorphic compound. Another factor is the difference in chemical properties of the two distinct moieties that usually form the mesomorphic compound. In particular, compounds that possess one of the following pairs of molecular combinations: aliphatic / aromatic, flexible / rigid, or polar / nonpolar, are promising candidates for liquid crystal phase formation. Most of the time, calamitic mesogens contain a rigid core linked to one or more flexible alkyl chain(s). Moreover, these moieties give a dual personality to the overall molecule, and different parts of the molecular structure interact locally with similar regions of neighbouring molecules causing a type of internal phase separation. Ideally, there should be a balance between these interactions (strong and weak) in order for both to operate, although they should be restricted to different regions. The stability of LC phases can be amplified by increasing the lengths or polarizability of the molecules,[19] for example by adding a terminal cyano group to enhance polar interactions between the molecules.

The length of the hydrocarbon chain(s) at terminal positions of the mesogen plays an important role in determining the phase structure. As a general rule,[20] the compounds having short alkyl chains tend to be nematogens, while those having longer alkyl chains are smectogens.

A classical example of a room-temperature mesogen is the *n*-cyanobiphenyl or *n*CB family, shown in Figure 1.3. The rigid core is a *para* substituted biphenyl unit, having a flexible tail, an alkyl chain of n carbons $\left(C_nH_{2n+1}\right)$ at one end, and a polar cyano group at the other.

(a)

(b)

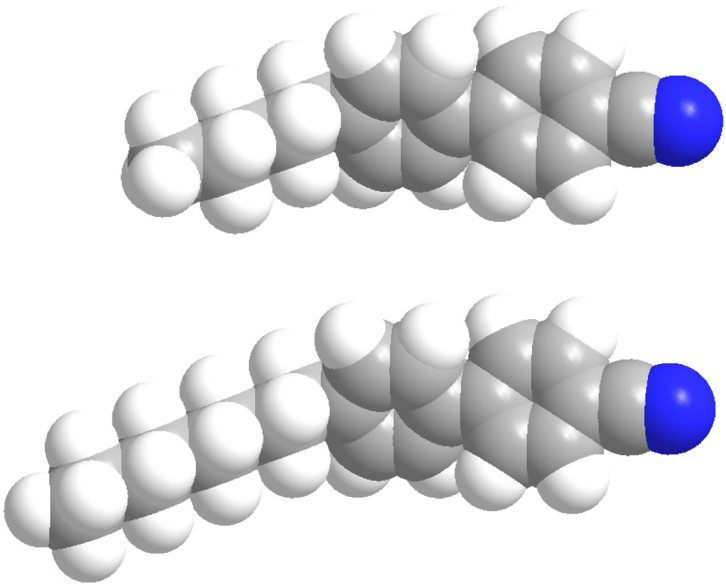

Figure 1.3 The 4-pentyl-4'-cyanobiphenyl (5CB) (a), and 4-octyl-4'-cyanobiphenyl (8CB) (b) molecules.

The influence of the alkyl chain length is apparent from a comparison of the phase sequence of 5CB and 8CB, in which a longer alkyl chain adds a smectic phase on top of a nematic phase:

5CB: *Crystal* $23^{\circ}C$ *Nematic* $35^{\circ}C$ *Isotropic*

8CB: *Crystal* $21^{\circ}C$ *SmC* $32.5^{\circ}C$ *Nematic* $40^{\circ}C$ *Isotropic*

Another standard demonstration of the strong coupling between the molecular structure and phase behavior is the so-called "odd-even" effect, which corresponds to large alternations in the properties and the phase transition temperatures for the homologous series containing an *n*-alkyl chain, as *n* varies from even to odd (Table 1.1).

Table 1.1 The phase sequence of the first four homologues of the phenyl alkyl-4-(4'-cyanobenzylidene)aminocinnamate series

Alkyl chain length	Phase Sequence					
n=0:	*Crystal*	169.0° *C*	*Nematic*	280.0° *C*	*Isotropic*
n=1:	*Crystal*	38.6° *C*	*Nematic*	160.6° *C*	*Isotropic*
n=2:	*Crystal*	146.0° *C*	*Nematic*	187.8° *C*	*Isotropic*
n=3:	*Crystal*	36.5° *C*	*Nematic*	95.0° *C*	*Isotropic*

In the case of phenyl alkyl-4-(4'-cyanobenzylidene)aminocinnamate series, the large difference in transition temperature is qualitatively explained[21, 22] by the observation that the terminal phenyl ring lies in line with the long molecular axis in the most extended conformation only for the n=0,2 alkyl chain spacers (Figure 1.4).

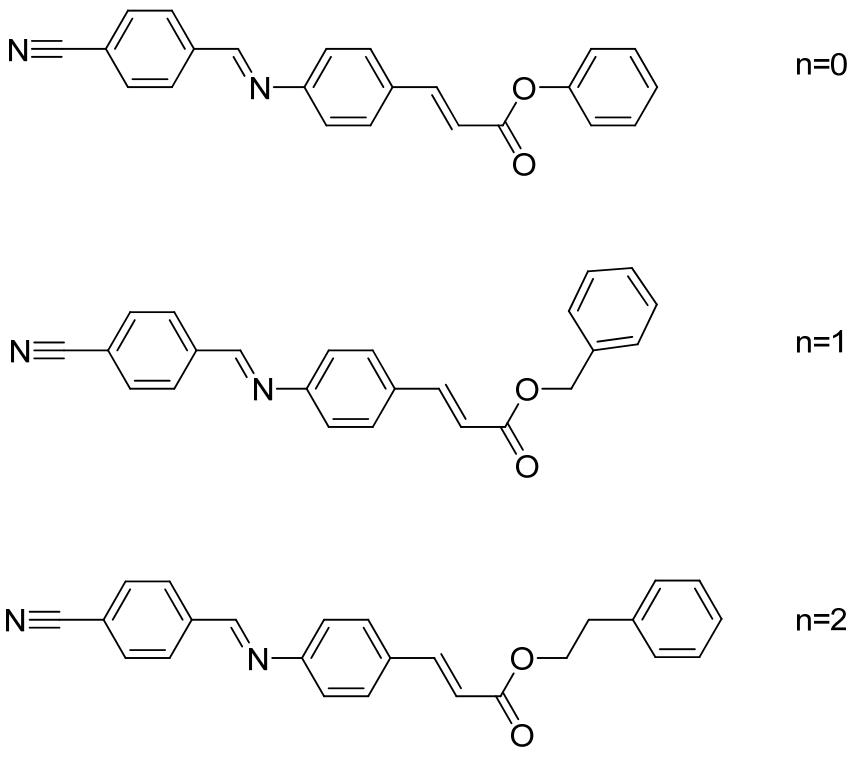

Figure 1.4 The first three homologues of the phenyl alkyl-4-(4'-cyanobenzylidene)-amino-cinnamate series and the odd-even change of the shape of the fully extended conformation.

Consider the dihedral angle of the alkyl chain attached to the terminal phenyl ring. The *gauche* conformations of the even alkyl chain dihedral angle permit the chain to lie along the molecular axis, such that the nematic phase is favored. Contrarily, the *gauche* conformations of odd alkyl chains force the ring to be positioned at an angle to the molecular axis, so that the nematic phase is disfavored. In this case, the position of the phenyl ring relative to the molecular axis defines the overall shape of the molecule, which in turn influences the transition temperatures.

1.4 Chiral Induction in Liquid Crystal Phases

Chiral liquid crystal phases can either consist of exclusively chiral molecules or an achiral phase with a chiral dopant dissolved throughout.

When a small amount of chiral molecule (dopant) is added to an achiral mesogen (host), it can transmit its chirality to the bulk system giving the liquid crystal a right- or left-handed helical twist. Thus, chiral bulk properties, such as the helical structures of chiral nematic (N*) and chiral smectic C (SmC*), and the spontaneous polarization of the SmC* phase, can be induced in achiral liquid crystals. The dopant itself may or may not have a liquid crystalline phase. The sign and the magnitude of the chiral perturbation strongly depend on the type and quantity of the dopant used, the structures of the host and dopant molecules, as well as the temperature and pressure of the fluid. The helical twisting power is an intrinsic parameter to every host-dopant combination and expresses the efficiency with which a dopant induces a helical organization in an achiral liquid crystal host.

There are some advantages of doped LCs over the cholesteric LCs made up from chiral mesogens.[23] Specifically, the pitch can be tuned by changing the host-dopant ratio or/and the nature of the chiral dopant. Moreover, the colour of a doped liquid crystal can be adjusted by changing the concentration, enantiomeric excess or helical twisting power of the chiral dopant. A quantitative correlation between the structures of chiral dopant molecule and the helicity of the chiral liquid crystal phase exists only for a few classes of

coumpounds.[17] A complete description of the structure/response relationship is still lacking.

Ferro-electric liquid crystals suitable for display applications are usually induced SmC* phases obtained by mixing a small amount of a chiral dopant with high polarization power into a SmC liquid crystal host having low viscosity and broad temperature range.[24]

Simulations of achiral host molecules are the focus of this thesis. The liquid crystal molecules considered in this thesis, namely the 2-(4-butyloxyphenyl)-5-octyloxypyrimidine (2PhP), and 5-(4-butyloxyphenyl)-2-octyloxy-pyrimidine (5PhP), possess both aliphatic and aromatic regions as well as flexible and rigid parts. These mesogens have been well-characterized experimentally,[25, 26] in particular, with respect to the chirality transfer into these "hosts" when chiral dopants are added. The two liquid crystals are presented in Figure 1.5 while their phase sequences are shown in Figure 1.6.

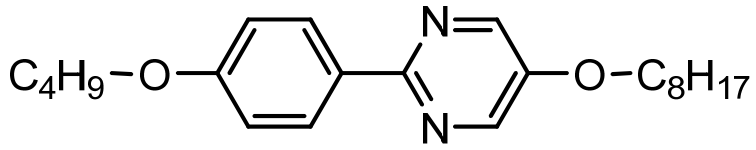

2PhP

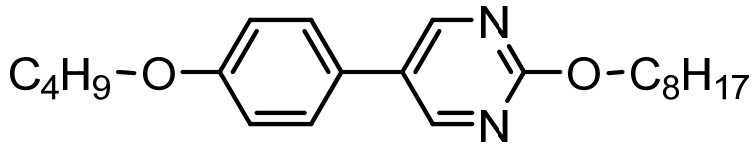

5PhP

Figure 1.5 Structures of 2-(4-butyloxyphenyl)-5-octyloxypyrimidine (2PhP), and 5-(4-butyloxyphenyl)-2-octyloxypyrimidine (5PhP) liquid crystal molecules.

Despite the close resemblance of the shape of the two liquid crystals, their phase sequences are quite different: the 2PhP molecule shows a broad SmC phase, a SmA phase, and a narrow nematic phase[25] while the 5PhP forms only a SmA phase[26] between the crystal and liquid phases. The different positions of the nitrogen atoms in the pyrimidine rings of the two mesogens are the main factor influencing the distinction between their phase sequences.

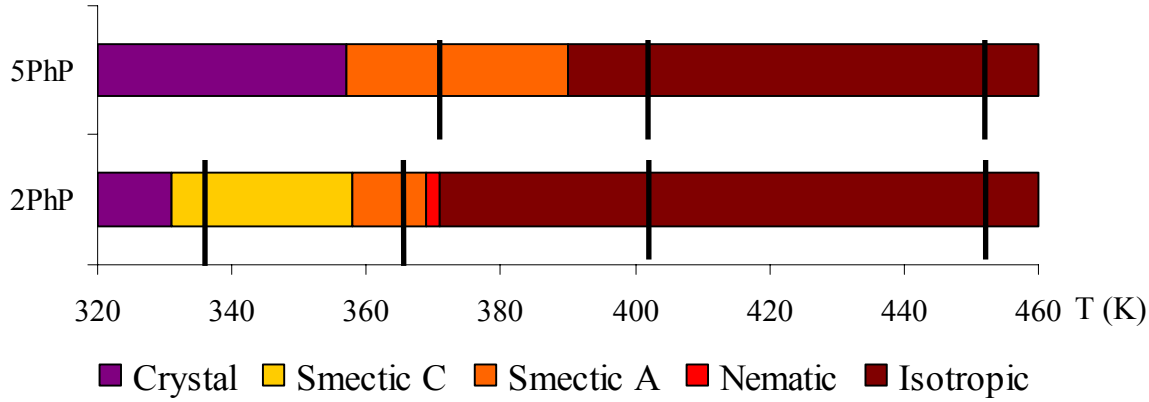

Figure 1.6 The phase sequences[25,26] for the 2PhP, and 5PhP molecules. Black vertical lines identify the temperatures (in Kelvin) under consideration in this thesis.

The chiral dopants used to induce chirality into a liquid cystal host are classified, depending on the position of the chiral element, as follows: (1) a type I chiral dopant, in which the chiral center(s) is situated in an alkyl side chain, and (2) a type II chiral dopant, bearing chiral center(s) in the rigid core.[27] Characteristic of the type I chiral dopant is the fact that, generally, the magnitude of the induced polarization power does not depend significantly on the structure of the SmC host. On the contrary, the polarization power of a type II chiral dopant depends on the nature of the SmC host. For these reasons, type I

chiral dopants are known as “passive dopants” whilst the type II chiral dopants are been seen as “active dopants”. [24, 28]

For example, the 5,5’-bis(heptyloxy)-2,2’-spirobi[indene]-1,1’(3*H*,3’*H*)-dione (named Spiro) and the 2,2’,6,6’-tetramethyl-3,3’-dinitro-4,4’-bis[(4-alkyloxybenzoyl)-oxy]biphenyl (abbreviated Dop5X-NO_2, where X indicates the length of the attached alkoxy chains) are chiral molecules acting as type II dopants in many experimental studies. Specifically, it has been shown experimentally that the polarization power (δ_P) of Dop5X-NO_2 dopants depends strongly on the core structure of the achiral SmC host.[25] For instance, the polarization power of Dop5a-NO_2 dopant (the alkoxy chain has only one carbon atom) varies from -1738 nC/cm^2 (in the 2PhP host) to less than -30 nC/cm^2 (in a host with a phenyl benzoate core) depending on the nature of SmC host, over the same mole fraction range.[25] Moreover, measurements of δ_P as a function of the length of the Dop5X-NO_2 dopants side chains revealed that the spontaneous polarization power induced in the 2PhP is influenced by the length of the alkoxy side chains, so that δ_P is highest with octyloxy side chains (*i.e.* -1738 nC/cm^2), and decreases sharply as the side chains are shortened (*e.g.* -505 nC/cm^2 for the butyloxy derivative). The effect of increasing the length of the dopant side-chains on δ_P is correlated with an increase of the orientational order of the dopant in the smectic layer which enforces the propagation of chiral perturbation via core-core interactions.[29]

More recent studies proved that it is possible to amplify the polarization power induced by the chiral atropisomeric biphenyl dopants in the SmC 2PhP achiral host by

using achiral hosts as additives.[30] These results confirmed that it is possible to rationally design achiral additives capable of amplifying the polarization power exerted by a chiral dopant in a SmC host. For instance, the reduced polarizations have been measured in the SmA* and SmC* liquid crystal phases formed by 4 mol% mixtures of the chiral 2,2',6,6'-tetramethyl-3,3'-dinitro-4,4'-bis[(4-alkyloxybenzoyl)-oxy]biphenyl in the binary host mixture of 2PhP and 5PhP over the mole fraction range $0 \leq x_{5PhP} \leq 0.24$. It has been found that the chiral perturbation propagates more effectively in the presence of the 5PhP as co-host, due to its twisted chiral core conformation.

Furthermore, the axially chiral dopant (R)-5,5'-bis(heptyloxy)-2,2'-spirobi-[indene]-1,1'(3*H*,3'*H*)-dione (Spiro) has been synthesized in optically pure form,[31] and has been doped in four achiral liquid crystal hosts to give SmC* phases with spontaneous polarizations that vary with the core structure of the host. In particular, the addition of Spiro chiral dopant to the 2PhP liquid crystal host causes a severe destabilization of the SmC phase, whilst the calculated polarization power (δ_P) reaches a value of +749 nC/cm^2.[32] The high positive value of the polarization power evaluated for Spiro dopant in the 2PhP host is correlated to the length of the host core (9.7 Å).

1.5 Computer Modelling of Liquid Crystals

Molecular modelling investigations permit finding a link between microscopic and macroscopic properties and have been successfully applied in the field of liquid crystals, mainly restricted to achiral liquid crystals, *e.g.* nematic and smectic phases.

1.5.1 Model Potentials for Liquid Crystal Phases

At the heart of any simulation is the model potential describing how the molecules interact with each other. Different types of model potentials appropriate for the modelling of liquid crystals have been developed. Generally, model potentials can be divided into four classes: (1) lattice models, (2) single-site models, (3) atomistic models, and (4) multi-site coarse-grained models.

In the idealized *lattice model*, proposed by *Lebwohl and Lasher,*[33] the system is considered as a set of classical spin vectors located on the sites of a cubic lattice, with nearest neighbor interactions of the following form:

$$U_{ij} = -\frac{\varepsilon}{2}\left(3\cos^2\theta_{ij} - 1\right) \tag{1.1}$$

where θ_{ij} is the angle between the two vectors, and ε is an energy parameter. Particular to this model is the representation of a small region of the liquid by each site, symbolizing the locally-arranged nematic ordering within, and not necessarily a single molecule.

The *single-site off-lattice models*, the next step in increasing the complexity of the molecular model adopted, include both hard and soft non-spherical models. The hard non-spherical model considers that the liquid structure is dominated by the sharply repulsive interactions that occur between the atoms as they approach each other at short distances, and models these interactions using an infinitely steep hard sphere potential. The effects of attractive interactions are omitted. A characteristic of the hard models is that the phase behavior is governed by the entropy alone; as such it is not influenced by the temperature but it changes with density. Hard spheroids[34] have been well-studied and they form only nematic phases. Hard spherocylinders,[35-37] in contrast, arrange themselves in SmA, SmC, and nematic phases.

Soft non-spherical models introduce some degree of complexity when describing the liquid structure by representing the molecular shape as a soft body. The interaction potential features a steep repulsive part, modelling the overlap between the electron clouds, and an attractive tail at larger intermolecular separations. Applications of this soft ellipsoid model are dominated by variants of the Gay-Berne (GB) potential,[38] basically an anisotropic version of the Lennard-Jones (LJ) inverse 12-6 potential.[39] The GB potential has been used to predict material properties, such as elastic constants,[40, 41] rotational viscosities,[42] and helical twisting powers.[43-46] The Lennard-Jones pair potential will be discussed in more detail in Section 2.4.

The soft non-spherical model was first developed in 1972 by *Berne and Pechukas*[47], and corrected in 1981 by *Gay and Berne*[38] to give a reasonable fit to a linear arrangement of four Lennard-Jones sites. This resulted in the first orientation-dependent

potential to describe an uniaxial ellipsoid of revolution, named the Gay-Berne (GB) potential:

$$U_{AB}\left(\hat{u}_A,\hat{u}_B,r_{AB}\right)=4\varepsilon\left(\hat{u}_A,\hat{u}_B,\hat{r}_{AB}\right)\left[\mathrm{R}^{12}-\mathrm{R}^{6}\right] \tag{1.2}$$

$$R=\frac{\sigma_0}{r_{AB}-\sigma\left(\hat{u}_A,\hat{u}_B,\hat{r}_{AB}\right)+\sigma_0} \tag{1.3}$$

where $\hat{u}_A$ and $\hat{u}_B$ are unit vectors describing the orientations of the two particles A and B, r_{AB} is the center-to-center distance, and $\hat{r}_{AB}$ is the unit vector along the intermolecular vector, $\vec{r}_{AB}$ (shown in Figure 1.7).

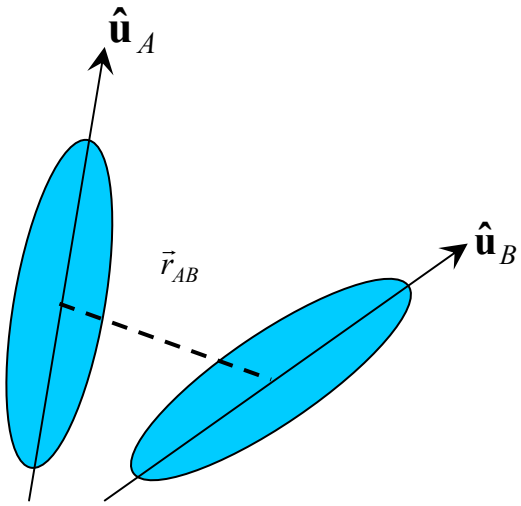

Figure 1.7 The relative orientation of two ellipsoidal particles defined by the vectors $\hat{u}_A$ and $\hat{u}_B$, describing the orientations of the two particles A and B, and the intermolecular vector $\vec{\mathbf{r}}_{AB}$.

The anisotropic contact distance, $\sigma(\hat{u}_A, \hat{u}_B, \hat{r}_{AB})$, and interaction anisotropy term, $\varepsilon(\hat{u}_A, \hat{u}_B, \hat{r}_{AB})$, for ellipsoidal molecules depend on the orientations of the two molecules and the intermolecular vector, as follows:

$$\sigma(\hat{u}_A, \hat{u}_B, \hat{r}_{AB}) = \sigma_0 \left\{ 1 - \frac{\chi}{2} \left[\frac{(\hat{u}_A \cdot \hat{r}_{AB} + \hat{u}_B \cdot \hat{r}_{AB})^2}{1 + \chi(\hat{u}_A \cdot \hat{u}_B)} + \frac{(\hat{u}_A \cdot \hat{r}_{AB} - \hat{u}_B \cdot \hat{r}_{AB})^2}{1 - \chi(\hat{u}_A \cdot \hat{u}_B)} \right] \right\}^{-\frac{1}{2}} \tag{1.4}$$

$$\varepsilon(\hat{u}_A, \hat{u}_B, \hat{r}_{AB}) = \varepsilon_0 \varepsilon_1^{\nu}(\hat{u}_A \cdot \hat{u}_B) \varepsilon_2^{\mu}(\hat{u}_A, \hat{u}_B, \hat{r}_{AB}) \tag{1.5}$$

The strength anisotropy function depends now on the adjustable exponents μ and ν, as well as the two terms defined as follows:

$$\varepsilon_1(\hat{u}_A, \hat{u}_B) = \left[1 - \chi^2 (\hat{u}_A \cdot \hat{u}_B)^2 \right]^{-1/2} \tag{1.6}$$

$$\varepsilon_2(\hat{u}_A, \hat{u}_B, \hat{r}_{AB}) = 1 - \frac{\chi'}{2} \left[\frac{(\hat{u}_A \cdot \hat{r}_{AB} + \hat{u}_B \cdot \hat{r}_{AB})^2}{1 + \chi'(\hat{u}_A \cdot \hat{u}_B)} + \frac{(\hat{u}_A \cdot \hat{r}_{AB} - \hat{u}_B \cdot \hat{r}_{AB})^2}{1 - \chi'(\hat{u}_A \cdot \hat{u}_B)} \right] \tag{1.7}$$

A vital component of the uniaxial Gay-Berne potential is the shape anisotropy parameter, χ, that depends on the length-to-breath ratio, $k = \sigma^{ee} / \sigma^{ss}$, where σ^{ee} and σ^{ss} are the length and breadth of the molecule, respectively. The shape anisotropy parameter is defined as:

$$\chi = \frac{k^2 - 1}{k^2 + 1} \tag{1.8}$$

Particularly, the elongated molecules have $\sigma^{ee} > \sigma^{ss}$ and $\chi > 0$, whilst flat discotic molecules have $\sigma^{ee} < \sigma^{ss}$ and $\chi < 0$. The anisotropy of the potential well depth is reflected by χ', which is given by:

$$\chi' = \frac{k'^{1/\mu} - 1}{k'^{1/\mu} + 1} \tag{1.9}$$

The quantity k' provides a measure of the anisotropy of the well depth and it is defined as $k' = \varepsilon^{ss} / \varepsilon^{ee}$ (following Luckhurst notation[48]), where ε^{ss} and ε^{ee} are the maximum well depths for the side-by-side and end-to-end interactions, respectively.

From Figure 1.8, the Gay-Berne potential can be seen to take a similar shape to the well-known 12:6 Lennard-Jones potential. However, the relative orientation of the two particles influences both the distance at which the attractive and repulsive energies cancel, and the depth and width of the attractive well.

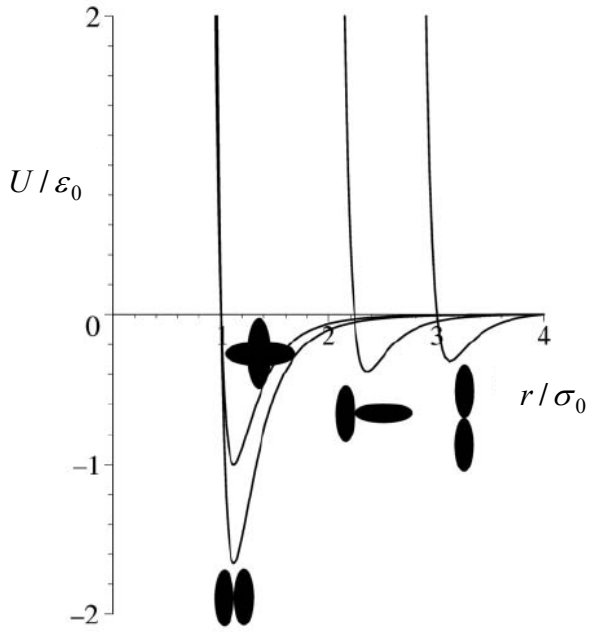

Figure 1.8 The Gay-Berne potential for $k = 3$, $k' = 5$, $\nu = 2$, and $\mu = 1$ plotted in reduced units for four fixed relative orientations: side-to-side, cross, T-shape, and end-to-end.[42] The distance is plotted in terms of σ_0 whilst the potential is in terms of ε_0.

The Gay-Berne potential is characterized normally by six adjustable parameters $\sigma_0, \varepsilon_0, k, k', \nu,$ and μ, which control the overall form of the potential. The σ_0 and ε_0 parameters are generally used to define length and energy scales within simulations. Since there are an infinite number of possible parameterizations, *Bates and Luckhurst*[49] proposed to symbolize a particular set of parameters by the notation GB$\left(k, k', \mu, \nu\right)$, where $k = \sigma^{ee} / \sigma^{ss}$ and $k' = \varepsilon^{ss} / \varepsilon^{ee}$. The flexibility of the model makes the Gay-Berne potential very versatile. As it was pointed out by *Zannoni,*[50] the choice GB$\left(k, k', 0, 0\right)$ corresponds to a soft ellipsoid whilst GB$\left(0, 0, \mu, \nu\right)$ reduces to a spherical Lennard-Jones potential. The first parameterization, GB(3, 5, 1, 2), suggested in the original work of *Gay and Berne*,[38] shows a spontaneous isotropic to nematic transition.[51] A slightly different parameterization GB(3, 5, 2, 1), used by *Luckhurst et al.,*[52] produced nematic, smectic A, and smectic B phases. Although the GB(3, 1/5, 3, 1) parameterization also formed nematic and smectic phases, it is worth noting that the increase of μ gives rise to a wider nematic range.[53] A considerably different parameterization GB(4.4, 39.6, 0.74, 0.80) was used by *Luckhust and Simmonds*[54] in the first attempt to model a real molecule, p-terphenyl. Later, *Bates and Luckhurst*[49] showed that the mesogen GB(4.4, 20, 1, 1) exhibits nematic, smectic A, and smectic B phases depending on the choice of the pressure, and that the phase diagram of this mesogen is in good agreement with those expected for such real rod-like mesogens.

Unfortunately, the form of the GB potential presented in Equations (1.2) to (1.9) applies to identical uniaxial particles. Some extensions of the Gay-Berne model have

been proposed to overcome this limitation by generalization to biaxial particles,[55] dissimilar particles,[56] and dissimilar biaxial particles.[57]

The rapid increase in computer power over the last decades has allowed an atomistic representation of liquid crystals via computer simulations. In a *full atomistic model*, the coordinates of all atoms including hydrogens are explicitly considered. Typically, these models will include bond stretching, angle bending, and torsional dihedral interactions. Using an atomistic model, *Berardi et al.*[21] have reported the need of over 10-40 ns runs for the equilibration of a system of 98 molecules for each of the first three homologues of the phenyl alkyl-4-(4'-cyanobenzylidene)-aminocinnamates. More recently, *Peláez and Wilson*[58] have reported the growth of a nematic phase from an isotropic liquid over a 100 ns timescale for a multi-component liquid crystal mixture simulated at a fully atomistic level. Making use of an atomistic model, *Cacelli et al.*[59] have reached a stable nematic phase for the 4-n-pentyl-4'-cyanobiphenyl over a 40 ns simulation starting from three different initial configurations.

Despite the potential to better reproduce the properties of a molecular system, at present, detailed atomistic simulations simply cannot handle reasonable system sizes or the time scales required to predict phase behaviour in liquid crystal systems. Recently, progress has been made in this field through the development of effective parallel Molecular Dynamics methods,[60-62] through significant increases in computer speed, multiple time step methods,[63] and efficient treatment of long range interactions.[64] However, fully atomistic simulations of a realistic number of molecules bearing atomic charges over tens to hundreds of nanoseconds are still prohibitive.

Some limitations of atomistic models have been surmounted by united atom and coarse-grained approaches, capable of capturing the main physics of the problem while reducing computational expense. In the *united-atom* approach, the hydrogens covalently bound to non-electronegative atoms are combined to yield a *united atom* site, which is represented in simulations by a spherical Lennard-Jones potential. For a united atom site, the mass and charge are taken as a sum of the values for the involved atoms.

The united-atom approach is frequently used in hybrid schemes where the flexible chains are represented in term of united atoms whilst the rigid parts are modeled as Gay-Berne sites. For instance, a nonpolar united atom model for 4,4'-di-n-pentyl-bibicyclo[2.2.2]octane has been used by *McBride et al.*[22] to grow a nematic phase from an isotropic liquid over a period of 6-10 ns. A similar approach has been employed by *McDonald and Hanna*[65] in the simulation of 4-n-octyl-4'-cyanobiphenyl and they found that the simulations required around 10-15 ns for the equilibration of the system. Using the united-atom potential to eliminate hydrogens and neglecting electrostatic interactions are major simplifications made in order to satisfy the need for computational efficiency without sacrificing too many atomistic details.

Reducing the degrees of freedom via an effective-atom representation, as is done in a coarse-graining approach, leads to an important reduction in computational expenses, but may result in some loss of chemical realism. The philosophy behind the *multi-site coarse-grained* approach is to achieve a simpler description of the effective interactions while not losing the ability of the resulting models to predict the properties of interest. In particular, groups of atoms are treated as one "super atom" with one set of force field

parameters. Various coarse-grained approaches have been developed based on this idea.[66, 67] For example, attempts have been made to replace the biphenyl cores of 4-n-pentyl-4'-cyanobiphenyl by large spherical sites at the centre of each ring.[68] There have been attempts to represent each aromatic ring by a single ellipsoidal GB site in the p-*n*-oligophenyl series,[69] in a typical 4,4'-dialkylbiphenyl,[70] 4-n-alkyloxy-4'cyanobiphenyl, and 4'-n-alkyloxy-4-F-benzylidene-aniline[71] liquid crystal mesogens.

Moreover, multi-site coarse-grained models are capable of describing the structure and dynamics of complex macromolecular liquid crystals, such as liquid crystal polymers and liquid crystal dendrimers. *Stimson and Wilson*[72] used a multi-site coarse-grained method to study the behaviour of a side-chain liquid crystal polymer, in which the flexible siloxane backbone and the alkyl spacers are modeled as spherical Lennard-Jones sites while the coarse-grained mesogenic moieties are represented as Gay-Berne sites. Later, *Ilnytskyi and Neher*[73] applied the same formalism in order to analyze the structure and dynamics of various liquid crystalline phases of a side-chain liquid crystal polymer. A similar concept has been used by *Wilson et al*.[74] in the modelling of a third generation liquid crystalline dendrimer in isotropic, nematic, and smectic A solvent. More recently, the bulk structure of the liquid and smectic A phases of a liquid crystal dendrimer[75] and the role played by terminal or lateral substitution in influencing its structure have also been studied.[76]

Despite the recent progress in using coarse-grained models, there is still work to be done towards determining a "general" (*i.e.* transferable) set of Gay-Berne parameters

to be used in a simple coarse-grained force-field that, along with the particular molecular flexibility, will correctly represent the bulk phase behavior of real mesogenic compounds.

1.5.2 The Origin of the Tilt in the SmC Phase

Over the last decades quite a number of experimental and theoretical studies have focused on the formation of the tilted SmC phase.[70-90] Unfortunately, none of them are able to describe completely the origin of the SmC phase formation and the SmA-SmC phase transition. There are two main theoretical approaches to the SmC phase description: one based on purely steric interactions, and another relying upon electrostatic interactions between the constituent molecules.

The *zigzag* model, based on steric repulsion, proposes that the origin of the tilt is associated with the Z-like molecular shape, usually due to the presence of two end alkyl chains attached to a rigid part of constituent molecules.[77-79] The idea of a particular organization of core and tail tilt was motivated by the large discrepancy observed between the X-ray and optical microscopy data for the molecular tilt angle in SmC materials.[80, 81] Specifically, a molecule within a SmC layer can be symbolized by a tilted central part (*i.e.* rigid core) measured by optical means, and two terminal parts, corresponding to the disorganized aliphatic chains, which are less tilted on average than the central part and that can be deduced from X-ray investigations.[16]

After studying zigzag-shaped molecules, *Wulf*[79] has concluded that the tilted SmC phase is solely a result of the steric interactions between the constituent mesogens. *Maiti et al.*[82] have studied a system of rigid zigzag-shaped molecules and reported that the

excluded-volume interactions arising from the molecular shape are sufficient to produce the tilted SmC phase even in the absence of electrostatic interactions. More recently, infrared (IR) dichroism and atomistic computer simulations have been employed by *Jang et al*.[83] in order to prove that in molecules having a "zigzag" structure with tails visibly less tilted from the layer normal than the cores, the disordering of the tails near the core contribute to the layer shrinkage in SmC phases.

A different approach is based on the idea that the tilted SmC phase originates from the formation of specific intermolecular electrostatic interactions. A number of studies have investigated the effects of electrostatic dipole and quadrupole moments on mesogenic behavior. In all the cases, these electrostatic interactions have been incorporated into established soft and hard particle potentials. *McMillan*[84] and *Cabib and Benguigui*[85] propose that electric dipole-dipole interactions are at the origin of the tilt in the SmC phase. Particularly, *Meyer and McMillan*[86] associate the tilt apparition to the presence of terminal dipoles, exerting a torque on the system of rod-like molecules. The importance of dipolar interactions has been revealed by experimental studies done by *Goodby et al.*[87] and *DeJeu*.[88] Theoretical studies proved that the smectic phase stability is enhanced by adding central longitudinal dipoles[89-91] to a Gay-Berne system, while the nematic phase is favored by moving the dipoles to a terminal location.[92] To summarize, the magnitude, direction (either longitudinal or transversal), and location of the dipole (terminal or central) have an effect on the local molecular correlation in smectic phases. Models based on quadrupolar interactions, that induce a SmA-SmC transition, have been proposed by *Goossens*,[93] and by *Poniewierski and Sluckin*.[94] More recently, *Neal and*

Parker[95-97] have demonstrated that the formation of a SmC phase is sensitive to the direction (longitudinal or transversal) and magnitude of a point quadrupole added to an elongated Gay-Berne model.

Despite the interest in the molecular origin of the tilted SmC phase formation, which has been an issue of debate ever since the first observation of the temperature-dependent tilt angle in the early 1970s,[98] there is no satisfactory molecular theory to explain it. Moreover, existing theories cannot fully explain the properties of novel smectic liquid crystals with weak layer contraction. Most of the time, when a liquid crystal undergoes a transition from the SmA phase to the SmC phase, the layer spacing decreases by a factor of $\cos\theta$, where θ is the tilt angle.[99] Recently, it has been observed that there are some materials which do not show a contraction of the smectic layers across the SmA-SmC phase transition. This is extremely interesting from the point of view of pure research but also is a key issue in the development of electro-optical devices, as layer shrinkage is problematic in the manufacturing and operation of such devices. A qualitative model to describe the absence of the layer shrinkage, known as *de Vries model*, has been developed by *de Vries*[100-103] and *Leadbetter and Norris.*[104]

1.6 Organization of the Thesis

The scope of this thesis is to simulate smectic phases of two common liquid crystal mesogens. To achieve this goal, a coarse-grained model potential has been specifically designed to accurately represent the intra- and intermolecular interactions.

This thesis is organized as follows. In Chapter 2, the theory and practical details of Quantum Mechanics, Molecular Dynamics, and hybrid Molecular Dynamics/Monte Carlo methods used in this thesis are presented. A variety of properties that have been used to identify and analyze smectic phases are also described. Chapter 3 presents the approach applied in this thesis in order to model the smectic liquid crystal phases, and the parameterization route for the intra- and intermolecular parts of the potential suited for the two smectogens. Extensive molecular dynamics simulations of liquid crystalline phases are performed and the results are presented in Chapter 4. Brief conclusions are presented in Chapter 5.

Chapter 2

Computational Methods for Liquid Crystal Simulations

This chapter presents an overview of the *ab initio* methods and computer simulation techniques used in the investigation of liquid crystal phases.

Quantum Mechanical applications generally involve computational evaluation of many-electron molecular wave functions (or electron density distribution functions), through approximate solutions of Schrödinger's equation. *Ab initio* and *semi-empirical* quantum mechanical methods are commonly used to compute electronic structure and molecular properties derived from the wave function. An alternative to wave function based methods is *Density Functional Theory* (DFT), which has become widely used in chemistry and physics in the past 25 years. A brief presentation of both *ab initio* and DFT methods is given in this chapter.

Molecular Mechanics methods do not use quantum mechanical wave functions, but rather classical physics to view the molecule as a collection of atoms held together by bonds. The molecular energy is represented by a force field with embedded empirical parameters. To evaluate the average of a property by means of molecular mechanics one can either generate configurations time step after time step in their natural time sequence (Molecular Dynamics method), or generate random configurations consistent with their

equilibrium probability distribution (Monte Carlo approach). In this chapter, Molecular Dynamics and hybrid Molecular Dynamics - Monte Carlo methods used in this work are reviewed.

2.1 Quantum Mechanics Methods

This section reviews the basics of the quantum mechanical approach, with an emphasis on the time-independent Schrödinger equation, and the Born-Oppenheimer approximation. The *ab initio* approach is one of the strategies to obtain accurate values for the electronic energy and properties of a system as a function of its nuclear coordinates, by solving the electronic Schrödinger equation for the electronic energy at each nuclear configuration, while making as few assumptions as possible. Although *ab initio* methods give very accurate results, the huge computational cost has necessitated the development of much cheaper alternatives.

The DFT method is introduced by discussing the Hohenberg-Kohn[105] theorem that provides the justification for using the electron density as the central quantity in electronic structure calculations, and the Kohn-Sham equation[106] that offers a route for using the DFT method in practical calculations.

A different approach to solving the Schrödinger equation while keeping the computational cost in hand is to use the so-called *semi-empirical* methods, which introduce approximations into the time-consuming parts of the calculation. The approximations use various empirical parameters chosen so that the results of the calculations agree with experimental data or with the results of accurate *ab initio* calculations.

2.1.1 *Ab initio* Method

All we need to know in order to describe a state of a system in quantum mechanics is the wave function or state function, Ψ, which depends on the coordinates of all the electrons and nuclei, that contains all the possible information about the system.

In quantum mechanics, the numerical value of the energy, E, described by state function, Ψ, can be obtained by solving the *time-independent, non-relativistic Schrödinger equation*:

$$\hat{H}\Psi = E\Psi \tag{2.1}$$

where $\hat{H}$ is the Hamiltonian operator for the molecular system. This quantum mechanical operator corresponds to the classical total kinetic and potential energies of the system.

Using i and j to index electrons, and A and B to index nuclei, we can write the Hamiltonian operator, $\hat{H}$, representing the total energy of a system of N electrons and M nuclei:

$$\hat{H} = -\frac{1}{2}\sum_{A=1}^{M}\frac{1}{M_A}\nabla_A^2 - \frac{1}{2}\sum_{i=1}^{N}\nabla_i^2 - \sum_{A=1}^{M}\sum_{i=1}^{N}\frac{Z_A}{r_{Ai}} + \sum_{A=1}^{M}\sum_{B>A}^{M}\frac{Z_A Z_B}{r_{AB}} + \sum_{i=1}^{N}\sum_{j>i}^{N}\frac{1}{r_{ij}} \tag{2.2}$$

where atomic units have been used. The Laplacian operator is $\nabla^2 \equiv \frac{\partial^2}{\partial x^2} + \frac{\partial^2}{\partial y^2} + \frac{\partial^2}{\partial z^2}$, M_A, Z_A and M_B, Z_B are the masses and charges of nuclei A and B, respectively, in multiples of the mass of an electron (atomic units) and electron charge. The variables r_{AB}, r_{Ai}, and r_{ij} are the separation distances between the nucleus A and the nucleus B,

the nucleus A and the electron i, and the i and j electrons, respectively. The kinetic energy is split into two summations: one over nuclei, and one over electrons. Similarly, the potential energy is divided into terms representing the attractive electrostatic interaction between the electrons and nuclei, and the repulsive potential due to the electron-electron and nucleus-nucleus interactions.

The Schrödinger equation can be further simplified if we take advantage of the *Born-Oppenheimer approximation*, which assumes that in molecules the electronic motion can be separated from the nuclear motion. This is a valid approximation as the electrons are roughly 2000 times lighter than the nuclei. Thus, if the nuclei are considered fixed in space and do not move, their kinetic energy is zero and the potential energy due to nucleus-nucleus repulsion is merely a constant. Taking into consideration the *Born-Oppenheimer approximation*, the purely electronic Hamiltonian is:

$$\hat{H}_{elec} = -\frac{1}{2}\sum_{i=1}^{N}\nabla_i^2 + \sum_{i=1}^{N}\sum_{j>i}^{N}\frac{1}{r_{ij}} - \sum_{A=1}^{M}\sum_{i=1}^{N}\frac{Z_A}{r_{Ai}} = \hat{T}_e + \hat{V}_{ee} + \hat{V}_{Ne} \tag{2.3}$$

where $\hat{T}_e$ represents the kinetic energy operator, and $\hat{V}_{ee}$ and $\hat{V}_{Ne}$ are the potential energy operators, due to electron-electron repulsion and nuclear-electronic attraction, respectively. Thus, the total potential energy of a system is a sum of a constant nuclear repulsion energy term, $E_{nuc} = \sum_{A=1}^{M}\sum_{B>A}^{M}\frac{Z_A Z_B}{r_{AB}}$, and the electronic energy, E_{elec}, expressed as follows:

$$\hat{H}_{elec}\Psi_{elec} = E_{elec}\Psi_{elec} \tag{2.4}$$

The electronic energy, E_{elec}, is a function of nuclear positions, often having a very complex form, that defines the Potential Energy Surface of a system, that in turn influences the interactions between the nuclei, and the dynamics and structure of the system.

To solve the Schrödinger equation for an arbitrary molecule, we have to know first the Hamiltonian that is specific to the quantum system at hand. From Equation (2.3), this is straightforward. Then, we have to find the eigenfunctions Ψ_{elec} and the corresponding eigenvalues E_{elec} of the Hamiltonian. Once the Ψ_{elec} are determined, all the properties of interest can be evaluated by applying the appropriate operators to the wave function. Unfortunately, there is no known strategy to solve exactly the Schrödinger equation for atomic and molecular systems, except for a few simple systems, because the wave function is a highly dimensional function which cannot be obtained exactly from Equation (2.4). As a result, it is necessary to obtain approximate wavefunctions and associated energies. The *variational principle* is used for this. According to this principle, the energy evaluated using an approximate wave function will always be equal to or greater than the exact ground state energy, E_0. The challenge is to identify the lowest possible energy, and this leads to a minimization process.

In the context of the Hartree-Fock (HF) method,[107] a many-electron wavefunction of a particular electronic state of a system is expressed as an antisymmetrized product of N one-electron wave functions, usually referred as a *Slater determinant*, Φ_{SD}. Once the form of the wave function is known, the variational principle is used to find the *best*

Slater determinant, *i.e.* the particular Φ_{SD} which yields the lowest energy. The only flexibility in a Slater determinant is provided by the spin orbitals. A spin-orbital is a product of a spin-function and a spatial molecular orbital (MO).

HF theory is viewed as a stepping stone on the way to exact solution of the Schrödinger equation. HF theory provides a very well-defined energy, one which can converge in the limit of an infinite basis set. The difference between the exact non-relativistic energy (*i.e.* the energy calculated by the Born-Oppenheimer approximation) and the converged HF energy is known as the *correlation energy* of the molecule. It is a measure of the error introduced through the HF scheme. Electron correlation is caused by instantaneous repulsion of electrons, which is not covered by the effective HF potential. It is vital to recover some of this correlation energy, either by using wavefunction-based methods (such as the configuration interaction method,[107] Möller-Plesset perturbation theory,[108] and the coupled cluster[109] approach) or electron density methods.

2.1.2 Density Functional Theory Method

Density Functional Theory (DFT) does not attempt to evaluate the molecular wavefunction, Ψ, but calculates the molecular electron probability density, $\rho(\vec{r})$, and, with this in hand, the energy can be obtained.[110]

The motivation for DFT is that the ground state properties of a system can be described by considering the ground state electron density. The real advantage is the fact that for an N electron system, the wave function is a complicated function of $3N$ (or

$4N$ if the spin is included) variables, while the electron density is a function of only three variables.

The Hohenberg-Kohn theorem[105] states that the energy of the ground state of a system of electrons is a functional of the electronic density. The energy is at a minimum if the density corresponds to the exact density for the ground state. Once the energy is obtained, all other properties can be determined by the ground state density alone. However, this theorem does not provide any guidance as to how the functional should be constructed; it just proves that a functional of the density must *exist*.

It is the Kohn-Sham method[106] that introduced a formalism for the evaluation of the ground state electron density and the ground state energy by combining wavefunctions and the density approach. Kohn and Sham realized that it would be considerably simpler if only the Hamiltonian operator was one for a *non-interacting* system of electrons. They considered a *fictitious* system of N *non-interacting* electrons (*i.e.* the electrons do not interact with each other via Coulomb repulsion) experiencing the same external potential energy function, $v_s(\vec{r})$, so that the exact ground state electron density, $\rho_s(\vec{r})$, equals the exact ground state density of the *real* system, $\rho(\vec{r})$, where the electrons *do* interact. The ground state energy of the real system is repartitioned into the following terms:

$$E[\rho(\vec{r})] = -\frac{1}{2}\sum_i^N \left\langle \theta_i^{KS}(\vec{r}) \middle| \nabla_i^2 \middle| \theta_i^{KS}(\vec{r}) \right\rangle + \frac{1}{2}\iint \frac{\rho(\vec{r}_1)\rho(\vec{r}_2)}{r_{12}} d\vec{r}_1 d\vec{r}_2 + \\ -\sum_i^N \int \sum_A^M \frac{Z_A}{r_{1A}} \left|\theta_i^{KS}(\vec{r}_1)\right|^2 d\vec{r}_1 + E_{XC}[\rho(\vec{r})] \tag{2.5}$$

where the first term is the kinetic energy of *non-interacting* electrons, $T_s[\rho(\vec{r})]$, the second term is the classical electron-electron repulsion energy, the third term is the exact nuclear-electron attractive electrostatic energy, and the remainder, $E_{XC}[\rho(\vec{r})]$, contains not only the non-classical effects of self-interaction correction, exchange, and electron correlation, which are contributions to the potential energy, but also the part of the true kinetic energy not covered by the $T_s[\rho(\vec{r})]$(*i.e.* deriving from the interacting nature of the electrons). The only unknown term is of course $E_{XC}[\rho(\vec{r})]$. Similar to the HF approximation, we now apply the variational principle and ask: what condition should the *Kohn-Sham spin orbitals* θ_i^{KS} fulfill in order to minimize this energy expression? The resulting equation is:

$$\left[-\frac{1}{2}\nabla_i^2 + v_{eff}(\vec{r})\right]\theta_i^{KS}(\vec{r}) = \varepsilon_i^{KS}\theta_i^{KS}(\vec{r}) \tag{2.6}$$

where the one-electron Kohn-Sham operator contains the effective potential, $v_{eff}(\vec{r})$. The effective potential of the reference system is uniquely determined and it is chosen so that the resulted density is equal to the ground state density of the real system of interacting electrons:

$$\rho(\vec{r}) = \rho_s(\vec{r}) = \sum_i^N \left|\theta_i^{KS}(\vec{r})\right|^2 \tag{2.7}$$

Once $E_{XC}[\rho(\vec{r})]$ is known, the exchange-correlation potential is found as the functional derivative of the exchange-correlation energy:

$$\hat{V}_{XC}(\vec{r}) = \frac{\delta E_{XC}[\rho(\vec{r})]}{\delta \rho(\vec{r})} \tag{2.8}$$

For his work in the development of DFT, Walter Kohn shared the 1998 Nobel Prize in Chemistry.[111]

DFT would yield the exact ground state electron density if the exchange-correlation functional is known. In practice, the exact functional is not known, but one can use some approximate form. New variants of the exchange-correlation functionals are published on a regular basis. A hierarchy of exchange-correlation functionals in ascending complexity and accuracy should refer to: the *local density approximation* (LDA), that gives good structural properties but fails in binding energies, the *generalized gradient approximation*[112] (GGA) for the exchange-correlation energy (*e.g.* Perdew-Wang's 86, Becke's 88, Perdew-Wang's 91, Becke's 1988 exchange functional and the Lee-Yang-Parr correlation functional or BLYP), which provide fairly accurate results with an average error of 5 kcal/mol for atomization energies, and finally the *hybrid functionals*, that achieve the best performance in many applications nowadays.

The hybrid approach, first introduced by *Becke* in 1993,[113] is based on the idea of incorporating a portion of the exact exchange from Hartree-Fock theory with exchange and correlation from other sources. The most important examples of this class are the B3PW91 (*i.e.* Becke, three-parameter exchange, Perdew-Wang, 1991) and the B3LYP (*i.e.* Becke, three-parameter exchange, Lee-Yang-Par correlation) hybrid exchange-correlation functionals. Today, the B3LYP has become the "workhorse" or default choice for practical applications in the organic chemistry community despite the significant

errors[107] that this functional has. More recently, the *hyper-generalized gradient approximation*[114] (HGGA) combines exact exchange with an existing semi-local functional that models dynamical correlation and an exchange-like functional developed to model static correlation, in an attempt to develop models that capture the exchange-correlation effects. It is beyond the limit of this thesis to mention all the approaches developed over the years; however, the reader can find detailed coverage of *orbital-dependent functionals* in a recent review presented by *Kümmel and Kronik.*[115]

2.1.3 Basis Functions and Basis Sets

A basis set represents a set of mathematical functions from which the molecular orbitals, that determine the wave function, are constructed. A large collection of basis sets is available in the literature and can be used to build approximate wave functions.

In conventional wave function based approaches, such as the Hartree-Fock scheme, *Gaussian-type orbitals* (GTOs), are typically employed for the basis functions, and these have the general form: $\eta^{GTO} = Nx_a^l y_a^m z_a^n e^{-\alpha r^2}$, where N is a normalization factor, x_a, y_a, z_a are the Cartesian coordinates with the origin at nucleus a. The powers l, m, n are non-negative integers, and α is a positive orbital exponent used to define the compactness of the resulting function. The preference for GTO basis functions is motivated by the computational advantages these functions offer, as many efficient algorithms for the analytical calculation of the very large number of four-center-two-electron integrals are available.

From a physical point of view, the natural choice for the basis set is the *Slater-type orbital* (STO) that resembles the exact wave functions for the hydrogen atom. An STO is expressed as: $\eta^{STO} = Nr_a^{n-1}e^{-\varsigma r_a}\mathrm{Y}_l^m(\Theta,\phi)$, where n corresponds to the principal quantum number, N is a normalization constant, ς is the orbital exponent, and $\mathrm{Y}_l^m(\Theta,\phi)$ are the usual spherical harmonics describing the angular part of the function.

The main difference between the STO and GTO expressions is the power of r in the exponent, which determines their form at the nucleus (when $r = 0$): a zero slope for GTO and a cusp for STO. It is important to point out that one usually needs several times more GTOs than STOs to achieve the same accuracy. For example, STO-3G is an approximation of a Slater-type orbital using three Gaussian functions in the approximation. For nonlinear molecules, it is very difficult to compute using STO basis functions, since no analytical techniques are available.

In an attempt to improve accuracy while keeping computational cost in check, several Gaussian functions ("primitives") are combined into a fixed linear combination to give one *contracted Gaussian-type orbital* (CGTO), of the following form: $\eta_\tau^{CGTO} = \sum_a d_{a\tau}\eta_a^{GTO}$, where the coefficients $d_{a\tau}$ are fixed.

The *minimal* basis set, the simplest expansion of the molecular orbitals, uses only one basis function (or contracted function in the case of CGTO) for each atomic orbital (AO) up to and including the valence orbitals. A typical minimal basis set is the STO-3G basis set, in which three primitive GTO functions are combined into one CGTO. *Double-*

zeta (DZ) and *triple-zeta* (TZ) basis sets have the sets of functions doubled, and tripled, respectively. Another possibility is to use *split-valence type* sets where the valence AOs are represented by doubled or tripled sets of functions, whilst using a minimal set for the inner core electrons. The 3-21G and 6-31G Gaussian basis sets, developed by *Pople et al.*,[116] are typical examples of this kind of basis set. A more complex example, the 6-311G basis set represents each inner-shell AO as a sum of six Gaussians, while each valence-shell AO is split into three parts as follows: the contracted part is a sum of three Gaussian primitives, a more diffuse part as one Gaussian primitive and a most diffuse part as one Gaussian primitive.

In most applications, *polarization functions* are added to the basis sets to ensure that the atomic orbitals can distort away from their original atomic symmetry and better adapt to the molecular environment. The distortion of the atomic orbitals from their original shape, when the bonds are formed in molecules, is mimicked by adding basis functions representing an angular momentum higher than what is represented by the valence orbitals of the atom.[110] Examples of polarization functions are *p*-functions on each hydrogen atom or *d*-functions for the first-row elements, such as the polarized double-zeta set 6-31G(d,p), which is equivalent to 6-31G** in the Pople-type notation. In general, polarization functions significantly improve the description of molecular geometries (bond lengths and angles).[110]

The role of the *diffuse basis functions* added to a basis set is to allow the charge density of negative charge bearing atoms to expand. In the "Pople nomenclature", the presence of diffuse functions is indicated by a '+' in the basis set name. For example, the

6-31+G(d) basis set is the 6-31G(d) basis set in which the heavy atoms have been augmented with an additional four diffuse functions (s, p_x, p_y, p_z). The "++" version, 6-31++G(d), is the 6-31G(d) basis set with diffuse functions added to the heavy atoms as well as hydrogen atoms (s type only).

2.2 Molecular Dynamics

The *Molecular Dynamics* (MD) simulation method, utilized for the first time by *Alder and Wainwright*[117, 118] in the late 1950's, has been used as a powerful tool to describe the microscopic properties and structures of systems ranging from simple liquids to complex materials, such as liquid crystals, polymers, proteins, biological membranes, and macromolecules.[119]

MD is a computer simulation technique in which the time evolution of a set of interacting atoms or molecules is followed by numerically integrating their equations of motion. When the system is considered equilibrated, the actual measurement of the system's properties can be done. From the trajectories, one can also obtain information about the dynamics of the atoms and molecules, and/or compute structural properties of a given system.

A system consisting of N particles is described by the classical Hamiltonian, the sum of kinetic and potential energy terms:

$$\mathcal{H}(\vec{p}_i, \vec{r}_i) = \sum_i^N \frac{\vec{p}_i^{\,2}}{2m_i} + U(\vec{r}_i) \tag{2.9}$$

where $m_i, \vec{p}_i, \vec{r}_i$ are the mass, momentum, and position of i^{th} particle, and $U(\vec{r}_i)$ is the potential energy. The Hamiltonian is a function of $6N$ independent variables, the $3N$ particle momenta and the $3N$ particle positions.

In classical MD, the laws of classical mechanics are followed, specifically Newton's law: $\vec{F}_i = m_i \vec{a}_i$ for each particle i in a system comprised of N particles, where $\vec{a}_i = d^2\vec{r}_i / dt^2$ is the acceleration of the i^{th} particle, and $\vec{F}_i$ is the force acting upon it, due to its interactions with the other particles.

Typically, a classical MD simulation program follows the steps:[120]

- *Specification of the conditions of the run*: defining the number of particles, temperature, density, pressure, time step, simulation cell, etc.
- *Initialization of the system*: setting up the positions and velocities initially assigned to all N particles of the system;
- *Calculation of the force acting on every particle* at each step by applying Newton's law of motion to each particle. In Cartesian coordinates, the equations of motion become:

$$\frac{d\vec{p}_i}{dt} = -\frac{\partial U(\vec{r}_i)}{\partial \vec{r}_i} = \vec{F}_i \tag{2.10}$$

$$\frac{d\vec{r}_i}{dt} = \frac{\vec{p}_i}{m_i} \tag{2.11}$$

where $\frac{d\vec{p}_i}{dt}$ are the momenta derivatives (the forces), $\frac{d\vec{r}_i}{dt}$ are the coordinate derivatives (the velocities), and the potential energy is obtained from a molecular mechanics force field.

For a system containing N atoms, the potential energy can be divided into terms involving the coordinates of individual atoms, pairs, triplets, etc.:

$$U\left(\vec{r}^{\,N}\right)=\sum_{i}u^{(1)}\left(\vec{r}_i\right)+\sum_{i}\sum_{j>i}u^{(2)}\left(\vec{r}_i,\vec{r}_j\right)+\sum_{i}\sum_{j>i}\sum_{k>j>i}u^{(3)}\left(\vec{r}_i,\vec{r}_j,\vec{r}_k\right)+\ldots \qquad (2.12)$$

where $u^{(1)}$ accounts for the potential due to an external field, and the remaining terms represent particle interactions. Usually, in computer simulation of liquids the third and higher terms are rarely used since their evaluation is extremely time consuming.

Within the framework of a MD simulation, the *pairwise approximation* gives a good approximation of the many-body effects by using an *effective pair potential,* $u^{(2)}_{effective}$, where the parameters are adjusted based on fluid properties:

$$U\left(\vec{r}^{\,N}\right)\approx\sum_{i}u^{(1)}\left(\vec{r}_i\right)+\sum_{i}\sum_{j>i}u^{(2)}_{effective}\left(\vec{r}_i,\vec{r}_j\right) \qquad (2.13)$$

- *Integration of the equations of motion*: combining the forces on all particles with current positions and velocities, one can generate new positions and velocities a short time ahead, by integrating Newton's equations of motion using an appropriate algorithm. The algorithm used throughout this thesis is presented in section 2.2.3;
- *Computation of the properties of the system*: at the end of the simulation run, the averages of measured quantities are obtained by summing up over M time steps:

$$\langle A\rangle=\frac{1}{M}\sum_{i=1}^{M}A_i \qquad (2.14)$$

where A_i is the instantaneous value of the property A.

The natural ensemble for an isolated system evolving under Newton's equations of motion is one in which the total energy is conserved; this corresponds to the *microcanonical ensemble* (N,V,E) simulation. However, using a thermostat it is possible to simulate a *canonical ensemble* with (N,V,T) fixed. Other ensembles can also be simulated, including constant pressure[121, 122] and constant enthalpy systems.[123-125]

When atomistic details are fully taken into account, it is unfeasible to simulate large macromolecular systems over microsecond time scales using the MD simulation within a reasonable wall clock time. This is why some reasonable assumptions have to be made in order to reduce the computational time of a simulation.

2.2.1 Periodic Boundary Conditions

In MD calculations it is common to use *periodic boundary conditions*[119] (PBC) in order to reduce the computer time and to avoid surface effects due to the finite size of the simulation box. As the number of particles in a fixed volume is small (it is many orders of magnitude less than 10^{23}), the fraction of particles near an interface is similar to the fraction in the bulk and the simulation results do not reflect those of an infinite system. Periodic boundary conditions eliminate the interface and allow feasible bulk simulations to proceed. In PBC, the simulation cell is replicated in all directions in space to form a lattice. When a particle "leaves" the system by passing through a "boundary", an identical "image particle" enters through the opposite boundary.

The number of operations required for calculating the interparticle force on a given system is in principle proportional to the total number of pair interactions in the system, if we ignore the many-body interactions. For large systems it would be time-consuming and unrealistic to include interactions between all of the $N(N-1)/2$ pairs of particles, since with PBC, N is infinite. Generally we would expect the interaction strength to decrease sharply beyond a modest number of neighbouring molecules. To limit the number of non-covalent interactions in the PBC, the *minimum image convention* and a *spherical cutoff* (see Figure 2.1) have been used.

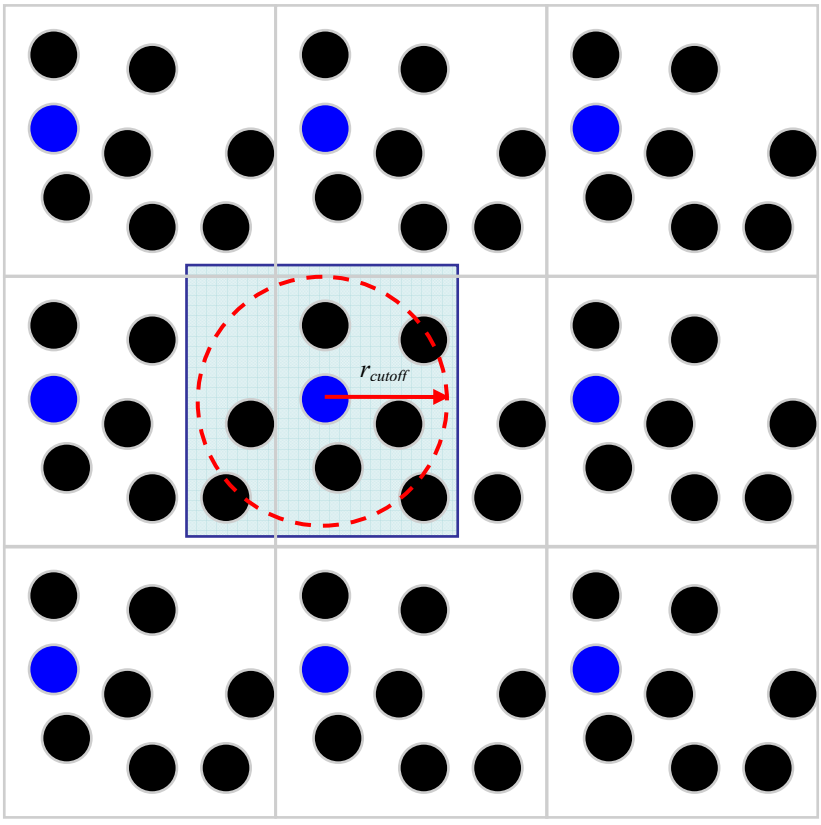

Figure 2.1 A 2D periodic lattice built from square unit cells. The colored square illustrates the minimum image representation and the dashed circle shows a spherical cutoff.

In this scheme, a sphere of radius r_{cutoff} is centered at the particle of interest and each particle interacts with the nearest images of the other $N-1$ particles that are inside that sphere but particles outside the sphere are excluded from interacting with the central particle. The r_{cutoff} is less than $L/2$, where L is the smallest dimension of the simulation box. In this thesis, I choose $r_{cutoff} = L/2.05$. This ensures that I employ the largest possible cutoff distances considering only the interactions of a given particle i with the nearest periodic image of any other particle j.

The use of the simple truncation method has shown to introduce significant errors and artificial behaviour in a MD simulation[120] due to its impact on the potential and the force. To account for some of the errors introduced by the use of a spherical cutoff, the potential is truncated and shifted, so that the potential vanishes at the cutoff radius, as follows:

$$U^{truncated-shifted}(r) = U(r) - U(r_{cutoff}), \quad r < r_{cutoff} \tag{2.15}$$

$$U^{truncated-shifted}(r) = 0, \quad r \geq r_{cutoff} \tag{2.16}$$

where $U^{truncated-shifted}(r)$ is the effective interaction potential energy function. The main advantage is that the force, based on $U^{truncated-shifted}(r)$, is continuous at all interparticle separations.

2.2.2 Ewald Summation Technique

In order to simulate the properties of bulk systems with long-range electrostatic interactions it is necessary to sum these interactions over all the periodic images of the simulation cell.

Consider a system of N point charges (q_i) at positions ($\vec{r}_i$) that satisfy the charge neutrality condition, $\sum_{i=1}^{N} q_i = 0$, in a rectangular simulation cell of size L_x, L_y, and L_z, and their infinite replicas obtained from the application of PBC. The total electrostatic energy can be written as:

$$U = \frac{1}{2} \sum_{\vec{n}} {}' \sum_{i=1}^{N} \sum_{j=1}^{N} \frac{q_i q_j}{\left| \vec{r}_{ij} + \vec{n} \right|} \tag{2.17}$$

where q_i is the charge of the i^{th} particle, $\vec{n} = \left(n_x L_x, n_y L_y, n_z L_z \right)$ is the cell-coordinate vector with n_x, n_y, n_z integers. The original cell is located at $\vec{n} = (0,0,0)$ with image cells located at $n_x L_x, n_y L_y, n_z L_z$ intervals in all three dimensions. The prime of the first sum indicates that the summation does not include the term for $i = j$ when $\vec{n} = (0,0,0)$, since a charge does not interact with itself. The factor $1/(4\pi\varepsilon_0)$ is omitted for simplicity (ε_0 is the vacuum permittivity).

The problem with the summation shown in Equation (2.17) is that the summation of $U(r_i) \propto \frac{1}{r^m}$ is conditionally convergent for $m \leq 3$, which means that in the case of

charge-charge, charge-dipole, dipole-dipole, and change-quadrupole interactions the result depends on the order of summation.

The *Ewald summation* technique, introduced in 1921,[126] is a solution to the above problem and the most common way to sum the long-range interactions between the particles and all their infinite periodic images efficiently. The Ewald sum splits the summation presented in Equation (2.17) into the following terms:[119,127]

$$U_{EWALD} = U^r + U^m + U^o + J\left(\vec{M}, P\right) \tag{2.18}$$

The idea is that each point charge in the system is viewed as being surrounded by a Gaussian charge distribution of equal magnitude and opposite sign (as shown in Figure 2.2). To counteract this induced Gaussian distribution, a second Gaussian charge distribution of opposite sign but with the same magnitude as the original distribution is added for each point charge. This canceling distribution reduces the potential to that due to the original charges. A third term (of a negative sign) must be added to the total potential to correct for the self-interaction energy. In addition, a shape-dependent term, depending on the dielectric constant of surroundings and the total dipole moment of the unit cell, is needed for a rectangular simulation cell.

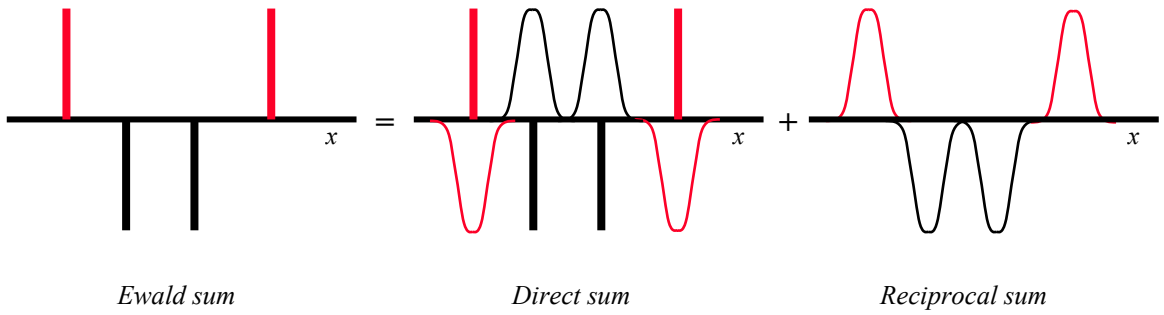

Figure 2.2 The Ewald sum components of a one-dimensional point charge system.[128]

The direct space sum, U^r, works in real space and calculates the interactions originating from the Gaussian charge distribution:[119]

$$U^r = \frac{1}{2}\sum_{i,j}^{N}\sum_{\vec{n}} q_i q_j \frac{erfc\left(\alpha\left|\vec{r}_{ij}+\vec{n}\right|\right)}{\left|\vec{r}_{ij}+\vec{n}\right|} \tag{2.19}$$

Here, the function $erfc(x)$ is the complementary error function that decreases monotonically to zero as x goes to infinity. In practice, the parameter α is chosen such that this sum converges when only $\vec{n} = (0,0,0)$ is considered.

The reciprocal sum, U^m, is evaluated as follows:[119]

$$U^m = \frac{1}{2\pi V}\sum_{i,j}^{N} q_i q_j \sum_{\vec{k}\neq 0} \frac{4\pi^2}{k^2}\cos\left(\vec{k}\cdot\vec{r}_{ij}\right)\exp\left(-\frac{k^2}{4\alpha}\right) \tag{2.20}$$

where V is the volume of the simulation cell given by $L_x \times L_y \times L_z$, and $\vec{k}$ is the reciprocal-space vector given by $\left(\frac{2\pi n'_x}{L_x}, \frac{2\pi n'_y}{L_y}, \frac{2\pi n'_z}{L_z}\right)$ with n'_x, n'_y, n'_z integers.

There is also a self-energy correction term, U^o, which cancels the interactions of each of the introduced artificial counter-charges with itself:

$$U^o = -\frac{\alpha}{\sqrt{\pi}} \sum_{i=1}^{N} q_i^2 \tag{2.21}$$

The shape-dependent correction term for a rectangular prism cell,[127] $J\left(\vec{M}, P\right)$, depends on the shape of the summation geometry P, and on the total dipole moment of the unit simulation cell $\vec{M} = \sum_{i=1}^{N} q_i \vec{r}_i$: for example, when a spherical geometry is used for the summation, the shape-dependent term becomes:

$$J\left(\vec{M}, P\right) = \frac{2\pi}{(2\varepsilon_S + 1)V} \vec{M}^2 \tag{2.22}$$

where V is the volume of the unit simulation cell, and ε_S is the dielectric constant of the surrounding medium. If the medium has an infinite dielectric constant, this term disappears, which corresponds to *tin-foil boundary conditions.*[129]

Finally, the total electrostatic energy becomes:

$$U_{EWALD} = \frac{1}{2} \sum_{i,j}^{N} \sum_{\vec{n}} q_i q_j \frac{erfc\left(\alpha \left| \vec{r}_{ij} + \vec{n} \right| \right)}{\left| \vec{r}_{ij} + \vec{n} \right|}$$
$$+ \frac{1}{2\pi V} \sum_{i,j}^{N} q_i q_j \sum_{\vec{k} \neq 0} \frac{4\pi^2}{k^2} \cos\left(\vec{k} \cdot \vec{r}_{ij}\right) \exp\left(-\frac{k^2}{4\alpha} \right) - \frac{\alpha}{\sqrt{\pi}} \sum_{i=1}^{N} q_i^2 + J\left(\vec{M}, P\right) \tag{2.23}$$

The accuracy of the Ewald summation method depends on the approximations made. In Equation (2.23), the convergence of the sum is controlled by $\vec{k}_{\mathbf{max}}$, which limits the summation range in reciprocal-space, and the Ewald convergence parameter, α, that determines the relative rate of convergence between the real and reciprocal sums.

The precision and speed of the Ewald algorithm depend upon a careful balancing of these parameters. A large α reduces the number of real space interactions while increases the number of reciprocal space terms to be evaluated in order to obtain comparable accuracy in the energies and forces. On the other hand, a small value of α increases the number of real space terms and decreases the reciprocal space summation. In practice, the value of α has to be carefully chosen for each system, so that the real space sum can be calculated in the minimum image convention without increasing too much the number of reciprocal space terms ($\vec{k}_{\mathbf{max}}$ vectors).[129]

2.2.3 Velocity Verlet Algorithm for Integration of Equations of Motion

One of the simplest and best available algorithms to integrate the equations of motion, is the *normal Verlet algorithm:*[130]

- Consider a truncated Taylor expansion of coordinates forward and backward in time:

$$\vec{\mathrm{r}}(t+\delta t) = \vec{\mathrm{r}}(t) + \frac{1}{m}\vec{\mathrm{p}}(t)\delta t + \frac{1}{2m}\vec{F}(t)\delta t^2 \tag{2.24}$$

$$\vec{\mathrm{r}}(t-\delta t) = \vec{\mathrm{r}}(t) - \frac{1}{m}\vec{\mathrm{p}}(t)\delta t + \frac{1}{2m}\vec{F}(t)\delta t^2 \tag{2.25}$$

- Add these together:

$$\vec{\mathrm{r}}(t+\delta t)+\vec{\mathrm{r}}(t-\delta t)=2\vec{\mathrm{r}}(t)+\frac{1}{m}\vec{F}(t)\delta t^2 \tag{2.26}$$

- Rearrange:

$$\vec{\mathrm{r}}(t+\delta t)=2\vec{\mathrm{r}}(t)-\vec{\mathrm{r}}(t-\delta t)+\frac{1}{m}\vec{F}(t)\delta t^2 \tag{2.27}$$

where $\vec{\mathrm{r}}(t)$, and $\vec{F}(t)$ are the position and force at the time t, m is the particle's mass, $\vec{r}(t-\partial t)$ and $\vec{r}(t+\partial t)$ are the backward and forward positions, and δt is the time step.

The normal Verlet algorithm has an important drawback in that the velocities of the atoms are not among the variables used in integrating the equations of motion, although they can be obtained with extra effort (*i.e.* the velocities at time t are available only once the positions at time $t+\delta t$ have been calculated). A slightly modification of these equations produce an algorithm called "velocity" version of the Verlet algorithm,[131] in which the velocities are explicitly calculated as part of solving the equations of motion.

The *Velocity-Verlet* integration of equations of motion that yield the microcanonical ensemble (NVE) can be implemented in the following stages:

- Evaluate the force, $\vec{F}(t)$, compute the position at new time, $\vec{\mathrm{r}}(t+\delta t)$, and advance the velocity a half time step, $\vec{\mathrm{v}}\left(t+\frac{\delta t}{2}\right)$:

$$\vec{\mathrm{r}}(t+\delta t)=\vec{\mathrm{r}}(t)+\vec{\mathrm{v}}(t)\delta t+\frac{1}{2m}\vec{F}(t)\delta t^2 \tag{2.28}$$

$$\vec{v}\left(t+\frac{\delta t}{2}\right)=\vec{v}(t)+\frac{1}{2m}\vec{F}(t)\delta t \tag{2.29}$$

- Evaluate new force, $\vec{F}(t+\delta t)$, and fully advance the velocity to obtain the velocity at new time, $\vec{v}(t+\delta t)$:

$$\vec{v}(t+\delta t)=\vec{v}\left(t+\frac{\delta t}{2}\right)+\frac{1}{2m}\vec{F}(t+\delta t)\delta t \tag{2.30}$$

This algorithm of integration of equation of motions is preferred over the Verlet and Leap-frog[132] algorithms due to its convenience, numerical stability, and simplicity.

2.2.4 RATTLE Algorithm

In the framework of Molecular Dynamics simulations, complex systems experience different kinds of motions with various time scales. For example, the period for intramolecular vibrations can be as little as tens of femtoseconds while the reorientational motions or conformational changes have longer time scales (from few picoseconds to hundreds of nanoseconds). In a standard integration of Newtonian equations, all these motions, regardless of their time scale, have to advance by the same time step, whose size should be inversely proportional to the frequency of the fastest motion present in the system. In this context, stretches involving hydrogen atoms have very fast vibrational frequencies and unless the integration time step used in the MD simulation is much smaller than the vibrational period, the simulation will be problematic.

To alleviate this problem, the bond distances can be constrained to their equilibrium lengths using the popular SHAKE or RATTLE algorithms[133, 134] for

integration of equations of motion subject to intramolecular constraints. By freezing the fast degrees of freedom in the system (*e.g.* fast vibrational motions), the SHAKE and RATTLE algorithms allow the use of a larger time step. For the current simulations, the RATTLE algorithm is employed.

The equations for constrained dynamics are:

$$m_i \frac{d^2 \vec{r}_i}{dt^2} = \vec{F}_i + \vec{G}_i \tag{2.31}$$

where $\vec{F}_i$ is the force on atom i due to the intermolecular and intramolecular interactions not associated with the constraints, and $\vec{G}_i$ is the force on atom i due to the constraints.

The constrained force is directed along the bond, and is given by:

$$\vec{G}_i = -\sum_j{}' \lambda_{ij} \vec{r}_{ij} \tag{2.32}$$

where the prime shows that the summation goes only over the atoms j that are connected with atom i by a constraint, λ_{ij} are the unknown time-dependent Lagrange multipliers associated with the intramolecular constraint forces, and $\lambda_{ij} = \lambda_{ji}$. In practice, the algorithm involves calculation of the λ_{ij} multiplier.

RATTLE is based on the Velocity-Verlet algorithm, and it guarantees that the coordinates and velocities of the atoms in a molecule satisfy, at each time *t,* the internal

constraints within a specified tolerance. It employs two different constraint forces, $\vec{G}_{RR}(t)$ and $\vec{G}_{RV}(t)$, to be used in the position and velocity equations, respectively.

Within the framework of the Velocity-Verlet algorithm, the equations of RATTLE become:

$$\vec{\mathrm{r}}_i(t+\delta t) = \vec{\mathrm{r}}_i(t) + \vec{\mathrm{v}}_i(t)\delta t + \frac{1}{2m_i}\left[\vec{F}_i(t) + \vec{G}_{RRij}(t)\right]\delta t^2 \tag{2.33}$$

$$\vec{\mathrm{v}}_i(t+\delta t) = \vec{\mathrm{v}}_i(t) + \frac{1}{2m}\left\{\left[\vec{F}_i(t) + \vec{G}_{RRij}(t)\right] + \left[\vec{F}_i(t+\delta t) + \vec{G}_{RVij}(t+\delta t)\right]\right\}\delta t \tag{2.34}$$

where $\vec{G}_{RRij}(t) = -\sum_j{}' \lambda_{RRij}(t)\vec{r}_{ij}(t)$, $\vec{G}_{RVij}(t+\delta t) = -\sum_j{}' \lambda_{RVij}(t+\delta t)\vec{r}_{ij}(t+\delta t)$, and $\vec{r}_{ij}(t) = \vec{r}_i(t) - \vec{r}_j(t)$.

Using the iterative procedure of *Ryckaert et al.*,[134] the $\lambda_{RRij}(t)$ multiplier is chosen so that the new positions, $\vec{r}_i(t+\delta t)$, satisfy the constraints. With this in hand, the $\lambda_{RVij}(t+\delta t)$ multiplier is selected so that the velocities are also consistent with the constraints. At each step of the simulation, an iterative procedure, where each constraint is applied in turn, is continued until all the constraints are satisfied to within the acceptable tolerance.

2.2.5 Nosé-Hoover Thermostat

MD simulations within the *microcanonical (N,V,E) ensemble* are easier to perform but commonly the type of system considered is a closed system, with a fixed volume, V, a

fixed number of particles, N, simulated at a constant temperature, T. Such a system is represented by a *canonical ensemble* or constant (N,V,T).

In the *canonical ensemble*, the system can be considered to be in contact with a reservoir, assumed to be sufficiently large that any transfer of energy does not change its temperature. On the contrary, the temperature of the original (real) system fluctuates in time and the instantaneous kinetic energy K is related to the instantaneous temperature $\mathscr{T}$ through:

$$\mathsf{T} = \frac{2}{3}\frac{\mathsf{K}}{Nk_B} = \frac{1}{3Nk_B}\sum_{i=1}^{N}\frac{\vec{p}_i^{\,2}}{m_i} \tag{2.35}$$

where N is the number of particles in the system, k_B is Boltzmann's constant, and $\vec{p}_i$ and m_i are the momentum and mass of the i^{th} particle, respectively.

The *Nosé-Hoover thermostat*, initially introduced by Nosé[135-137] and later modified by Hoover,[138, 139] has been selected for my MD simulations. The idea behind this extended system method is to include an additional degree of freedom s associated with a mass $Q > 0$ as well as a velocity, $\dot{s}$.

The Hamiltonian for a system of N particles, with coordinates $\vec{r}_i$, masses m_i, and potential energy $U(\vec{r}_1, \vec{r}_2, ..., \vec{r}_N)$, plus additional coordinate s is given by:

$$\mathrm{H}_{Nose'} = \sum_{i=1}^{N}\frac{\vec{p}_i^{\,2}}{2m_i s^2} + U(\vec{r}_1, \vec{r}_2, ..., \vec{r}_N) + \frac{\vec{p}_s^{\,2}}{2Q} + gk_B T \ln s \tag{2.36}$$

where Q is a constant corresponding to the *mass* of the particle and controlling the rate of fluctuations, $\vec{p}_s$ is the conjugate momentum of s, g is the number of degrees of freedom in the physical system, and $\vec{r}_i$ is the position of the i^{th} particle. The form of the last term, $gk_B T \ln s$, is chosen to guarantee that the algorithm produces averages consistent with a canonical ensemble.

The Nosé-Hoover equations of motion sample a microcanonical ensemble in the extended system, with a constant Nosé's Hamiltonian ($H_{Nosé}$). However, the energy of the real system is not constant. The equations of motions from Nosé's Hamiltonian are:

$$\frac{d\vec{r}_i}{dt} = \frac{\vec{p}_i}{m_i} \tag{2.37}$$

$$\frac{d\vec{p}_i}{dt} = -\frac{dU(\vec{r}_1, \vec{r}_2, ..., \vec{r}_N)}{d\vec{r}_i} - \zeta \vec{p}_i \tag{2.38}$$

$$\frac{d\zeta}{dt} = \frac{1}{Q}\left(\sum_{i=1}^{N} \frac{\vec{p}_i^2}{m_i} - gk_B T\right) \tag{2.39}$$

$$\frac{ds}{sdt} = \frac{d\ln s}{dt} = \zeta \tag{2.40}$$

where ζ is a thermodynamic friction coefficient. Eqs. (2.37) to (2.39) form a closed set, and Equation (2.40) is used to check the conservation of the Nosé's Hamiltonian. Accompanying fluctuations of ζ, the temperature of the system is regulated as follows. When ζ is negative, the particles move faster raising the temperature of the system as seen in Equation (2.38). When the system temperature increases above T, the time

derivative of ζ becomes positive due to Equation (2.39), and the particles slow down. Vice versa, when ζ is positive the particles slow down until the temperature decreases below T.

In this thesis, two independent Nosé-Hoover[135, 136, 138] thermostats (one for translational and another for rotational motion) have been employed in order to generate the canonical NVT ensemble. For isotropic fluids, the use of independent thermostats should have little impact but, for the present study, separate thermostats ensure that the aromatic rings are not rotationally cold.

The corresponding conserved quantity, the Nosé-Hoover Hamiltonian, is:

$$H_{NH} = E^{full} + \frac{Q_t}{2}\xi_t^2 + g_t k_B T \ln s_t + \frac{Q_r}{2}\xi_r^2 + g_r k_B T \ln s_r \tag{2.41}$$

where E^{full} is the total kinetic and potential energy of the system, and new terms appear corresponding to the rotation and translation (denoted with an r and t subscript, respectively). Thus, Q_t and Q_r are the masses of two fictitious variables, noted s_t and s_r, and g_t, and g_r are the corresponding degrees of freedom. The Velocity Verlet integration of the equations of motion that yields the canonical NVT ensemble follows the scheme proposed by *Martyna et al*.[140]

2.3 Hybrid Molecular Dynamics - Monte Carlo Method

In this thesis, MD simulations have been carried out initially in the canonical NVT ensemble. Unfortunately, as the temperature-density relationships for the simulated molecular systems are not available to us, a large number of simulations have to be performed to arrive at a crude phase diagram for the liquid crystal molecules.

Molecular simulations at constant pressure are attractive as they mimic the conditions encountered in laboratory experiments. Generally, MD simulations in the NPT ensemble involve isotropic volume changes which are not well suited for smectic phase simulations due to different impacts on the intralayer and interlayer spacing. Anisotropic volume changes, where only one cell dimension is changed, are far more appropriate. In particular, this will allow independent adjustment of the interlayer spacing.

Although anisotropic changes in the simulation cell can be accommodated within the Lagrangian formalism,[121] the method becomes significantly more complicated due to the complexity of the simulated mesogens. Instead, for the isothermal-isobaric (NPT) simulations of liquid crystal phases in this thesis, I have opted to employ a combination of the MD and MC methods, in which the shape and dimensions of the box are allowed to vary in order to accommodate different structures and structural spacing (*i.e.* the simulation cell must accommodate an integral number of smectic layers).

This hybrid MD-MC method follows the steps:

- During the production time of a simulation, identify when a MC move is attempted (*i.e.* an attempt is made every 256 iterations), and evaluate the potential energy of the current state U_{old}, and the volume V_{old};

- A random number generated from a uniform distribution in the interval [0,1] is used to decide which side of the simulation cell (*i.e.* L_x, L_y, or L_z) will be changed, and the maximum allowed volume change (δV);

- The coordinates of all the atoms in the simulation box have to be changed, since an increase in volume will lead to cavities forming at the boundaries of the simulation box, while a decrease in volume will lead to overlap of molecules in same regions. Specifically, the coordinates of all molecules in the simulation box are changed by scaling the coordinates of the centers of mass of each molecule by the scaling factor evaluated as the ratio of the *new* to the *old* box lengths, so that the whole molecule is moved whilst its intramolecular configuration (*i.e.* internal geometry) is left unchanged;

- The potential energy of the new state U_{new}, and the volume V_{new} are evaluated;

- The selection criterion for accepting the move from the *old* state to the *new* state is:[119]

$$acc(old \to new) = \exp\left\{\beta\left[\left(U_{new} - U_{old}\right) + p\left(V_{new} - V_{old}\right)\right] - (N+1)\ln\left(\frac{V_{new}}{V_{old}}\right)\right\} \tag{2.42}$$

where p is the pressure of the system, $\beta = 1/k_B T$, and k_B and T are Boltzmann's constant and the system temperature, respectively.

- If $\beta\left[\left(U_{new} - U_{old}\right) + p\left(V_{new} - V_{old}\right)\right] - \left(N+1\right)\ln\left(\frac{V_{new}}{V_{old}}\right) > 0$, then *accept* the move, otherwise:
- If $\exp\left\{\beta\left[\left(U_{new} - U_{old}\right) + p\left(V_{new} - V_{old}\right)\right] - \left(N+1\right)\ln\left(\frac{V_{new}}{V_{old}}\right)\right\}$ is greater than a random number between [0,1] *accept* the move, otherwise *reject* it.

- If the move is accepted, then the positions of all the molecules are updated, a new cutoff distance for the LJ potential is possibly required, and the new density is evaluated. The MD sequence continues.
- If the move is rejected, the old positions are kept and the MD sequence is continued.

It is important to note, that since the scaling of the simulation cell is anisotropic, this algorithm allows the simulation cell to change shape and size.

2.4 Force Field

Interactions between particles are treated using potential functions derived from classical mechanics. Individual potential functions are used to describe different types of interactions (*e.g.* bonded and non-bonded interactions). The combination of all these potential energy functions and the parameters used for their evaluation is known as a "force field".[110] An accurate force field, used to supply the potential energy for molecular dynamics computations, plays an important role in the success of any simulation.

There are many efficient force fields to be use in computer simulations. Traditionally, force fields are derived from high-quality experimental data and/or high-level quantum mechanical calculations. Different force fields make use of special forms of interactions within and between the particles of a system depending on the intended use.[129] For instance, the MM family of force fields (*i.e.* MM2,[141-144] MM3,[145] and MM4[146]) is regarded as the "gold standard" as they have been derived and parameterized based on the most comprehensive and highest quality experimental data.[110] They have been designed to accurately predict the molecular structure and properties of small organic molecules (*e.g.* alkanes, non-conjugated alkenes, aldehydes, ketones, ethers, esters, alcohols, acids). Particular to this type of force field is the fact that in order to reproduce accurately the experimental data it is necessary to use complicated functional forms. Consider the MM3 force field.[145] It employs harmonic functional terms only for bond stretching, and takes into account nine different interactions of which there are

several types of cross terms, in addition to modelling the non-bonding potential via a combination of electrostatic and Hill terms.

On the other hand, the OPLS[147, 148] (Optimized Potential for Liquid Simulations), CHARMM[149] (Chemistry at HARvard Macromolecular Mechanics) and AMBER[150-152] (Assisted Model Building with Energy Refinement) force fields have been designed to model large biological molecules (*e.g.* proteins, nucleic acids, and DNA in the case of AMBER[110]). As a result, this type of force field often uses simpler functional forms (*i.e.* only harmonic terms for the bond stretching and bending), may employ the united atom approximation, and models the non-bonding interactions via Lennard-Jones and electrostatic potentials.

Usually, force fields use potentials of the general form:[110]

$$U = U^{stretch} + U^{bend} + U^{torsion} + U^{imp-torsion} + U^{electr} + U^{vdW} \quad (2.43)$$

in which the potential energy of a system, describing the $3N$ positions of its atoms, is composed of intramolecular parts, accounting for the bonded interactions, and intermolecular parts, representing the nonbonded interactions.

The intramolecular part of a force field typically includes bond stretching ($U^{stretch}$), bending (U^{bend}), improper torsion ($U^{imp-torsion}$), and torsional ($U^{torsion}$) energies. In order to improve the accuracy of the models, some force fields include additional terms to account for effects that are not covered by the terms above. For instance, cross term energies (U^{cross}) are required to account for some interactions, like

the stretch-stretch, stretch-bend, bend-bend, stretch-torsion, bend-torsion, or torsion-torsion coupling.[110, 129]

The stretching and bending potentials are usually treated similarly; the energy increases with the displacement of the bond between atoms A and B or the bond angle from equilibrium values, r_{eq} and θ_0, respectively, where k_b and k_θ are the corresponding force constants, while N_{bonds} and N_{bends} are the corresponding numbers of bonds and bends (see Figure 2.3):

$$U^{stretch} = \sum_{i=1}^{N_{bonds}} k_b \left(r^i - r_{eq}^i\right)^2 \tag{2.44}$$

$$U^{bend} = \sum_{i=1}^{N_{bends}} k_\theta \left(\theta^i - \theta_0^i\right)^2 \tag{2.45}$$

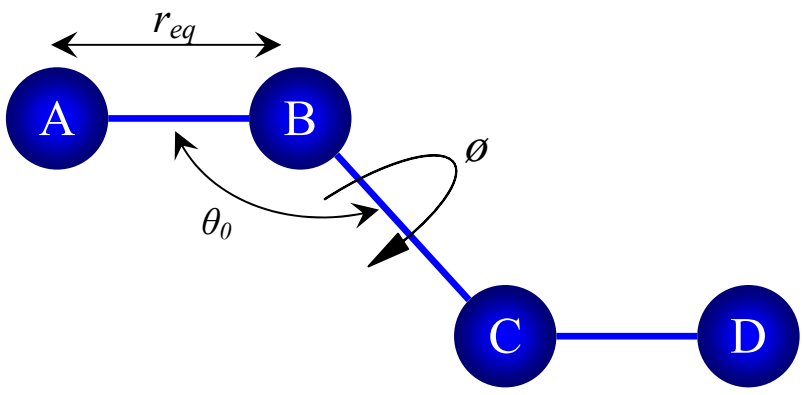

Figure 2.3 Schematic representation of the intramolecular equilibrium parameters r_{eq}, θ_0, and ϕ.

The total torsional energy, $U^{torsion}$, is the sum of the torsional energies of all $N_{dihedral}$ dihedral angles, ϕ. Each term captures the torsional cost of motion between

atoms separated by three bonds, such as the atoms A and D in Figure 2.3. The energy of this motion is modeled via a Ryckaert-Bellmans potential:[153]

$$U^{torsion} = \sum_{i=1}^{N_{dihedrals}} \sum_{n=0}^{6} c_n (\cos\phi_i)^n \tag{2.46}$$

where c_n is the torsional force constant.

To ensure that the arrangement of a four atom system ABCD (Figure 2.4), where the central atom D is bonded to other three atoms (*e.g.* a sp^2 hybridized carbon atom in carbonyl group), remains essentially planar, an improper torsion term is defined:

$$U^{imp-torsion} = \sum_{i=1}^{N_{impropers}} k_\omega (\omega^i - \omega_0^i)^2 \tag{2.47}$$

where k_ω is the force constant, and, ω^i and ω_0^i are the current out-of-plane i^{th} angle and its equilibrium value.

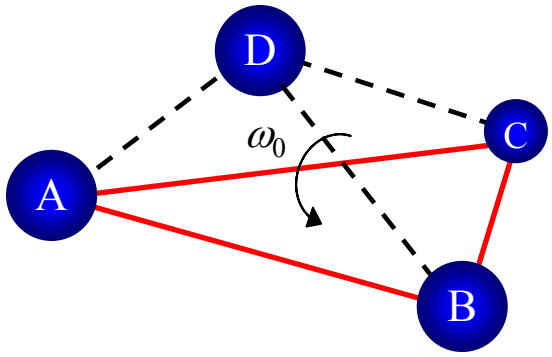

Figure 2.4 Schematic representation of an ABCD improper dihedral angle.

As seen in Figure 2.4, the angle torsion defined in this case, ω , usually referred as an "improper torsion" (dihedral ABCD), is the angle between the plane containing the

first three atoms (ABC) and the plane containing the last three (BCD). The use of a harmonic potential ensures that the additional energy contribution coming from this particular improper torsion is zero when the angle between the two planes is at its equilibrium value ω_0^i.

The nonbonded interactions account for the electrostatic interactions described via a Coulomb potential (U^{electr}) as well as the dispersion and short-ranged repulsion interactions captured by a Lennard-Jones potential (U^{LJ}). A third type of non-bonding energy term considered in some force fields is the polarization energy.[129]

Most of the time, the electrostatic energy is obtained by summing the pairwise Coulombic interactions between atoms i and j with partial charges q_i and q_j according to Equation (2.17).

The Lennard-Jones[39] inverse 12:6 potential, U^{LJ}, capturing dispersion interactions and short-range repulsive interactions, has the form:

$$U^{LJ} = 4\sum_{i=1}^{N}\sum_{j>i}^{N}\varepsilon_{ij}\left[\left(\frac{\sigma_{ij}}{r_{ij}}\right)^{12} - \left(\frac{\sigma_{ij}}{r_{ij}}\right)^{6}\right] \tag{2.48}$$

where r_{ij} is the distance between the centre of particle j and the centre of particle i, ε_{ij} is the well depth parameter, and σ_{ij} is the length parameter. A schematic representation of the Lennard-Jones potential is plotted in Figure 2.5. The $1/r_{ij}^{12}$ term produces the repulsive part of the curve, while the $1/r_{ij}^{6}$ term is responsible for the attractive part.

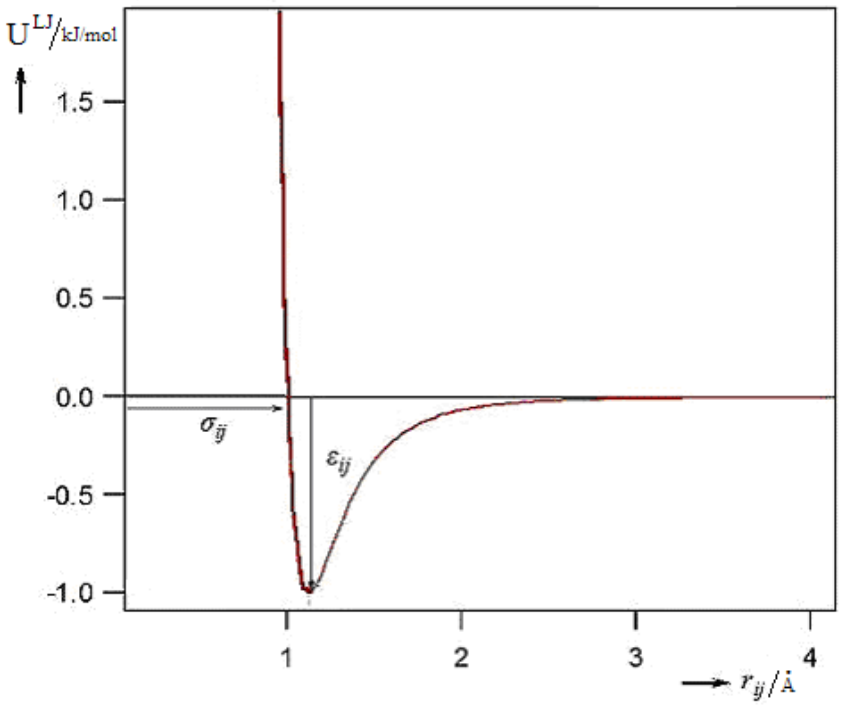

Figure 2.5 Representation of the Lennard-Jones potential as a function of interatomic separation.

To summarize, the reliability of molecular mechanical force fields relies on the parameters and the potential energy functions used to describe the total energy of a model. Parameters have to be optimized for a particular set of potential energy functions, and thus they are usually not transferable to other forms of force fields.

2.5 Analysis of Simulation Data

Knowledge of the order parameter(s) and pair distribution functions provides a route to the identification of the phase of the molecular system being simulated and the characterization of its structure. Moreover, "snapshots" offer a complementary way to analyze the phase structure. Specifically, a snapshot provides an instantaneous picture of the molecular organization in the phase at a certain time during the simulation but it is not the average structure. By blending snapshots taken during the simulation runs, a movie reflecting the movement of the molecules in time can be obtained. To characterize the dynamic properties of a phase, the diffusion coefficients have also been evaluated.

Properties of liquid crystal phases are often expressed relative to the director and layer normal. To measure the long-range order in the simulated systems, one can define orientation vectors within the molecules, such as the bonds in alkyl chain or the long axis of a rigid molecular segment. Then, with a chosen molecular vector, $\vec{u}_\alpha(t)$, the instantaneous average over these molecular types of vectors defines a director, $\vec{D}(t)$. Order relative to the director is assessed by evaluating:

$$P_n(t) = \frac{1}{N}\sum_{\alpha=1}^{N} P_n(\cos\theta_\alpha) \tag{2.49}$$

where the sum runs over all N molecules in the simulation cell, $P_n(\cos\theta)$ is a Legendre polynomial, and $\cos\theta_\alpha = \left(\vec{u}_\alpha(t)\cdot\vec{D}(t)\right)/\left(u_\alpha D\right)$. For a given choice of vector, consistency in alignment of the vectors between the molecules in the fluid indicates the degree of

orientational ordering. $P_2(t)$ is the most commonly used order parameter. It vanishes in a completely disordered isotropic phase and it is equal to unity for a perfectly ordered phase.

In practice, $P_2(t)$ is evaluated by constructing the Q tensor. By summing over all N molecules in the system and averaging over all configurations, the Q tensor is evaluated as:[119]

$$Q_{\alpha\beta} = \frac{1}{2N}\sum_{\alpha=1}^{N}\left[3u_{\alpha a}u_{\alpha b} - \delta_{ab}\right] \quad a,b = x,y,z \tag{2.50}$$

where $u_{\alpha a}$ is the a component of the chosen orientational vector for molecule α. The largest eigenvalue of the Q tensor defines the $P_2(t)$ order parameter of the fluid, and the corresponding eigenvector is the director of the fluid, $\vec{D}(t)$.

For example, in the 2PhP and 5PhP molecules (Figure 1.5) three vectors have been defined as follows: the most relevant vector joins the phenyl and pyrimidine rings in the molecular core, and the other two vectors are along the carbon-carbon bonds decoding the order within the hydrocarbon tails. For each of these three vectors, the $P_n(t)$, for $n = 1-4$, along with the associated directors have been calculated, and the instantaneous and time averaged order parameters, $P_n(t)$ and $P_n = \langle P_n(t)\rangle$ respectively, will be reported in Chapter 4.

It is important to note that in a SmA layer, the molecular orientation is on average perpendicular to the layer plane, so that the layer normal and the director coincide (Figure

1.1 (b)). On the contrary, in a SmC phase, the molecules tilt within layers, thus the layer normal is tilted to the director by a nonzero angle. The instantaneous layer normal has been calculated within the simulations to identify the presence of tilted SmC phase. A layer normal definition is conceptually very simple but difficult to calculate within simulations of complicated mesogens. After several attempts, I ultimately defined the local layer normal, $\vec{L}_i(t)$, for each molecule and evaluate the global layer normal, $\vec{L}(t)$, and associated $P_2(t)$ order parameter via Equation (2.49).

Specifically, the local layer calculation[154] proceeds by choosing a site within the molecular core and finding equivalent sites in all neighbouring molecules within a radius of 6.36 Å. This distance is chosen so that at least two other molecules are generally found within the volume but molecules from neighbouring smectic layers are too far away to contribute to the calculation of local layer normal. In my case, the chosen site is one of the rings, and I have verified that both phenyl and pyrimidine rings yielded equivalent results, as did the normal defined using the midpoint of the ring centers. With the molecular site chosen, the position of this site along with the positions of all equivalent sites within nearby molecules are least squares fitted to a plane, and the vector normal to this plane is defined as the local layer normal, $\vec{L}_i(t)$. In cases where too few neighbours are found, the molecule is not assigned a local layer normal. The global layer normal, $\vec{L}(t)$, is obtained by summing over all N molecules in the system with a local layer defined and averaging over all of these local layer normals.

Moreover, the instantaneous angle between the phase director, $\vec{D}(t)$, and the global layer normal, $\vec{L}(t)$, provides information on the phase; thus a SmA phase is expected to yield an angle of roughly zero while a SmC phase will have a nonzero average angle. The assessment of the phase via the angle between the director and the global layer normal is difficult within a simulation since the layers may be tilted relative to each other, due to constraints imposed by the size and shape of the simulation cell. Consider the following two definitions of the relative angle:

$$\theta_1 = \left\langle \cos^{-1}\left(\vec{D}(t)\cdot \vec{L}\ (t)\right)\right\rangle \tag{2.51}$$

$$\theta_2 = \frac{1}{N}\left\langle \sum_{\alpha=1}^{N} \cos^{-1}\left\{\vec{u}_\alpha(t)\cdot \vec{L}_\alpha(t)/(u_\alpha L_\alpha)\right\}\right\rangle \tag{2.52}$$

where the angular brackets denote time averaging. For θ_1, all molecules contribute to the global director and layer normal, and the angle is calculated based on these average directions. This method implicitly includes any tilting between layers. The second method, yielding θ_2, is based on local differences in molecular tilt and local layering. Equation (2.52) will yield angles that are insensitive to relative layer orientations.

When all local layers normal coincide with all local directors, θ_1 and θ_2 will average to zero. If the local layers are always perpendicular to the molecular director, then θ_2 will average to 90 degrees. These results are straightforward but, since the local layer normal can point in either direction (up and down from the layer), an ambiguity exists in the calculation of θ_2. By convention I always choose the smallest angle between

the local layer normal, $\vec{L}_\alpha(t)$, and the local director, $\vec{u}_\alpha(t)$, so that completely random relative orientations yield a value of 57.3 degrees for θ_2. Both global and average tilt angles are important tools in order to distinguish between a titled and a nontilted smectic phase.

More information about the structure of a phase is contained in *pair distribution functions*, which give the probability of finding two particles with particular positions and orientations, relative to that for a completely random distribution at the same density (*i.e.* the ideal gas). The simplest of these is the *radial distribution function* (RDF), $g(r)$, which gives the probability of finding a particle at a distance r from another, irrespective of their orientations. A schematic representation of $g(r)$ is shown in Figure 2.6.

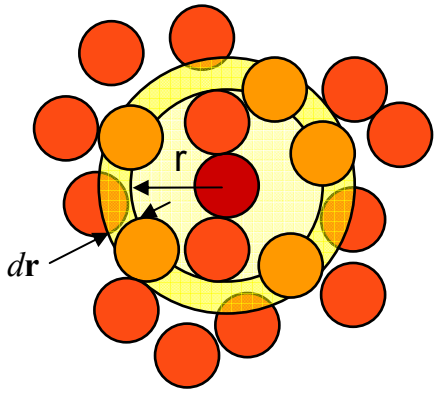

Figure 2.6 Radial distribution function uses a spherical shell of thickness $d\mathbf{r}$ around the central particle.

The radial distribution function is normalized, such that in the absence of positional correlations it is unity. It is defined as:[119]

$$g(r) = \frac{V}{N^2}\left\langle \sum_{i}^{N}\sum_{j\neq i}^{N} \delta\left(\mathbf{r} - \mathbf{r}_{ij}\right)\right\rangle \tag{2.53}$$

where $\delta(r)$ is the Dirac delta function, $\frac{V}{N^2}$ normalizes the RDF relative to the probability expected for a completely random distribution at the same density, and r_{ij} is the interparticle separation. In computer simulations, $g(r)$ is calculated by counting the number of pairs found between r and $r + \delta r$ and comparing to the number expected in an unstructured fluid.

The RDF is a useful tool to describe the structure of a system. For an unstructured fluid, the RDF is equal to unity, as there is an equal probability of finding another particle at any given separation in space. The RDF of a liquid is intermediate between those of a solid and a gas and shows a smaller number of peaks with a decay in the height of the peaks at short distances and an eventual converge to unity (*i.e.* there is no long-range order).

For complex molecules, it is typical to calculate a number of *site-site distribution functions* as well. Here, a "site" may be an entire ring or atoms within a ring. Consider, for instance, the case of a benzene simulation by means of an atomistic model. It is customary to define $g(r)$ not only in terms of molecular centre-of-mass but also in terms of site-site RDFs with a particular RDF for each possible distinguishable atomic combinations, such as $g_{CC}(r)$, $g_{CH}(r)$, and $g_{HH}(r)$. One advantage of using the

interatomic radial distribution functions is that they can be directly correlated with information obtained from neutron scattering and X-ray experiments.[155]

The anisotropy of liquid crystal phases requires the introduction of additional *positional distribution functions* to reflect this structural feature (*i.e.* the properties of a material depend on the direction in which they are measured). Using the director, $\vec{D}(t)$, or layer normal, $\vec{L}(t)$, as reference vectors, intermolecular distributions are divided into components parallel and perpendicular to the chosen vector. If the layer normal is given by $\vec{L}(t)$, then the vectors $\vec{r}_{\parallel}^{\,L}$ and $\vec{r}_{\perp}^{\,L}$ are obtained as $\vec{r}_{\parallel}^{\,L} = (\vec{r}_{ij} \cdot \vec{L})\vec{L}$ and $\vec{r}_{\perp}^{\,L} = \vec{r}_{ij} - \vec{r}_{\parallel}^{\,L}$, as shown in Figure 2.7 (a).

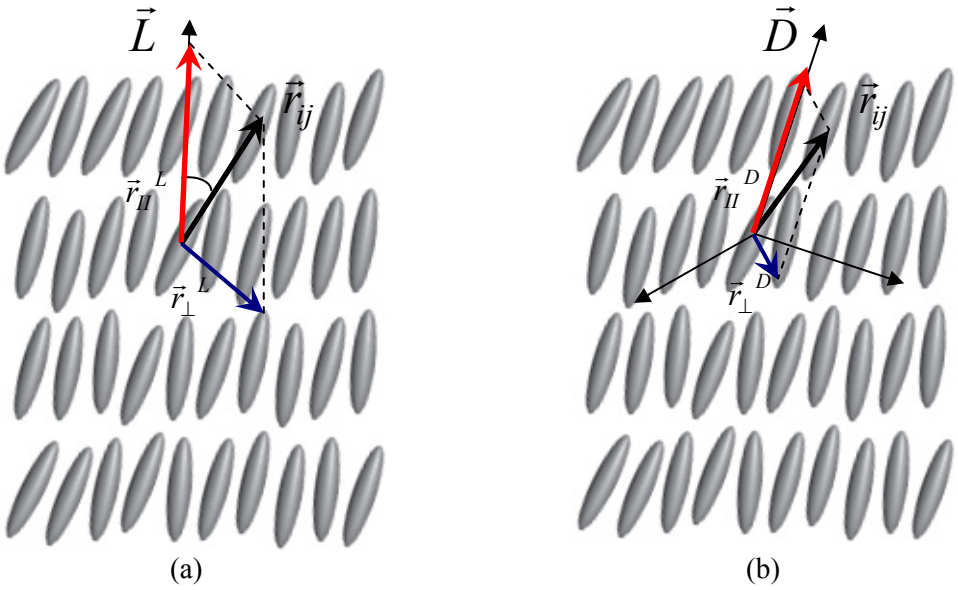

(a) (b)

Figure 2.7 Schematic representation of the $\vec{r}_{\parallel}^{\,L}$ and $\vec{r}_{\perp}^{\,L}$ vectors relative to layer normal $\vec{L}$ in (a), and of the $\vec{r}_{\parallel}^{\,D}$ and $\vec{r}_{\perp}^{\,D}$ vectors relative to director $\vec{D}$ in (b). The interparticle vector, $\vec{r}_{ij}$, is identified by a thick black arrow.

The *longitudinal* radial distribution function, $g_{\parallel}^{D/L}(r_{\parallel})$, is defined as:[156]

$$g_{\parallel}^{D/L}(r_{\parallel}) = \frac{\langle n \rangle_{r_{\parallel}, r_{\parallel}+\delta r_{\parallel}}}{\langle n_0 \rangle_{r_{\parallel}, r_{\parallel}+\delta r_{\parallel}}} \tag{2.54}$$

where $r_{\parallel}$ is the component of separation between the two particles resolved along the chosen vector (either director, $\vec{D}(t)$, or layer normal $\vec{L}(t)$), and $\langle n \rangle_{r_{\parallel}, r_{\parallel}+\delta r_{\parallel}}$ is the number of intermolecular pairs with a projection along the same vector between $r_{\parallel}$ and $r_{\parallel} + \delta r_{\parallel}$. $\langle n_0 \rangle$ is the corresponding number expected in an unstructured fluid.

Analogously, there is a *transversal* radial distribution function, $g_{\perp}^{D/L}(r_{\perp})$, evaluated as:

$$g_{\perp}^{D/L}(r_{\perp}) = \frac{\langle n \rangle_{r_{\perp}, r_{\perp}+\delta r_{\perp}}}{\langle n_0 \rangle_{r_{\perp}, r_{\perp}+\delta r_{\perp}}} \tag{2.55}$$

where $r_{\perp}$ is the component of the separation resolved perpendicular to the chosen vector, and $\langle n \rangle_{r_{\perp}, r_{\perp}+\delta r_{\perp}}$ is the number of intermolecular pairs with a projection perpendicular to the vector between $r_{\perp}$ and $r_{\perp} + \delta r_{\perp}$.

In a SmA phase, where the director and layer normal coincide, the choice of vector is irrelevant, and $g_{\parallel}^{D/L}(r_{\parallel})$ describes interlayer structure (*i.e.* determines, at least

approximately, the spacing - called "layer spacing" - between the smectic layers), whilst $g_{\perp}^{D/L}(r_{\perp})$ illustrates the molecular distribution within the layer.

Furthermore, longitudinal distribution functions $g_{\parallel}^{D}(r_{\parallel})$ and $g_{\parallel}^{L}(r_{\parallel})$ allows us to find a third approach to the calculation of a relative angle. The peak position in the former will appear at longer separations than for the latter in a SmC phase (see Figure 2.7). The angle extracted from these peak positions is directly comparable to the tilt angle obtained from optical measurements.[16]

Another function useful for characterizing the structure of a fluid, is the *second-order correlation function*, $g_2(r)$, evaluated as:

$$g_2(r) = \left\langle P_2\left(\cos\theta_{\alpha\beta}\right)\right\rangle_r \tag{2.56}$$

where $\theta_{\alpha\beta}$ is the angle between the orientational vectors of molecules α and β. This function vanishes when the molecular orientations are uncorrelated, reaches -0.5 when the molecules are in an orthogonal arrangement and approaches unity when parallel molecular alignment is highly probable. Characteristic of the isotropic phase is that $g_2(r)$ is short ranged but the range increases for nematic and smectic phases. At large separations, $g_2(r)$ approaches the square of the second rank order parameter, *i.e.* $g_2(r) \to \langle P_2 \rangle^2$ when $r \to \infty$.

In addition to collecting structural information, time correlation functions characterizing the dynamic properties of a system have been considered. The mean

square displacement (MSD) is a measure of the average distance a particle travels and it is evaluated as: $MSD = \left\langle \left| \vec{r}_i(t) - \vec{r}_i(0) \right|^2 \right\rangle$, where $\vec{r}_i(t)$ is the position vector of the i^{th} particle at time t. The angle brackets indicate that the magnitude of this vector is averaged over many such time intervals; often, it is averaged also over all N particles in the system. For fluids, the mean square displacement continually increases with time, varying linearly at long times according to the generalized Einstein formula:[119]

$$D = \lim_{t \to \infty} \frac{\left\langle \left| \vec{r}_i(t) - \vec{r}_i(0) \right|^2 \right\rangle}{2dt} \tag{2.57}$$

where D is the diffusion coefficient, d is the dimensionality of the system (usually in three dimensions), and $\vec{r}_i(0)$ and $\vec{r}_i(t)$ are the i^{th} particle positions at zero time and time t. For solids, the mean square displacement becomes constant rather than continually increasing with time.

Chapter 3

Molecular Models

The development of accurate, reliable, and computationally feasible interaction models is the scope of molecular modelling. There are different types of model potentials which can be used for liquid crystal molecules, as follows: fully atomistic (FA),[21] united atom (UA),[22] and coarse-grained (CG) models.[157] Although coarse-graining can be carried out at a variety of levels,[157] the common idea is to design a way of retaining information about the chemical structure while limiting computational expense.[158] The implementation of CG models is usually divided into two distinct stages: the partition of the system into larger CG structural units, and the construction of an effective force field to describe the CG units. Depending on the way the system is partitioned, there are two possible ways of coarse graining, namely single-site and multi-site CG models. Unlike the single-site CG model which assimilates a whole molecule into a non-spherical site, the multi-site CG model commonly uses both spherical and non-spherical sites to represent a molecule.

For example, the 5CB mesogen (Figure 3.1) can be represented by only one site if the single-site coarse-grained model is used (a), by nine sites if a multi-site coarse-grained model is employed (b), by 19 sites in the case of a united atom model, and by 38 sites in a fully atomistic representation model (c).

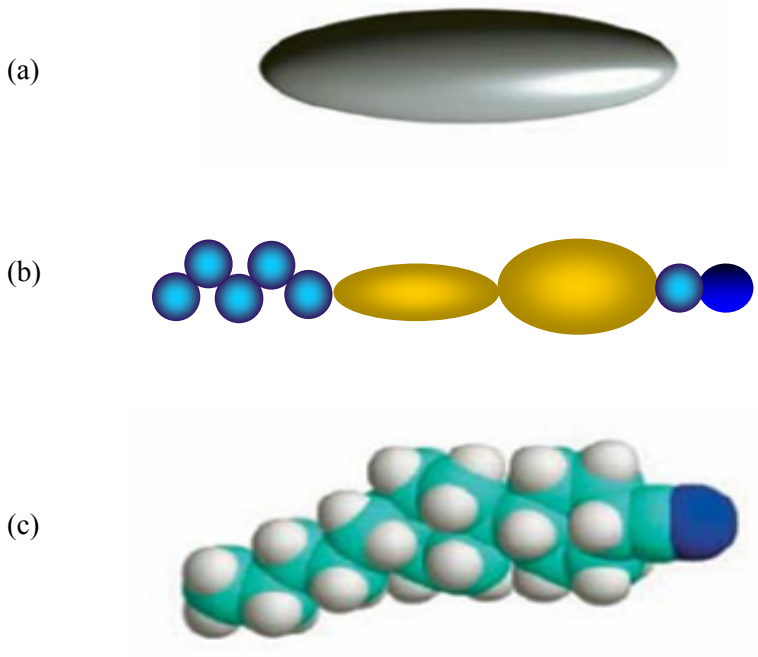

Figure 3.1 Single-site coarse-grained (a), multi-site coarse-grained (b), and full atomistic[50] (c) model representations of the 4'-n-pentyl-4-cyanobiphenyl (5CB) mesogen.

In choosing which of the model potentials to use, one needs to consider the complexity of the real mesogenic molecule, the required simulation time, and the number of molecules to be simulated. In the case of 2PhP and 5PhP molecules (Figure 1.5), adopting the single-site representation comes with the cheapest computational cost at the expense of losing the particularities of each mesogen. In other words, a single-site CG model will not be able to distinguish between the two mesogens. In contrast, using a full atomistic representation comes with the highest and almost unfeasible computational cost but the difference between the two mesogens is completely taken into account. My

approach for representing the two mesogens is to use a multi-site CG model that explicitly considers the inter-ring torsion while significantly reducing the computational cost. The molecular flexibility is important since the complex phase behavior of mesogenic molecules is the result of a delicate balance between subtle energetic and entropic effects.[159] In fact, small changes of chemical structure can lead to significantly different organization (large positional and orientational order) in a particular phase, and hence to fundamentally different macroscopic properties.

The multi-site coarse-grained potential, adopted in this thesis, contains intramolecular terms, controlling the energetic costs for molecular conformations, and intermolecular terms, accounting for the interactions between all pairs of atoms on different molecules, or within the same molecule if the atoms are not close to each other.

In this hybrid model, all aromatic units are represented as discotic ellipsoidal Gay-Berne (GB) sites, and the flexible chain units by spherical Lennard-Jones (LJ) sites. For instance, in the 2PhP and 5PhP models both benzene and pyrimidine rings are represented as GB ellipsoids, and the methyl and methylene groups of the alkyl chains, as well as the oxygen atoms, are represented as spherical LJ sites. Thus, in the multi-site coarse-grained model adopted in this thesis, the force field contains three different non-bonding terms to account for pairwise dispersion and repulsive interactions. The intermolecular potential is given by the sum of the electrostatic potential, with the form of Equation (2.17), and by the sum of the interaction potentials between two identical (LJ/LJ or GB/GB) or unlike (LJ/GB) sites:

$$U_{\text{intermolecular}} = \sum_{A=1}^{N_{ch}} \sum_{B>A}^{N_{ch}} U_{AB}^{Coul} + \sum_{A=1}^{N_{LJ}} \sum_{B>A}^{N_{LJ}} U_{AB}^{LJ/LJ} + \sum_{A=1}^{N_{LJ}} \sum_{B=1}^{N_{GB}} U_{AB}^{LJ/GB} + \sum_{A=1}^{N_{GB}} \sum_{B>A}^{N_{GB}} U_{AB}^{GB/GB} \quad (3.1)$$

where N_{LJ}, N_{GB}, and N_{ch} represent the number of Lennard-Jones, Gay-Berne, and total number of charges, respectively.

The interactions between any two spherical sites, representing the oxygen atoms as well as methylene and methyl units, are modeled using the Lennard-Jones[39] inverse 12:6 potential, $U_{AB}^{LJ/LJ}$, given by Equation (2.48). For the LJ sites, values of $\sigma_0^{LJ} = 3.93$ Å and $\varepsilon_0^{LJ} = 0.5986$ kJ/mol, taken from the work of *Leggetter and Tildesley*,[160] are used throughout this thesis. To describe the interactions between two aromatic rings, a Gay-Berne interaction potential, $U_{AB}^{GB/GB}$, is employed. Finally, when a methylene or methyl unit interacts with an aromatic ring, the potential is described by the $U_{AB}^{LJ/GB}$ potential. Specifically, the intermolecular potential is calculated for all pairs of atoms except when two atoms belong to the same molecule and are less than four bonds apart.

The first section of this chapter describes the development of molecular models for the host and dopant molecules based on extensive series of density functional calculations. The form of the Gay-Berne potential, $U_{AB}^{GB/GB}$, is presented and discussed in the second part of this chapter. Here, the approach used in order to parameterize the GB potential is described along with the work done in order to check the validity of the selected sets of GB parameters to model more complex mesogenic molecules.

3.1 Intramolecular Potential

The *ab initio* methods, described in Section 2.1, have been used to calculate the bond lengths, bond angles, dihedral angles, improper dihedral angles, and charges on all atoms of each molecule. A broad set of *ab initio* geometry optimizations have been done to examine the structure and flexibility of the host and dopant molecules. Since the molecules are so large, each terminal alkyl chain has been replaced with a single methyl group for the *ab initio* calculations. This truncation was done for all the molecules, except for one of the dopant molecules (*i.e.* the Dop5a-NO_2 shown in Figure 3.6), in which the ethyl group has been considered explicitly. Due to this simplification, the atomic charges corresponding to the part of flexible alkyl chains that was not optimized are set to zero.

The geometry optimizations have been carried out using the GAUSSIAN 03[161] electronic structure program, using Density Functional Theory, with the B3LYP functional[162] and the 6-311++G(d,p) basis set.[163, 164] Polarization and diffuse functions were used in order to capture the interactions between atoms that are relatively far apart. The basis set employed was also imposed by the complexity of the molecules. Using the CHELPG algorithm[165] at the global energy minimum of each molecule, the atomic charges have been evaluated. For the aromatic rings, a partial charge, equal to the net charge on the ring atoms, is placed at the centre of the ring. The charge on each individual site (*i.e.* atom or group of atoms) along with the site numbering is available in Appendices A and B, for the host and dopant molecules, respectively.

The full intramolecular potential used in this thesis contains energetic contributions from angle bending, and dihedral torsions, except for the Dop5a-NO_2 molecule in which an improper torsion term, $U^{imp-torsion}$, has been added to restrict the out-of-plane motion of the carbonyl group:

$$U_{\text{intramolecular}} = U^{bend} + U^{torsion} \tag{3.2}$$

The bond stretching potential, $U^{stretch}$, given by Equation (2.44), is omitted in this thesis as all the bond lengths have been kept fixed at their equilibrium value using the RATTLE algorithm.[133] The equilibrium bond lengths have been extracted from the global energy minimum structure for the 2PhP, 5PhP, Dop5a-NO_2, and Spiro molecules. For the alkyl chain, the equilibrium bond lengths and the corresponding force constants are taken from the work of *Leggetter and Tildesley*.[160]

The bending potential is given by Equation (2.45). The equilibrium angles are obtained from the global minimum energy configuration. The corresponding force constants are obtained from a least-squares fit to eleven B3LYP/6-311++G(d,p) restricted geometry optimizations, where the angle of interest is given a value within $\theta_0 \pm 5^0$, but the remaining degrees of freedom are allowed to relax. For the alkyl chain, the equilibrium angle value and the bond angle force constant are taken from the work of *Leggetter and Tildesley*.[160] Since the GB sites are bonded via their centres of mass, it is necessary to include an angle term for each site bonded to a GB particle. These terms, involving the angle between the long axis of the GB sites and the bond between them and the attached LJ sites, prevent the free rotation of GB particles around their centres of

mass. For these angles, values of $\theta_o = 180^\circ$ and force constants of values similar to the C-C-C bond angles are assigned.

A Ryckaert-Bellemans[153] type potential is used for torsional motion. Between eighteen to thirty-six B3LYP/6-311++G(d,p) restricted geometry optimizations, in which the selected dihedral angle is frozen at a fixed value while the other degrees of freedom are allowed to vary, were performed in order to describe each torsion. The expression of the torsional potential is specified by Equation (2.46). For the alkyl chain, the c_n expansion coefficients are taken from the *Leggetter and Tildesley*'s work.[160]

An improper torsional potential, expressed by Equation (2.47), has been used to impose planarity around the carbonyl groups inside the Dop5a-NO_2 dopant molecule during simulations. The equilibrium angle values are extracted from the global minimum energy configuration. The corresponding force constants are obtained from least-squares fits to twenty B3LYP/6-311++G(d,p) restricted optimization calculations for angles within $\pm 5^\circ$ of the corresponding equilibrium values.

3.1.1 Host Models

The host molecules considered in this thesis are: 2-(4-butyloxyphenyl)-5-octyloxy-pyrimidine (2PhP), and 5-(4-butyloxyphenyl)-2-octyloxypyrimidine (5PhP). A schematic representation of 2PhP and 5PhP molecules, using the multi-site coarse-grained approach employed in this thesis, is presented in Figure 3.2 (a).

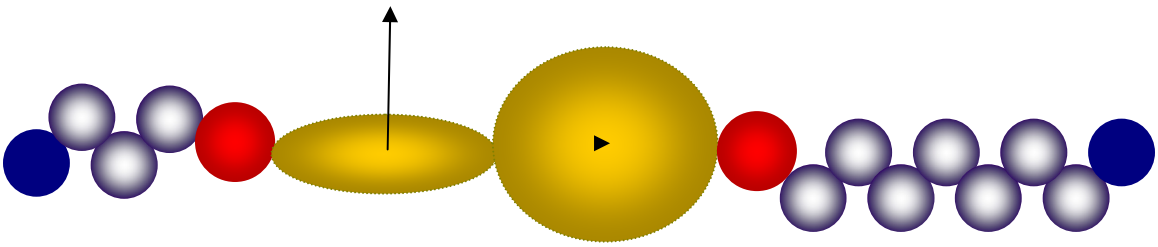

(a)

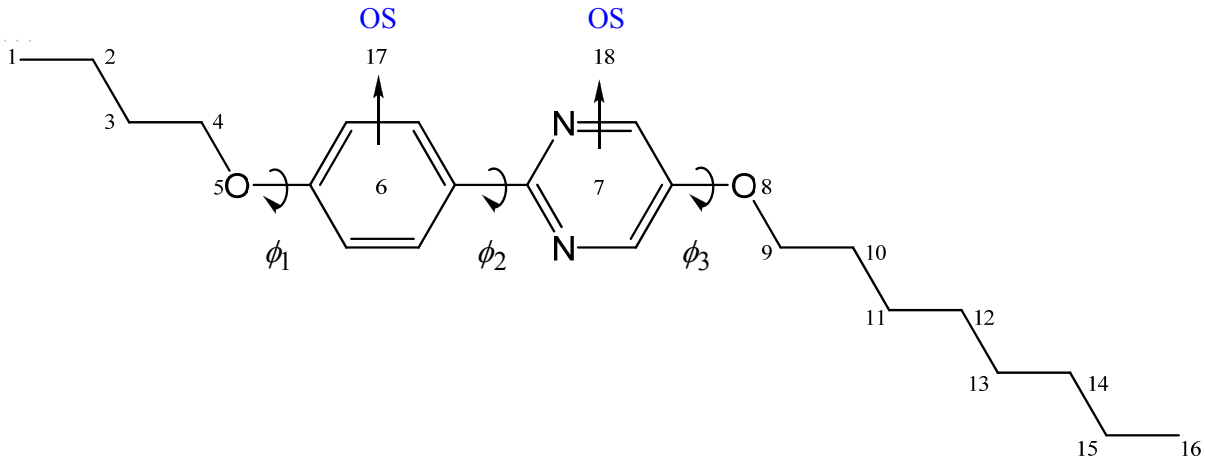

(b)

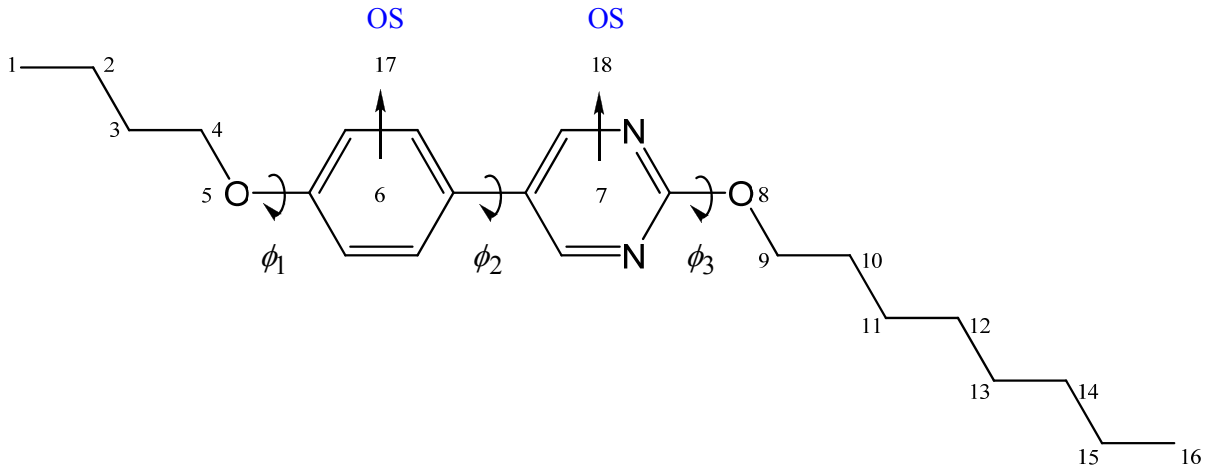

(c)

Figure 3.2 (a) A schematic multi-site coarse-grained representation of the 2PhP and 5PhP molecules. The aromatic units, oxygen atoms, methylene groups, and methyl groups are shown in yellow, red, grey, and blue, respectively. (b) Structure of the 2PhP molecule. (c) Structure of 5PhP molecule. The site numbering and the torsion indexing will be used throughout this thesis.

Furthermore, Figures 3.2 (b) and (c) show the site numbering used to identify atoms or group of atoms and the "ghost' orienting sites (noted OS), corresponding to the C_∞ symmetry axis of the GB sites.

Both host molecules are represented by an equal number and type of sites (*i.e.* 14 spherical LJ and two discotic ellipsoidal GB sites). On the other hand, the models are still unlike in that the torsional potentials between the phenyl and pyrimidine rings as well as the charges on the two GB sites are different. The inter-ring torsions are vital in modelling the liquid crystalline phases of the 2PhP and 5PhP molecules. Figure 3.3 presents a comparison of the 360º rotation over the GB(7)-GB(6) bond, corresponding to the inter-ring ϕ_2 dihedral angle in both 2PhP and 5PhP molecules.

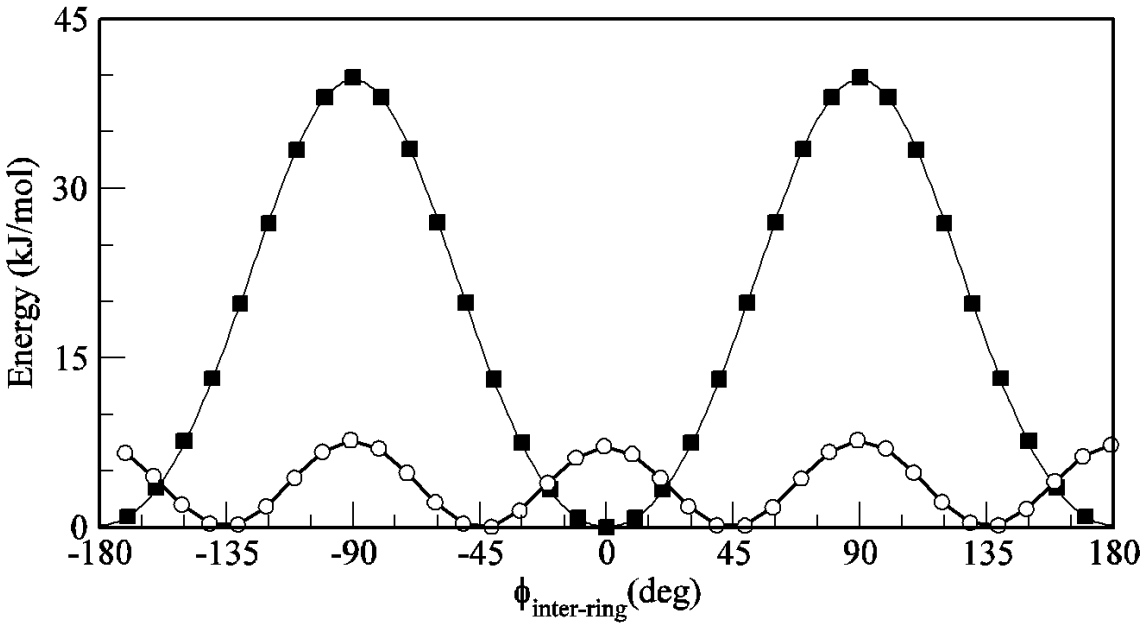

Figure 3.3 Comparison between the phenyl-pyrimidine angle torsional energies. *Ab initio* points are represented by filled squares for 2PhP molecule and open circles for 5PhP molecule, respectively. The solid lines show the torsional potentials obtained by fitting.

As it is well-known for the biphenyl molecule,[166, 167] the ring-ring torsional barrier is influenced by the competition between the steric repulsion of the *ortho* neighbouring hydrogen atoms belonging to the two rings, minimized when the two rings are orthogonal, and stabilization arising from the inter-ring π conjugation, enhanced by the planar configuration. In the case of 2PhP molecule, the planar configuration is preferred. In contrast, in the case of the 5PhP molecule, the competition gives a global minimum at around 40º, as the steric repulsion is equalized by the inter-ring π conjugation. The different positions of the nitrogen atoms in the pyrimidine ring of the two host molecules account for the difference in the preferred relative ring orientations and the significant difference in the associated torsional energy barriers (*i.e.* 40 kJ/mol, and 8 kJ/mol for the 2PhP and 5PhP molecules, respectively).

In the host molecules, *ab initio* calculations have been performed for all motions involving an aromatic ring. Within the core, bending potentials are introduced to preserve linearity along the O(5)-GB(6)-GB(7)-O(8) axis (see Figures 3.2 (b) and (c)). Since the ring atoms are not explicitly included in the potential, each ring is represented by its center via a GB site, and by a "ghost" site placed on the vector normal to ring plane and passing through the centre. These "ghost" sites are identified as orienting sites OS(17) and OS(18) in Figures 3.2 (b) and (c). Bending distortions of the ring can be represented via these two points. For instance, an O(5)-GB(6)-GB(7) potential accounts for the in-plane energetic cost of a bend at GB(6). Likewise, an OS(17)-GB(6)-O(5) bend potential provides an energetic cost for out-of-plane motion of the ring.

Consider first the 2PhP host molecule. The force constants corresponding to the C(9)-O(8)-GB(7), and GB(6)-O(5)-C(4) bends have been calculated as 347.82 kJ mol^{-1} rad^{-2}, and 368.81 kJ mol^{-1} rad^{-2}, respectively. Likewise, the torsions about the GB(6)-O(5), and O(8)-GB(7) bonds, corresponding to ϕ_1 and ϕ_3 dihedral angles (see Figure 3.2 (b)) have been considered. The fitted potentials, presented in Figure 3.4, reproduce very well the *ab initio* energies. Each dihedral angle has a minimum at around 0º, so that the C(4) and C(9) are in the same plane as their nearest ring. The energy barriers have been evaluated at 11.30 kJ/mol and 14.27 kJ/mol for the motion about GB(6)-O(5) and O(8)-GB(7) bonds, respectively.

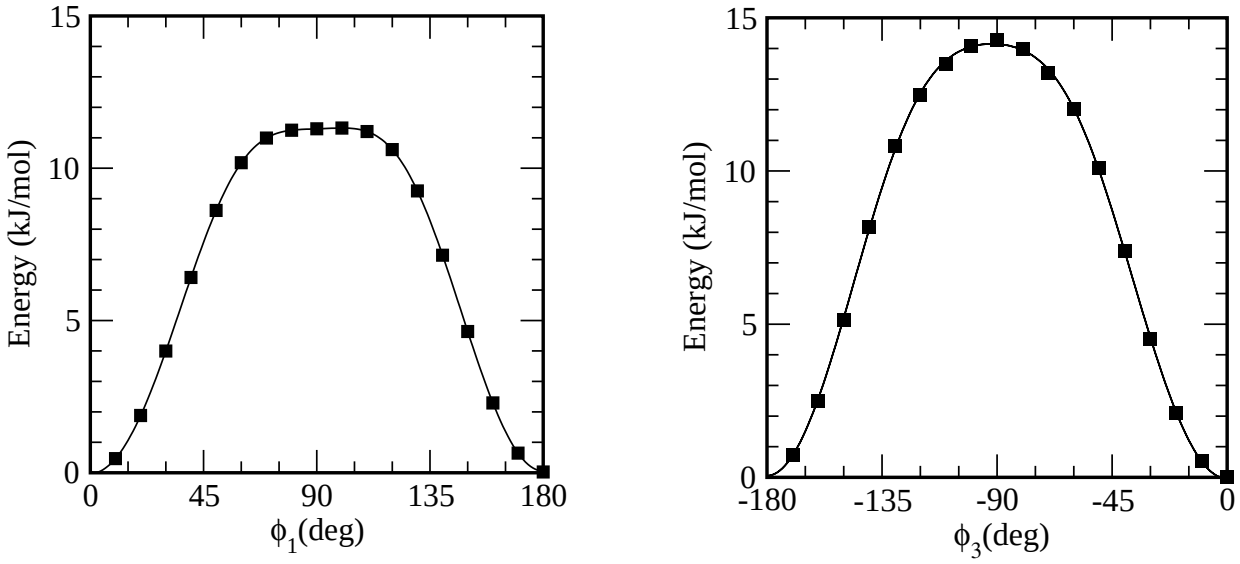

(a) (b)

Figure 3.4 Torsional barriers from B3LYP/6-311++G(d,p) *ab initio* calculations. The torsional potentials are given for the rotation about (a) GB(6)-O(5), and (b) O(8)-GB(7) bonds in the 2PhP molecule, corresponding to the ϕ_1 and ϕ_3 dihedral angles, respectively. *Ab initio* points are represented by filled squares and fitted potentials by solid lines.

For the 5PhP host molecule, the force constants corresponding to the C(9)-O(8)-GB(7) and GB(6)-O(5)-C(4) bends have been calculated. The corresponding force constants are 350.69 kJ mol^{-1} rad^{-2}, and 379.77 kJ mol^{-1} rad^{-2}, respectively. The motions about the GB(6)-O(5) and O(8)-GB(7) bonds, corresponding to ϕ_1 and ϕ_3 dihedral angles in the 5PhP molecule (see Figure 3.2 (c)) have been evaluated and the comparison between the fitted and *ab initio* potentials is shown in Figures 3.5 (a) and (b), respectively.

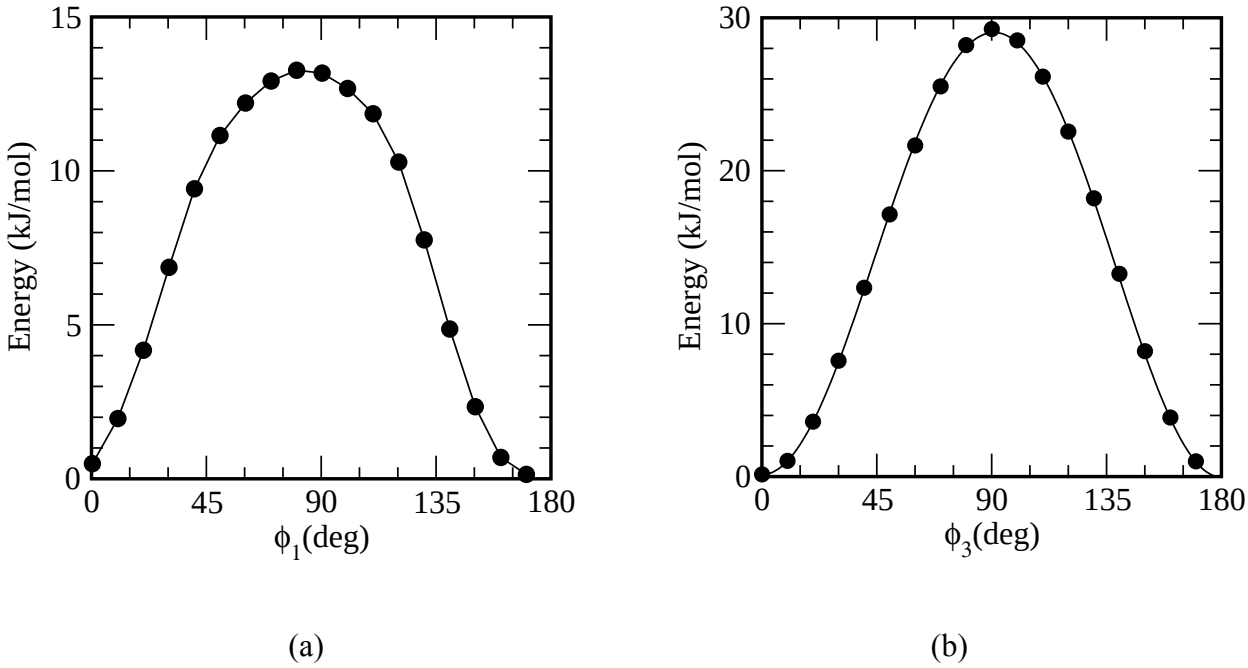

(a) (b)

Figure 3.5 Torsional barrier from B3LYP/6-311++G(d,p) *ab initio* calculations. The torsional potential are given for the rotation about (a) GB(6)-O(5), and (b) O(8)-GB(7) bonds in the 5PhP molecule, corresponding to the ϕ_1 and ϕ_3 dihedral angles, respectively. *Ab initio* points are represented by filled circles and fitted potentials by solid lines.

Both dihedral angles have their minimum at around 0º, with the C(4) and C(9) atoms in the same plane with the nearest ring. The torsional energy barriers are higher than for the 2PhP molecule; barriers of 13.33 kJ/mol and 29.26 kJ/mol for the motion about GB(6)-O(5) and O(8)-GB(7) bonds, respectively.

The charge on each individual site, along with the equilibrium bond lengths, as well as the full sets of bending, and torsional potential parameters, calculated in this thesis or that have been taken from literature,[160] are presented for the two host molecules in Appendix A.

3.1.2 Dopant Models

The 5,5'-bis(heptyloxy)-2,2'-spirobi[indene]-1,1'(3*H*,3'*H*)-dione (Spiro) and the 2,2',6,6'-tetramethyl-3,3'-dinitro-4,4'-bis[(4-alkyloxybenzoyl)-oxy]biphenyl (Dop5X-NO_2) are the two chiral molecules acting as dopants in the presence of the 2PhP and 5PhP hosts. As mentioned in Section 1.4, in the family of Dop5X-NO_2 molecules the alkyl chain length is represented by X, and it is formed of 1, 8, and 9 carbon atoms in the Dop5a-NO_2, Dop5d-NO_2, and Dop5e-NO_2 molecules, respectively. The discussion that follows refers exclusively to the Dop5a-NO_2 molecule, given that the main difference between these dopants is the length of the hydrocarbon chains. Since literature potentials are used for the hydrocarbon chains, the other dihedral angles, bending angles, improper dihedral angles, and the corresponding force constants calculated for the Dop5a-NO_2 molecule would be transferable to other Dop5X-NO_2 molecules.

Figure 3.6 (a) shows the schematic multi-site coarse-grained representation of the Dop5a-NO_2 molecule. Consider the site numbering presented in the Figure 3.6 (b), where the "ghost" orienting sites assigned to the rings are numbered as OS(15), OS(16), OS(17), and OS(18). For Dop5a-NO_2 molecule, the intramolecular motion is divided into 18 bends, 13 torsions, and two improper torsions.

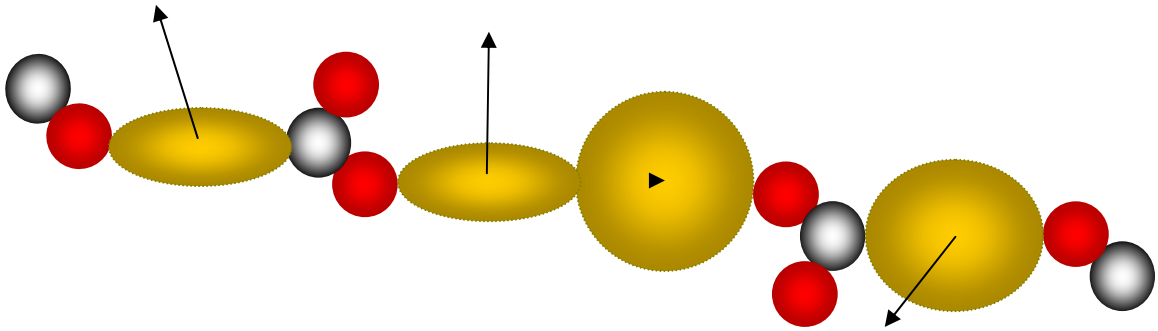

(a)

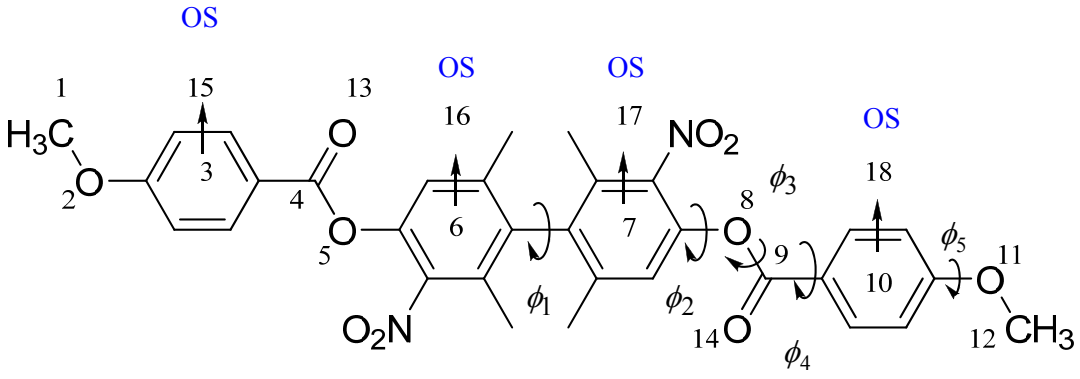

(b)

Figure 3.6 (a) Schematic multi-site coarse-grained representation of Dop5a-NO_2 molecule. The ellipsoidal GB sites are colored yellow, the oxygen atoms and the methylene and methyl groups are represented by red and grey spherical LJ sites, respectively. (b) Structure of the Dop5a-NO_2 molecule. The site numbering and the torsion indexing will be used throughout this thesis.

Within the ring regions, four bending potentials have been included in order to maintain linearity along C(4)-GB(3)-O(2), GB(7)-GB(6)-O(5), O(8)-GB(7)-GB(6), and O(11)-GB(10)-C(9) axes, while another four are used to describe the out-of-plane motion of the rings (*i.e.* OS(15)-GB(3)-O(2), OS(16)-GB(6)-O(5), OS(17)-GB(7)-GB(6), and OS(18)-GB(10)-C(9)). The discussion focuses only on five twisting motions, as follows: ϕ_1 – corresponding to torsion about OS(17)-GB(7)-GB(6)-OS(16); ϕ_2 – corresponding to torsion about OS(17)-GB(7)-O(8)-C(9); ϕ_3 – corresponding to torsion about O(14)-C(9)-O(8)-GB(7); ϕ_4 – corresponding to torsion about OS(18)-GB(10)-C(9)-O(8), and finally, ϕ_5 – corresponding to torsion about OS(18)-GB(10)-O(11)-C(12). Other torsions can be obtained by symmetry, since this dopant molecule has a C_2 symmetry axis.

For the inter-ring torsion about the GB(7)-GB(6) bond (see Figure 3.7), the almost orthogonal conformation of the two phenyl rings corresponds to the minimum energy. This is due to the steric repulsion between the 2,2' and 6,6' methyl group substituents. The energy barrier between the minimum and planar conformations is a significant 150 kJ/mol. The fitted potential shows that a degree of flexibility is still present, since at room temperature the dihedral angle is allowed to twist ±20º around the minimum with less than 10 kJ/mol energy penalty.

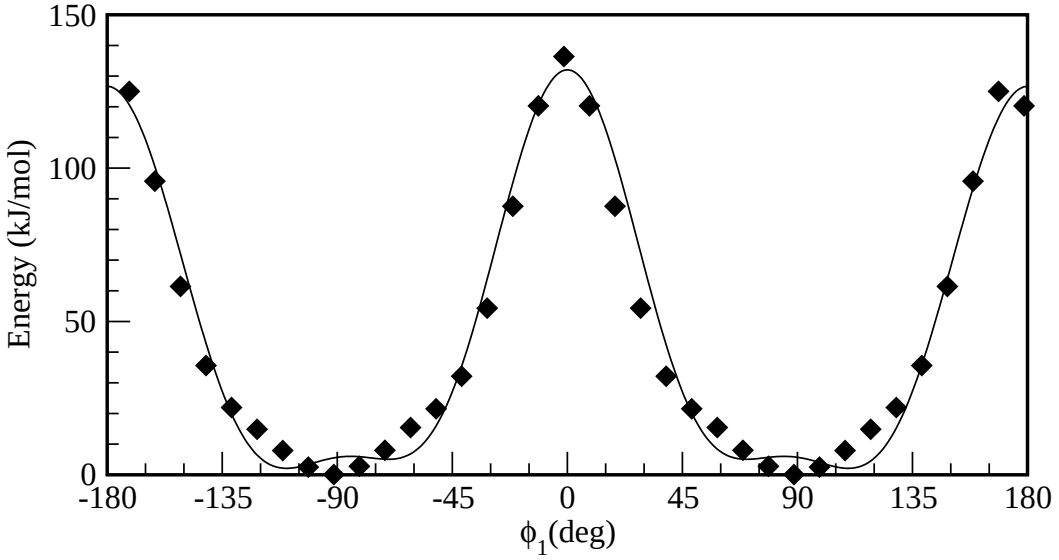

Figure 3.7 Torsional barrier from B3LYP/6-311++G(d,p) *ab initio* calculations for the rotation about the GB(7)-GB(6) bond corresponding to the ϕ_1 dihedral angle in the Dop5a-NO_2 molecule. *Ab initio* points are represented by filled diamonds and the fitted potential is given by a solid line.

The OS(17)-GB(7)-O(8)-C(9) torsion, noted ϕ_2, with a minimum at -152º, controls the orientations of the last six sites (*i.e.* O(8), C(9), GB(10), O(11), C(12) and O(14)) relative to the two dimethyl-nitro phenyl fragments that form the molecular core. Figure 3.8 (a) indicates that the energetic cost of having the nitro substituent of the dimethyl-nitro phenyl ring, GB(7), in the closest position to the O(14) atom is around 38 kJ/mol.

The O(14)-C(9)-O(8)-GB(7) dihedral angle, noted ϕ_3 and presented in Figure 3.8 (b), has a minimum at around 0º, and keeps the nitro substituent of the dimethyl-nitro phenyl ring, GB(7), in the most distant conformation relative to the O(14) atom. The barrier to rotation is relatively high (*i.e.* 40 kJ/mol). However, there is flexibility near the

minimum, so that the O(14) atom is allowed to move around 45° below and above the GB(7) ring within 10 kJ/mol of the torsional minimum energy.

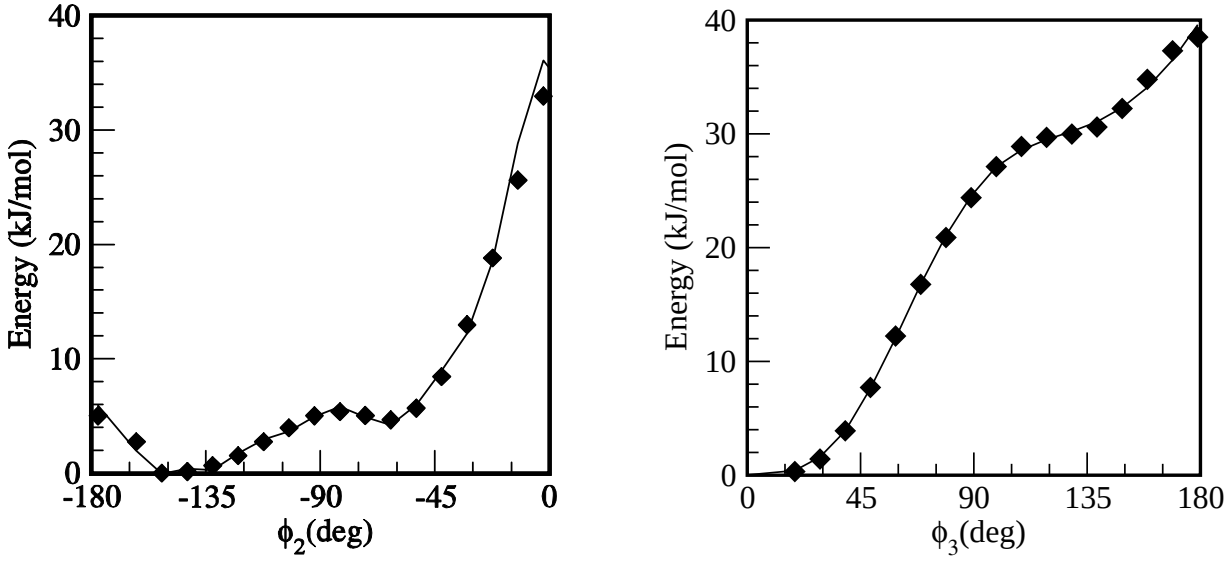

(a) (b)

Figure 3.8 Torsional barrier from B3LYP/6-311++G(d,p) *ab initio* calculations for the rotation about the GB(7)-O(8) bond corresponding to the ϕ_2 dihedral angle (a), and the O(8)-C(9) bond corresponding to the ϕ_3 dihedral angle (b), in the Dop5a-NO_2 molecule. *Ab initio* points are represented by filled diamonds and the fitted potentials are given by solid lines.

The OS(18)-GB(10)-C(9)-O(8) dihedral angle (shown in Figure 3.9 (a)) has the global minimum at around 0º separated by an energetic barrier from a local minimum at 180º. The energetic barrier to rotation is relatively high (*i.e.* 38 kJ/mol), so that the probability of passing from *trans* to *cis* arrangement of the orienting site OS(18) relative to the O(14) atom is virtually nonexistant at room temperature.

The potential for rotation about the O(11)-GB(10) bond, corresponding to the ϕ_5 dihedral angle, shown in Figure 3.9 (b), has a minimum at 0º, imposing an almost planar arrangement of the C(12), O(11), GB(10), C(9), and O(14) sites in the minimum energy configuration. However, the 18 kJ/mol rotation barrier may be surmounted to yield a conformation where the C(12) site (*i.e.* methyl group) is opposite to the O(14) atom.

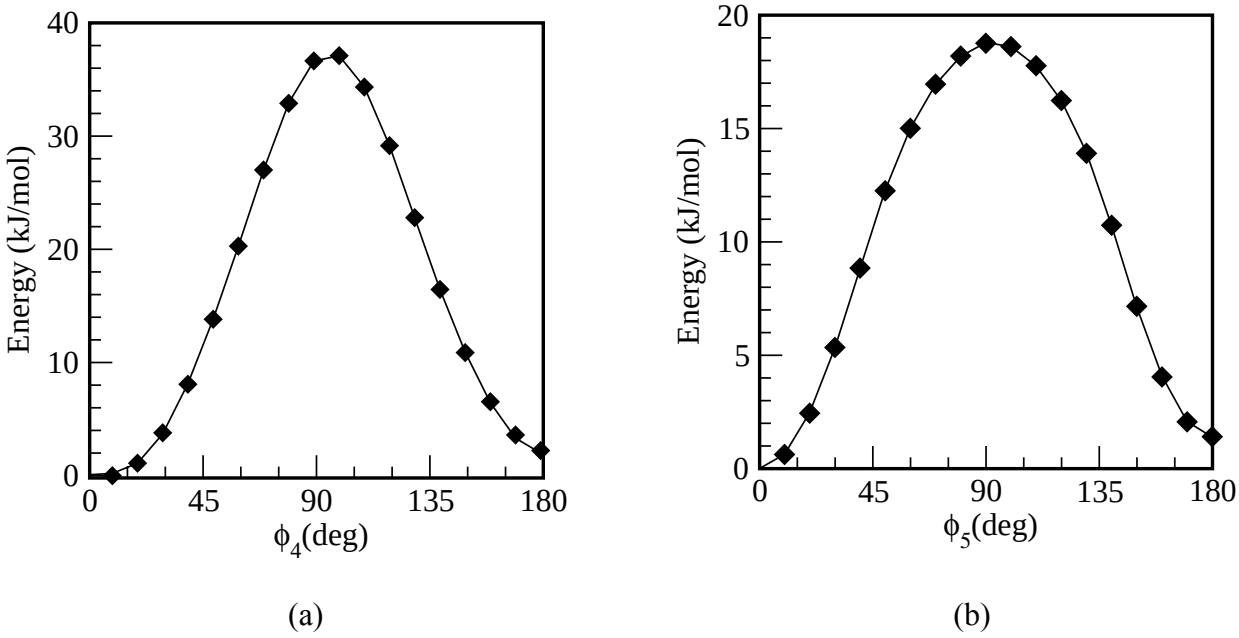

Figure 3.9 Torsional barrier from B3LYP/6-311++G(d,p) *ab initio* calculations for the rotation about GB(10)-C(9) corresponding to the ϕ_4 dihedral angle, in (a), and the O(11)-GB(10) bond, corresponding to the ϕ_5 dihedral angle, in (b), in the Dop5a-NO_2 molecule. *Ab initio* points are represented by filled diamonds and the fitted potentials are given by solid lines.

To constrain the planarity of carbonyl groups, two improper torsions around C(4) and C(9) carbonyl atoms, having their minima at around 0º, have been included in the force field. Without these terms, C(4) and C(9) atoms will have an exaggerated tendency

to oscillate above and below the plane of the neighbouring atoms. Force constants of 533.02 kJ mol^{-1} rad^{-2} and 554.30 kJ mol^{-1} rad^{-2} have been calculated for the two improper torsional angles, respectively.

In the Spiro chiral dopant molecule, the rigid core is replaced by two GB sites, while the oxygen atoms along with the methylene, and methyl groups are represented as LJ sites. A schematic multi-site coarse-grained representation of Spiro dopant molecule is shown in Figure 3.10 (a). As shown in Figure 3.10 (b), the two GB sites are directly bonded and "ghost" orienting sites assigned to them are numbered as OS(19) and OS(20). Bending potentials are explicitly included to account for the in-plane energetic cost of bending at GB(9) and GB(10) (*i.e.* to preserve linearity along the GB(10)-GB(9)-O(8), and O(11)-GB(10)-GB(9) axes) as well as for the out-of-plane motion of the two rings. Due to the presence of a carbon atom common to the two rigid cores, the rotation of one rigid core over the other is very improbable. Therefore, there are only two bending angles, GB(9)-O(8)-C(7) and C(12)-O(11)-GB(10), and two torsional motions, about the GB(9)-O(8), and O(11)-GB(10) bonds, that have been parameterized using results from *ab initio* calculations. Potential energy terms for the alkyl chains are parameterized using potentials taken from literature.[160] All in all, the spirobi[indene] core is rigid and the flexibility allowed here is given by the movement of the alkyl chains alone.

The force constants corresponding to the GB(9)-O(8)-C(7), and C(12)-O(11)-GB(10) bending have been calculated as 360.31 kJ mol^{-1} rad^{-2}, and 336.56 kJ mol^{-1} rad^{-2}, respectively. Likewise, the torsions about the GB(9)-O(8), and O(11)-GB(10) bonds,

corresponding to ϕ_1, and ϕ_2 dihedral angles (see Figure 3.10 (b) for torsion indexing) have been considered.

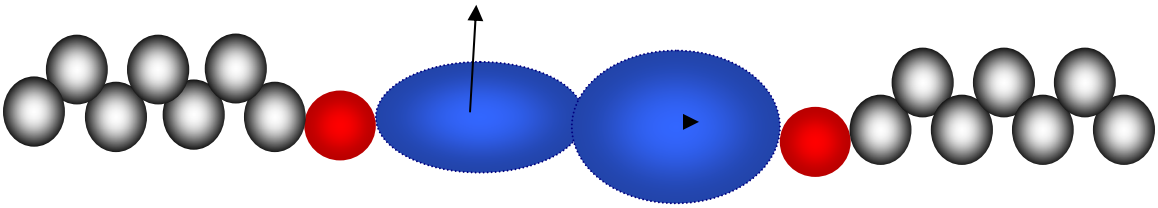

(a)

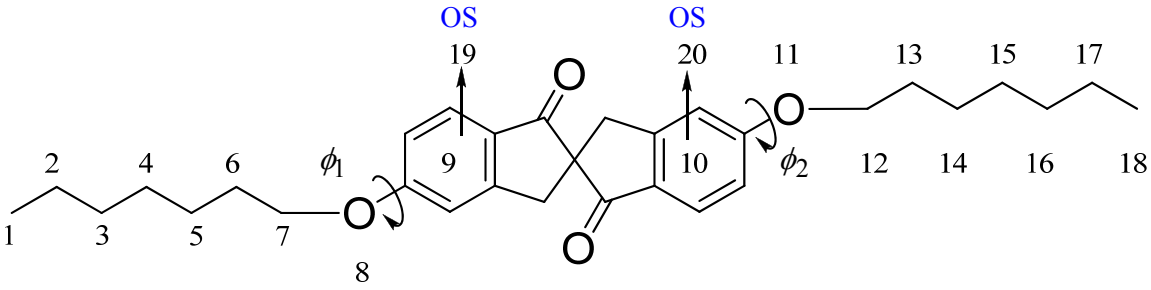

(b)

Figure 3.10 (a) A schematic multi-site coarse-grained representation of Spiro molecule. The ellipsoidal GB sites, replacing the spirobi[indene] cores, are colored blue, the oxygen atoms and the methylene and methyl groups are represented by red and grey spherical LJ sites, respectively. (b) Structure of the Spiro molecule. The site numbering and the torsion indexing will be used throughout this thesis.

Figure 3.11 shows the torsional barriers for the rotation over GB(9)-O(8) bond. Both alkyl chains are partially flexible as it costs a finite but achievable amount of energy (*i.e.* 15 – 17 kJ/mol) to rotate about the bond that joins each of them to the rigid core. The fitted potential reproduces very well the *ab initio* energies.

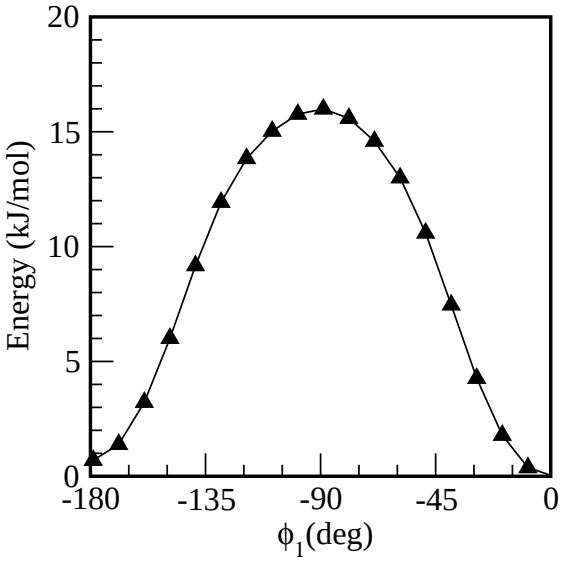

Figure 3.11 Torsional barrier from B3LYP/6-311++G(d,p) *ab initio* calculations for the rotation about GB(9)-O(8) bond corresponding to the ϕ_1 dihedral angle in the Spiro dopant molecule. *Ab initio* points are represented by filled triangles and the fitted potential is given by a solid line.

For the dopant molecules, details about the site types, charges values, equilibrium bond lengths, and the full sets of bending, torsional and improper torsional potential parameters (calculated in this thesis or taken from literature[160]) are given in Appendix B.

3.2 Aromatic Rings

Since the ellipsoidal GB sites have been chosen to represent aromatic rings, my starting point was to find a set of Gay-Berne parameters able to reproduce the properties of the smallest and simplest aromatic molecule (*i.e.* benzene), to test the effectiveness of the model at representing a larger molecule (*i.e.* biphenyl), and finally to study the transferability of this model to other, more complex, mesogenic molecules.

The approach proposed in this thesis for the parameterization of GB units is schematically presented in Figure 3.12. In the 1st step of this procedure, the form of the Gay-Berne potential is chosen and its parameters are fitted to the *ab initio* interaction energies of the benzene dimer in the gas phase. The resulting model potential combines the uniaxial form of the Gay-Berne potential with a point quadrupole placed along the ring axis to indirectly reflect the impact of the π charge cloud. In step 2, the fitted model has been used to simulate the bulk properties of liquid benzene. Since this model, fitted to *ab initio* data of benzene dimer, did not reproduce the real bulk structure of liquid benzene (see Section 3.2.3), its parameters have been used as a starting point to generate multiple combinations of sets of GB parameters in the 3rd step. In the 4th step, all combinations of GB parameters along with three different point quadrupole values have been used in MD simulations of liquid benzene. The structure of liquid benzene has been analyzed in terms of intermolecular distribution functions, $g_{com-com}(r)$, and self-diffusion coefficients, D. In the 5th step, only six sets of GB models have been chosen following a two-step selection process in which the calculated properties (*i.e.* intermolecular

distribution functions and self-diffusion coefficients) have been compared to the corresponding experimental data. Next, in step 6, the six selected ring models have been used to simulate liquid biphenyl over a wide range of temperatures, and the calculated self-diffusion coefficients have been compared with experimental data and other theoretical investigations. Moreover, the six selected ring models are used to obtain the potential energy curves for the sandwich, T-shaped, and parallel-displaced configurations of the benzene dimer. The comparison between those curves to the *ab initio* curves as well as the fitted ring model helps to understand how much the *ab initio* fitted model's parameters have been changed to better predict the bulk structure of liquid benzene. Finally, the 6561 initial ring models have been reduced to four. These are the best sets of GB parameters to be used in representing small ellipsoidal sites (*e.g.* phenyl and pyrimidine groups in the 2PhP molecule) via computer simulations in this thesis.

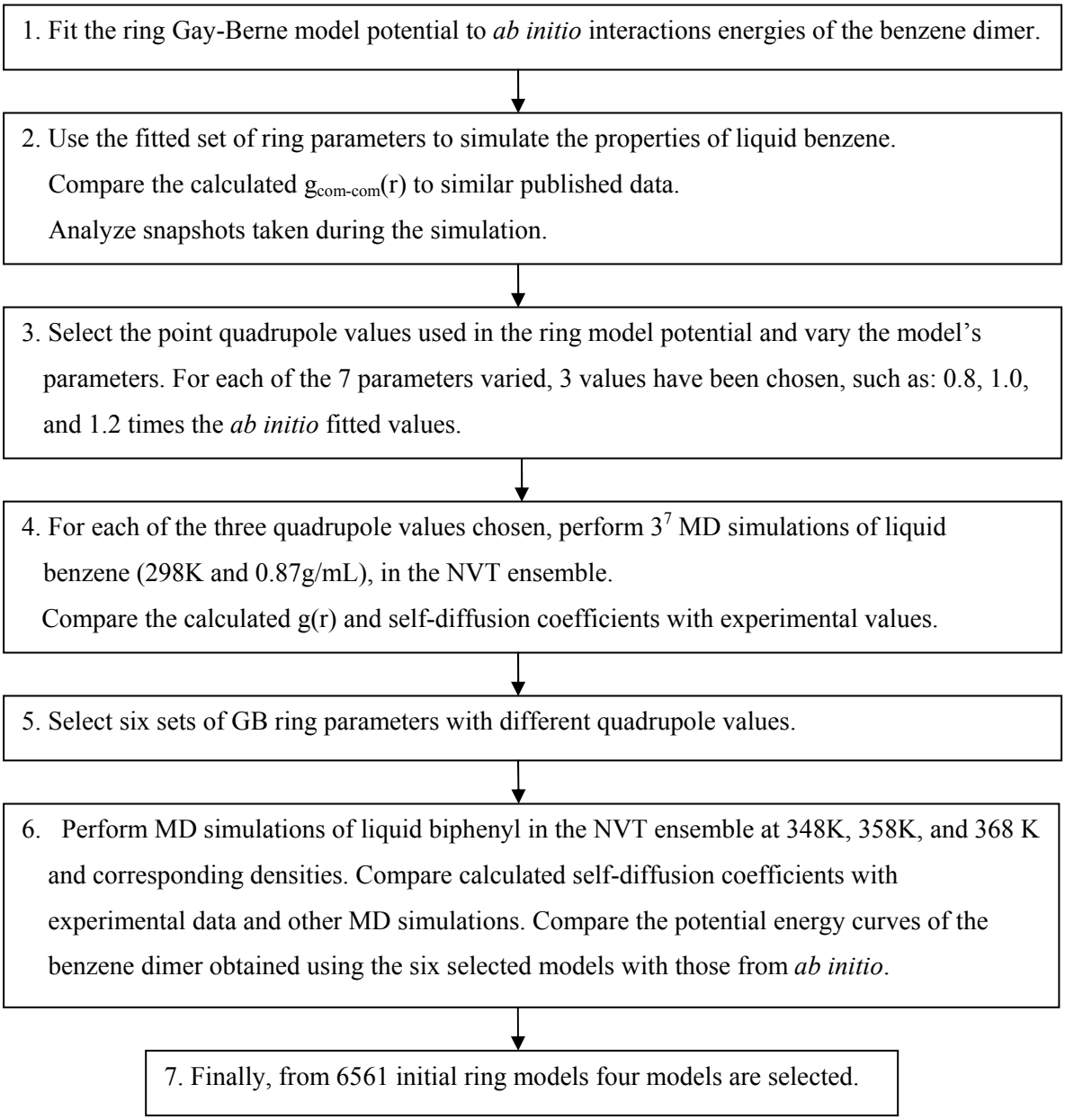

Figure 3.12 Schematic explanation of the parameterization procedure of the GB potential.

3.2.1 Gay-Berne Models

The generalized Gay-Berne model potential preserves the functional form of the Lennard-Jones potential with attractive and repulsive interactions decreasing as 6 and 12 inverse powers of the intersite distance. When the two sites (A and B) are distinct and uniaxial ellipsoids, the generalized Gay-Berne potential has the form[49] presented in Equations (1.2) and (1.3) except that the R term depends on ξ_{AB}, as follows:

$$R = \frac{\xi_{AB}\sigma_{AB}^{0}}{r_{AB} - \sigma_{AB}\left(\hat{u}_A, \hat{u}_B, \hat{r}_{AB}\right) + \xi_{AB}\sigma_{AB}^{0}} \tag{3.3}$$

The ξ_{AB} is a dimensionless parameter helpful in varying the width of the potential well independently of its depth and position, thus improving the model flexibility. The orientations of the two anisotropic sites, A and B, are denoted by the unit vectors $\hat{u}_A$ and $\hat{u}_B$, respectively, whilst the vector joining the ring centers, and the corresponding unit vector are $\vec{r}_{AB}$ and $\hat{r}_{AB}$, respectively. The unit vector points along the C_∞ symmetry axis of the ellipsoid. ε_{AB}^{0} and σ_{AB}^{0} are the overall well depth and particle size, respectively.

The anisotropy of the interactions is contained in the expressions for $\varepsilon_{AB}\left(\hat{u}_A, \hat{u}_B, \hat{r}_{AB}\right)$, and $\sigma_{AB}\left(\hat{u}_A, \hat{u}_B, \hat{r}_{AB}\right)$. The total well-depth parameter $\varepsilon_{AB}\left(\hat{u}_A, \hat{u}_B, \hat{r}_{AB}\right)$ is a product of two functions:

$$\varepsilon_{AB}\left(\hat{u}_A, \hat{u}_B, \hat{r}_{AB}\right) = \varepsilon_{AB}^{0} \cdot \left[\varepsilon_{AB}^{(1)}\left(\hat{u}_A, \hat{u}_B\right)\right]^{\nu_{AB}} \cdot \left[\varepsilon_{AB}^{(2)}\left(\hat{u}_A, \hat{u}_B, \hat{r}_{AB}\right)\right]^{\mu_{AB}} \tag{3.4}$$

where

$$\varepsilon_{AB}^{(1)}\left(\hat{u}_A, \hat{u}_B\right) = \left[1 - \chi_{AB}^{2}\left(\hat{u}_A \cdot \hat{u}_B\right)^2\right]^{-1/2} \tag{3.5}$$

and

$$\varepsilon_{AB}^{(2)}\left(\hat{\mathrm{u}}_A,\hat{\mathrm{u}}_B,\hat{r}_{AB}\right)=$$
$$1-\left[\frac{\chi'_{AB}\alpha'^{2}_{AB}\left(\hat{\mathrm{u}}_A\cdot\hat{\mathrm{r}}_{\mathrm{AB}}\right)^2+\chi'_{AB}\alpha'^{-2}_{AB}\left(\hat{\mathrm{u}}_{\mathrm{B}}\cdot\hat{\mathrm{r}}_{\mathrm{AB}}\right)^2-2\chi'^{2}_{AB}\left(\hat{\mathrm{u}}_A\cdot\hat{\mathrm{r}}_{\mathrm{AB}}\right)\left(\hat{\mathrm{u}}_B\cdot\hat{\mathrm{r}}_{\mathrm{AB}}\right)\left(\hat{\mathrm{u}}_A\cdot\hat{\mathrm{u}}_B\right)}{1-\chi'^{2}_{AB}\left(\hat{\mathrm{u}}_A\cdot\hat{\mathrm{u}}_B\right)^2}\right] \tag{3.6}$$

The range parameter, $\sigma_{AB}\left(\hat{\mathrm{u}}_A,\hat{\mathrm{u}}_B,\hat{r}_{AB}\right)$, is given by:

$$\sigma_{AB}\left(\hat{\mathrm{u}}_A,\hat{\mathrm{u}}_B,\hat{r}_{AB}\right)=\sigma_{AB}^{0}$$
$$\times\left[1-\left\{\frac{\chi_{AB}\alpha_{AB}^{2}\left(\hat{\mathrm{u}}_A\cdot\hat{\mathrm{r}}_{\mathrm{AB}}\right)^2+\chi_{AB}\alpha_{AB}^{-2}\left(\hat{\mathrm{u}}_B\cdot\hat{\mathrm{r}}_{\mathrm{AB}}\right)^2-2\chi_{AB}^{2}\left(\hat{\mathrm{u}}_A\cdot\hat{\mathrm{r}}_{\mathrm{AB}}\right)\left(\hat{\mathrm{u}}_B\cdot\hat{\mathrm{r}}_{\mathrm{AB}}\right)\left(\hat{\mathrm{u}}_A\cdot\hat{\mathrm{u}}_B\right)}{1-\chi_{AB}^{2}\left(\hat{\mathrm{u}}_A\cdot\hat{\mathrm{u}}_B\right)^2}\right\}\right]^{-1/2} \tag{3.7}$$

The parameters χ_{AB}, χ'_{AB}, α_{AB}, ν_{AB}, and μ_{AB} dictate the shape and depth of the potential energy surface as the GB sites approach with particular relative orientations.

In practice, the model is defined for a pair of identical GB sites. That is, σ_{AA}^{0}, ε_{AA}^{0}, ξ_{AA}, ν_{AA}, and μ_{AA} are the optimized parameters for the a pair of interacting A sites. Likewise, σ_{BB}^{0}, ε_{BB}^{0}, ξ_{BB}, ν_{BB}, and μ_{BB} parameters are optimized for B sites. From these two sets, mixing rules are employed for a pair of unlike GB sites interacting. Cleaver *et al.*[56] suggest the following combination rules to calculate $\chi_{AB}\alpha_{AB}^{2}$ and $\chi_{AB}\alpha_{AB}^{-2}$ from the set of parameters characterizing each GB site:

$$\chi_{AB}\alpha_{AB}^{2}=\frac{\left(\sigma_{AA}^{ee}\right)^2-\left(\sigma_{AA}^{ss}\right)^2}{\left(\sigma_{AA}^{ee}\right)^2+\left(\sigma_{BB}^{ss}\right)^2} \tag{3.8}$$

$$\chi_{AB}\alpha_{AB}^{-2} = \frac{\left(\sigma_{BB}^{ee}\right)^2 - \left(\sigma_{BB}^{ss}\right)^2}{\left(\sigma_{BB}^{ee}\right)^2 + \left(\sigma_{AA}^{ss}\right)^2} \tag{3.9}$$

$$\chi_{AB}^2 = \frac{\left[\left(\sigma_{AA}^{ee}\right)^2 - \left(\sigma_{AA}^{ss}\right)^2\right]}{\left[\left(\sigma_{AA}^{ee}\right)^2 + \left(\sigma_{BB}^{ss}\right)^2\right]} \cdot \frac{\left[\left(\sigma_{BB}^{ee}\right)^2 - \left(\sigma_{BB}^{ss}\right)^2\right]}{\left[\left(\sigma_{BB}^{ee}\right)^2 + \left(\sigma_{AA}^{ss}\right)^2\right]} \tag{3.10}$$

where σ_{AA}^{ee} and σ_{AA}^{ss} define the end-to-end and side-by-side distances for two identical sites A, respectively. Likewise, analogous notations are used for two identical B sites.

In order to calculate the other quantities, the Lorentz-Berthelot approach[168, 169] for the standard Lennard-Jones mixing rules has been followed:

$$\varepsilon_{AB}^0 = \left(\varepsilon_{AA}^0 \varepsilon_{BB}^0\right)^{1/2} \tag{3.11}$$

$$\sigma_{AB}^0 = \frac{1}{2}\left(\sigma_{AA}^0 + \sigma_{BB}^0\right) \tag{3.12}$$

The μ_{AB} and ν_{AB} exponents and the parameter ξ_{AB} were combined as:

$$\mu_{AB} = \frac{1}{2}\left(\mu_{AA} + \mu_{BB}\right) \tag{3.13}$$

$$\nu_{AB} = \frac{1}{2}\left(\nu_{AA} + \nu_{BB}\right) \tag{3.14}$$

$$\xi_{AB} = \left(\xi_{AA}\xi_{BB}\right)^{1/2} \tag{3.15}$$

Mixing rules for the remaining parameters are:[170]

$$\chi'_{AB}\,\alpha'^2_{AB} = \frac{\left(\varepsilon_{AA}^{ss}\right)^{\frac{1}{\mu_{AA}}} - \left(\varepsilon_{AA}^{ee}\right)^{\frac{1}{\mu_{AA}}}}{\left(\varepsilon_{AA}^{ss}\right)^{\frac{1}{\mu_{AA}}} + \left(\varepsilon_{BB}^{ee}\right)^{\frac{1}{\mu_{BB}}}} \tag{3.16}$$

$$\chi'_{AB}\,\alpha'^{-2}_{AB} = \frac{\left(\varepsilon^{ss}_{BB}\right)^{\frac{1}{\mu_{BB}}} - \left(\varepsilon^{ee}_{BB}\right)^{\frac{1}{\mu_{BB}}}}{\left(\varepsilon^{ss}_{BB}\right)^{\frac{1}{\mu_{BB}}} + \left(\varepsilon^{ee}_{AA}\right)^{\frac{1}{\mu_{AA}}}} \tag{3.17}$$

$$\chi'^{2}_{AB} = \frac{\left[\left(\varepsilon^{ss}_{AA}\right)^{\frac{1}{\mu_{AA}}} - \left(\varepsilon^{ee}_{AA}\right)^{\frac{1}{\mu_{AA}}}\right]\left[\left(\varepsilon^{ss}_{BB}\right)^{\frac{1}{\mu_{BB}}} - \left(\varepsilon^{ee}_{BB}\right)^{\frac{1}{\mu_{BB}}}\right]}{\left[\left(\varepsilon^{ss}_{BB}\right)^{\frac{1}{\mu_{BB}}} + \left(\varepsilon^{ee}_{AA}\right)^{\frac{1}{\mu_{AA}}}\right]\left[\left(\varepsilon^{ss}_{AA}\right)^{\frac{1}{\mu_{AA}}} + \left(\varepsilon^{ee}_{BB}\right)^{\frac{1}{\mu_{BB}}}\right]} \tag{3.18}$$

where ε^{ee}_{AA} and ε^{ss}_{AA} are the energy well depths for the end-to-end and side-by-side configurations of the two identical A sites. Analogous notations are used for two identical B sites.

It is important to point out that the above mixing rules (*i.e.* Equations (3.8) to (3.18)) correctly reproduce the GB interactions in the limiting case of two identical sites (*i.e.* $A = B$). For example, when $\sigma^{ee}_{AA} = \sigma^{ee}_{BB} = \sigma^{ee}$, $\sigma^{ss}_{AA} = \sigma^{ss}_{BB} = \sigma^{ss}$, $\varepsilon^{ee}_{AA} = \varepsilon^{ee}_{BB} = \varepsilon^{ee}$, $\varepsilon^{ss}_{AA} = \varepsilon^{ss}_{BB} = \varepsilon^{ss}$, and $\mu_{AA} = \mu_{BB} = \mu$, Equation (3.10) reduces to Equation (1.8), and likewise, Equation (3.18) reduces to Equation (1.9), since $k = \sigma^{ee}/\sigma^{ss}$ and $k' = \varepsilon^{ss}/\varepsilon^{ee}$. Furthermore, the generalized GB potential can be use to model interactions between an anisotropic GB site and a spherical LJ site. Consider the site A as being a spherical LJ site having the parameters: $\sigma^{ee}_{AA} = \sigma^{ss}_{AA} = \sigma^{0}_{AA}$, $\varepsilon^{ee}_{AA} = \varepsilon^{ss}_{AA} = \varepsilon^{0}_{AA}$, and $\mu_{AA} = \nu_{AA} = 1$. In the interaction between a LJ site A and a GB site B, σ_{AB} term, given by the Equation (3.7), reduces to:

$$\sigma_{AB}\left(\hat{\mathrm{u}}_B, \hat{r}_{AB}\right) = \sigma^{0}_{AB}\left[1 - \chi_{AB}\alpha^{-2}_{AB}\left(\hat{\mathrm{u}}_B \cdot \hat{\mathrm{r}}_{\mathrm{AB}}\right)^2\right]^{-1/2} \tag{3.19}$$

In this case, σ_{AB} depends only on the angle between the LJ site A and GB site B, and the GB orientation vector, $\hat{u}_B$.

All in all, the generalized GB model potential is completely defined by a set of thirteen parameters: σ_{AB}^0, ε_{AB}^0, σ_{AA}^{ee}, σ_{BB}^{ee}, σ_{AA}^{ss}, σ_{BB}^{ss}, ε_{AA}^{ee}, ε_{BB}^{ee}, ε_{AA}^{ss}, ε_{BB}^{ss}, μ_{AB}, ν_{AB}, and ξ_{AB}. For two identical GB sites, the number of parameters is reduced, as follows: σ_{AA}^0, ε_{AA}^0, k_{AA}, k'_{AA}, μ_{AA}, ν_{AA}, and ξ_{AA}, where $k_{AA} = \sigma_{AA}^{ee} / \sigma_{AA}^{ss}$, and $k'_{AA} = \varepsilon_{AA}^{ss} / \varepsilon_{AA}^{ee}$ describe the shape and well depth anisotropy, respectively.

3.2.2 Quadrupolar Contribution

The benzene molecule has a significant quadrupole moment perpendicular to the ring. This is typically neglected in simulations because an all atom force field cannot account for it. By directly incorporating the quadrupolar moment within the benzene model, I expect to recover its real bulk structure by reflecting the impact of the π charge cloud. Therefore, a point quadrupole has been added to the centre of the ellipsoidal site along the ring axis and its effect on modelling aromatic molecules using the proposed model potential has been investigated. As a result, the proposed GB ring potential becomes a sum of two terms: a generalized Gay-Berne interaction, $U(\hat{u}_A, \hat{u}_B, r_{AB})$, given by Equation (1.2), and a quadrupole-quadrupole contribution, $U_{QQ}(\hat{u}_A, \hat{u}_B, \hat{r}_{AB})$.

The interaction energy for a pair of point quadrupoles is given by:

$$U_{QQ}(\hat{u}_A, \hat{u}_B, \hat{r}_{AB}) = \frac{3}{4} \frac{Q_A Q_B}{r_{AB}^5} \left[\begin{array}{l} 1 + 2(\hat{u}_A \cdot \hat{u}_B)^2 - 5(\hat{u}_A \cdot \hat{r}_{AB})^2 - 5(\hat{u}_B \cdot \hat{r}_{AB})^2 \\ -20(\hat{u}_A \cdot \hat{r}_{AB})(\hat{u}_B \cdot \hat{r}_{AB})(\hat{u}_A \cdot \hat{u}_B) + 35(\hat{u}_A \cdot \hat{r}_{AB})^2 (\hat{u}_B \cdot \hat{r}_{AB})^2 \end{array} \right] \quad (3.20)$$

where Q_A and Q_B are the quadrupole moment values of the interaction sites A and B, respectively, and the unit vectors have been already defined for the GB interaction potential.

3.2.3 *Ab initio* Fit

Benzene dimer has been extensively studied, both experimentally[171-174] and theoretically,[175-179] in an attempt to obtain a clear picture of the strength and directionality of $\pi - \pi$ interactions. There are three prototype configurations that are usually considered in studies of the benzene dimer; they are presented in Figure 3.13. The sandwich configuration places both benzenes on top of each other, the T-shaped configuration has one molecule pointed at the centre of the other one, and the parallel-displaced configuration is reached from the sandwich configuration by a parallel shift of one ring away from the other.

(a) (b) (c)

Figure 3.13 Sandwich (a), T-shaped (b), and parallel-displaced (c) configurations of the benzene dimer.[176]

High-quality potential energy curves as a function of intermonomer distance R of the sandwich and T-shaped configurations, and of $R1$ and $R2$ distances for the parallel-displaced configuration of the benzene dimer (see Figure 3.13) have been reported by Sinnokrot *et al*.[180, 181] At the MP2 level, potential energy curves are computed using the aug-cc-pVQZ* (truncated aug-cc-pVQZ) basis set, and high-quality CCSD(T) potential energy curves are estimated by combining the MP2 values with a ΔCCSD(T) correction. These data (*i.e.* pair energies for 118 benzene dimer configurations) form the starting point in the development of GB set of parameters.

Following the first step in Figure 3.12, the parameters of the ring potential have been fitted to reproduce the nonbonded part of the *ab initio* interaction energy by minimizing the least-squares function:

$$F_{fit} = \sum_{k} \left[\; E^{(k)}_{abinitio}(\vec{r}_k) - E^{(k)}_{potential}(\vec{r}_k) \; \right]^2 \tag{3.21}$$

where the sum is over all the distances where *ab initio* data is available, and $E^{(k)}_{abinitio}(\vec{r}_k)$ and $E^{(k)}_{potential}(\vec{r}_k)$ are the *ab initio* and GB potential dimer energy in configuration *k,* respectively. The $\vec{r}_k$ defines the vector of atomic coordinates (*i.e.* intermonomer distances R, R1, and R2 in Figure 3.13). The $E^{(k)}_{potential}(\vec{r}_k)$ is calculated for each dimer configuration considering a fixed quadrupole moment of -1.38×10^{-39} C m^2. This quadrupole underestimates the experimental value[182] (*i.e.* -2.9×10^{-39} C m^2) for a single benzene molecule but it is consistent with the quadrupole values recommended by *Cacelli et al.*[183] for a quadrupolar benzene model.

The optimized GB parameter set, which reproduces the *ab initio* potential energy curves very accurately, is named GBQ1 and is given in Table 3.1.

Table 3.1 The GBQ1 set of parameters obtained by fitting to *ab initio* potential energy curves[180, 181] of benzene dimer.

Parameter	GBQ1 model
ε_0 (kJ/mol)	3.9507
σ_0 (nm)	0.5562
$\varepsilon_0^{ss} / \varepsilon_0^{ee}$	0.5581
$\sigma_0^{ee} / \sigma_0^{ss}$	4.3860
ξ	0.7088
μ	-2.5102
ν	0.3070
Q (10^{-39} C m^2)	-1.3800

With this set of parameters in hand, MD simulations in the canonical NVT ensemble for a system of 500 benzene molecules were performed. A cubic simulation box under periodic boundary conditions was used. The temperature and density have been set to 300 K and 0.87 g/mL,[184] respectively. A total of 100000 iteration steps was employed with an equilibration period of 20000 steps. To gain information about the bulk structure of liquid benzene, the centre-centre radial distribution function, $g_{com\text{-}com}(r)$, has been evaluated using the procedure outlined in Chapter 2.6, and it is given in Figure 3.14.

The calculated center of mass pair distribution function, $g_{com\text{-}com}(r)$, shows three visible peaks at 5.1 Å, 9.0 Å, and 13.5 Å, and two minima delimiting the solvation shells at 7.0 Å, and 11.5 Å, respectively.

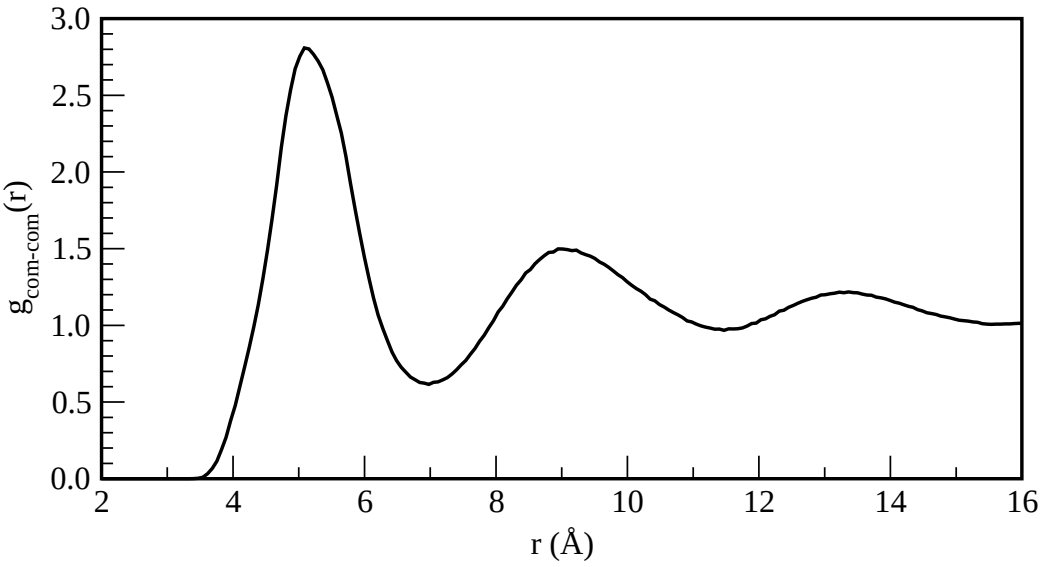

Figure 3.14 The centre-centre radial distribution function, $g_{com\text{-}com}(r)$, evaluated from MD simulation of liquid benzene, using the GBQ1 set of parameters.

To judge the quality of my model potential, I compare the calculated distribution to available theoretical[183, 185-190] as well as experimental (*i.e.* neutron diffraction) results.[191-194] I observe that the overall agreement is satisfactory, and I note that the peak positions appear shifted to smaller separation distances and that the height of the first peak overestimates the values reported in those studies. This is an indication of a better packing of the molecules in the first shell of neighbors. For example, the calculated first

peak's height overestimates by almost 40% the value reported by *Tao et al.*[190] in a MD simulation study. It is important to note that, in this particular study, benzene was described by a 12-site model consisting of a rigid hexagonal ring of C-H groups, thus the centre of mass was not directly represented. Nevertheless, the main features of the centre of mass distribution function are preserved when working with the proposed set of fitted GBQ1 parameters.

Despite the fact that this model potential is obtained by fitting the *ab initio* curves and the fact that the evaluated structural quantities of the liquid benzene *(i.e.* centre-of-mass radial distribution functions) are in reasonable agreement with published theoretical and experimental results, a closer inspection of snapshots made during the simulations (see Figure 3.15) revealed holes inside the liquid structure.

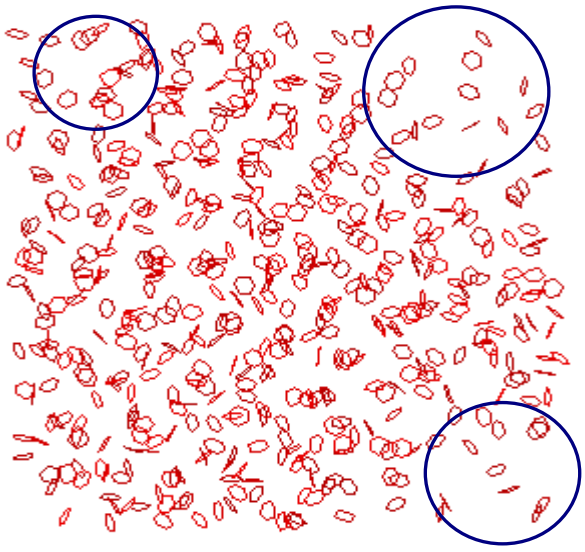

Figure 3.15 A snapshot obtained from the MD simulation of 500 liquid benzene molecules by employing the fitted GBQ1 set of parameters. The circles identify low density regions.

It is important to realize that the *ab initio* potential energy curves are obtained from two isolated benzene molecules in the gas phase. The presence of holes in the snapshots is a clear indication that a benzene molecule *in the bulk* is reasonably distinct from one in *a dimer*. In other words, many body effects impact the potential. This is why a different approach had to be taken to further refine the Gay-Berne parameters in order to reproduce the experimental data and to provide a real representation of benzene molecules in the bulk.

3.2.4 Fits to X-ray Data of Benzene

To capture the real bulk properties of liquid benzene, new sets of parameters for the ring model potential have been least-squares fitted to experimental data, specifically, the structure of benzene from X-ray data.[155] Besides the X-ray experiments, the structure of liquid benzene has been extensively studied by neutron diffraction experiments[191-194] as well as by computer simulations.[183, 185-190]

Three different point quadrupole values have been selected in order to assess the influence of the quadrupolar moment on the model potential. Specifically, the magnitudes of the quadrupole moment used, in reduced units, are: -0.2486 for A set, and -0.1989 for B set. To quantify the influence of quadrupolar interactions on the behavior of GB sites, an extra set of parameters for uncharged sites, noted C, has been used. To summarize, in S.I. units, the magnitudes of point quadrupole used for the A and B sets varies between -0.63×10^{-39} C m^2 and -2.68×10^{-39} C m^2 while the C set explores the absence of the point

quadrupole. It is important to note that the selected quadrupole values are still underestimating the experimental gas phase value.[182]

For each of the seven parameters of GB model potential, three values have been considered: 80%, 100%, and 120% of the value obtained by optimization to *ab initio* pair potentials. Thus, it has been assumed that the dimer pair potentials obtained by fitting to *ab initio* data are roughly correct but the parameters have to be adjusted to some extent for bulk benzene. The values of the GB parameters used in least-squares fitting to experimental data of liquid benzene are given in Table 3.2.

Table 3.2 Parameters of the GB model potential.

Parameter	First set	Second set	Third set
ε_0 (kJ/mol)	3.1606	3.9508	4.7410
σ_0 (nm)	0.4450	0.5562	0.6674
$\varepsilon_0^{ss} / \varepsilon_0^{ee}$	0.4465	0.5581	0.6697
$\sigma_0^{ee} / \sigma_0^{ss}$	3.5088	4.3860	5.2632
ξ	0.5671	0.7088	0.8506
μ	-2.0082	-2.5102	-3.0122
ν	0.2456	0.3070	0.3684

For each set with a particular quadrupole value, a total of 3^7 (2187) canonical MD simulations of 500 benzene molecules, in liquid phase (*i.e.* 300 K and 0.87 g/mL), have been carried out using the procedure outlined in the previous section. Fluid structure is

assessed after 100000 iterations. Since the X-ray scattering experiments[155] measure the pair distribution function of carbon atoms rather than that of molecular centres, the centre-centre radial distribution function, $g_{com\text{-}com}(r)$, has been computed and the site-site radial distribution function, $g_{C\text{-}C}(r)$, has been calculated for the GB model by reintroducing the six carbon atom positions into each GB ellipsoid. Since the calculations employ the GB potential, where the carbon atoms are not directly present, the six "atoms" are actually six "ghost" sites at locations corresponding to the carbon atoms.

Assessment of the calculations proceeded by least-squares fitting to the experimental distribution between ring carbons: $\sum_{1}^{N}\left[\left(g_{exp}(r)-g_{th}(r)\right)\right]^2 / N$, where r is the distance between the two carbon atoms, and N is the number of r values used in the comparison. $g_{exp}(r)$ and $g_{th}(r)$ are the radial distribution functions from experiment and simulation, respectively. A second sum of squares biased toward larger separations has also been employed, $\sum_{1}^{N}\left[\left(g_{\mathbf{exp}}(r)-g_{th}(r)\right)\right]^2 \cdot r / N$. Based on these least-squares errors, ten models have been chosen for further consideration. These are identified as: GBQ2-An, Bn, and Cn, where GBQ2 implies that this is the quadrupolar GB ring model designed by fitting to experimental data, n is the model number, and the letters A, B, C identify the quadrupole moment value. The ten selected models are presented in Table 3.3, Table 3.4, and Table 3.5. It is important to note that many other parameter sets give comparable least-squares errors but these ten are chosen based on their diverse optimized parameters sets.

Table 3.3 The six selected GBQ2-A n sets of parameters ($Q^* = -0.2486$ reduced units).

Parameter	A1	A2	A3	A4	A5	A6
ε_0 (kJ/mol)	3.1606	3.1606	3.9508	4.7410	4.7410	4.7410
σ_0 (nm)	0.6674	0.6674	0.6674	0.6674	0.6674	0.6674
$\varepsilon_0^{ss} / \varepsilon_0^{ee}$	3.5088	3.5088	3.9508	3.5088	3.5088	3.5088
$\sigma_0^{ee} / \sigma_0^{ss}$	0.4465	0.4465	0.4465	0.4465	0.4465	0.4465
ξ	0.5671	0.7088	0.8506	0.5671	0.7088	0.8506
μ	-2.5102	-2.5102	-2.0082	-2.5102	-2.5102	-2.5102
ν	0.2456	0.3684	0.3684	0.3684	0.3684	0.3684
Q (10^{-39} C m^2)	-2.1872	-2.1872	-2.4450	-2.6787	-2.6787	-2.6787
$\sum_1^N \left[\left(g_{\mathbf{exp}}(r) - g_{th}(r)\right)\right]^2 / N$	0.002313	0.002389	0.002628	0.003066	0.003102	0.002673
$\sum_1^N \left[\left(g_{\mathbf{exp}}(r) - g_{th}(r)\right)\right]^2 \cdot r / N$	0.009411	0.009987	0.011046	0.011369	0.012606	0.011349

Table 3.4 The three selected GBQ2-B n sets of parameters ($Q^* = -0.1868$ reduced units).

Parameter	B1	B2	B3
ε_0 (kJ/mol)	3.1606	3.1606	3.1606
$\varepsilon_0^{ss} / \varepsilon_0^{ee}$	3.5088	3.5088	5.2632
σ_0 (nm)	0.6674	0.6674	0.6674
$\sigma_0^{ee} / \sigma_0^{ss}$	0.4465	0.4465	0.4465
ξ	0.5671	0.5671	0.5671
μ	-2.0081	-2.5102	-3.0122
ν	0.3070	0.2456	0.3684
Q (10^{-39} C m^2)	-1.7497	-1.7497	-1.7497
$\sum_1^N \left[\left(g_{\mathbf{exp}}(r) - g_{th}(r)\right)\right]^2 / N$	0.002746	0.002710	0.012895
$\sum_1^N \left[\left(g_{\mathbf{exp}}(r) - g_{th}(r)\right)\right]^2 \cdot r / N$	0.011080	0.010960	0.003167

Table 3.5 The selected GBQ2-Cn set of parameters (no point quadrupole).

Parameter	C1
ε_0 (kJ/mol)	3.1606
ε_0^{ss} / ε_0^{ee}	3.5088
σ_0 (nm)	0.6674
σ_0^{ee} / σ_0^{ss}	0.4465
ξ	0.5671
μ	-2.0081
ν	0.3070
Q(10^{-26} esu cm^2)	0.0000
$\sum_1^N \left[\left(g_{\mathbf{exp}}(r) - g_{th}(r)\right)\right]^2 / N$	0.002605
$\sum_1^N \left[\left(g_{\mathbf{exp}}(r) - g_{th}(r)\right)\right]^2 \cdot r / N$	0.011088

A comparison between the calculated and experimental[155] carbon-carbon radial distribution functions, $g_{C\text{-}C}(r)$, is reported in Figure 3.16 for liquid benzene at 300K. The experimental distribution is characterized by the presence of a small peak at 4.0 Å, and three peaks at 6.3 Å, 10.9 Å, and 16.0 Å. In addition, the peak at 6.3 Å has a prominent shoulder at 5.8 Å. These "close contact" features are more sensitive to the atomic structure of the ring. As a result, the GBQ2 ring models cannot fully capture these structural details and predicts instead a broad peak between 5.2 Å and 6.3 Å. Beyond this region, the GB model performs well and reproduces the depth and position of interlayer minimum and the details of the following solvation shells. It is interesting to note that the ring model that does not include a quadrupole moment (*i.e.* GBQ2-C1 model) is clearly inferior and consistently predicts an understructured fluid.

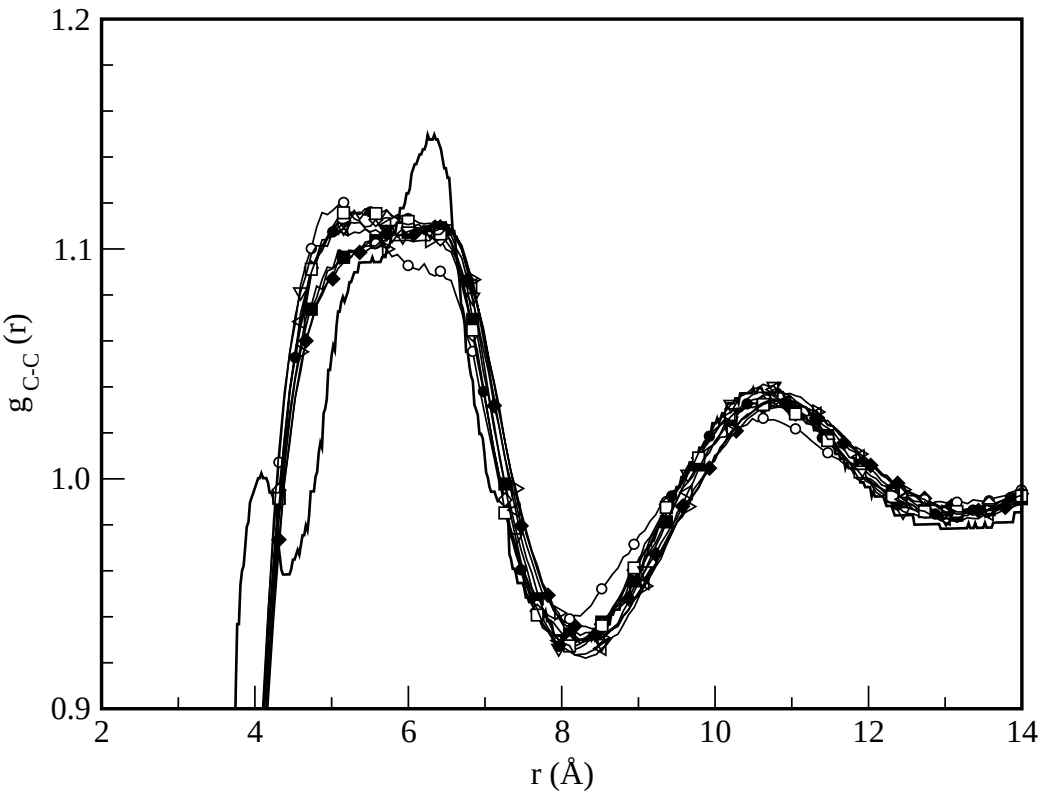

Figure 3.16 Comparison between the C-C radial distribution function of liquid benzene at 300K from X-ray data[155] and the ten selected GBQ2 sets of parameters. Results for ten GBQ2 ring models are shown: A1 (filled squares), A2 (filled diamonds), A3 (open triangle up), A4 (open triangle down), A5 (filled triangle up), A6 (filled triangle down), B1 (open squares), B2 (filled circles), B3 (open diamonds), and C1 (open circles). The *ab initio* data is shown by solid line.

For the ten selected sets of GB parameters, different trends are observed, as follows: (1) when using the GBQ2-A1, A2, A3, and A6 sets, the first peak appears around 6.3 Å and it has a visible left shoulder at 5.0 Å, while the second and the third peaks occur around 10.8 Å and 15.7 Å, respectively; (2) when using the GBQ2-A4, and A5 sets, the first peak is characterized by a broad plateau visible between 4.7 Å and 6.4 Å, while the second and third peaks are observed at 10.8 Å, and 15.8 Å, respectively, (3)

when using the GBQ2-B1, B2, and B3 sets, a broad first peak having a maximum at 5.4 Å and a shoulder at 6.0 Å are evident, whilst the second and third peaks are visible at 10.7 Å and 15.6 Å, respectively; (4) when using the GBQ2-C1 set, the first peak has a maximum at 5.1 Å and a broad shoulder at 6.4 Å, and the second and third peaks are slightly reduced in intensity and shifted to smaller distances. This shows that the addition of a point quadrupole improves the accuracy of the GBQ2 model potential at least in terms of the carbon-carbon distribution in the liquid phase of benzene.

The self-diffusion coefficient of liquid benzene (D) has been calculated from the long time behavior of the MSD via the Einstein relation[119] given by Equation (2.57). To be precise, D values has been calculated from the slope of the MSD between 20 ps and 160 ps. The calculated D values are compared with experimental data[195-198] and other MD simulations[185, 188, 189, 199] in Table 3.6. The range of self-diffusion coefficient values is significant for the ten models. As a general trend, simulations typically underestimate the experimental self-diffusion in benzene.[195-198] Moreover, the importance of the quadrupole magnitude has been previously reported by *Chelli et al*.,[199] which showed that an increase of the quadrupole magnitude is followed by a decrease of the calculated D below the experimental value. In my case, for six of the models (*i.e.* A1, A2, B1, B2, B3, and C1), the calculated D are comparable with the values reported in other theoretical studies.[187-189, 199] To summarize, four of the selected GBQ2 models with the lowest self-diffusion coefficients have been eliminated from further consideration.

Table 3.6 Comparison of calculated and experimental self-diffusion coefficients of liquid benzene.

D x 10^{-9} (m^2/sec)	**T (K)**	**Density (g/mL)**	**Source**	**Observations**
2.27	298.15	0.874	Ref.[195]	experimental
2.15	298.15	0.874	Ref.[196]	experimental
2.13	298.15	0.874	Ref.[197]	experimental
2.21	298.15	0.874	Ref.[198]	experimental
1.20	300.00	0.872	Ref.[185]	MD / NVE
2.17	303.15	0.879	Ref.[188]	MD / NVT
1.25	303.15	0.972	Ref.[189]	MD / NPT
1.40	290.00	0.897	Ref.[199]	MD / NVE
1.90	290.00	0.873	Ref.[199]	MD / NVE
1.29	300.15	0.870	This thesis	MD / NVT GBQ2-A1
1.17	300.15	0.870	This thesis	MD / NVT GBQ2-A2
0.91	300.15	0.870	This thesis	MD / NVT GBQ2-A3
0.60	300.15	0.870	This thesis	MD / NVT GBQ2-A4
0.74	300.15	0.870	This thesis	MD / NVT GBQ2-A5
0.72	300.15	0.870	This thesis	MD / NVT GBQ2-A6
1.27	300.15	0.870	This thesis	MD / NVT GBQ2-B1
1.26	300.15	0.870	This thesis	MD / NVT GBQ2-B2
0.97	300.15	0.870	This thesis	MD / NVT GBQ2-B3
1.20	300.15	0.870	This thesis	MD / NVT GBQ2-C1

Thus, from the initial 6561 ring models, only six models (*i.e.* A1, A2, B1, B2, B3, and C1) will be used in further study. Notice that the GBQ2-C1 model has been selected in order to assess the influence of the molecular quadrupole on the GB model potential,

despite the fact that this model does not do as well as the other models in representing the bulk structure of liquid benzene.

3.2.5 Potential Energy Curves of Benzene

The six selected GBQ2 sets of parameters (*i.e.* A1, A2, B1, B2, B3, and C1 sets) have been used to evaluate the binding energies of benzene dimer in order to compare the results to the *ab initio* data. Since the GBQ2 sets of parameters have been obtained by fitting to bulk properties of liquid benzene (*i.e.* C-C radial distribution functions from experimental X-ray data), it is not expected to agree perfectly with the gas-phase *ab initio* calculations.

The resulting potential energy curves have been plotted in Figures 3.20 (a), (b), and (c), for the sandwich, T-shaped, and parallel-displaced configurations, respectively. These three arrangements of the benzene dimer have been sketched in Figure 3.13. For the T-shaped and sandwich configurations, the centre-to-centre distance, R, was systematically varied. For the parallel-displaced configurations the vertical distance, R1, was systematically varied, and the horizontal distance between the centres of mass, R2, was kept constant at 3.2 Å.

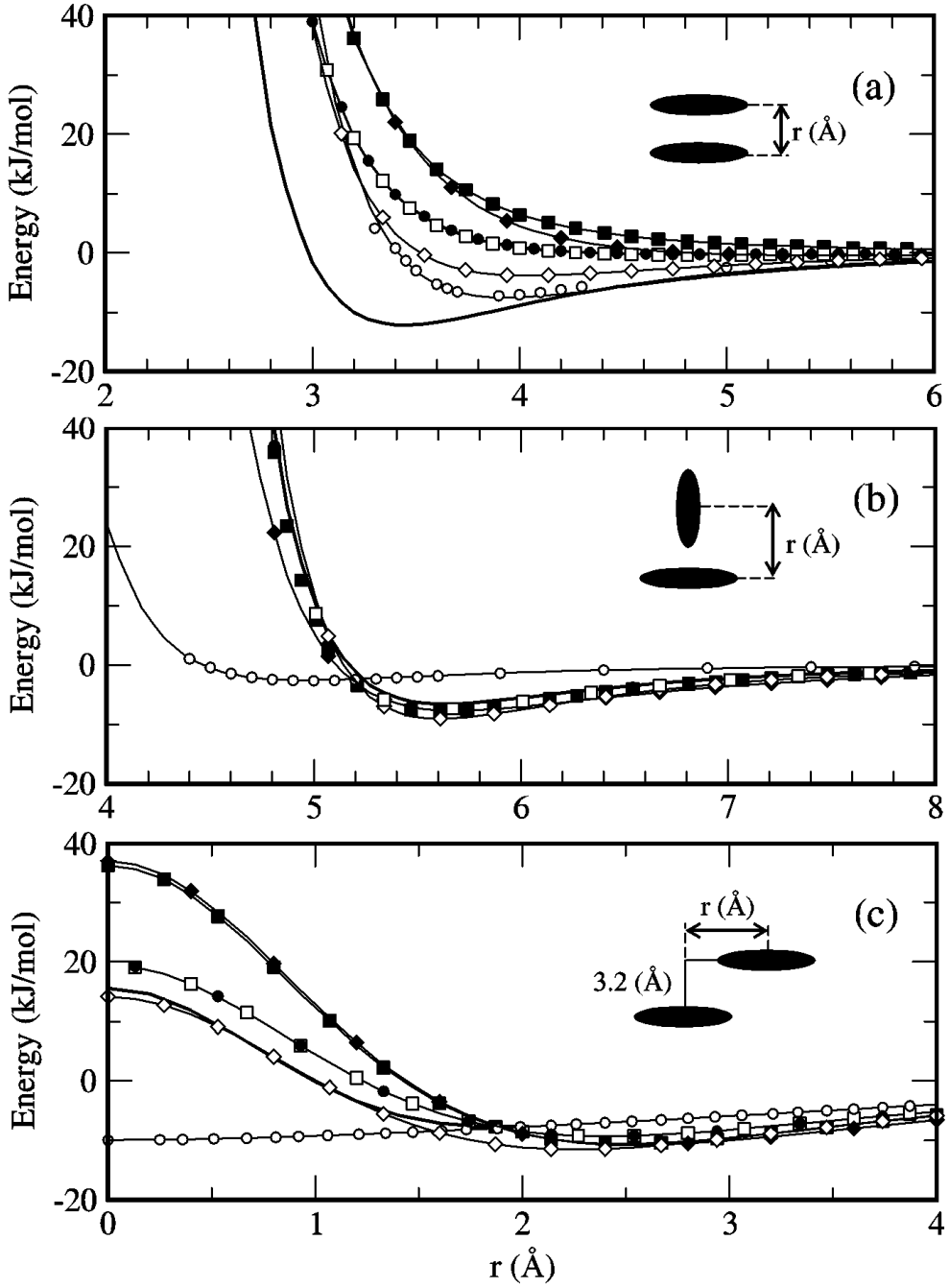

Figure 3.17 Potential energy curves of benzene dimer computed using the GB ring models developed in this thesis and the *ab initio* data:[180] (a) face-to-face or sandwich configuration, (b) T-shaped configuration, and (c) slipped–parallel configuration. Results for six selected GBQ2 ring models are shown: A1 (filled squares), A2 (filled diamonds), B1 (open squares), B2 (filled circles), B3 (open diamonds), and C1 (open circles). The *ab initio* curves are shown by solid lines.

The sandwich dimer configuration (see Figure 3.17 (a)) is not favored when using the GBQ2-A1 set, as the interaction energies are very large at smaller intermolecular R distances (*i.e.* 3.95 Å) and remain repulsive even for larger R values. A similar trend is observed when using the GBQ2-A2, GBQ2-B1, and GBQ2-B2 sets, except for the apparition of slightly attractive interaction energies (< -0.5 kJ/mol) at intermolecular distances over 4.5 - 5.0 Å. On the contrary, the interaction energy evaluated for the sandwich benzene dimer is attractive at intermolecular distances larger than 3.5 - 4.0 Å when using the GBQ2-B3 set. The GBQ2-C1 set stabilizes the sandwich configuration by an additional 5 kJ/mol compared to the *ab initio* binding energy (*i.e.* -7.21 kJ/mol), at a smaller equilibrium monomer distance of 3.5 Å.

For all six GBQ2 sets of parameters fitted to experimental data, the T-shaped benzene dimers separated by intermonomer distances larger than 5.1 - 5.2 Å have favorable binding energies (compared to the *ab initio* distance of only 4.5 Å), with the binding energy becoming small (< -2 kJ/mol) for dimers situated at more than 8 Å apart (see Figure 3.17 (b)). Moreover, the minimum energies evaluated using the GBQ2-A1 (*i.e.* -7.79 kJ/mol), GBQ2-A2 (*i.e.* -7.67 kJ/mol), GBQ2-B1 (*i.e.* -7.41 kJ/mol), GBQ2-B2 (*i.e.* -7.29 kJ/mol), GBQ2-B3 (*i.e.* -9.01 kJ/mol), and GBQ2-C1 (*i.e.* -6.51 kJ/mol) sets are less attractive than the estimated *ab initio* energy of -10.92 kJ/mol.

The sandwich configuration of the benzene dimer represents a maximum (saddle point) along the horizontal displacement coordinate, R2, which connects two equivalent parallel-displaced configurations.

Comparing the benzene dimer interaction energy of the slipped-parallel configuration evaluated using the four selected sets of GBQ2 parameters to the corresponding *ab initio* energies (see Figure 3.17 (c)), it is apparent that the interaction energies are more repulsive (positive) when using the GBQ2-A1, and A2 sets, and slightly repulsive when using the GBQ2-B1, and B2 sets. The only interaction energy comparable to the reported *ab initio* energy was calculated using the GBQ2-B3 set of parameters, which is slightly less attractive (*i.e.* 14.15 kJ/mol vs. 15.53 kJ/mol) at R2 = 0 Å and more repulsive (*i.e.* -11.50 kJ/mol) at R2 = 2.27 Å, for a constant vertical distance of R1 = 3.2 Å. A more attractive interaction energy is apparent for the GBQ2-C1 set of parameters, for any intermolecular horizontal R2 distance for a constant vertical distance R1 < 3.2 Å. In this situation the minimum interaction energy (*i.e.* -9.94 kJ/mol) is obtained at R2 = 0 Å and R1 = 3.2 Å. Since the GBQ2-C1 set has no quadrupole contribution added to the potential energy, it proves that when the quadrupole is switched off the proposed ring model potential is not able to accurately reproduce the *ab initio* calculation of the interaction energy of the benzene dimer in slipped-parallel configuration.

The potential energy curves of benzene dimer calculated using the six selected GBQ2 model potentials point out the magnitude of refining that has been done to the *ab initio* fitted GBQ1 model in order to adequately represent the bulk structure of liquid benzene.

3.2.6 A Test Case: Liquid Biphenyl

The biphenyl molecule has been extensively studied both experimentally[200-202] and theoretically,[203-212] since it is seen as a "building block" for the molecular core of many mesogens. Of particular interest is the low barrier to rotation about the inter-ring C-C bond. The potential associated with the inter-ring rotation has a minimum at the equilibrium dihedral angle, $\theta_{\mathbf{min}}$. Studies of biphenyl by experimental techniques, such as X-ray diffraction[201] (solid phase), electron diffraction[213] (gas phase) and Raman spectroscopy[214] (liquid phase), showed that $\theta_{\mathbf{min}}$ is strongly affected by the medium. For instance, the magnitude of the equilibrium dihedral angle has been found to increase with temperature, such that the $\theta_{\mathbf{min}}$ is around 0° in crystalline phase, 32° in the liquid phase, and around 44° in the gas phase. Generally speaking, the conformational nature of biphenyl is determined by the interplay between the conjugation of π orbitals in different rings, favoring planarity, and the inter-ring steric repulsion between the *ortho* hydrogen atoms, favoring an orthogonal arrangement of phenyl rings.

The biphenyl molecule is represented in this study as two GB sites with centres 4.279 Å apart. The inter-ring distance is set based on the distance between the centres of the mass of the two phenyl groups that form the biphenyl molecule. A torsional potential has been used to explicitly account for the relative orientation of the two rings so that the internal flexibility of the molecule is considered. The torsional potential of *Cacelli et al.,*[166] developed employing the B3LYP density functional with the 6-311G(2d,p) basis set, has been chosen to describe this torsional motion.

The transferability of my six proposed GBQ2 model potentials has been tested by simulating the structure of liquid biphenyl at three temperatures (*i.e.* 348K, 358K, 368K) and the corresponding densities. MD simulations of bulk liquid biphenyl are performed in the canonical (NVT) ensemble with periodic boundary conditions on a system of 500 molecules. The Nosé-Hoover thermostat was employed to keep the temperature constant. The velocity Verlet algorithm, with a time step of 0.5fs, has been used throughout the runs to integrate the equations of motion. A cubic simulation cell was used. A total of 100000 iteration steps have been employed with an equilibration period of 20000 steps. The radial distribution functions along with the mean square displacements have been evaluated. Intramolecular pairs are not included in radial distributions reported in this thesis. To my knowledge, there are no experimental radial distribution functions for liquid biphenyl. A snapshot of 500 biphenyl molecules simulated using the GBQ2-A1 set of parameters at 348 K and 0.9914 g/mL density[215] is presented in Figure 3.18.

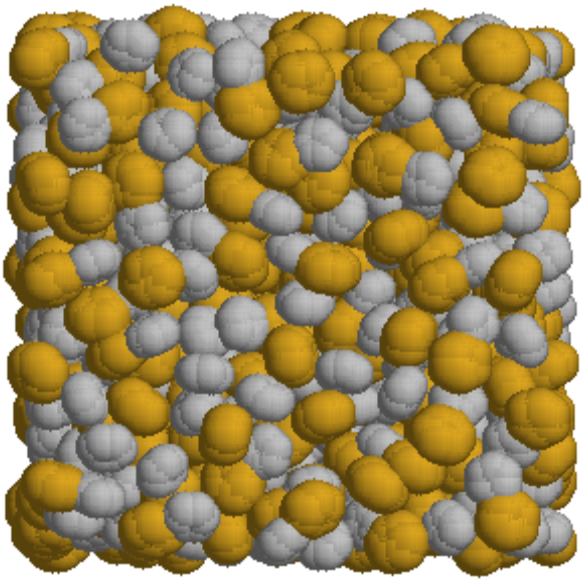

Figure 3.18 Snapshot of liquid biphenyl at 348 K and 0.9914 g/mL using GBQ2-A1 set of parameters. Each GB site of the biphenyl molecule is colored differently, to better show the random arrangement inside the liquid bulk structure.

From the perspective of their centres of mass, the radial distribution functions, presented in Figure 3.19, show two visible shells at phenyl-phenyl distances, $r_{Ph\text{-}Ph}$, between 4 Å and 8 Å, and between 8 Å and 12 Å, respectively. All the GBQ2 ring models predict similar distributions except at small separations, where a shoulder is absent for the ring model that does not include a quadrupole (*i.e.* GBQ2-C1 model). A closer inspection of the snapshots indicates that this shoulder originates from crossed pairs of molecules, and this arrangement is energetically favored by the quadrupole.

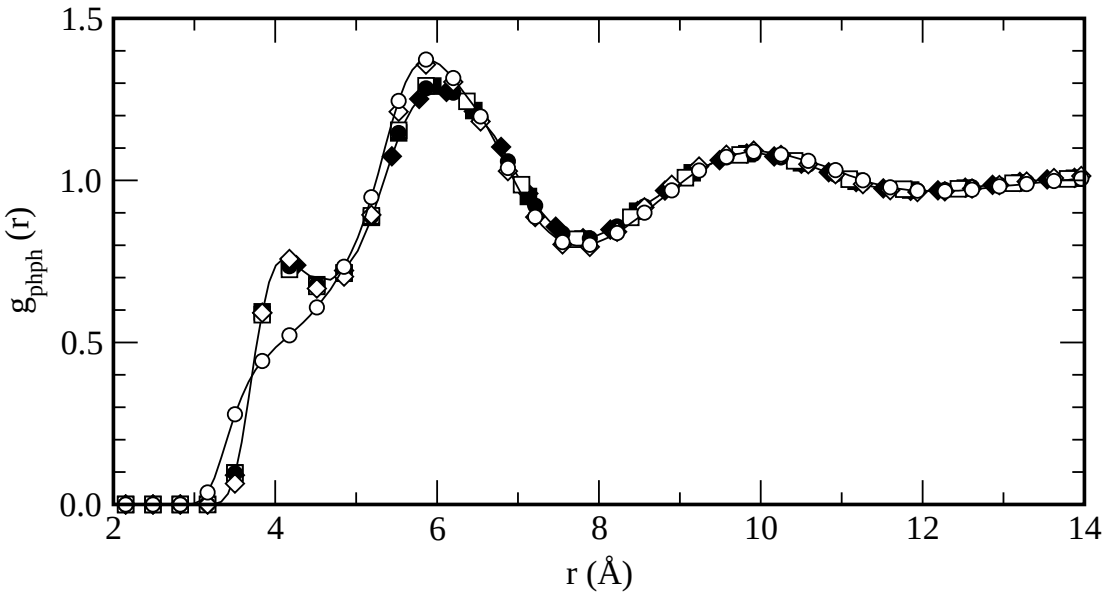

Figure 3.19 The phenyl ring centre - phenyl ring centre radial distribution functions for liquid biphenyl at 348 K and 0.9914 g/mL, calculated using the six selected GBQ2 sets of parameters. Results for six GBQ2 ring models are shown: A1 (filled squares), A2 (filled diamonds), B1 (open squares), B2 (filled circles), B3 (open diamonds), and C1 (open circles).

Figure 3.20 contains the results of a MD simulation of liquid biphenyl (*i.e.* 348 K and 0.9914 g/mL), using an atomistic model, reported by *Tao et al*.[190] Despite the fact that in this study the values of ring-ring dihedral angle were fixed at 30° or 90°, their results are in good agreement with ours, except that the spike at 4.2 Å corresponds to the fixed distance between intramolecular phenyl rings.[190]

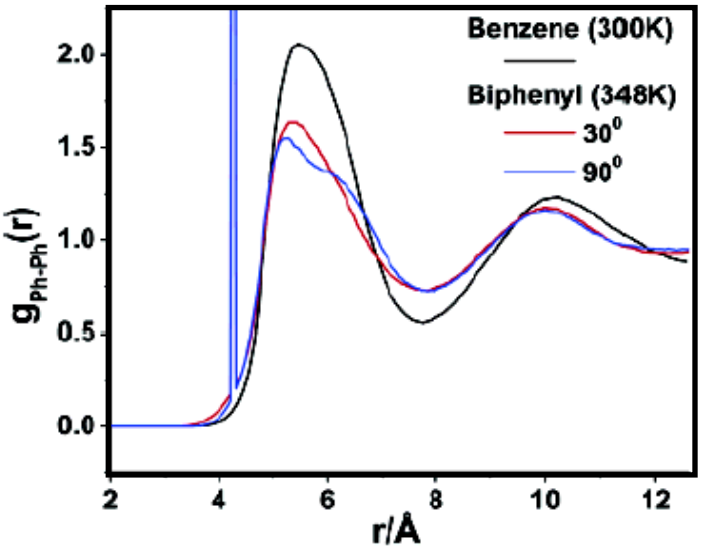

Figure 3.20 The phenyl ring centre-phenyl ring centre radial distribution functions for liquid benzene and biphenyl, with two different choices of biphenyl ring-ring dihedral angle ($\phi = 30^\circ$ and 90°). The biphenyl MD simulations were carried out at 348 K and 0.9914 g/mL (reproduced from *Tao et al.*'s work[190]).

Self-diffusion coefficients have been evaluated at several temperatures and they are presented in Figure 3.21. The density of the liquid biphenyl has been evaluated as a function of temperature.[216] The results have been compared to experimental temperature-dependent diffusion coefficients reported by Červená.[217]

It is interesting and encouraging to note that the agreement with experiment is significantly better for biphenyl than for benzene. Based on self-diffusion coefficients, only four of the six GBQ2 ring models (*i.e.* A1, B1, B2, and C1) have been retained.

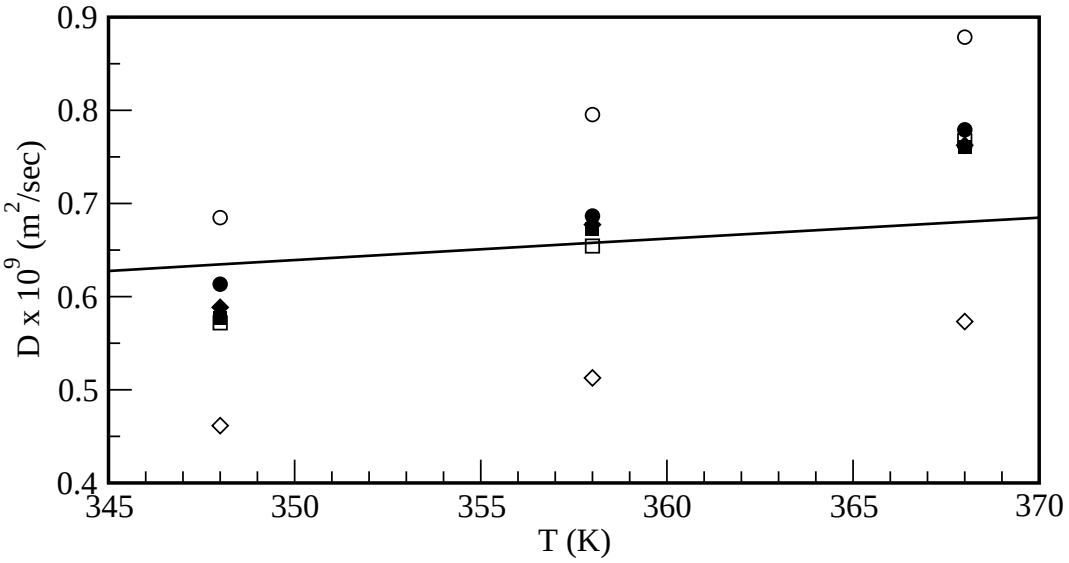

Figure 3.21 Comparison of the calculated and estimated self-diffusion coefficients of liquid biphenyl. Results for six GBQ2 ring models are shown: A1 (filled squares), A2 (filled diamonds), B1 (open squares), B2 (filled circles), B3 (open diamonds), and C1 (open circles). The experimental diffusion coefficients are shown in black line.

Models GBQ2-A1 and GBQ2-B2 are related in that the ring quadrupole value of B2 model is 80% of the value of A1 model. Likewise, GBQ2-B1 and GBQ2-C1 models are identical except for the ring quadrupole, with the latter not having a quadrupole. The GBQ2-C1 model potential has been selected in order to assess the influence of the absence of the quadrupolar contribution to the parameterized GB set, despite the fact that this model shows higher diffusion coefficients with a stronger temperature dependence.

3.3 Conclusions

In order to attain total simulation times that are, at least, several nanoseconds, with at least several hundreds of molecules, it is imperative to choose an appropriate interaction model for the liquid crystal simulations.

An adequate treatment of intramolecular interactions plays an important role in modelling the subtle differences between mesophases. To capture the intramolecular flexibility of 2PhP and 5PhP, the internal degrees of freedom of each molecule have to be studied in detail to better understand the role of the aromatic cores and flexible tails on the preferred arrangements of the molecules in the bulk system. As a result, a realistic description of the inter-ring and alkyl-aryl connections has been undertaken. Dihedral angles, bending potentials, and improper-torsional potentials have been specifically designed for the molecules under investigation. They contribute to the description of the structure-shape relationship, which in turn, has a major impact on the phase behaviour. Models of the host and dopant molecules based on a comprehensive series of *ab initio* calculations are described in Section 3.1. Full details are provided in Appendices A and B.

In the multi-site coarse-grained model potential used in this thesis, the non-bonding interactions are modeled via LJ/LJ, LJ/GB, GB/GB, and electrostatic potentials. As usual, the intermolecular potential is calculated for all pairs of sites (*i.e.* atoms or groups of atoms) on different molecules, or within the same molecule if the sites are not very close to each other. In this regard, sites separated by fewer that four bonds are

considered close. The parameterization of the GB/GB potential designed to model the aromatic rings (*e.g.* benzene and pyrimidine in the host molecules) is discussed in detail in Section 3.2.

The main advantages of using a coarse-grained approach are that it leads to an important reduction in computational expense and that it allows ring quadrupoles to be included. Fitting a set of GB parameters to the *ab initio* data of the benzene dimer has not given a correct representation of the bulk structure of liquid benzene. This occurs since benzene *in the bulk* is significantly different from the benzene in *a dimer*. To arrive at a satisfactory effective ring potential for benzene in the bulk, the parameters of the GB model potential have been least-squares fit to radial distributions from X-ray experiments.[155] Specifically, for each of the nine parameters, three values were considered: 80%, 100%, and 120% of the value obtained by optimization to *ab initio* pair potentials. Thus, I assume that the pair potentials are roughly correct representations of the effective pair potentials, and adjust the parameters accordingly. Consistent to this approach, a range of quadrupole values varying from 21% to 92% of the experimental qaudrupole value was examined. In total, 6561 parameters sets have been examined, and six sets have been retained based on least-squares errors. Moreover, these six selected sets of GB parameters have been used to acquire potential energy curves of benzene dimer in order to characterize the interactions between the corresponding pairs of molecules. The number of sets of GB parameters has been further reduced by comparison of the diffusion coefficients of liquid biphenyl obtained over a range of temperatures with available experimental data. To summarize, from the initial 6561 GBQ2 ring models only

four models have been selected and they are termed as GBQ2-A1, GBQ2-B1, GBQ2-B2, and GBQ2-C1 (Tables 3.3, 3.4, and 3.5). From now on, I will only consider these four ring models and the "GBQ2" notation will be dropped. Models A1 and B2 are related in that the ring quadrupole value of the B2 model is 80% of the value of A1 model. Likewise, B1 and C1 models are identical except for the ring quadrupole, with the latter not having a quadrupole.

To summarize, this Chapter describes the model development for the host and dopant molecules, particularly the steps implemented to arrive to a suitable representation of the ring potentials.

Chapter 4

Liquid Crystal Simulations

Liquid crystals, by virtue of being intermediate between isotropic liquids and crystalline solids, display a range of unique properties. Their practical uses, most notably for displays on telephones, televisions, watches, computers, cameras and video recorders, are well known.[15, 218, 219] Chiral smectic C liquid crystals exhibit ferroelectric properties and, for this reason, hold considerable promise for application purposes.[220, 221] In most cases, chiral smectic phases are produced by the addition of a small amount of a chiral dopant to an achiral host. Systematic experimental studies have been undertaken[28, 222, 223] to correlate host and dopant characteristics with the pitch and polarization of the phase. Multiple mechanisms for the chirality transfer have been proposed[27, 28, 159] based on experimental results. However, theoretical studies have been restricted to predictions based on the attributes of the chiral additive alone.[44, 45, 224, 225] While these studies have yielded important insights into the dopant impact, by design they cannot provide detailed molecular information on the mechanism of dopant-to-host chirality transfer. As a first step, the characteristics of the hosts and their phases must be understood. To this end, a comprehensive study of 2PhP, a well-known liquid crystal host,[25, 30-32, 226-228] is carried out in this thesis. A similar mesogen, 5PhP, which differs from 2PhP only in the molecular core, is also examined. 5PhP has not been studied as a host but it has been

employed as a co-host for 2PhP where it enhanced the electroclinic coefficient[26, 229] in the chiral SmA phase and the polarization power of the SmC phase.[230] The experimental phase diagram of 2PhP is characterized by the presence of a SmC phase extending from 58 degrees Celsius to 85 degrees Celsius whereas 5PhP only shows a SmA phase. The structure of 2PhP and 5PhP and their experimental phase diagrams have been provided in Figures 1.5 and 1.6.

Molecular dynamics simulations have provided important details on intermolecular structure and orientational order for many liquid crystalline phases. Typical simulations employ simple models, such as multipolar ellipsoids,[231, 232] cylinders,[233, 234] or fused ellipsoids or cylinders.[235, 236] Despite their simplicity, many of these models display a rich phase structure. The SmC phase, however, has proved elusive[95] for many of these models. In 1998, *Neal and Parker*[95] found that the introduction of a longitudinal quadrupole to an ellipsoidal molecular model produced SmC phases. Quadrupoles are also of interest in this work and I explore their impact for the aromatic rings of 2PhP and 5PhP. The feasibility of more realistic molecular models has been discussed by *Zannoni et al*.[50] The progression from simple models to complex ones is challenging for several reasons: the computational costs increase for a more sophisticated molecular representation; many molecules are required in the simulation cell to properly model the phase structure; and longer simulations (tens of nanoseconds) are needed as the dynamics slow down due to molecular entanglement. Despite these challenges, many mesogens require accurate molecular models to capture their phase behavior. A comparison between 2PhP and 5PhP, for example, requires detailed

molecular representations since their structures are very similar. To this end, I have developed multi-site coarse-grained models, where the aromatic rings are represented by soft quadrupolar ellipsoids, but the chains are given united atom representations. In order to fully analyze the impact of the core representation, four ring models are explored for each mesogen. *Ab initio* calculations are employed to properly explore the energetic costs for bends and torsions, and these are used in the development of the molecular models. The inclusion of quadrupoles complicates and lengthens the simulations, but proper ring-ring interactions are necessary to correctly represent core-core interactions between neighboring molecules. All-atom force fields appear to provide a superior alternative to my chosen models for 2PhP and 5PhP, however these models cannot account for the quadrupole that arises from the electron clouds above and below the plane of the ring. I show, by a detailed exploration of pair interaction energies, that the quadrupolar ring model leads to a crucial energetically favorable crossed-core conformation that is ultimately responsible for the presence of the SmC phase of 2PhP. I have also found that the proper representation of the phenyl-pyrimidine torsion within the molecular core is essential, and the phase difference between 2PhP and 5PhP is attributable to their different preferred arrangements (*i.e.* planar arrangement for 2PhP and twisted core conformation for 5PhP).

With suitable molecular models in hand, detailed MD simulations of 2PhP and 5PhP are conducted to examine the smectic phases. I consider several order parameters, some defined by the molecular cores and others obtained for the alkoxy tails. The layer normal and associated order parameter are also evaluated. Three corresponding directors

are obtained along with the layer normal. Intermolecular structure is analyzed via the decomposition of pair distributions parallel or perpendicular to the director and the layer normal. A comparison of these distributions differentiates SmC from SmA and reveals layer spacing as a function of temperature. Orientational distributions are also evaluated and show the relative positions of neighboring molecules. I find that the molecular cores are ordered but the alkoxy tails are fluid and their distribution is liquid-like.

4.1 The Starting Configuration

In the beginning of any simulation, a starting configuration (*i.e.* a complete definition of the positions and velocities of all N particles in the system) has to be assigned. The choice of the initial configuration is in principle arbitrary since equilibration will eventually be achieved. In practice, for liquid crystal simulations, the choice matters because phase formation and equilibration may require significant computer time.

In this thesis, the following procedure has been used in order to create the starting configuration. Consider the simulation of a $4(n)^3$ molecules system. Initially, a perfectly ordered lattice formed by $4(n+1)^3$ molecules is generated inside the simulation cell. Some of the molecules will be chosen at random and eliminated from the cell, so that only $4(n)^3$ molecules remain. Next, orientations have to be assigned (either random or not) to the remaining molecules. Following this, the system is relaxed by isotropically expanding the volume of the simulation cell in 5% increments of the box length. These expansions continue until all molecular overlaps have been eliminated, as confirmed by a calculation of the potential energy. After this, a sequence of Monte Carlo cycles (each consisting of 10000 attempted translations and rotations) has been used in order to "relax" the cell. Next, an isotropic compression of the volume of the simulation cell, in 5% decrements of the box length, is introduced and followed by another sequence of Monte Carlo cycles. Finally, random linear and angular velocities are assigned to the molecules, consistent with the chosen temperature.

Initially, an isotropic starting configuration was constructed following the above procedure, with random initial orientations assigned to the molecules. All attempts to grow smectic phases from this isotropic starting configuration (order parameter $P_2 <$ 0.05) were not successful since, even after 6 ns, the order parameter had not grown significantly. This is in agreement with the results of *McDonald et al.*[65] who were able to grow nematic phases starting from an isotropic configuration, only after a lengthy equilibration period of 10-15 ns. They employed a simplified model of the 8CB molecule (Figure 1.3 (b)) that completely neglected the electrostatic interactions and used the united-atom approach to eliminate all hydrogens. However, they noted[65] that "it is possible for an imprint of the starting configuration to persist for longer time scales". Furthermore, *Berardi et al.*[21] reported that long equilibration runs, typically between 10-40 ns, were required to equilibrate the nematic phase of complex cinnamate from an ordered starting configuration (P_2 around 0.65). In this case, the simulations were performed at the atomistic level and the electrostatic interactions were fully accounted for. All in all, the time necessary for the equilibration of a liquid crystal system indicates that only samples preliminarily prepared with some order have been found to require feasible computational time.

As a consequence, a nematic-like initial configuration was generated starting from a perfectly ordered lattice formed by $4(n)^3$ molecules inside of the simulation cell. The initial orientations of the molecules have now been forced to be similar to a perfect crystal (*i.e.* order parameter P_2=1). This system has then been expanded and contracted

using the already mentioned procedure. The MC cycles lead to reduced $\langle P_2 \rangle$ order parameters, between 0.56 and 0.81, after the recompression process. The equilibration period of the MD simulation will begin with this arrangement of molecules. Figure 4.1 presents a snapshot of the initial configurations of 256 2PhP molecules arranged into a cubic cell.

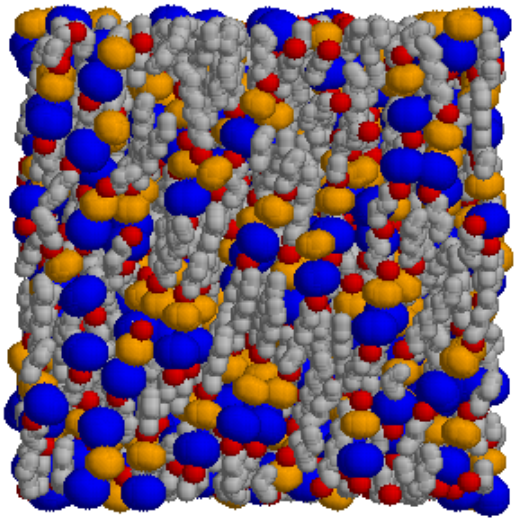

Figure 4.1 Initial nematic-like starting configuration of 256 2PhP molecules simulated in the NVT ensemble at 0.90 g/mL in a cubic simulation cell, using the A1 ring model. The alkyl chains are represented as grey spheres while the oxygen atoms are shown in red. The phenyl and pyrimidine rings are represented as bulky blue and orange spheres, respectively.

As there is no literature data on the temperature dependence of the density for either of the simulated systems (*i.e.* 2PhP or 5PhP host molecules), a crude phase diagram scan is performed by varying the system density systematically with temperature.

Specifically, 4 ns MD simulations of 256 host molecules, for a total of 6656 interaction sites, starting from this nematic-like configuration have been carried out in the NVT ensemble to provide a preliminary survey of the phase diagram. As a reference point, the density of the 8CB molecule[65] is known and the smectic phases occur between 1.05 g/mL and 0.95 g/mL. Considering that the length of the fully extended model of 8CB molecule (~22 Å) is slightly less than that of the 2PhP or 5PhP host molecules (~25 Å) and that 8CB also included two aromatic rings, the apparition of smectic phases is expected at similar densities for the 2PhP and 5PhP.

With this in mind, a series of densities and temperatures have been explored for 2PhP and 5PhP. Results of NVT simulations will be presented in detail in the following section.

4.2 Preliminary Simulations in the NVT Ensemble

For the NVT simulations done in this thesis, practical limitations quickly emerged with the initial starting configuration of the system, the size of the simulated system, and the shape of the simulation cell.

The simulation cell shape is an important factor to consider when simulating smectic phases in the NVT ensemble. While the boundary conditions have little effect on the structure of a nematic or isotropic phase, a strong dependence of the simulation cell dimensions is observed in smectic phases due to the presence of some positional order in these fluids. Imposing a cubic simulation cell may constrain the system when it forms a smectic-like structure. Specifically, the layers may not be clearly defined, and the calculated order parameter can be lower than expected. In smectic phases, the director reorients itself such that the periodicity of the simulation cell along the director will correspond exactly to an integral multiple of the smectic layer spacing. Thus, the box dimensions influences the director orientation and the number of smectic layers.

To evaluate the impact of the constant box shape constraint, systems of 256 2PhP molecules in different but constant cell shape (*i.e.* 1:1:1, 1:1:1.5, and 1:1:2 ratios of the side lengths) have been simulated. Following the procedure detailed in Section 4.1, new starting configurations for systems of 256 molecules were obtained for each box shape. Tables 4.1 and 4.2 summarize the NVT ensemble simulations of systems of 256 2PhP and 5PhP molecules, respectively, at different densities and temperatures.

Table 4.1 Calculated average $\langle P_2 \rangle$ order parameters for systems of 256 2PhP host molecules simulated in the NVT ensemble using the A1 ring model, in parallelepipedic cells of different box length ratios.

T (K)	*Box length ratio* $x : y : z$	Density (g/mL)							
		0.82	0.85	0.88	0.90	0.92	0.95	1.00	1.08
320	*1:1:1*	-	-	-	-	-	0.54	0.64	0.62
335		-	-	-	0.57	-	0.58	0.66	-
350		-	0.23	0.37	0.52	0.54	0.53	0.60	-
365		-	-	0.36	-	-	0.52	0.53	-
380		-	0.13	-	0.41	-	0.56	0.51	-
400		0.13	0.11	-	-	-	-	-	-
450		-	-	-	0.26	-	0.47	-	-
350	*1:1:1.5*	-	-	-	0.24	-	-	-	-
380		-	0.18	-	-	-	-	-	-
335	*1:1:2*	-	-	-	0.57	-	0.32	-	-
350		-	-	-	0.49	-	0.32	-	-
380		-	0.24	-	-	-	-	-	-

Table 4.2 Calculated average $\langle P_2 \rangle$ order parameters for systems of 256 5PhP host molecules simulated in the NVT ensemble using the A1 ring model, in parallelepipedic cells of 1:1:2 box length ratio.

T (K)	*Box length ratio* $x : y : z$	Density (g/mL)				
		0.85	0.88	0.90	0.92	0.95
360	*1:1:2*	-	-	0.45	0.38	0.52
370		-	-	0.49	0.37	0.48
380		-	0.22	-	-	-
420		0.26	-	-	-	-

By changing the simulation cell lengths ratio from $x:y:z$ =1:1:1 to 1:1:1.5 and further to 1:1:2, the smectic structure often stabilizes faster and easier. This is evident from the snapshots of 256 2PhP molecules simulated in the NVT ensemble at 350K and 0.90 g/mL using the A1 ring model and varying the box length ratios (see Figure 4.2). In addition, the interdigitation between the layers and weak correlation between the neighbouring layers are slowly disappear when the box shape is changed by increasing the z axis relative to the x and y axes. On the whole, Tables 4.1 and 4.2 show that the shape of the simulation cell and the density strongly impact the structure of the fluid. For this reason, the NVT ensemble is not well suited to a study of smectic phases.

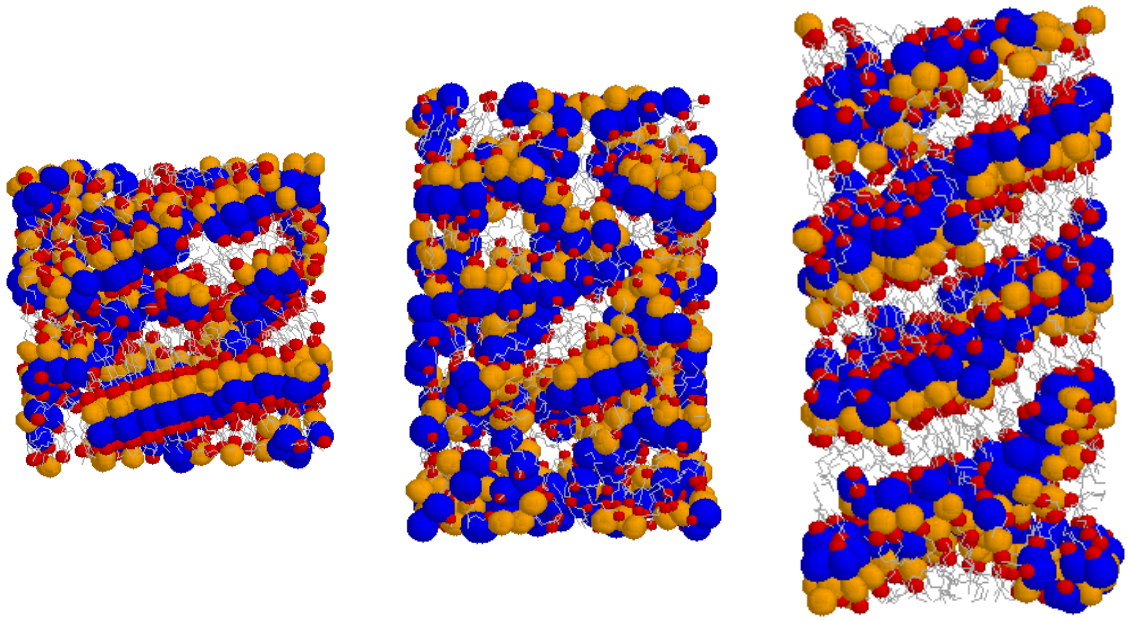

1 : 1 : 1 **1 : 1 : 1.5** **1 : 1 : 2**

Figure 4.2 Snapshots of 256 2PhP host molecules simulated in the NVT ensemble at 350K and 0.90 g/mL, using the A1 ring model, in simulation cells having different box length ratios. The alkyl chains are represented as grey lines, and oxygen atoms are shown in red. The phenyl and pyrimidine rings are represented as bulky blue and orange spheres, respectively.

To study the influence of the system size, a system of 108 2PhP molecules, at 350K and 0.90 g/mL in a 1:1:2 ratio simulation cell was studied in the NVT ensemble. Simulation times are faster in a system of 108 molecules, but too few layers were formed rendering the result difficult to assess. As a result, I have chosen to simulate systems of 256 molecules.

The isothermal-isobaric (NPT) ensemble, being closer to the experimental conditions, is a better tool to understand the behavior of real liquid crystals. The NPT ensemble simulations can be done in two different ways, by using either a fixed aspect ratio[121] (isotropic volume change), or a shape-varying cell[140, 237] (anisotropic volume change). A smectic phase is not well suited to isotropic changes due to different impacts on the intralayer and interlayer spacing. An attempt to enlarge the cell, for example, may be favorable to the layer spacing but the additional space within the layers may be energetically unfavorable. Anisotropic volume changes, where only one cell dimension is changed, are far more appropriate since they allow independent adjustment of the interlayer spacing. Although anisotropic changes in the simulation cell can be accommodated within the extended Lagrangian formalism,[121] the method becomes significantly more complicated. I have opted instead to employ Monte Carlo volume changes. By using a hybrid MD-MC method (presented in Section 2.3), the limitations coming from the constant box shape constraint are eliminated and the natural arrangement of smectic phases is promoted, by allowing the shape of the simulation cell and density of the simulated system to fluctuate.

4.3 Pair Energies

Before examining the phase behavior of 2PhP and 5PhP, it is instructive to begin by considering interactions between pairs of molecules. To explore the effect of the ring quadrupole, "docking" studies have been performed for each mesogen, using the four ring models.

Two minimization algorithms have been used to gain insights into the conformational characteristics of 2PhP and 5PhP dimers. First, to ensure a broad sampling of the potential energy surface and the conformations represented by it, between 800 and 1850 randomly generated starting configurations have been used for each of the four selected sets of ring parameters (*i.e.* A1, B1, B2, and C1 ring models shown in Tables 3.3, 3.4, and 3.5) and both host molecules. Specifically, two molecules are positioned randomly at the center of a very large simulation cell. Following this, MD simulations are performed for 50000 iterations with the temperature (initial at 300K) being halved every 10000 iterations. This "downhill" method does not easily allow crossing of energy barriers, and I have been able to identify local minima close to the point from which the minimization procedure started, for each of the dimers and all four selected sets of ring parameters, respectively. A schematic representation of the minimization procedure used in this thesis is shown in Figure 4.3. This minimization procedure helps us to identify the ease of finding a particular energy minimum, which is related to the density of points in a region.

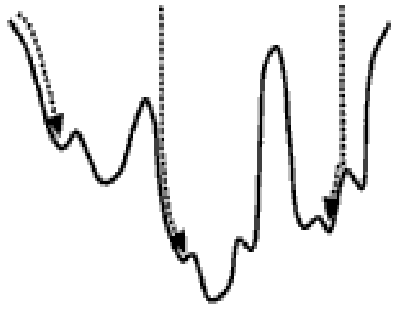

Figure 4.3 A schematic representation of a minimization procedure leading to the closest local minimum.

In addition, in order to determine the lowest possible pair energies, a large number of simulations have been performed imposing fixed core-core angles. Specifically, at least 800 diverse starting configurations have been used for each core-core angle constrained at $n \times 20$ degrees, where $n = 0 - 9$.

Figures 4.4 and 4.5 show the results of docking studies for the 2PhP and 5PhP liquid crystal molecules and each of the four selected ring models. In each panel, the pair energy is plotted as a function of relative core angle, thus each point corresponds to the final energy of a simulation. Each open circle represents an energy minimization following a random initial structure of the dimer. Each filled circle represents the lowest energy achieved for a series of fixed core-core angle simulation.

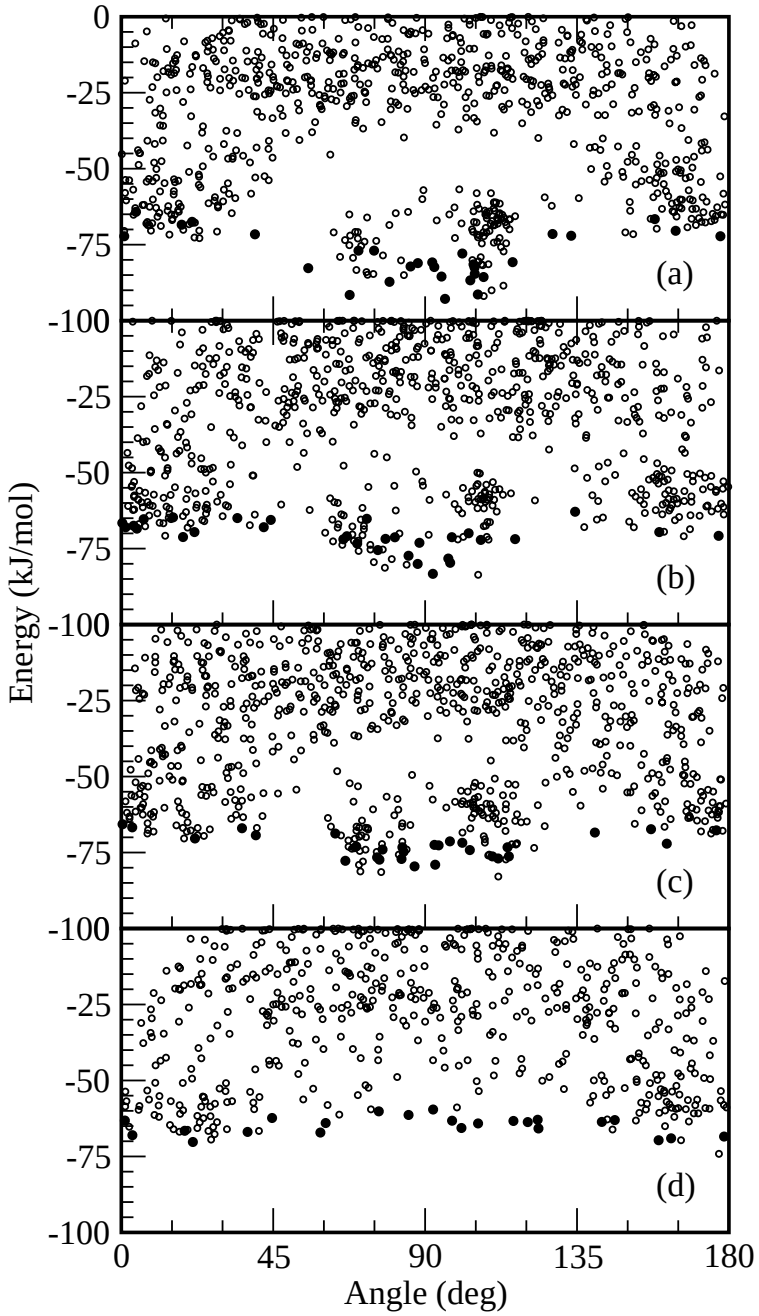

Figure 4.4 The pair energy plotted as a function of relative angle between two 2PhP molecules, by means of using the: (a) A1, (b) B1, (c) B2, and (d) C1 ring models, respectively. Each open circle represents an energy minimization following a random initial structure of the dimer while every filled circle shows the lowest dimer energy obtained with a fixed core-core angle.

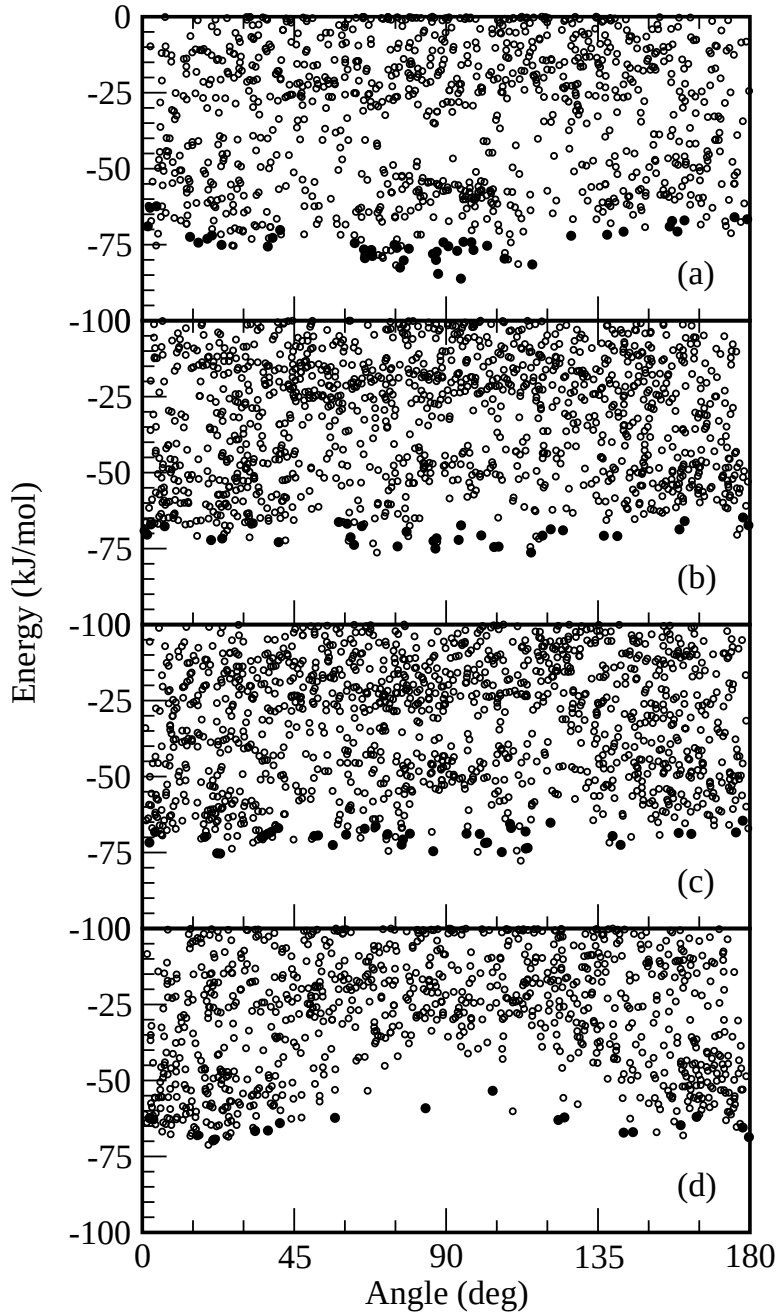

Figure 4.5 The pair energy plotted as a function of relative angle between two 5PhP molecules, by means of using the: (a) A1, (b) B1, (c) B2, and (d) C1 ring models, respectively. Each open circle represents an energy minimization following a random initial structure of the dimer while every filled circle shows the lowest dimer energy obtained with a fixed core-core angle.

The arrangements of dimers have been first classified taking into consideration the angle between the axes bonding the two GB sites of the same molecules, as *syn, anti,* or *crossed.* The angle is obtained from the dot product of the ring-ring bonds in both molecules. Next, it is important to distinguish between docked structures where the rings are *face-to-face* or *parallel* as opposed to *slipped-parallel*. For instance, Figure 4.6 presents some of the arrangements that appear in the docking studies of the 2PhP and 5PhP dimers.

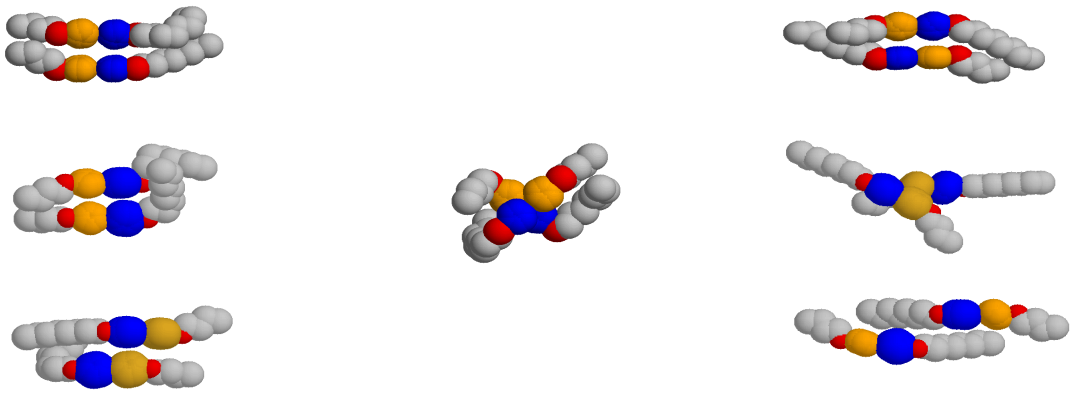

Figure 4.6 Possible arrangements of 2PhP and 5PhP dimers. The alkyl chains and oxygen atoms are represented by grey and red spheres, respectively. The phenyl and pyrimidine rings are represented by bulky yellow and blue spheres, respectively.

Consider Figure 4.4 (a), which shows the results of docking studies for 2PhP when the A1 ring model is used. Clearly, in this case, the lowest pair energy occurs when

the rings are crossed, but the density of points in this region indicates that this energy minimum is somewhat difficult to reach, relative to conformations where the rings are parallel, or close to parallel. Overall, these docking studies indicate that within the simulations parallel arrangements may be entropically favored but energetics favor crossed arrangements.

When the ring quadrupole decreases, the energetic bias towards crossed arrangements also decreases and this is evident by the smaller energy gap for parallel versus crossed arrangements when the B1 and B2 ring models are used (see Figures 4.4 (b) and (c)). This gap vanishes entirely in the absence of a ring quadrupole (*i.e.* C1 ring model). Even in this case, the density of points indicates that parallel and anti-parallel arrangements are more easily found despite the absence of ring quadrupoles. This result is important in explaining the influence of the quadrupole to the ring model potential.

Docking energies for 5PhP dimer are shown in Figure 4.5. Comparing between the two mesogens, the quadrupole has a smaller energy lowering effect for 5PhP. The non-planarity of the core region in 5PhP frustrates to a larger extent the energy lowering achievable for crossed core configurations. Low energy conformations are more evenly distributed among core angles for 5PhP suggesting that these molecules should display a broader array of core arrangements within the simulations.

Figure 4.7 (a) shows the results of the docking study for 2PhP when the A1 ring model is used. Color coding is introduced within the figure to separate the docking minima according to the distance between the phenyl rings. Specifically, the energy minima below –10 kJ/mol are shown for phenyl-phenyl distances between 3.4 and 7.3 Å.

The green color identifies that the phenyl rings are within 3.4 and 4.4 Å, and this occurs exclusively for crossed configurations with a relative core angle of around 70 degrees with the phenyl rings closer together. At slightly different distances, between 4.4 and 5.8 Å, two configurations (shown in red) contribute at energies below -10 kJ/mol. Either the molecules are roughly parallel, with face-to-face phenyl rings, or a crossed configuration with an inter-core angle of around 110 degrees occurs (*i.e.* anti-crossed). At larger distances, between 5.8 and 7.3 Å, anti-parallel configurations appear along with less energetically favorable parallel and crossed configurations (shown in blue). The latter tend to have an intercore twist so that the edge-to-edge ring arrangements occur.

Figure 4.7 (b) categorizes all docking minima, with energies below -10 kJ/mol, according to the distance between the phenyl rings. The spatial subdivision reveals three definite regions: around 3.9 Å, around 4.8 Å, and around 6.5 Å. With the information in Figure 4.7 (a), only crossed configurations occur at small separations, parallel and anti-crossed configurations occur between 4.4 and 5.8 Å, and anti-parallel configurations are the largest contributor between 5.8 and 7.3 Å. The correlation between phenyl-phenyl ring distance, docking energies, and intercore angle in Figures 4.7 (a) and (b) prove useful in understanding the structure in the smectic phases.

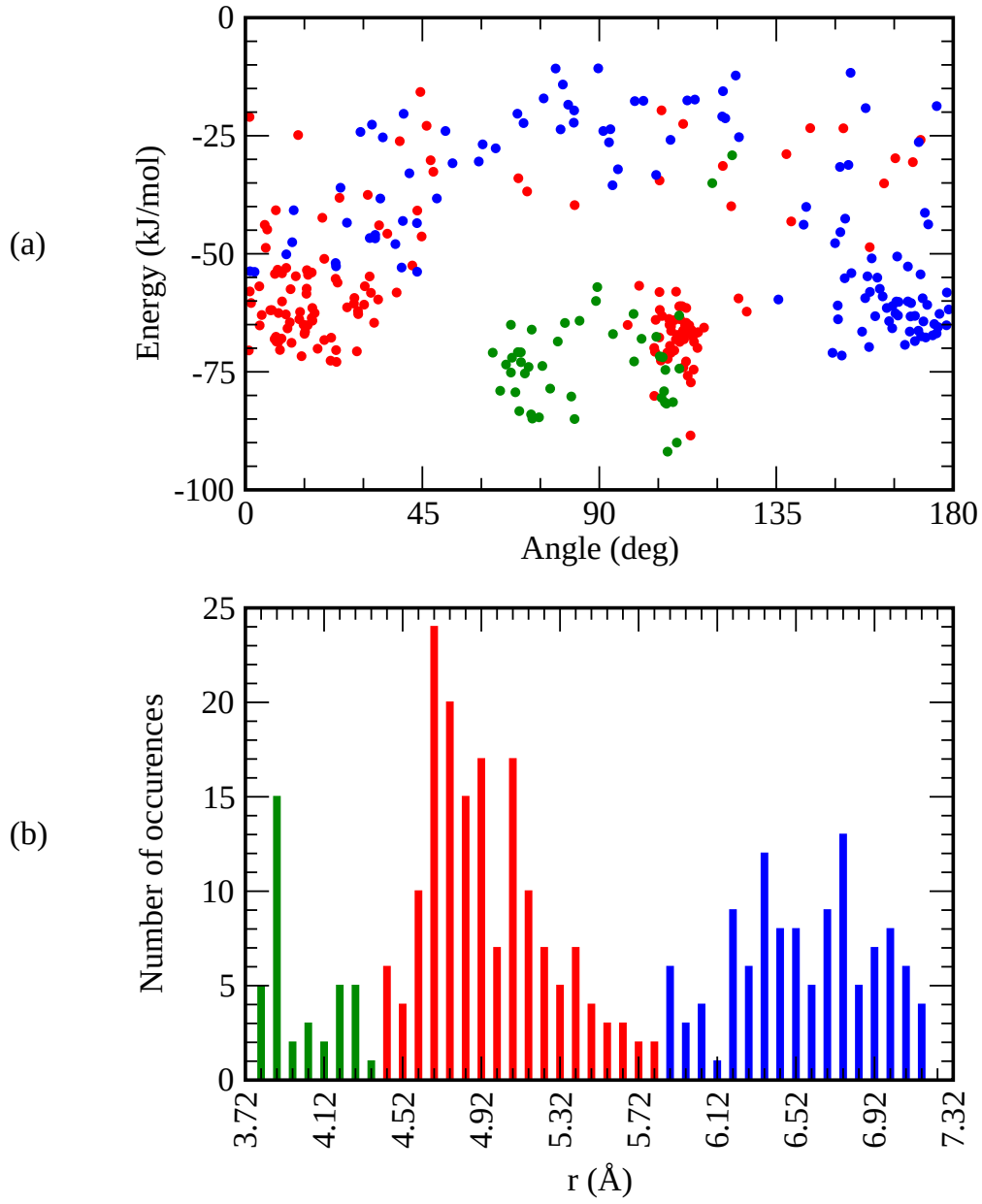

Figure 4.7 The pair energy plotted as a function of relative angle between two 2PhP molecular cores in (a) and as a function of phenyl-phenyl ring separation in (b). Each dot in (a) represents an energy minimization following a random initial structure of the dimer. Results are presented for the A1 model. In (a), green, red, and blue circles identify configurations where the inter-phenyl distance is between 3.4-4.4 Å, 4.4-5.8 Å, and 5.8-7.3 Å, respectively. Only configurations with an energy less than -10 kJ/mol contribute in (b).

4.4 Simulations of Liquid Crystals in the NPT Ensemble

4.4.1 Simulations Details

This section presents MD-MC simulations in the NPT ensemble for 2PhP and 5PhP mesogens. 2PhP is examined at four temperatures (335K, 365K, 400K, and 450K), which span the temperature range for SmC, SmA, nematic, and isotropic phases (Figure 1.6).[25] 5PhP is examined at three temperatures (370K, 400K, and 450K), where SmA and isotropic phases are observed experimentally (Figure 1.6).[26]

Results are presented for simulations of 256 molecules. This number is sufficient for 3-4 layers to form within the simulation cell. The methods of generating starting configurations have been discussed in detail in Section 4.1. The starting configuration typically has a P_2 order parameter between 0.56 and 0.81 (see Appendix C), and visual inspection shows nematic-like positional order. This starting procedure is ideal for 2PhP and 5PhP since the latter does not have a stable nematic phase while the nematic phase of 2PhP is only stable over a very narrow temperature range. At the lower temperatures, where smectic phases are expected, I find that layers form very quickly. An equilibration period of 0.5 ns is sufficient as the density in the simulation cell and the order parameters have stabilized after this time. The molecules are initially aligned as mentioned above, and once layers form, few molecules turn over the duration of the simulations. Thus, the P_3 order parameters tend to be nonzero. The impact of this initial aligned configuration will be discussed in Section 4.4.4, but here I note that a few runs starting from an antiparallel molecular alignment were also performed and will be discussed later.

As discussed in Section 2.3, changes in the shape and size of simulation cell are allowed within the NPT ensemble simulations and these change the density of the systems. Specifically, at each iteration a random variable is chosen to decide upon whether a volume change is to be attempted. On average, an attempt is made every 256 iterations. If the volume will be changed, the cell dimension to be changed is decided randomly, and the magnitude of the change is randomly chosen, subject to a maximum. The latter is adjusted during the equilibration so that the success rate is between 30% and 70%.

The initial density is 0.90 g/mL for all simulations, which is close to but slightly lower than densities employed for related mesogens.[65] For all simulations, the density rapidly drops to around 0.77 g/mL as the nematic starting configuration reorganizes into layers. The density then gradually increases back to between 0.88 g/mL and 0.92 g/mL, with the lower average density for the C1 ring model at higher temperatures and the higher density for the quadrupolar models at 335K.

Two types of simulations are performed: a series of short 2 ns runs, and longer 8-14 ns runs. For the shorter runs, five independent runs are performed for 2PhP at 335K, 2PhP at 365K, and 5PhP at 370K. For both mesogens, three independent simulations are performed at 400K, and results are reported from two independent simulations at 450K. Averaged results from the independent simulations, for a given temperature and mesogen, are reported below. All simulations are repeated for the A1, B1, B2, and C1 ring models. In total, results from eighty 2 ns simulations are reported below. These

results are complemented by 8-14 ns runs for the B1 and C1 ring models of 2PhP at 365K and 5PhP at 370K.

Within the 2PhP and 5PhP simulations, both phenyl and pyrimidine rings are represented as multipolar ellipsoids whilst the flexible tails are represented as spherical LJ sites. The non-polar portion of the ring representation is contained within the GB potential, and identical GB parameters are used for both rings. The ring models for phenyl and pyrimidine are very similar, but not identical. Specifically, they differ in the magnitude of the ring charge, as calculated from the CHELPG algorithm[165] applied to the global energy minimum, and in their intramolecular potentials. The current models do employ identical ring quadrupoles and GB potential parameters and, likely, the differences between the rings are underestimated. Full details of the force field used are given in Chapter 3.

Returning to the ring representation, the inclusion of a ring quadrupole means that multipolar interactions include charge-charge, charge-quadrupole, and quadrupole-quadrupole terms. Only the last of these was present for the model tests on benzene and biphenyl. For 2PhP and 5PhP, I have chosen to replace the point ring quadrupole by four charges placed above and below the ring plane, along the symmetry axis. The charges are defined so that they exactly reproduce the desired quadrupole moment, have a net charge of zero, do not introduce a net dipole on the ring, and they are located close to the ring center inside the repulsive wall of the GB potential. Specifically, the charges are located at ±1 Å and ±0.5 Å from the center of the GB site along the symmetry axis, and the magnitudes of the charges are ±0.9101 |e| for model A1 and ±0.7281 |e| for models B1

and B2. This simple representation of the ring quadrupole allows the use of charge-charge Ewald summations[64] for all electrostatic interactions within the fluid. The Ewald convergence parameter of $\alpha = 3.5\,\text{Å}^{-1}$ has been tested and chosen for all the simulations with a reciprocal space cutoff of $k^{*2} \leq 46$. Periodic boundary conditions[119] and an initial rectangular 1:1:2 simulation cell were employed. A spherical cut-off ($r_{cut-off}$ = smallest box length/2.05) was used for the LJ and GB interactions. A Nosé-Hoover thermostat[135-139] is used to maintain a constant average temperature. In particular, separate rotational and translational thermostats have been implemented. After testing four different time steps, a time step of 0.25 fs is chosen for the simulations. Interatomic distributions, inter-ring distributions, and order parameters are evaluated every 100 iterations. Distribution functions are averaged every 250000 iterations. Snapshots of the simulation cell are collected every 250000 iterations. A typical short simulation consists of 8 million iterations, with an equilibration period of 500000 iterations. Although the simulations are relatively short for liquid crystalline phases, it is important to realize that the system adopts a layered structure very quickly and that my systems are large, given the level of molecular detail. All simulations were performed with the MDMC program,[238] which has been modified to include GB-GB and GB-LJ potential and force calculations.

4.4.2 Convergence Issues

Figure 4.8 (a) compares radial distributions for five independent 2 ns simulations of 2PhP, at 365K, as predicted from the B1 model. The distributions in Figure 4.8 (a), and all distributions involving rings, report probabilities as a function of the distance between

the ring centres. Clearly, all the simulations predict equivalent ring-ring distributions beyond separations of 6 Å. At closer distances, where the rings are in contact, the simulations show the same peaks but with some differences evident in the peak intensities. The average of these distributions is also compared with the distributions from a single 12 ns run in Figure 4.8 (b).

The simulations reported in this section begin with parallel molecules in the simulation cell. In Figure 4.8 (c) the phenyl-phenyl distribution is shown for an antiparallel starting configuration. Keeping in mind that the latter is a 2 ns simulation, the difference between the average over five simulations is consistent with the distributions in Figure 4.8 (a). Thus, the intermolecular structure in the fluid is similar for both starting configurations.

The use of multiple short simulations provides a simple and efficient means of exploring the fluid structure. This is particularly true for 2PhP and 5PhP where equilibration from a nematic starting configuration is rapid. Five independent simulations have been employed for the lower temperatures, where smectic phases are expected, and two or three simulations at higher temperatures, where isotropic phases occur. This number of simulations is sufficient to tentatively identify the phases and qualitatively analyze the fluid structure and order, but a greater number of simulations would be required to ensure full convergence of the properties of the fluid. In particular, the larger simulations suggest that a single long simulation would require over 100 ns to generate converged fluid properties.

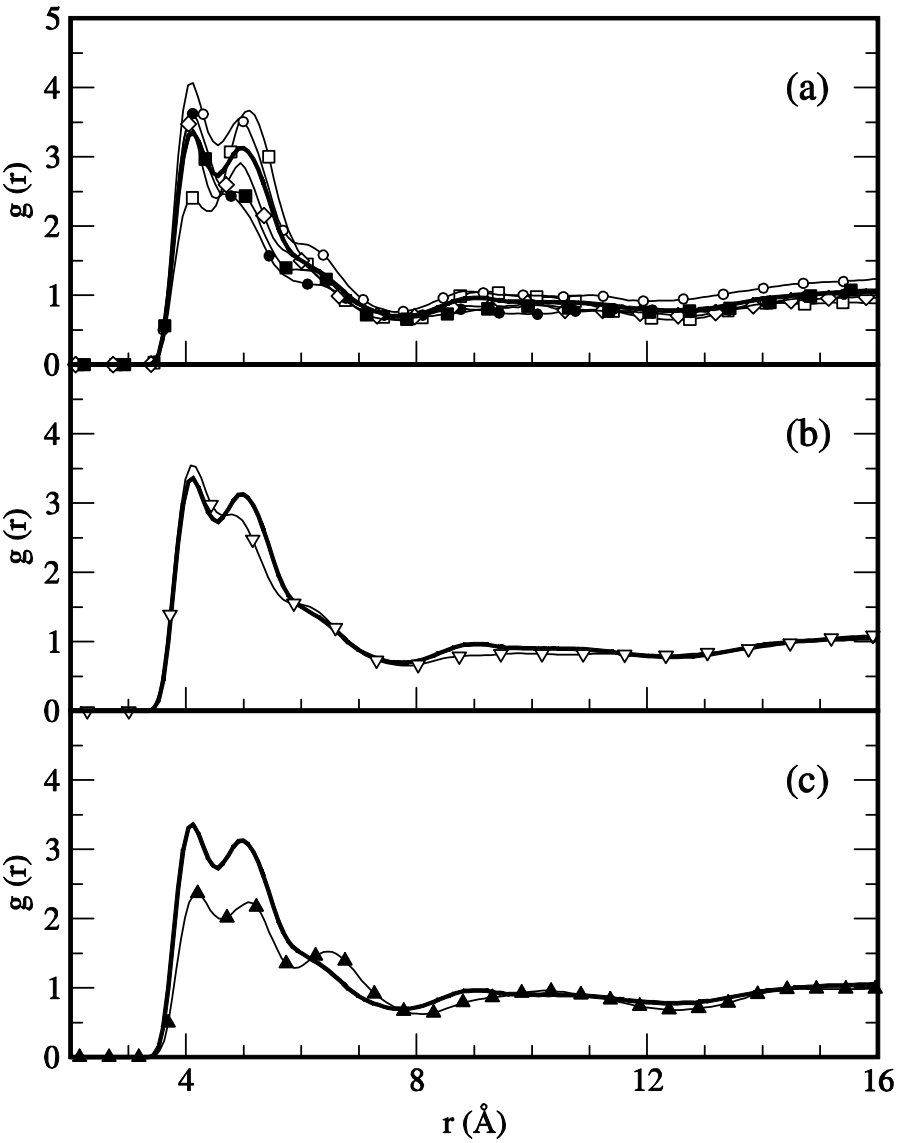

Figure 4.8 Convergence tests illustrated for 2PhP (B1 ring model) at 365K. (a) Phenyl-phenyl radial distributions are shown for five independent 2 ns simulations (open circles, filled circled, open diamonds, open squares, filled squares). Their average is shown with a thick solid line. (b) The distribution from a single 12 ns simulation (open triangle down) is compared with the average over five independent 2 ns simulations (thick solid line). (c) Aggregate distribution functions parallel (thick solid line) and anti-parallel (filled triangle up) starting configurations.

A detailed dynamical analysis of neighbouring molecular pairs was performed for the B1 model of 2PhP at 335K. The analysis reveals that neighbour interaction time decreases exponentially but that prior neighbours are highly likely to re-establish their neighbour status. That is, dynamic fluctuations lead to temporary loss of neighbour status but the molecules quickly restore their proximity. I find that over two-thirds of molecular pairs identified as neighbours maintain their status, with brief interruptions, for longer than 1 ns. In viewing movies of the simulations, interlayer fluctuations are often more pronounced than intralayer fluctuations, partial layers tend to form in the simulation cell, and these are very slow to change once formed.

4.4.3 The Impact of Ring Quadrupole

The quadrupole moment perpendicular to the plane of an aromatic ring is substantial and an important contributor to ring-ring interactions. A typical atomistic molecular mechanics ring model cannot represent this quadrupole since the ring atoms are within the ring plane. In order to capture this effect, dummy atoms above and below the plane are required. A coarse-grained model is more readily adapted to incorporate a quadrupole and, in this section, I investigate the impact of the quadrupole on the structure of the liquid crystal phases. Figure 4.9 illustrates the impact of the ring quadrupole by examining the ring-ring distribution between the phenyl rings of 2PhP at 365K. Average distributions of five short runs (2ns) started from different parallel starting configurations are compared.

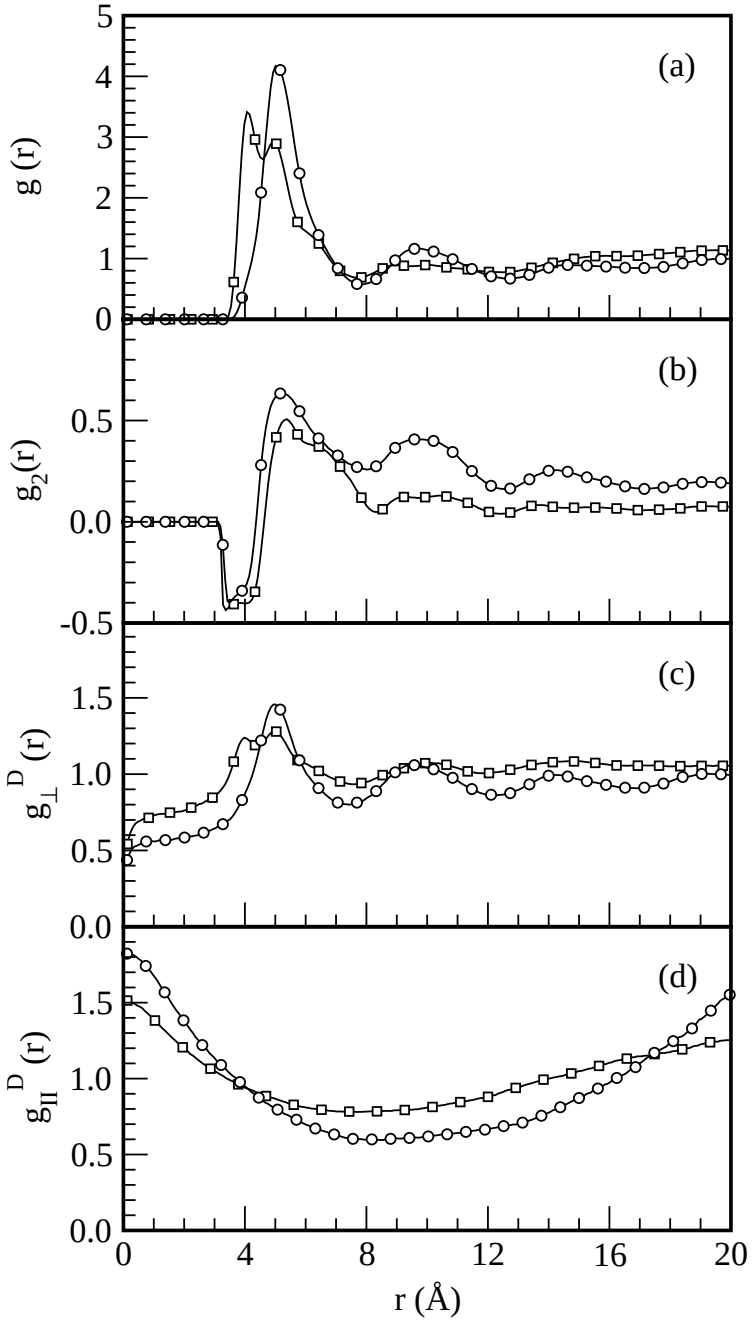

Figure 4.9 The impact of the ring quadrupole on the liquid crystal phase of 2PhP at 365K. Phenyl-phenyl distributions are compared for B1 model (open squares) and C1 model (open circles). Radial distributions, second order correlations, structure perpendicular to the director, and structure parallel to the director are compared in (a), (b), (c), and (d) respectively.

Specifically, the figure compares inter-ring radial distributions *g(r)*, the inter-ring orientational distribution $g_2(r)$, the inter-ring distribution perpendicular to the director $g_{\perp}^{D}(r_{\perp})$, and the inter-ring distribution along the director $g_{\parallel}^{D}(r_{\parallel})$. Results for the B1 and C1 ring models, which differ only in the presence of a quadrupole for the former, are shown.

The addition of a quadrupole to the ring has a dramatic impact on the fluid structure. Without a quadrupole, the phenyl-phenyl radial distribution has a simpler structure with a side-by-side contact peak at 5 Å and a second peak at 9.5 Å. The first peak corresponds to a contact peak, and, from Figure 4.7 (a), it originates primarily from parallel molecular cores, with some contribution from anti-crossed pairs. The presence of a quadrupole on the ring splits the contact peak, with the introduction of a feature at 4 Å. This peak is due to crossed-core molecular pairs that, according to Figure 4.7 (a), are now energetically favored. A shoulder at 6.2 Å also appears and this feature reflects a higher probability for anti-crossed arrangements when the rings include quadrupoles. The first minimum in the radial distribution appears at 7.8 Å regardless of the ring model. I can therefore easily and directly compare coordination numbers, obtained from integrating *g(r)* between 0 and 7.8 Å. I find that, on average, a given 2PhP molecule has 4.4 nearest neighbours regardless of the presence of the quadrupole. Thus, the quadrupole dramatically alters the orientation and position of the nearest neighbours without changing the overall number of neighbours.

Second order correlations are shown in Figure 4.9 (b). At large distances, this distribution function approaches $(P_2)^2$. This limit is clearly higher in the absence of the

ring quadrupole indicating a more ordered fluid. Structure perpendicular and parallel to the director (see Figures 4.9 (c) and (d)) is also stronger in the absence of the quadrupole. All of these features are indicative of a simpler layer structure, with more order within the layers, when the rings do not include quadrupoles. It is important to realize, however, that the director is defined by the molecular core and with the introduction of crossed configurations the assessment of the order is more problematic.

4.4.4 Structure and Order

Figure 4.10 compares distributions within the core region with distributions in the tails. Average distributions of five independent 2ns runs started from different parallel starting configurations are compared. Specifically, distributions between C(1)-C(1) and C(16)-C(16), the end groups in the hydrocarbon tails (Figure 3.2), are compared with the core phenyl-phenyl and pyrimidine-pyrimidine distributions. From the radial distributions in Figure 4.10 (a), the C(1)-C(1) and C(16)-C(16) distributions are similar even though the tails differ in length. In both cases, the radial distributions are liquid-like with a broad contact peak at around 4.3 Å and a weak secondary peak at around 8.5 Å. Unlike typical liquid distributions, the radial distribution function shows a broad region of low probability between 10 and 20 Å corresponding to separations where aromatic molecular cores are found. The ring-ring distributions are, by contrast, more structured with pronounced contact and secondary peaks. As with the end groups, the distributions show a broad region of low probability. In this case, the region corresponds to separations where alkoxy tails are found in the layered fluid.

The distribution functions can be subdivided into components parallel and perpendicular to the director. The component perpendicular to the director, given in Figure 4.10 (b), shows that the 5PhP rings have a well-defined intralayer structure with three peaks evident at 5 Å, 10 Å, and 15 Å. These peaks correspond to neighbour, next-nearest neighbour, and next-next-nearest neighbouring rings, with a preference for parallel core alignment. In contrast, the distributions between tail atoms indicate that their structure is short ranged and weaker: $g_{\perp}^{D}(r_{\perp})$ shows only a small, broad contact peak from neighboring molecular tails. Structure along the director, $g_{\parallel}^{D}(r_{\parallel})$, shown in Figure 4.10 (c), reflects the layer spacing and impacts both core and tail atoms.

Although the phenyl-pyrimidine axis is the most obvious choice for defining a director, other choices can be made. Directions defined from the C(1)-C(2) and C(15)-C(16) bonds have been chosen for comparison. Figure 4.10 (d) shows the angular correlation between these chosen axes within neighbouring molecules. The inter-core axis distribution shows that, when the molecular cores are very close together, they prefer to be in a crossed configuration. If all molecules adopted this configuration then $g_2(r) \to P_2(\cos\theta) \to -0.5$. The angular correlation between the phenyl-pyrimidine axes reaches this limit at small separations. The inter-core $g_2(r)$ quickly becomes positive at larger separations as parallel core arrangements begin to contribute to the orientational distribution. In contrast, the alkoxy tails show very little orientational correlation except at very small separations.

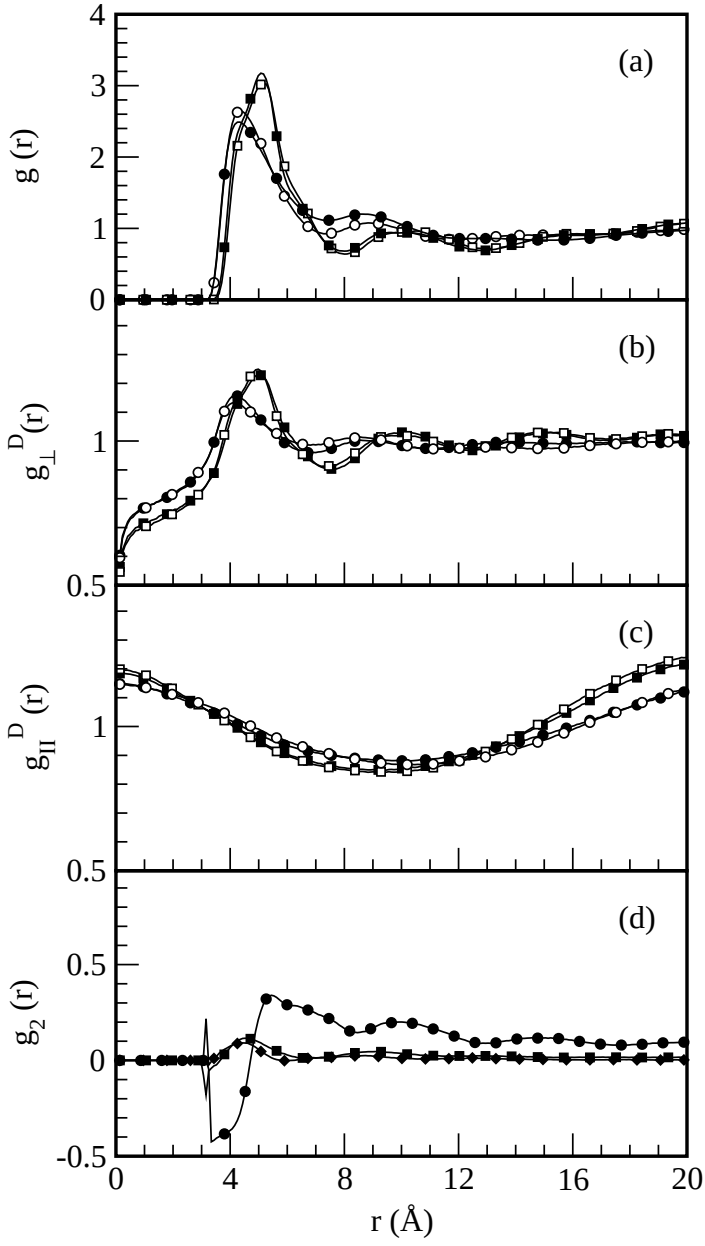

Figure 4.10 A comparison between tail and core structures in the 5PhP liquid crystal phase at 370K, as predicted from the B1 model. In (a), (b), and (c), distributions between C(1)-C(1), phenyl-phenyl, pyrimidine-pyrimidine, and C(16)-C(16) are shown by solid circles, solid squares, open squares, and open circles, respectively. Panel (a) compares radial distribution functions while perpendicular and longitudinal distributions, relative to the director obtained from the phenyl-pyrimidine core axes, are shown in (b) and (c). Panel (d) shows intermolecular orientational distribution functions as determined from the phenyl-pyrimidine axis (solid circles), C(1)-C(2) axis (solid squares), and the C(15)-C(16) axis (solid diamonds).

The orientational distribution function tends to $\langle P_2 \rangle^2$ at large separations and Figure 4.10 (d) shows that the molecular cores have long-ranged orientational order but the tails do not. Thus, the region occupied by the tails is liquid-like in regards to structure and ordering.

The time evolution of the fluid order is shown in Figure 4.11 for 5PhP at 370K and as represented by the B1 model. The starting configuration for the simulation is a nematic fluid. For the simulation shown, the starting P_2 order parameter was 0.75 for the inter-ring axis and quickly dropped to between 0.4 and 0.5. This pattern is consistent for all my simulations: the order initially imposed is reduced once the molecules form the layered structure. This is due, in part, to the absence of electrostatic charges during the preparation of the starting configuration. Once the charges are included, the fluid structure becomes more complex and the order parameter decreases. In particular the introduction of crossed configurations will lead to a reduction of P_2, due to my protocol for the evaluation of the order rather that to a true reduction in order. The complexity of the molecular structure also leads to a lower order parameter, and values observed for simpler models[50] are not expected to be observed here.

A P_2 order parameter for the layer normal, $P_2^L(t)$, is also provided in Figure 4.11. This quantity reflects consistency between the local molecular layers normal, determined for each molecule by evaluating the normal to a plane defined by neighbour positions. From Figure 4.11 (a), the consistency between the local layers normal is higher than the agreement between the inter-ring axes through most of the simulation. This is due, in part, to the larger impact of crossed configurations to the order associated with the

director. The P_2 order parameter obtained from the molecular tails is also shown. It is consistently low (< 0.2), as expected since the tails are less organized than the cores. However, P_2 is slightly larger for C(1)-C(2), the shorter "tail", than for C(15)-C(16). It follows that the order in the tail region will be smaller for atoms/bonds that are farther from the molecular core: the core ordering is transferred, to some extent, to nearby bonds in the hydrocarbon chains. In 5PhP, a small amount of order remains for atoms five bonds away from the core, but not for atoms nine bonds away.

The P_3 and P_4 order parameters are also provided in Figures 4.11 (b) and (c). The P_3 order parameter is not zero, although it is small, due to molecular propensity to align in the simulations. When simulations are started with parallel or antiparallel molecules, the original alignment is largely preserved over a 2 ns simulation. To be more precise, for a parallel starting configuration, the P_3 order parameter drops initially as the fluid transitions away from a nematic to a smectic. Once the layers are formed, the P_3 order parameter stabilizes, as shown in Figure 4.11 (b), and further decreases are very slow. Clearly, if the original configuration was isotropic, then the molecules would align with random orientations since energetics do not favour a particular alignment (see Figure 4.5). A few simulations were also started with antiparallel molecules and, as expected, the P_3 order parameter is zero (aside from instantaneous fluctuations) throughout the simulation.

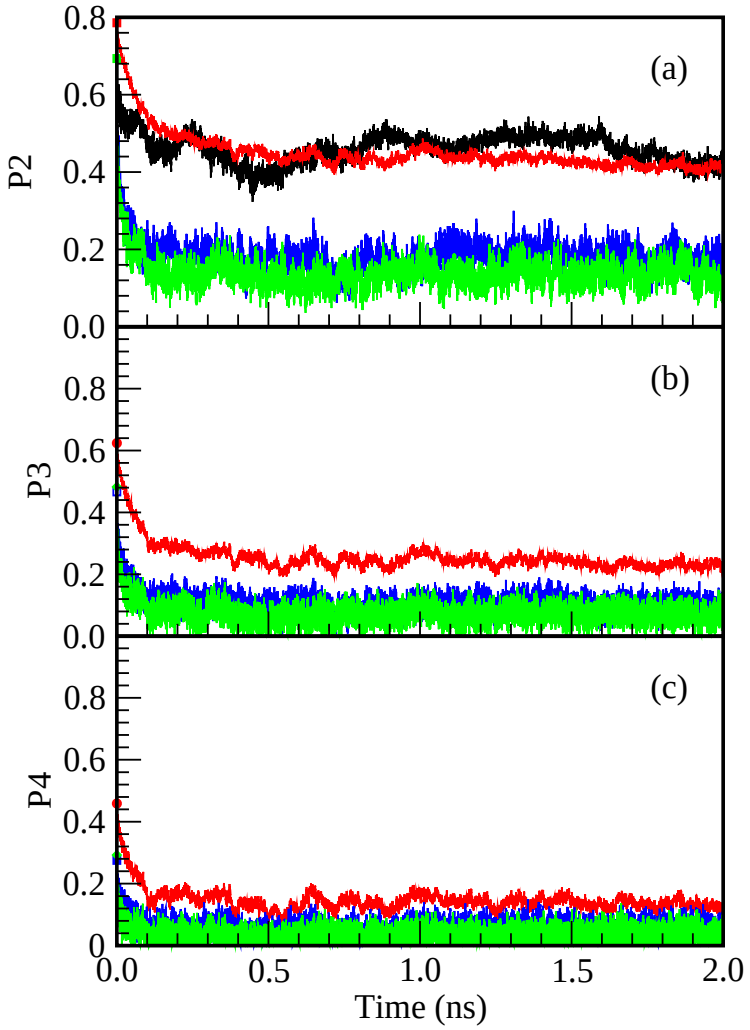

Figure 4.11 The time evolution of order parameters for 5PhP, at 370K, as represented by the B1 model. Order relative to the "directors" defined from the phenyl-pyrimidine, C(1)-C(2), and C(15)-C(16) axes are represented by red, blue, and green, respectively. The P_2, P_3, and P_4 order parameters are shown in (a),(b), and (c), respectively. In (a), the P_2 order parameter describing the consistency between local (molecular) layers normal is shown in black.

4.4.5 Layering and Phase Behaviour

The layers formed by 2PhP and 5PhP often do not extend through the simulation cell or conform to the simple layering patterns observed for simpler models.[77, 154, 239] This is evident from Figure 4.12 where a series of snapshots illustrates the partial layering. Several factors contribute to the formation of partial layers. First, the molecules are large and flexible, and "perfect" layers may not be realistic for molecules of this complexity. Second, the dynamics of layer reorganization is slow and extends beyond the time frame of the simulations. Nonetheless, the molecular cores clearly aggregate into layers with some crossed-core configurations and some parallel cores evident within the layers.

Although the layers tend to align in parallel planes, this is not always the case, as shown by the central panel in Figure 4.12 (b), where the partial layers are oriented in several different directions.

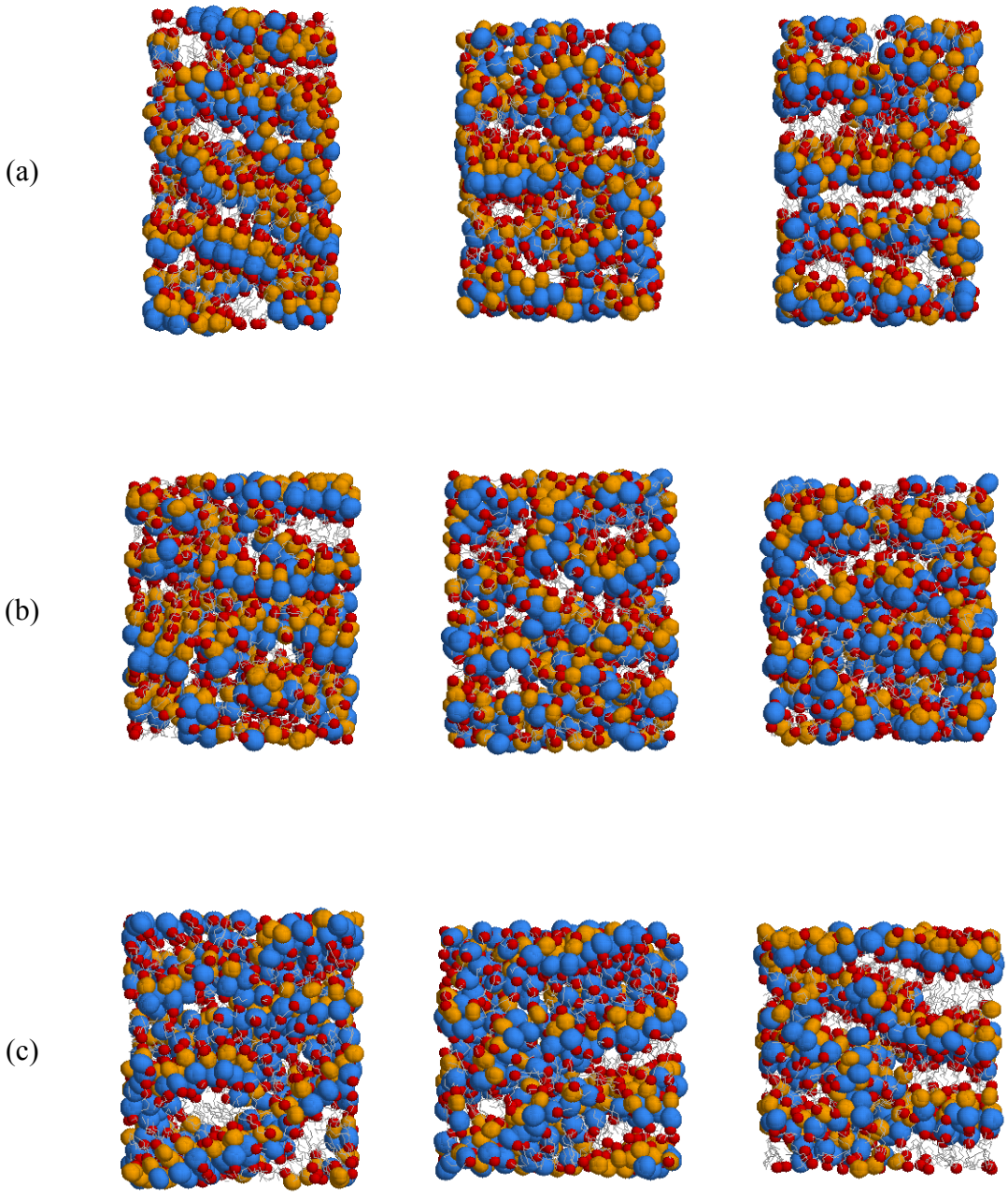

Figure 4.12 Snapshots from the 256 molecule simulations using the B1 model. Snapshots from three independent simulations are shown for (a) 2PhP at 335 K, (b) 2PhP at 365K, and (c) 5PhP at 370K. The alkyl chains are represented as grey lines, and oxygen atoms are shown in red. The phenyl and pyrimidine rings are represented as bulky blue and orange spheres, respectively.

Figures 4.13 and 4.14 present the most important results of this thesis. These figures show the phenyl-phenyl ring distributions in 2PhP and 5PhP, subdivided according to components parallel and perpendicular to the layer normal and the director. From Figure 4.13, the layer normal and the director are not equivalent for 2PhP at 335K and 365K. This is evident from the difference between $g_{\parallel}^{D}(r_{\parallel})$ and $g_{\parallel}^{L}(r_{\parallel})$. At 365K, the latter indicates that the layers are roughly 16 Å apart whereas the former indicates a separation of 20 Å. From these peak positions, I calculate a relative angle of roughly 37 degrees. The peaks, and indeed the curves, coincide at 400K, as expected for a SmA phase, and a layer spacing of 20 Å is predicted. Both $g_{\parallel}^{D}(r_{\parallel})$ and $g_{\parallel}^{L}(r_{\parallel})$ are nearly unity at 450K indicating that the phase is isotropic.

Layer spacing has been measured[26] for 2PhP at several temperatures. The experimental spacing is higher, varying from 24 Å in the SmC phase to 26 Å at the transition to SmA. The calculated values show the correct increase with temperature near the SmC to SmA transition, but they are smaller. This is due, in large part, to some retention of the initial parallel molecular orientation. Specifically, the tails are not of equal length – they are roughly 5 and 10 Å long. An anti-parallel, or randomized, starting configuration is predicted to lead to layer spacing of 21-27 Å in much better agreement with experiment.

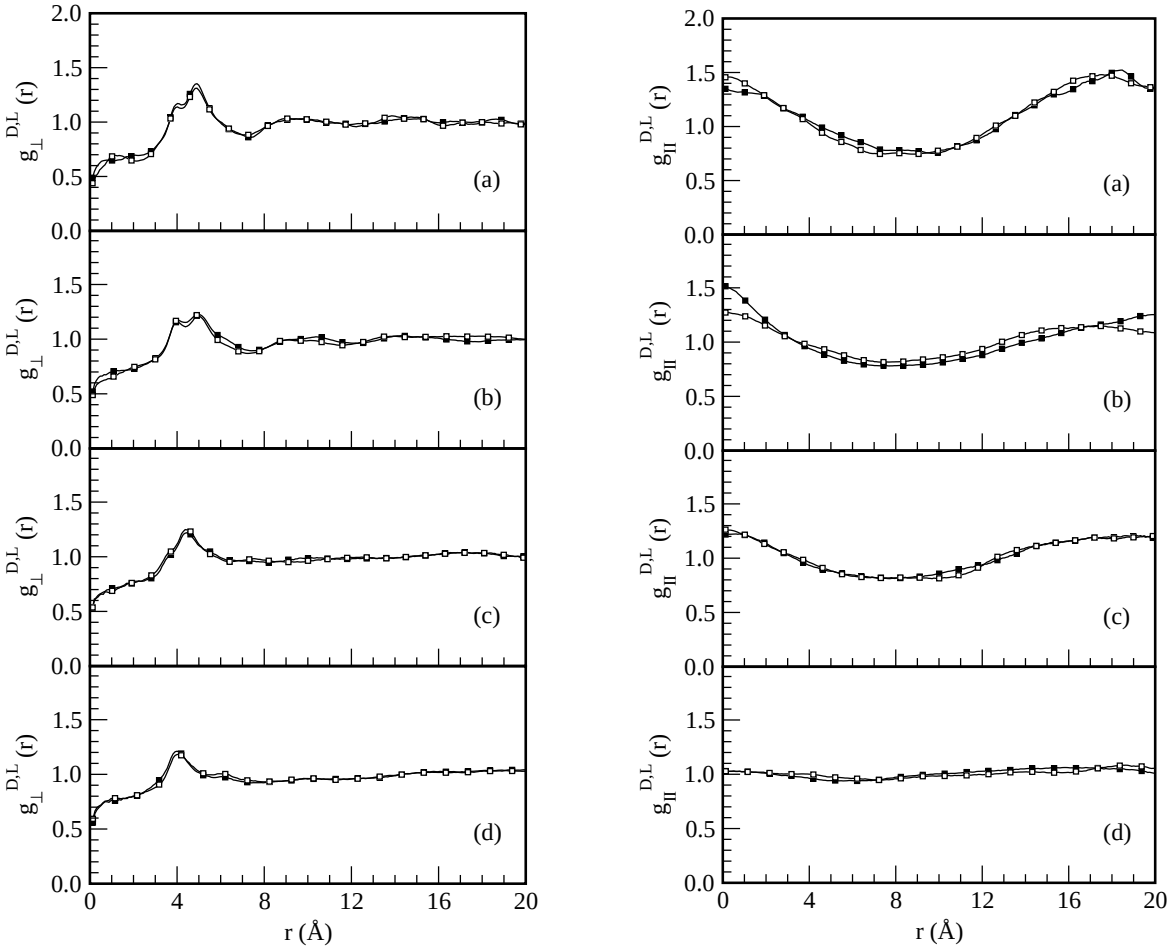

Figure 4.13 The distribution between phenyl rings in 2PhP (B1 ring model) analyzed according to contributions perpendicular and parallel to the director (filled squares) and the layer normal (open squares). Results are shown for 335K (a), 365K (b), 400K (c), and 450K (d).

Figure 4.14 shows that, at all three temperatures, the layer normal and the director are equivalent for 5PhP. As well, the layer spacing is predicted to decrease from 20 Å at 370K to 17 Å at 400K. While experimental layer spacings are not available for comparison, the spacing should decrease slightly with temperature. At 450K, $g_{\parallel}^{D}(r_{\parallel})$ and $g_{\parallel}^{L}(r_{\parallel})$ are nearly unity and 5PhP is correctly predicted to be isotropic.

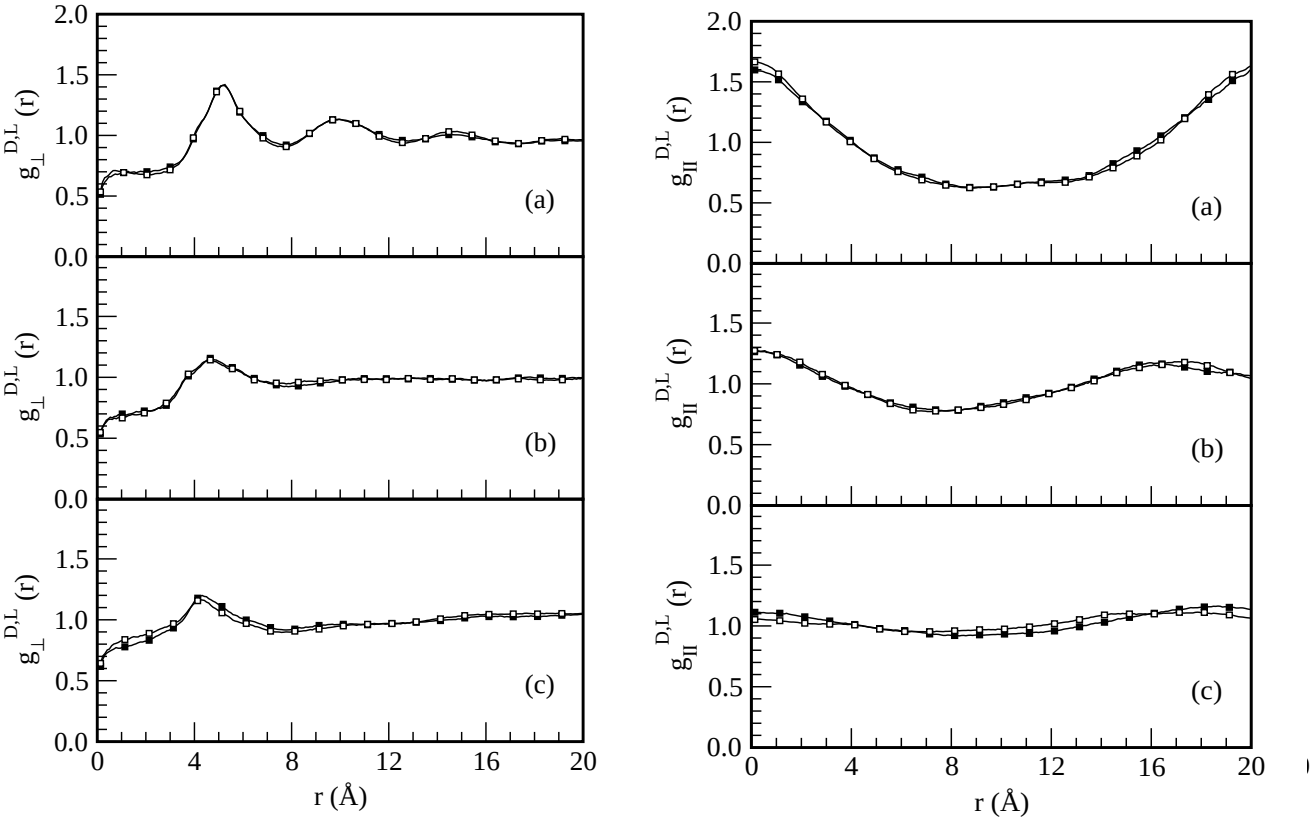

Figure 4.14 The distribution between phenyl rings in 5PhP (B1 ring model) analyzed according to contributions perpendicular and parallel to the director (filled squares) and the layer normal (open squares). Results are shown for 370K (a), 400K (b), and 450K (c).

A corresponding analysis of the 2PhP and 5PhP phases predicted from the C1 ring model shows that only SmA phases are predicted at all temperatures. This model clearly does not provide a satisfactory representation of 2PhP or 5PhP. Thus, the presence of the ring quadrupole is necessary to produce a SmC phase and to encourage a transition to an isotropic fluid. My simulations indicate that differences in the phase sequences of 2PhP and 5PhP are due to both the phenyl-pyrimidine torsion and to the ring quadrupole. Together these two factors lead to substantially lower pair energies for crossed-core pairs of 2PhP molecules but only modestly lower energies for 5PhP pairs.

Returning to the phase diagrams in Figure 1.6, both 2PhP and 5PhP are predicted to be isotropic at 400K. Clearly, the multi-site coarse-grained model has extended the SmA range to higher temperatures. In addition, the SmC phase is not expected beyond 358K for 2PhP although my model predicts this phase at 365K. Despite these differences, the tentative recovery of the proper phases for two structurally similar mesogens is very encouraging. Further model refinements may lead to better agreement with experiment.

4.4.6 Dynamics

Longer 8-14 ns simulations were performed for the B1 and C1 ring models of 2PhP at 365K and 5PhP at 370K. These simulations provide some indication of the time scale for layer reorganization. Figure 4.15 shows the instantaneous variations in the density, the P_2 order parameter for the director and the layer normal, and the P_2 order parameter for the C(1)-C(2) and C(15)-C(16) bonds in the alkoxy tails. The variation in the θ_1 and θ_2 angles, calculated from Equations (2.51) and (2.52), is also shown.

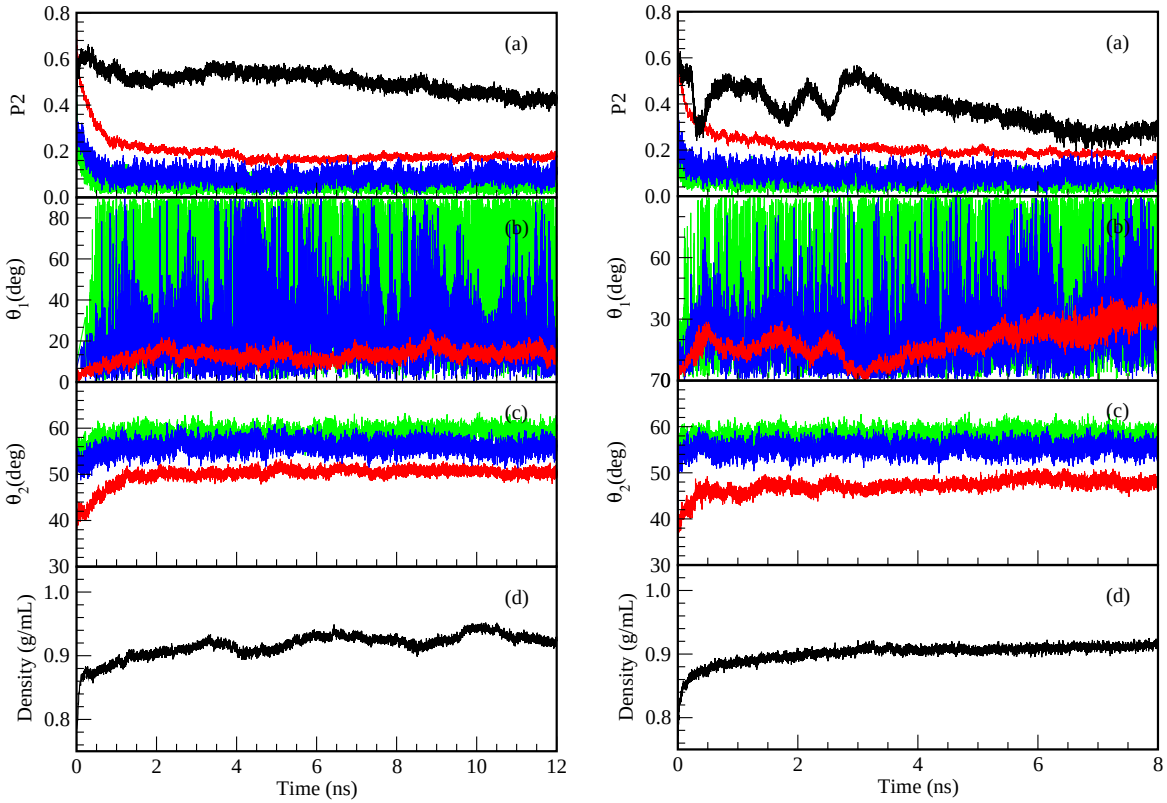

Figure 4.15 Instantaneous fluctuations for 2PhP at 365K (left) and 5PhP at 370K (right), as represented by the B1 model. Red, blue, and green pertain to the phenyl-pyrimidine, C(1)-C(2), and C(15)-C(16) vectors in the molecule, respectively. In (a), the P_2 order parameter describing the consistency between local (molecular) layers normal is shown in black. Fluctuations in the order parameter associated with each of the vectors are shown in (a). The angles θ_1 and θ_2, evaluated from Equations (2.51) and (2.52), are given in (b) and (c). Fluctuations in the density are shown in (d).

The uppermost panel in Figure 4.15 shows the P_2 order parameter for the layer normal, the director, and the C(1)-C(2) and C(15)-C(16) bonds in the alkoxy tails. The

order is consistently near zero for the alkoxy tails and generally higher for the layer normal than for the director.

The angle between the global layer normal, obtained from the average over all local layers normal, and the global director is captured by θ_1. Since this angle is measured based only on global vectors, all local contributions are averaged out, but contributions from imperfect layering will be observed. This angle has been calculated for the director and the alkoxy tail vectors C(1)-C(2) and C(15)-C(16). As one might expect from Figure 4.15 (b), the angle between the layer normal and the tail vectors oscillates rapidly between zero and ninety degrees. This indicates that the ends of the alkoxy tails are mostly uncorrelated with the layering in the core region. The oscillations are somewhat larger for C(15)-C(16) since these atoms are further removed from the molecular core. The correlation between the director and the layer normal is, by contrast, evident in Figure 4.15 (b). The average angle fluctuates between 0 and 30 degrees for 5PhP but is stable and less than 10 degrees for 2PhP.

A local picture of molecular orientation is provided by the angle between the local layer normal and the local director. The average of these angles is captured by θ_2 in Figure 4.15 (c). This angle is also calculated for the alkoxy tails, relative to the local layer normal, and the results show an average of 55-60 degrees. As discussed below Equation (2.52), if the tail orientations are uncorrelated with the local layer normal, an average angle of 57.3 degrees is expected. This is clearly the case for C(15)-C(16) and nearly true for C(1)-C(2). This indicates, once again, that the alkoxy tail region is isotropic. For the local director, defined by the phenyl-pyrimidine axis, a correlation with the local layer

normal is evident from the deviation from 57.3 degrees. Differences between 5PhP and 2PhP are evident but relatively small.

Correlations between the panels are evident and transition regions, such as the dip in both the order parameter and instantaneous density at 4 ns for the 2PhP at 365K, provide a rough measure of the time frame for layer reorganization. This is only a rough guide however.

Table 4.3 provides average angles, average densities, and average order parameters with the quantities obtained by accumulating instantaneous values over multiple 2 ns simulations. As expected, the density decreases with temperature. The results predicted from the C1 ring model indicate that the layer normal and the director are, within statistics, indistinguishable at all temperatures. The simulations also show that the C1 ring model predicts SmA phases at all temperatures although, at 450K, independent simulations for this model show very different order parameters. This signals that the transition from SmA to isotropic is occurring although the true fluids are isotropic at much lower temperatures. Between quadrupolar ring models, differences in order parameters and angles are less predictable. In my experience, the independent simulations are fairly distinct and the dynamics are slow for the A1 ring model. I suspect that the ring quadrupole is too large for this model. The properties evaluated from the B1 and B2 ring models are similar in most respects.

Table 4.3 Average tilt angles, in degrees, P_2 order parameters for the director and the layer normal, and the average density, in g/mL. Results are reported for the averages over for 5PhP at 370K and 2PhP at 335K and 365K. The angles θ_1 and θ_2 are evaluated from Equations (2.51) and (2.52), respectively. The properties for 2PhP at 335K and 365K and 5PhP at 370K represent averages over five independent 2 ns simulations. Properties at 400K are obtained from averages over three 2 ns simulations while 450K properties are obtained from averages over two 2 ns simulations.

Property	**2PhP results for each ring model**				**5PhP results for each ring model**			
	A1	**B1**	**B2**	**C1**	**A1**	**B1**	**B2**	**C1**
	335K							
θ_1 (degrees)	11	7	7	8				
θ_2 (degrees)	48	44	46	43				
P_2^D	0.21	0.33	0.27	0.44				
P_2^L	0.50	0.55	0.55	0.47				
<ρ> (g/mL)	0.89	0.92	0.91	0.89				
	365K				***370K***			
θ_1 (degrees)	12	9	12	7	14	14	15	10
θ_2 (degrees)	49	46	46	42	46	45	46	43
P_2^D	0.17	0.26	0.23	0.43	0.23	0.31	0.26	0.51
P_2^L	0.45	0.52	0.50	0.49	0.39	0.42	0.41	0.48
<ρ> (g/mL)	0.89	0.90	0.90	0.89	0.89	0.89	0.89	0.87
	400K				***400K***			
θ_1 (degrees)		8		4		11		17
θ_2 (degrees)		49		43		48		46
P_2^D		0.19		0.45		0.20		0.31
P_2^L		0.51		0.53		0.45		0.33
<ρ> (g/mL)		0.89		0.88		0.88		0.86
	450K				***450K***			
θ_1 (degrees)		23		8		32		10
θ_2 (degrees)		52		49		52		44
P_2^D		0.12		0.36		0.12		0.51
P_2^L		0.34		0.34		0.30		0.49
<ρ> (g/mL)		0.87		0.85		0.86		0.84

4.5 Conclusions

In this section, the phases of 2PhP and 5PhP are examined in detail. Molecular dynamics simulations form the basis of the analysis, with Ewald summations for the electrostatics, anisotropic changes in the cell shape and size, and multiple thermostats for translation and rotation. 2PhP is explored at 335K, 365K, 400K, and 450K. Over this temperature range, this mesogen forms SmC, SmA, nematic, and isotropic phases. A closely related mesogen, 5PhP, is also examined at several temperatures. Specifically, I examine the fluid at 370K, 400K, and 450K where SmA and isotropic phases are expected. A comparison of 5PhP and 2PhP is interesting since these two molecules are structurally very similar, with the most notable difference being a preference for planarity in the molecular core of 2PhP while 5PhP adopts a twisted core conformation due to steric constraints.

The essential results of this thesis can be summarized as follows. First, the presence of ring quadrupoles is essential to reproducing the phase behaviour of, and differences between, 2PhP and 5PhP. Without ring quadrupoles, only SmA phases occur and they persist to high temperatures where the true fluids are isotropic. Studies of pair energies indicate that the quadrupoles lead to energetically favoured crossed-core configurations but that the energy lowering is more significant for 2PhP. Simulations of the mesogens indicate that the tail regions are less structured, showing distributions consistent with isotropic fluids, and have no long-ranged order even when the cores are ordered. The simulations tentatively reveal that 2PhP has a SmC phase at the lower temperatures, where the layer normal and the director do not coincide, while 5PhP shows

only equivalence between these two quantities. Thus, the simulations capture the difference between 2PhP and 5PhP, which is ultimately attributable to the interactions from the ring quadrupoles and the difference in the relative orientations of the phenyl and pyrimidine rings. The apparition of the SmC phase, for the 2PhP mesogen at 365K, is the result of stronger core-core interactions, in which the quadrupole plays an important role. A closer exploration of the differences between the layer normal and the director reveals that, at a local level, differences are significant regardless of the phase.

The most relevant results of this thesis are obtained from averages over multiple 2 ns simulations. For liquid crystal simulations, these are considered quite short in duration. However, the fast transition from the initial nematic configuration renders this approach feasible. For the present study, the use of multiple simulations provides an exceedingly simple means of exploring the fluids without the need for prohibitively long simulations. A better approach is required in general but I note that simple annealing will not be helpful since any transition to an isotropic fluid will be irreversible on the time scale of the simulation. Clearly, algorithms that encourage partial loss of order, without the entanglement that occurs in the isotropic fluid, will improve the applicability of simulations to complex ordered fluids.

Phase characterization is challenging for 2PhP and 5PhP. In particular, the evaluation of order parameters is not straightforward. The director, in the present study, is determined from the phenyl-pyrimidine axis but, when crossed configurations become energetically favourable, this order parameter will necessarily decrease – there is less consistency between the molecules. The layer normal is also somewhat difficult to

calculate when the molecules are complex. The current approach of defining a set of neighbours, fitting a plane to their positions, and identifying the vector normal to the plane works well in general. The method is reasonably straightforward but does rely on the definition of a cutoff, beyond which molecules are not considered to be neighbours. The angle between the layer normal and the director is central to the characterization of the layered phase as either SmC or SmA. I have examined two definitions, shown in Equations (2.51) and (2.52), but each has advantages and drawbacks. However, the "local" angle from Equation (2.52) is relevant to the ideas of de Vries. In the end, analysis of the intermolecular structure parallel and perpendicular to the director and the layer normal proved to be more useful in terms of identifying the layered phases.

Chapter 5

Conclusions and Outlook

The main objective of this thesis is to examine, by means of molecular dynamics simulations, the phase characteristics of 2PhP and 5PhP. 2PhP and 5PhP display different phase sequences (Figure 1.6), despite having very similar molecular structures. In particular, the phase diagram of 2PhP is characterized by an extensive temperature range for the SmC phase, a large SmA phase, and a very narrow nematic phase. On the other hand, 5PhP only shows a SmA phase between the isotropic and crystalline phases. Both mesogens consist of joined phenyl and pyrimidine rings, and beyond the core, oxygen atoms connect to flexible hydrocarbon tails (Figure 3.2). In fact, the structures of the two molecules differ only in the connection point between the two rings. In order to capture the phase differences of 2PhP and 5PhP, it is important to derive realistic, feasible models for the two mesogens.

The methodology for the construction and validation of a force field suitable for liquid crystal molecules is presented in Chapter 3. Multi-site coarse-grained models offer many advantages over atomistic and fully coarse-grained models. Specifically, they can be easily adapted to include ring quadrupoles while capturing molecular flexibility and remaining computationally feasible. The multi-site coarse-grained model developed in this thesis represents the phenyl and pyrimidine rings as soft quadrupolar ellipsoids (*i.e.*

quadrupolar GB sites), while the flexible hydrocarbon chains and the oxygen atoms are given united atom representations (*i.e.* LJ sites). Model development is divided into two parts. First, *ab initio* studies of 2PhP and 5PhP yield intramolecular potentials and atomic charges. Second, a careful procedure for the development of ring models, starting with comparison to *ab initio* potentials for benzene dimers, is undertaken.

A comprehensive series of *ab initio* full and constrained geometry optimizations have been performed to examine the structure and flexibility of 2PhP and 5PhP mesogens. Torsional and bending motions within the models are fully represented, including the inter-ring torsion and the flexibility of the alkoxy end group. These are used in the development of the molecular models. Specifically, the inter-ring torsion is essential in order to understand the phenyl-pyrimidine relative orientations, and the phase difference between 2PhP and 5PhP is certainly strongly connected to the different preferences. The ring models for phenyl and pyrimidine are very similar, but not identical since the rings bear some charges, as calculated from the CHELPG algorithm applied to the global energy minimum. Between 2PhP and 5PhP, the cores differ in the ring charges, in the inter-ring torsions, and in all other intramolecular degrees of freedom.

A systematic approach to the determination of optimal GB parameters has been adopted for the aromatic rings of 2PhP and 5PhP. Importantly, quadrupole moments are embedded within the rings in order to account for the quadrupole that arises from the π electron clouds above and below the plane of the rings, and full multipolar interactions are included in the simulations. First, I optimized the potential parameters for benzene, based on comparison with *ab initio* potential energy curves[180, 181] for benzene dimers, and

by comparison with experimental distribution function and self-diffusion coefficients[185, 188, 189, 199] of bulk benzene. Then, I have proceeded to analyze the validity of the ring model for biphenyl.

As a start, the parameters of the GB potential have been fitted to reproduce *ab initio* pair interaction energies[180, 181] for the sandwich, T-shaped, and parallel-displaced configurations of the benzene dimers. Although simulations of liquid benzene, by means of using this ring model, yield radial distribution functions in reasonable agreement with published theoretical curves,[191-194] a closer inspection of snapshots reveals the presence of holes in the simulation cell. Clearly this model, although providing a very accurate representation of gas phase benzene dimers, does not provide a good representation for benzene *in the bulk*. Thus, I assume that the pair potentials are roughly correct representations of the *effective* pair potentials and adjust the ring parameters accordingly. In total, 6561 parameter sets have been examined, and based on comparison to experimental radial distributions and diffusion coefficients of bulk liquid benzene, six models have been chosen for further consideration. MD simulations of liquid biphenyl using these six ring models have been performed and, based on diffusion coefficients, I have eliminated two ring models. The four remaining ring models, being termed as A1, B1, B2, and C1, have been examined in detail. Models B1 and C1 are identical except for the ring quadrupole, with the latter model not having a quadrupole. Likewise, models A1 and B2 are related in that the ring quadrupole value of B2 model is 80% of the value of A1 model. Models B1 and B2 have identical quadrupole moments but differ in their GB parameters. The current models for 2PhP and 5PhP underestimate the differences

between the phenyl and pyrimidine rings, since identical GB parameters are used to represent both rings. Parameterisation of a ring model for pyrimidine is an obvious route to improvement of the molecular model. Less obvious, but possibly equally important, is the inclusion of in-the-plane ring quadrupoles.

In Chapter 4, extensive molecular dynamics simulations of 2PhP and 5PhP mesogens are conducted for the A1, B1, B2, and C1 ring models. 2PhP is examined at four temperatures (335K, 365K, 400K, and 450K) which correspond to temperature ranges for SmC, SmA, nematic, and isotropic phases. 5PhP is examined at three temperatures (370K, 400K, and 450K), where SmA and isotropic phases are experimentally observed. My simulations correctly suggest phases in agreement with experiment: SmC phase at 365K and SmA phases at 400K and 450K for 2PhP, and only a SmA phases for 5PhP regardless of the temperature considered.

Simulations of smectic phases are challenging due to many factors. First of all, simulations of smectogens cannot adequately represent a layered phase unless a minimum of a few hundred molecules are present in the cell. Moreover, the computational costs increase as the molecular representation gets more sophisticated. Generally, longer simulations (tens of nanoseconds) are needed for the equilibration of layered smectic phases as the dynamics slow down due to entanglement of complex and flexible molecules. From my studies, it is evident that the use of multiple short simulations is a simpler way to explore the liquid crystal phases although a greater number of simulations would be necessary for a full convergence of the fluid properties.

Analyzing the interactions between pairs of molecules, by means of performing "docking" studies, I learned that within the simulations parallel and anti-parallel arrangements may be entropically favored but, for the quadrupolar models, energetics favor crossed arrangements. Examining the smectic layers of the two mesogens, I find that intermolecular structure within the layers is complex, with parallel and crossed arrangements appearing for 2PhP and 5PhP.

One of the most important findings of this thesis is that the presence of ring quadrupole is essential for reproducing the phase behavior as well as the differences between the two mesogens. Specifically, my results illustrate the importance of explicitly considering the quadrupolar moment embedded into each ring to properly represent the phases. In the absence of ring quadrupoles, only SmA phases occur for both 2PhP and 5PhP mesogens at all the temperatures considered. Furthermore, the magnitude of the quadrupole is also an important factor to consider. In this regard, the quadrupole embedded into the A1 ring model is too large, so that the dynamics are very slow and layer frustration is increased. Moreover, the B1 and B2 ring models with similar quadrupoles attached give rise to similar fluid properties in most regards.

Chiral doped liquid crystals, obtained by doping a chiral guest into an achiral liquid crystal host or mixture of hosts, have many properties of interest for display applications.[15, 218, 219] For instance, the design of electroclinic SmA* materials as well as of ferroelectric SmC* liquid crystals with large spontaneous polarization power suitable for device applications has attracted great interest in the last decades. A range of chiral dopants have been considered, including the two dopants (*i.e.* Spiro and Dop5X-NO_2) for

which appropriate representations have been modeled in this thesis via extensive series of *ab initio* calculations. It has been experimentally confirmed that it is possible to rationally design achiral additives capable of amplifying the polarization power exerted by a chiral dopant in a SmC host. For instance, chiral perturbation induced by a dopant propagates more effectively on the 2PhP host in the presence of the 5PhP as co-host, due to its twisted chiral core conformation. As future work, simulations of host-dopant mixtures in the SmC temperature range as well as host - co-host - dopant mixtures in the SmC and SmA temperature ranges will allow the investigation of the relationship between the molecular structure of host - dopant or host - co-host – dopant on the magnitude of induced property. Finally, the impact of different chiral guests on the achiral liquid crystal host(s), as a function of the ratio between guest and host(s) concentrations, can be studied by means of computer simulations.

The development of ferroelectric liquid crystals for device applications can be experimentally pursued by designing efficient chiral dopants that can be added to modify the properties of an existing mesophase. However, this is a time-consuming process and may involve difficult syntheses or expensive starting materials. It is here that computer simulations can play an important role, as a complementary technique, for improving the understanding of behaviours, which are not fully accessible to experimental investigation.

Bibliography

(1) Sluckin, T. J.; Dunmur, D. A.; Stegemeyer, H. *Crystals that Flow: classic papers from the history of liquid crystals*; Taylor and Francis: London, UK, 2004.
(2) Demus, D. In *Topics in Physical Chemistry: Liquid Crystals*; Stegemeyer, H., Ed.; Springer, New York: Steinkopft Darmstadt, 1994; Vol. 3, pp 1.
(3) Friedel, M. G. *Annales de Physique B1* **1922**, *18*, 273.
(4) Stegemeyer, H. *Liquid Crystals*; Steinkopff: Darmstadt, 1994, pp 1.
(5) http://nobelprize.org/nobel_prizes/physics/laureates/1991/index.html, 1991; last accessed May 18, 2009.
(6) Biscari, P.; Peroli, G. G.; Sluckin, T. J. *Molecular Crystals and Liquid Crystals* **1997**, *292*, 91.
(7) Collings, P. J. *Liquid Crystals: nature's delicate phase of matter*; Princeton University Press: Princeton, New Jersey, 1990.
(8) Andersson, G.; Dahl, I.; Kuczynski, W.; Lagerwall, S. T.; Skarp, K.; Stebler, B. *Ferroelectrics* **1988**, *84*, 285.
(9) Bahadur, B. *Liquid Crystals: Applications and Uses*; World Scientific: Singapore, 1991.
(10) Jun, S.S., Samsung Electronics Co. Ltd. : Koreea, 2009; Vol. United States Patent 7495732
(11) Seddon, J. M.; Templerin, R. H. *Handbook of Biological Physics*; Elsevier: Amsterdam, 1995.
(12) Chandrasekhar, S.; Sadashiva, B. K.; Suresh, K. A. *Pramana* **1977**, *9*, 471.
(13) Reddy, R. A.; Tschierske, C. *Journal of Materials Chemistry* **2006**, *16*, 906.
(14) Barón, M. *Pure and Applied Chemistry* **2001**, *73*, 845.
(15) Woltman, S. J.; Jay, D. G.; Crawford, P. G. *Liquid Crystals: Frontiers in Biomedical Applications*, First ed.; World Scientific: Singapore, 2007.
(16) Guillon, D. In *Advances in Liquid Crystals: A Special Volume of Advances in Chemical Physics, Vol. 113*; Vij, J. K., Ed.; John Wiley & Sons Inc., 2000, pp 1.
(17) Kitzerow, H. S.; Bahr, C. *Chirality in Liquid Crystals*; Springer-Verlag: New York, 2001.
(18) Peltz, G.; Diele, S.; Weissflog, W. *Advanced Materials* **1999**, *11*, 707.
(19) Madhusudana, N. V. *Brazilian Journal of Physics [online]. 1998, vol.28, n.4; last accessed May 14 2009; ISSN 0103-9733. doi: 10.1590/S0103-97331998000400006., Available from: <http://www.scielo.br/scielo.php?script=sci_arttext&pid=S0103-97331998000400006&lng=en&nrm=iso>*.
(20) Care, C. M.; Cleaver, D. J. *Reports on Progress in Physics* **2005**, *68*, 2665.
(21) Berardi, R.; Muccioli, L.; Zannoni, C. *Chemphyschem* **2004**, *5*, 104.
(22) McBride, C.; Wilson, M. R.; Howard, J. A. K. *Molecular Physics* **1998**, *93*, 955.
(23) Feringa, B. M.; Eelkema, R. *Organic & Biomolecular Chemistry* **2006**, *4*, 3729.
(24) Vizitiu, D.; Halden, B. J.; Lemieux, R. P. *Chemical Communications* **1997**, 1123.
(25) Vizitiu, D.; Lazar, C.; Halden, B. J.; Lemieux, R. P. *Journal of the American Chemical Society* **1999**, *121*, 8229.
(26) Hartley, C. S.; Kapernaum, N.; Roberts, J. C.; Giesselmann, F.; Lemieux, R. P. *Journal of Materials Chemistry* **2006**, *16*, 2329.
(27) Stegemeyer, H.; Meister, R.; Hoffmann, U.; Sprick, A.; Becker, A. *Journal of Materials Chemistry* **1995**, *5*, 2183.

(28) Lemieux, R. P. *Accounts of Chemical Research* **2001**, *34*, 845.
(29) Hegmann, T.; Meadows, M. R.; Wand, M. D.; Lemieux, R. P. *Journal of Materials Chemistry* **2003**, *14*, 1.
(30) Hartley, C. S.; Lemieux, R. P. *Liquid Crystals* **2004**, *31*, 1101.
(31) Boulton, C. J.; Sutherland, J. J.; Lemieux, R. P. *Journal of Materials Chemistry* **2003**, *13*, 644.
(32) Boulton, C. J.; Finden, J. G.; Yuh, E.; Sutherland, J. J.; Wand, M. D.; Wu, G.; Lemieux, R. P. *Journal of the American Chemical Society* **2005**, *127*, 13656.
(33) Lebwohl, P. A.; Lasher, G. *Physical Review A* **1972**, *6*, 426.
(34) Talbot, J.; Kivelson, D.; Allen, M. P.; Evans, G. T.; Frenkel, D. *Journal of Chemical Physics* **1990**, *92*, 3048.
(35) McGrother, S. C.; Williamson, D. C.; Jackson, G. *Journal of Chemical Physics* **1996**, *104*, 6755.
(36) Veerman, J. A. C.; Frenkel, D. *Physical Review A* **1996**, *41*, 3237.
(37) Vieillard-Baron, J. *Molecular Physics* **1974**, *28*, 809.
(38) Gay, J. G.; Berne, B. J. *Journal of Chemical Physics* **1981**, *74*, 3316.
(39) Lennard-Jones, J. E. *Proceedings of the Royal Society of London Series A* **1924**, *106*, 463.
(40) Allen, M. P.; Warren, M. A.; Wilson, M. R.; Sauron, A.; Smith, W. *Journal of Chemical Physics* **1996**, *105*, 2850.
(41) Phuong, N. H.; Germano, G.; Schmid, F. *Journal of Chemical Physics* **2001**, *115*, 7227.
(42) Cuetos, A.; Ilnytskyi, J. M.; Wilson, M. R. *Molecular Physics* **2002**, *100*, 3839.
(43) Allen, M. P. *Physical Review E* **1993**, *47*, 4611.
(44) Cook, M. J.; Wilson, M. R. *Journal of Chemical Physics* **2000**, *116*, 1560.
(45) Earl, D. J.; Wilson, M. R. *Journal of Chemical Physics* **2004**, *120*, 9679.
(46) Germano, G.; Allen, M. P.; Masters, A. J. *Journal of Chemical Physics* **2002**, *116*, 9422.
(47) Berne, B. J.; Pechukas, P. *Journal of Chemical Physics* **1972**, *56*, 4213.
(48) Luckhurst, G. R. *Liquid Crystals* **2005**, *32*, 1335.
(49) Bates, M. A.; Luckhurst, G. R. *Journal of Chemical Physics* **1999**, *110*, 7087.
(50) Zannoni, C. *Journal of Materials Chemistry* **2001**, *11*, 2637.
(51) Adams, D. J.; Luckhurst, G. R.; Phippen, R. W. *Molecular Physics* **1987**, *61*, 1575.
(52) Luckhurst, G. R.; Stephens, R. A.; Phippen, R. W. *Liquid Crystals* **1990**, *8*, 451.
(53) Berardi, R.; Emerson, A. P. J.; Zannoni, C. *Journal of the Chemical Society-Faraday Transactions* **1993**, *89*, 4069.
(54) Luckhurst, G. R.; Simmonds, P. S. J. *Molecular Physics* **1993**, *80*, 233.
(55) Berardi, R.; Fava, C.; Zannoni, C. *Chemical Physics Letters* **1995**, *236*, 462.
(56) Cleaver, D. J.; Care, C. M.; Allen, M. P.; Neal, M. P. *Physical Review E* **1996**, *54*, 559.
(57) Berardi, R.; Fava, C.; Zannoni, C. *Chemical Physics Letters* **1998**, *297*, 8.
(58) Peláez, J.; Wilson, M. R. *Physical Chemistry Chemical Physics* **2007**, *9*, 2968.
(59) Cacelli, I.; Prampolini, G.; Tani, A. *Journal of Physical Chemistry B* **2005**, *109*, 3531.
(60) Ilnytskyi, J. M.; Wilson, M. R. *Computer Physics Communications* **2001**, *134*, 23.
(61) Ilnytskyi, J. M.; Wilson, M. R. *Computer Physics Communications* **2002**, *148*, 43.
(62) Wilson, M. R.; Allen, M. P.; Warren, M. A.; Sauron, A.; Smith, W. *Journal of Computational Chemistry* **1997**, *18*, 478.
(63) Proccaci, P.; Marchi, M. In *Advances in the Computer Simulations of Liquid Crystals*; Pasini, P., Zannoni, C., Ed.; Kluwer Academic Publishers: Dordrecht, 2000; Vol. 545, pp 333.
(64) Ewald, P. P. *Annalen Der Physik* **1921**, *64*, 253.
(65) McDonald, A. J.; Hanna, S. *Journal of Chemical Physics* **2006**, *124*, 164906.

(66) Babadi, M.; Everaers, R.; Ejtehadi, M. R. *Journal of Chemical Physics* **2006**, *124*, 174708.
(67) Izvekov, S.; Violi, A.; Voth, G. A. *Journal of Physical Chemistry B* **2005**, *109*, 17019.
(68) Cross, C. W.; Fung, B. M. *Journal of Chemical Physics* **1994**, *101*, 6839.
(69) Cacelli, I.; Cinacchi, G.; Geloni, C.; Prampolini, G.; Tani, A. *Molecular Crystals and Liquid Crystals* **2003**, *395*, 171.
(70) McBride, C.; Wilson, M. R. *Molecular Physics* **1999**, *97*, 511.
(71) LaPenna, G.; Catalano, D.; Veracini, C. A. *Journal of Chemical Physics* **1996**, *105*, 7097.
(72) Stimson, L. M.; Wilson, M. R. *Journal of Chemical Physics* **2005**, *123*, 034908.
(73) Ilnytskyi, J. M.; Neher, D. *Journal of Chemical Physics* **2007**, *126*, 174905.
(74) Wilson, M. R.; Ilnytskyi, J. M.; Stimson, L. M. *Journal of Chemical Physics* **2003**, *119*, 3509.
(75) Hughes, Z. E.; Wilson, M. R.; Stimson, L. M. *Soft Matter* **2005**, *1*, 436.
(76) Wilson, M. R.; Stimson, L. M.; Ilnytskyi, J. M. *Liquid Crystals* **2006**, *33*, 1167.
(77) Maiti, P. K.; Lansac, Y.; Glaser, M. A.; Clark, N. A. *Physical Review Letters* **2004**, *92*, 025501.
(78) Somoza, A. M.; Tarazona, P. *Physical Review Letters* **1988**, *61*, 2566.
(79) Wulf, A. *Physical Review A* **1975**, *11*, 365.
(80) Bartolino, R.; Doucet, J.; Durand, G. *Annales de Physique (Paris)* **1978**, *3*, 389.
(81) Guillon, D.; Skoulios, A. *Journal de Physique (Paris)* **1977**, *38*, 79.
(82) Maiti, P. K.; Lansac, Y.; Glaser, M. A.; Clark, N. A.; Rouault, Y. *Langmuir* **2002**, *18*, 1908.
(83) Jang, W. G.; Glaser, M. A.; Park, C. S.; Kim, K. H.; Lansac, Y.; Clark, N. A. *Physical Review E* **2001**, *64*, 051712.
(84) McMillan, W. L. *Phyical Review A* **1973**, *8*, 1921.
(85) Cabib, D.; Benguigui, L. *Journal de Physique (Paris)* **1977**, *38*, 419.
(86) Meyer, R. J.; McMillan, W. L. *Physical Review A* **1974**, *9*, 899.
(87) Goodby, J. W.; Gray, G. W.; McDonnell, D. G. *Molecular Crystals and Liquid Crystals Letter* **1977**, *34*, 183.
(88) De Jeu, W. H. *Journal de Physique (Paris)* **1977**, *38*, 1265.
(89) Houssa, M.; McGrother, S. C.; Rull, L. F. *Computer Physics Communications* **1999**, *122*, 259.
(90) Houssa, M.; Rull, L. F.; McGrother, S. C. *Journal of Chemical Physics* **1998**, *109*, 9529.
(91) Satoh, K.; Mita, S.; Kondo, S. *Liquid Crystals* **1996**, *20*, 757.
(92) Satoh, K.; Mita, S.; Kondo, S. *Chemical Physics Letters* **1996**, *255*, 99.
(93) Goossens, W. J. A. *Europhysics Lettters* **1987**, *3*, 341.
(94) Poniewierski, A.; Sluckin, T. J. *Molecular Physics* **1991**, *73*.
(95) Neal, M. P.; Parker, A. J. *Chemical Physics Letters* **1998**, *294*, 277.
(96) Neal, M. P.; Parker, A. J. *Molecular Crystals and Liquid Crystals* **1999**, *330*, 1809.
(97) Neal, M. P.; Parker, A. J. *Physical Review E* **2001**, *63*, 011706.
(98) Taylor, T. R.; Arora, S. L.; Fergason, J. L. *Physical Review Letters* **1970**, *25*, 722.
(99) Osipov, M. A.; Gorkunov, M. V.; Gleeson, H. F.; Jaradat, S. *The European Physical Journal E* **2008**, *26*, 395.
(100) De Vries, A. *Molecular Crystals and Liquid Crystals* **1970**, *11*, 361.
(101) De Vries, A. *Molecular Crystals and Liquid Crystals Letters* **1977**, *41*, 27.
(102) De Vries, A. *Journal of Chemical Physics* **1979**, *71*, 25.
(103) De Vries, A.; Ekachai, A.; Spielberg, N. *Molecular Crystals and Liquid Crystals Letters* **1979**, *49*, 143.

(104) Leadbetter, A. J.; Norris, E. K. *Molecular Physics* **1979**, *38*, 669.
(105) Hohenberg, P.; Kohn, W. *Physical Review* **1964**, *136*, B864.
(106) Kohn, W.; Sham, L. J. *Physical Review* **1965**, *140*, A1133.
(107) Levine, I. N. *Quantum Chemistry*, Fifth ed.; Prentice-Hall Inc.: New York, 2000.
(108) Bartlett, R. J. *Annual Review of Physical Chemistry* **1981**, *32*, 359.
(109) Bartlett, R. J. *Journal of Physical Chemistry* **1989**, *93*, 1697.
(110) Ramachandran, K. I.; Deepa, G.; Namboori, K. *Computational Chemistry and Molecular Modeling: Principles and Applications*; Springer-Verlag: Berlin Heidelberg, 2008.
(111) http://nobelprize.org/nobel_prizes/chemistry/laureates/1998/index.html; last accessed May 2, 2008.
(112) Perdew, J. P.; Kurth, S. In *A Primer in Density Functional Theory*; Fiolhais, C., Nogueira, F., Marques, M. A. L., Eds.; Springer: Berlin, 2003.
(113) Becke, A. D. *Journal of Chemical Physics* **1993**, *98*, 5648.
(114) Perdew, J. P.; Schmidt, K. In *Density Functional Theory and Its Application to Materials*; Van Doren, V., Van Alsenoy, C., Geerlings, P., Eds.; AIP: New York, 2001, pp 1.
(115) Kümmel, S.; Kronik, L. *Reviews of Modern Physics* **2008**, *80*, 3.
(116) Ditchfield, R.; Hehre, W. J.; Pople, J. A. *Journal of Chemical Physics* **1971**, *54*, 724.
(117) Alder, B. J.; Wainwright, T. E. *Journal of Chemical Physics* **1957**, *27*, 1208.
(118) Alder, B. J.; Wainwright, T. E. *Journal of Chemical Physics* **1959**, *31*, 459.
(119) Allen, M. P., Tildesley, D. J. *Computer Simulation of Liquids*; Oxford University Press: New York, 1994.
(120) Frenkel, D., Smit, B. *Understanding Molecular Simulation: From Algorithms to Applications*, First ed.; Academic Press: San Diego, 1996.
(121) Andersen, H. C. *Journal of Chemical Physics* **1980**, *72*, 279.
(122) Berendsen, H. J. C.; Postma, P. M.; van Gunsteren, W. F.; DiNola, A.; Haak, J. R. *Journal of Chemical Physics* **1984**, *81*, 3684.
(123) Haile, J. M.; Graben, H. W. *Journal of Chemical Physics* **1980**, *73*, 2412.
(124) Haile, J. M.; Graben, H. W. *Molecular Physics* **1980**, *40*, 1433.
(125) Ray, J. R. *Journal of Chemical Physics* **1981**, *79*, 5128.
(126) Ewald, P. P. *Annalen Der Physik* **1921**, *64*, 253.
(127) Yeh, I.; Berkowitz, M. *Journal of Chemical Physics* **1999**, *111*, 3155.
(128) Toukmaji, A. Y.; Board, J. A. *Computer Physics Communications* **1996**, *95*, 73.
(129) Field, M. J. *A Practical Introduction to the Simulation of Molecular Systems*, Second ed.; Cambridge University Press: Cambridge, 2007.
(130) Verlet, L. *Physical Review* **1967**, *159*, 98.
(131) Swope, W. C.; Andersen, H. C.; Berens, P. H.; Wilson, K. R. *Journal of Chemical Physics* **1982**, *76*, 637.
(132) Hockney, R. W.; Eastwood, J. W. *Computer Simulation Using Particles*; McGraw-Hill, 1981.
(133) Andersen, H. C. *Journal of Computational Physics* **1983**, *52*, 24.
(134) Ryckaert, J. P.; Ciccotti, G.; Berendsen, H. J. C. *Journal of Computational Physics* **1977**, *23*, 327.
(135) Nosé, S. *Molecular Physics* **1984**, *52*, 255.
(136) Nosé, S. *Journal of Chemical Physics* **1984**, *81*, 511.
(137) Nosé, S.; Klein, M. L. *Molecular Physics* **1983**, *50*, 1055.
(138) Hoover, W. G. *Physical Review A* **1985**, *31*, 1695.
(139) Hoover, W. G. *Physical Review A* **1986**, *34*, 2499.
(140) Martyna, G. J.; Tobias, D. J.; Klein, M. L. *Journal of Chemical Physics* **1994**, *101*, 4177.

(141) Allinger, N. L. *Journal of the American Chemical Society* **1977**, *99*, 8127.
(142) Allinger, N. L.; Sprague, J. T. *Journal of the American Chemical Society* **1973**, *95*, 3893.
(143) Allinger, N. L.; Sprague, J. T.; Liljefor.T *Journal of the American Chemical Society* **1974**, *96*, 5100.
(144) Sprague, J. T.; Tai, J. C.; Yuh, Y.; Allinger, N. L. *Journal of Computational Chemistry* **1987**, *8*, 581.
(145) Allinger, N. L.; Yuh, Y. H.; Lii, J. H. *Journal of the American Chemical Society* **1989**, *111*, 8551.
(146) Allinger, N. L.; Chen, K. S.; Lii, J. H. *Journal of Computational Chemistry* **1996**, *17*, 642.
(147) Jorgensen, W. L.; Maxwell, D. S.; TiradoRives, J. *Journal of the American Chemical Society* **1996**, *118*, 11225.
(148) Jorgensen, W. L.; Tiradorives, J. *Journal of the American Chemical Society* **1988**, *110*, 1657.
(149) Brooks, B. R.; Bruccoleri, R. E.; Olafson, B. D.; States, D. J.; Swaminathan, S.; Karplus, M. *Journal of Computational Chemistry* **1983**, *4*, 187.
(150) Bayly, C. I.; Cieplak, P.; Cornell, W. D.; Kollman, P. A. *Journal of Physical Chemistry* **1993**, *97*, 10269.
(151) Case, D. A.; Cheatham, T. E.; Darden, T.; Gohlke, H.; Luo, R.; Merz, K. M.; Onufriev, A.; Simmerling, C.; Wang, B.; Woods, R. J. *Journal of Computational Chemistry* **2005**, *26*, 1668.
(152) Case, D. A.; Pearlman, D. A.; Caldwell, J. W.; Cheatham, T. E., III; Ross, W. S.; Simmerling, C. L.; Darden, T. A.; Merz, K. M.; Stanton, R. V.; Cheng, A. L.; Vincent, J. J.; Crowley, M.; Tsui, V.; Radmer, R. J.; Duan, Y.; Pitera, J.; Massova, I.; Seibel, G. L.; Singh, U. C.; Weiner, P. K.; Kollman, P. A.; University of California: San Francisco, CA, 1999.
(153) Ryckaert, J. P.; Bellemans, A. *Chemical Physics Letters* **1975**, *30*, 123.
(154) Berardi, R.; Orlandi, S.; Zannoni, C. *Physical Review E* **2003**, *67*, 14.
(155) Narten, A. H. *Journal of Chemical Physics* **1977**, *67*, 2102.
(156) Ayton, G.; Wei, D. Q.; Patey, G. N. *Physical Review E* **1996**, *55*, 447.
(157) Wilson, M. R. *Chemical Society Reviews* **2007**, *36*, 1881.
(158) Wilson, M. R. *Journal of Chemical Physics* **1997**, *107*, 8654.
(159) Glaser, M. A. In *Advances in the Computer Simulations of Liquid Crystals*; Pasini, P., Zannoni, C., Ed.; Kluwer Academic Publishers: Dodrecht, 2000; Vol. 545, pp 263.
(160) Leggetter, S.; Tildesley, D. J. *Molecular Physics* **1989**, *68*, 519.
(161) Frisch, M. J. T., G. W.; Schlegel, H. B.; Scuseria, G. E.; Robb, M. A.; Cheeseman, J. R.; Montgomery, Jr., J. A.; Vreven, T.; Kudin, K. N.; Burant, J. C.; Millam, J. M.; Iyengar, S. S.; Tomasi, J.; Barone, V.; Mennucci, B.; Cossi, M.; Scalmani, G.; Rega, N.; Petersson, G. A.; Nakatsuji, H.; Hada, M.; Ehara, M.; Toyota, K.; Fukuda, R.; Hasegawa, J.; Ishida, M.; Nakajima, T.; Honda, Y.; Kitao, O.; Nakai, H.; Klene, M.; Li, X.; Knox, J. E.; Hratchian, H. P.; Cross, J. B.; Bakken, V.; Adamo, C.; Jaramillo, J.; Gomperts, R.; Stratmann, R. E.; Yazyev, O.; Austin, A. J.; Cammi, R.; Pomelli, C.; Ochterski, J. W.; Ayala, P. Y.; Morokuma, K.; Voth, G. A.; Salvador, P.; Dannenberg, J. J.; Zakrzewski, V. G.; Dapprich, S.; Daniels, A. D.; Strain, M. C.; Farkas, O.; Malick, D. K.; Rabuck, A. D.; Raghavachari, K.; Foresman, J. B.; Ortiz, J. V.; Cui, Q.; Baboul, A. G.; Clifford, S.; Cioslowski, J.; Stefanov, B. B.; Liu, G.; Liashenko, A.; Piskorz, P.; Komaromi, I.; Martin, R. L.; Fox, D. J.; Keith, T.; Al-Laham, M. A.; Peng, C. Y.; Nanayakkara, A.;

Challacombe, M.; Gill, P. M. W.; Johnson, B.; Chen, W.; Wong, M. W.; Gonzalez, C.; and Pople, J. A.: Gaussian, Inc., Wallingford CT, 2004.
(162) Becke, A. D. *Journal of Chemical Physics* **1993**, *98*, 5648.
(163) Clark, T.; Chandrasekhar, J.; Spitznagel, G. W.; Schleyer, P. V. *Journal of Computational Chemistry* **1983**, *4*, 294.
(164) Frisch, M. J.; Pople, J. A.; Binkley, J. S. *Journal of Chemical Physics* **1984**, *80*, 3265.
(165) Breneman, C. M.; Wiberg, K. B. *Journal of Computational Chemistry* **1990**, *11*, 361.
(166) Cacelli, I.; Prampolini, G. *Journal of Physical Chemistry A* **2003**, *107*, 8665.
(167) Tsuzuki, S.; Uchimaru, T.; Matsumura, K.; Mikami, M.; Tanabe, K. *Journal of Chemical Physics* **1999**, *110*, 2858.
(168) Berthelot; D.C. *(r) Hebdomadaires des Séances de l'Académie des Sciences, Paris* **1898**, *126*.
(169) Lorentz, H. A. *Annalen Der Physik* **1981**, *2*.
(170) Prampolini, G. *Journal of Chemical Theory and Computation* **2006**, *2*, 556.
(171) Arunan, E.; Gutowsky, H. S. *Journal of Chemical Physics* **1993**, *98*, 4294.
(172) Law, K. S.; Schauer, M.; Bernstein, E. R. *Journal of Chemical Physics* **1984**, *81*, 4871.
(173) Steed, J. M.; Dixon, T. A.; Klemperer, W. *Journal of Chemical Physics* **1979**, *70*, 4940.
(174) Venturo, V. A.; Felker, P. M. *Journal of Chemical Physics* **1993**, *99*, 748.
(175) Jaffe, R. L.; G.D., S. *Journal of Chemical Physics* **1996**, *105*, 2780.
(176) Sinnokrot, M. O.; Valeev, E. F.; Sherrill, C. D. *Journal of the American Chemical Society* **2002**, *124*, 10887.
(177) Špirko, V.; Engkvist, O.; Soldán, P.; Selzle, H. L.; Schlag, E. W.; Hobza, P. *Journal of Chemical Physics* **1999**, *111*, 572.
(178) Tsuzuki, S.; Honda, K.; Uchimaru, T.; Mikami, M.; Tanabe, K. *Journal of the American Chemical Society* **2002**, *124*, 104.
(179) Tsuzuki, S.; Uchimaru, T.; Sugawara, K.; Mikami, M. *Journal of Chemical Physics* **2002**, *117*, 11216.
(180) Sinnokrot, M. O.; Sherrill, C. D. *Journal of Physical Chemistry A* **2004**, *108*, 10200.
(181) Sinnokrot, M. O.; Sherrill, C. D. *Journal of Physical Chemistry A* **2006**, *110*, 10656.
(182) Battaglia, M. R.; Buckingham, A. D.; Williams, J. H. *Chemical Physics Letters* **1981**, *78*, 420.
(183) Cacelli, I.; Cinacchi, G.; Prampolini, G.; Tani, A. *Journal of Chemical Physics* **2004**, *120*, 3648.
(184) *CRC Handbook of Chemistry and Physics*; CRC Press: Boca Raton, 1997.
(185) Cabaço, M. I.; Danten, Y.; Besnard, M.; Guissani, Y.; Guillot, B. *Journal of Physical Chemistry B* **1997**, *101*, 6977.
(186) Chelli, R.; Procacci, P. *Journal of Chemical Physics* **2002**, *117*, 9175.
(187) Contreras-Camacho, O. R.; Ungerer, P.; Boutin, A.; Mackie, A. D. *Journal of Physical Chemistry A* **2004**, *108*, 14109.
(188) Kim, J. H.; Lee, S. H. *Bulletin of the Korean Chemical Society* **2002**, *23*, 441.
(189) Kim, J. H.; Lee, S. H. *Bulletin of the Korean Chemical Society* **2002**, *23*, 447.
(190) Tao, G. H.; Stratt, R. M. *Journal of Physical Chemistry B* **2006**, *110*, 976.
(191) Bartsch, E.; Bertagnolli, H.; Chieux, P. *Berichte der Bunsengesellschaft fur Physikalische Chemie* **1986**, *90*, 34.
(192) Bartsch, E.; Bertagnolli, H.; Schultz, G.; Chieux, P. *Berichte der Bunsengesellschaft fur Physikalische Chemie* **1985**, *89*, 147.
(193) Felici, R.; Cilloco, F.; Bosi, P. *Molecular Physics* **1990**, *70*, 455.
(194) Misawa, M., Fukunaga, T. *Journal of Chemical Physics* **1990**, *93*, 3495.

(195) Falcone, D. R.; Douglass, D. C.; Mccall, D. W. *Journal of Physical Chemistry* **1967**, *71*, 2754.
(196) Graupner, K.; Winter, E. R. S. *Journal of the Chemical Society* **1952**, 1145-1150.
(197) Hiraoka, H.; Osuji, J.; Jono, W. *Review of the Physical Chemistry Japan* **1958**, *28*, 52.
(198) Rathbun, R. E.; Babb, A. L. *Journal of Physical Chemistry* **1961**, *65*, 1072.
(199) Chelli, R.; Cardini, G.; Procacci, P.; Righini, R.; Califano, S.; Albrecht, A. *Journal of Chemical Physics* **2000**, *113*, 6851.
(200) Bastiansen, O.; Samdal, S. *Journal of Molecular Structure* **1985**, *128*, 115.
(201) Charbonneau, G. P.; Delugeard, Y. *Acta Crystallographica B* **1977**, *33*, 1586.
(202) Wise, W. B.; Kurland, R. J. *Journal of American Chemical Society* **1964**, *86*, 1877.
(203) Arulmozhiraja, S.; Fujii, T. *Journal of Chemical Physics* **2001**, *115*, 10589.
(204) Baranyai, A.; Welberry, T. R. *Molecular Physics* **1991**, *73*, 1317.
(205) Baranyai, A.; Welberry, T. R. *Molecular Physics* **1992**, *75*, 867.
(206) Celebre, G.; De Luca, G.; Longeri, M.; Catalano, D.; Veracini, C. A.; Emsley, J. W. *Journal of the Chemical Society-Faraday Transactions* **1991**, *87*, 2623.
(207) Chakrabarti, A.; Yashonath, S.; Rao, C. N. R. *Molecular Physics* **1995**, *84*, 49.
(208) Göller, A.; Grummt, U. *Chemical Physics Letters* **2000**, *321*, 399.
(209) Grein, F. *Journal of Physical Chemistry A* **2002**, *106*, 3823.
(210) Grein, F. *Journal of Molecular Structure (THEOCHEM)* **2003**, *624*, 23.
(211) Palke, W. E.; Catalano, D.; Celebre, G.; Emsley, J. W. *Journal of Chemical Physics* **1996**, *105*, 7026.
(212) Tsuzuki, S.; Tanabe, K. *Journal of Chemical Physics* **1991**, *95*, 139.
(213) Almenningen, A.; Bastiansen, O.; Fernholt, L.; Cyvin, B. N.; Cyvin, S. J.; Samdal, S. *Journal of Molecular Structure* **1985**, *128*, 59.
(214) Eaton, V. J.; Steele, D. *Journal of the Chemical Society-Faraday Transactions* **1973**, *69*, 1601.
(215) Cheung, D. L.; Clark, S. J.; Wilson, M. R. *Physical Review E* **2002**, *65*, 051709.
(216) Yaws, C. L. *Chemical Properties Handbook*; McGraw-Hill, 1999.
(217) Červená, J.; Bayer, R.; Schaferl, W. *Czechoslovak Journal of Physics* **1973**, *B 23*, 1187.
(218) Dijon, J. In *Liquid Crystals: Applications and Uses*; Bahadur, B., Ed.; Word Scientific: Singapore, 1990; Vol. 1.
(219) Lagerwall, S. T. In *Handbook of Liquid Crystals*; Demus, D., Goodby, J. W., Gray, G. W., Spiess, H. W., Vill, V., Eds.; Wiley-VCH: Weinheim, 1998; Vol. 2B.
(220) Goodby, J. W.; Blinc, R.; Clark, N. A.; Lagerwall, S. T.; Osipov, M. A.; Pikin, S. A.; Sakurai, T.; Yoshino, K.; Zeks, B. *Ferroelectric Liquid Crystals: Principles, Properties, and Applications*; Gordon & Breach Science: Philadelphia, 1991.
(221) Lagerwall, S. T. *Ferroelectric and Antiferroelectric Liquid Crystals*; Wiley-VCH: Weinheim, 1999.
(222) Elekema, R.; Feringa, B. L. *Organic & Biomolecular Chemistry* **2006**, *4*, 3729.
(223) Proni, G.; Spada, G. P. *Enantiomer* **2001**, *6*, 171.
(224) Earl, D. J.; Wilson, M. R. *Journal of Chemical Physics* **2003**, *119*, 10280.
(225) Wilson, M. R.; Earl, D. J. *Journal of Materials Chemistry* **2001**, *11*, 2672.
(226) Hartley, C. S.; Lazar, C.; Wand, M. D.; Lemieux, R. P. *Journal of the American Chemical Society* **2002**, *124*, 13513.
(227) Hartley, C. S.; Wang, R. Y.; Lemieux, R. P. *Chemistry of Materials* **2004**, *16*, 5297.
(228) Lazar, C.; Yang, K. X.; Glaser, M. A.; Wand, M. D.; Lemieux, R. P. *Journal of Materials Chemistry* **2002**, *12*, 586.
(229) Hegmann, T.; Lemieux, R. P. *Journal of Materials Chemistry* **2002**, *12*, 3368.

(230) Hegmann, T.; Meadows, M. R.; Wand, M. D.; Lemieux, R. P. *Journal of Materials Chemistry* **2004**, *14*, 1.
(231) de Miguel, E.; del Rio, E. M. *Physical Review Letters* **2005**, *95*, 21802.
(232) Capitan, J. A.; Martinez-Raton, Y.; Cuesta, J. A. *Journal of Chemical Physics* **2008**, *128*, 194901.
(233) Avendaño, C.; Gil-Villagas, A.; González-Tovar, E. *Journal of Chemical Physics* **2008**, *128*, 044506.
(234) Cuetos, A.; Martinez-Haya, B. *Journal of Chemical Physics* **2008**, *129*, 214706.
(235) Camp, P. J.; Allen, M. P.; Masters, A. J. *Journal of Chemical Physics* **1999**, *111*, 9871.
(236) Lansac, Y.; Maiti, P. K.; Clark, N. A.; Glaser, M. A. *Physical Review E* **2003**, *67*, 011703.
(237) Parrinello, M.; Rahman, A. *Physical Review Letters* **1980**, *45*, 1196.
(238) Cressman, E. D., Dunford, J.; Pecheanu, R.; Huh, Y.; Nita, S.; Paci, I.; Wang, S.; Zhao, C.; Cann, N. M., unpublished.
(239) Saha, J.; Bose, T. R.; Ghosh, D.; Saha, M. *Physics Letters A* **2005**, *336*, 396.

Appendix A

Interaction Potentials for Liquid Crystal Molecules

Table A1 Site types and charge values from the Density Functional Theory calculations for the 2PhP and 5PhP liquid crystal molecules. The charges are given in units of e^-, the electron charge, and are obtained using the CHEPLG algorithm[165] applied to the B3LYP/6-311++G(d,p) global energy minima. Lennard-Jones (LJ) and Gay-Berne (GB) parameters are identical for 2PhP and 5PhP and are obtained from the references listed below. Site numbering is provided in Figures 3.2 (a) and (b) for the 2PhP and 5PhP molecules, respectively.

SITE NO.	ATOM/GROUP	SITE TYPE	**2PhP** Charge (|e|)	**5PhP** Charge (|e|)
1	CH3	LJ	0.0	0.0
2, and 3	CH2	LJ	0.0	0.0
4	CH2	LJ	0.2469	0.2533
5	O	LJ	-0.3704	-0.4924
6	Phenyl	GB	0.2352	0.3118
7	Pyrimidine	GB	0.0570	0.1796
8	O	LJ	-0.3996	-0.5034
9	CH2	LJ	0.2309	0.2511
10, 11, 12, 13, 14, and 15	CH2	LJ	0.0	0.0
16	CH3	LJ	0.0	0.0

Table A2 Details of the equilibrium bond lengths of the 2PhP and 5PhP liquid crystal molecules from the B3LYP/6-311++G(d,p) global energy minimum. All carbon-carbon bond lengths, omitted from this table, are 0.1530 nm and are taken from literature.[160]

BOND	**2PhP** Bond length (nm)	**5PhP** Bond length (nm)
4-5	0.1421	0.1422
5-6	0.2769	0.2744
6-7	0.4236	0.4235
7-8	0.2708	0.2686
8-9	0.1424	0.1433

Table A3 Details of the bending potentials (see Equation (2.45)) for 2PhP and 5PhP liquid crystal molecules from B3LYP/6-311++G(d,p) constrained geometry optimizations. Bending potentials for carbons in the hydrocarbon tails are taken from literature,[160] and have equilibrium angles of 109.47 degrees with force constants of 520.55 kJ mol^{-1} rad^{-2}.

ANGLE	2PhP		5PhP	
	θ_{eq}(degree)	k_θ (kJ mol^{-1} rad^{-2})	θ_{eq}(degree)	k_θ (kJ mol^{-1} rad^{-2})
6,5,4	118.70	347.82	118.65	350.69
7,6,5	180.00	520.55	180.00	520.55
8,7,6	180.00	520.55	180.00	520.55
9,8,7	118.04	368.81	117.85	379.77
17,6,5	90.00	722.26	90.00	722.26
18,7,6	90.00	722.26	90.00	722.26

Table A4 Details of the torsion potentials (Equation (2.46)) for 2PhP and 5PhP liquid crystal molecules extracted from B3LYP/6-311++G(d,p) constrained geometry optimizations. All other torsions involve hydrocarbon C-C bonds or C-O bonds and have torsion parameters taken from literature,[160] in kJ/mol, as follows: c_0=9.2789, c_1=12.1557, c_2=-13.1202, c_3=-3.0597, c_4=26.2405, and c_5=-31.4952.

TORSIONAL ANGLE	Force Constant (kJ mol^{-1})						
	C_0	C_1	C_2	C_3	C_4	C_5	C_6
2PhP							
17,6,5,4	14.1815	-0.3000	-4.2736	-1.1496	-13.4783	1.4019	3.6093
18,7,6,17	39.7173	0.2148	-56.5847	-0.6538	22.1939	0.3690	-5.3310
18,7,8,9	11.2939	-0.1627	0.1449	-1.4771	-16.4432	1.5987	4.6900
5PhP							
17,6,5,4	13.3603	-1.3212	-8.1129	4.1272	-5.2828	-2.5142	-0.1608
18,7,6,17	7.7220	0.0026	-30.1835	-0.3058	29.3834	-0.2430	0.3252
18,7,8,9	28.9044	-0.8658	-26.5883	0.0976	-2.3290	0.8506	-0.0693

Appendix B

Interaction Potentials for Chiral Dopant Molecules

Table B1 Site types and charge values from the Density Functional Theory calculations for the Dop5a-NO_2 chiral dopant molecule. The charges are given in units of e^-, the electron charge, and are obtained using the CHELPG algorithm[165] applied to the B3LYP/6-311++G(d,p) global energy minima. Site numbering is provided in Figure 3.6 (b).

SITE NO.	ATOM/GROUP	SITE TYPE	Charge (|e|)
1	CH3	LJ	0.2409
2	O	LJ	-0.3881
3	Phenyl	GB	0.1708
4	C(CO)[a]	LJ	0.7304
5	O	LJ	-0.4340
6	GBB[b]	GB	0.1960
7	GBB[b]	GB	0.1960
8	O	LJ	-0.4349
9	C(CO) [a]	LJ	0.7307
10	Phenyl	GB	0.1710
11	O	LJ	-0.3887
12	CH3	LJ	0.2412
13	O(CO)[c]	LJ	-0.5156
14	O(CO) [c]	LJ	-0.5157

a - C(CO) represents the carbon atom from carbonyl group
b - GBB represents the 2,6-dimethyl-3-nitro-phenyl group
c- O(CO) represents the oxygen atom from carbonyl group

Table B2 Details of the equilibrium bond lengths of the Dop5a-NO_2 chiral dopant molecule from the B3LYP/6-311++G(d,p) global energy minimum.

BOND	Bond length (nm)
1- 2	0.1423
2- 3	0.2754
3- 4	0.2874
4-13	0.1203
4- 5	0.1384
5- 6	0.2778
6- 7	0.4309
7- 8	0.2778
8- 9	0.1384
9-14	0.1232
9-10	0.2875
10-11	0.2754
11-12	0.1423

Table B3 Details of the bending potentials (see Equation (2.45)) for the Dop5a-NO_2 chiral dopant molecule from B3LYP/6-311++G(d,p) constrained geometry optimizations.

ANGLE	θ_{eq}(degree)	k_θ (kJ mol^{-1} rad^{-2})
3,2,1	118.92	483.98
4,3,2	180.00	520.55
13,4,3	126.00	461.41
5,4,3	110.44	605.26
5,4,13	123.55	557.39
6,5,4	124.29	261.10
7,6,5	180.00	520.55
8,7,6	180.00	520.55
9,8,7	124.31	261.10
14,9,8	123.56	557.39
10,9,8	110.44	605.26
10,9,14	126.00	461.41
11,10,9	180.00	520.55
12,11,10	118.92	483.98
15,3,2	90.00	722.26
16,6,5	90.00	722.26
17,7,6	90.00	722.26
18,10,9	90.00	722.26

Table B4 Details of the torsional potentials (see Equation (2.46)) for the Dop5a-NO_2 chiral dopant molecule from B3LYP/6-311++G(d,p) constrained geometry optimizations.

TORSIONAL ANGLE	Force Constant (kJ mol^{-1})						
	C_0	C_1	C_2	C_3	C_4	C_5	C_6
15,3,2,1	18.9691	-1.0791	-9.0298	-0.9039	-12.9285	1.3096	3.9366
16,6,5,4	-30.0139	4.3999	7.4110	-9.1782	-47.5262	18.6368	56.2704
6,5,4,13	24.7293	-17.5359	-12.8985	3.4379	-8.3129	-5.0870	15.8061
5,4,3,15	36.6224	-9.6001	-50.5466	7.5763	14.9911	0.0854	-0.0002
6,5,4,3	27.2387	11.6175	-12.7658	-2.6950	5.9270	11.1139	-0.6461
13,4,3,15	37.3396	5.6299	-45.4565	-3.3915	12.4416	0.2343	-2.0275
17,7,6,16	-3.0561	4.2947	121.7769	-9.7056	-267.5822	6.4271	284.4751
18,10,9,14	37.3396	5.6299	-45.4565	-3.3915	12.4416	0.2343	-2.0275
10,9,8,7	27.2387	11.6175	-12.7658	-2.6950	5.9270	11.1139	-0.6461
18,10,9,8	36.6224	-9.6001	-50.5466	7.5763	14.9911	0.0854	-0.0002
14,9,8,7	24.7293	-17.5359	-12.8985	3.4379	-8.3129	-5.0870	15.8061
9,8,7,17	-30.0139	4.3999	7.4110	-9.1782	47.5262	18.6368	56.2704
12,11,10,18	18.9691	-1.0791	-9.0298	-0.9039	12.9285	1.3096	3.9366

Table B5 Details of the improper torsional potentials (see Equation (2.47)) for the Dop5a-NO_2 chiral dopant molecule from B3LYP/6-311++G(d,p) constrained geometry optimizations.

IMPROPER DIHEDRAL ANGLE	θ_{eq}(degree)	k_θ (kJ mol^{-1} rad^{-2})
13,5,3,4	0.02	553.03
14,8,10,9	0.02	554.30

Table B6 Site types and charge values from the Density Functional Theory calculations for the Spiro chiral dopant molecule. The charges are given in units of e^-, the electron charge, and are obtained using the CHELPG algorithm[165] applied to the B3LYP/6-311++G(d,p) global energy minimum. Site numbering is provided in Figure 3.10 (b).

SITE NO.	ATOM/GROUP	SITE TYPE	Charge (|e|)
1	CH3	LJ	0.0
2, 3, 4, 5, and 6	CH2	LJ	0.0
7	CH2	LJ	0.2357
8	O	LJ	-0.3835
9	SP*	GB	0.1489
10	SP*	GB	0.1489
11	O	LJ	-0.3814
12	CH2	LJ	0.2414
13, 14, 15, 16, and 17	CH2	LJ	0.0
18	CH3	LJ	0.0

***** SP represents a half of the 2,2'-spirobiindan-1,1'-dione group

Table B7 Details of the equilibrium bond lengths of the Spiro chiral dopant molecule from the B3LYP/6-311++G(d,p) global energy minimum. All carbon-carbon bond lengths omitted from this table are 0.1530 nm and are taken from Legetter and Tildesley's work.[160]

BOND	Bond length (nm)
7-8	0.1424
8-9	0.3850
9-10	0.4726
10-11	0.3850
11-12	0.1424

Table B8 Details of the bending potentials for the Spiro chiral dopant molecule from B3LYP/6-311++G(d,p) constrained geometry optimizations. Bending potentials for carbons in the hydrocarbon tails are taken from Legetter and Tildesley's work[160] and have equilibrium angles of 109.47 degrees with force constants of 520.55 kJ mol^{-1} rad^{-2}.

ANGLE	θ_{eq}(degree)	k_θ (kJ mol^{-1} rad^{-2})
9,8,7	119.27	360.31
10,9,8	180.00	520.55
11,10,9	180.00	520.55
12,11,10	119.04	336.56
19,9,8	90.00	722.26
20,10,9	90.00	722.26

Table B9 Details of the torsional potentials (see Equation (2.46)) for the Spiro chiral dopant molecule from B3LYP/6-311++G(d,p) constrained geometry optimizations. All other torsions involve hydrocarbon C-C bonds or C-O bonds and have torsion parameters taken from literature,[160] in kJ/mol, as follows: c_0=9.2789, c_1=12.1557, c_2=-13.1202, c_3=-3.0597, c_4=26.2405, and c_5=-31.4952.

TORSIONAL ANGLE	Force Constant (kJ mol^{-1})						
	C_0	C_1	C_2	C_3	C_4	C_5	C_6
19,9,8,7	16.0149	-0.0429	-9.2516	-2.1759	-6.6604	1.8743	0.0501
12,11,10,20	17.0287	0.2369	-9.1269	-2.5237	-7.6027	1.8557	0.0642

Appendix C

NPT Ensemble Simulations Details

Table C1 Details of the NPT ensemble simulations of 256 2PhP molecules. An initial 1:1:2 ratio simulation cell and a nematic-like parallel starting configuration at initial density of 0.90 g/mL has been used in all simulations. The temperature has been kept constant using two independent Nosé-Hoover thermostats, for rotational and translational motions. Five independent 2ns runs at 335K and 365K, three independent 2ns runs at 400K, and two 2ns runs for 450K have been simulated. All simulations at 335K and 365K have been repeated for the A1, B1, B2, and C1 ring models, while all simulations at 400K and 450K have been done using only the B1 and C1 ring models. In total, results from 50 independent shorter runs (2ns) have been reported for the 2PhP molecule. Longer runs at 365K using the B1 ring model (12ns) and the C1 ring models (14 ns) have also been employed. In addition, a short 2ns run starting from an anti-parallel initial configuration has been employed for 2PhP at 365K using the B1 ring model (initial P_2^D=0.80 and density=0.90 g/mL). The initial order parameters relative to the director, P_2^D, are shown.

Temperature	**335K**				**365K**			
Ring Model	**A1**	**B1**	**B2**	**C1**	**A1**	**B1**	**B2**	**C1**
Property	Initial P_2^D				Initial P_2^D			
Run 1	0.77				0.77			
Run 2	0.56				0.56			
Run 3	0.81				0.81			
Run 4	0.79				0.79			
Run 5	0.78				0.78			
Temperature	**400K**				**450K**			
Ring Model	**B1**		**C1**		**B1**		**C1**	
Property	Initial P_2^D				Initial P_2^D			
Run 1	0.81				0.78			
Run 2	0.79				0.79			
Run 3	0.76				-			

Table C2 Details of the NPT ensemble simulations of 256 5PhP molecules. An initial 1:1:2 ratio simulation cell and a nematic-like parallel starting configuration at initial density of 0.90 g/mL has been used in all simulations. The temperature has been kept constant using two independent Nosé-Hoover thermostats, for rotational and translational motions. Five independent 2ns runs at 335K and 365K, three independent 2ns runs at 400K, and two 2ns runs for 450K have been simulated. All simulations at 370K have been repeated for the A1, B1, B2, and C1 ring models, while all simulations at 400K and 450K have been done using only the B1 and C1 ring models. In total, results from 30 independent shorter runs (2ns) have been reported for the 2PhP molecule. Longer runs at 370K using the B1 ring model (8ns) and the C1 ring models (12 ns) have also been employed. The initial order parameters relative to the director, P_2^D, are shown.

Temperature	**370K**				**400K**		**450K**	
Ring Model	**A1**	**B1**	**B2**	**C1**	**B1**	**C1**	**B1**	**C1**
Property	Initial P_2^D				Initial P_2^D		Initial P_2^D	
Run 1	0.77				0.81		0.78	
Run 2	0.79				0.79		0.79	
Run 3	0.81				0.76		-	
Run 4	0.79				-		-	
Run 5	0.78				-		-	